Applications of Dynamic Force Microscopy to Molecular-Scale Investigations on Organic Ultrathin Films

Takeshi Fukuma

January, 2003

Contents

Chapter 1

Introduction

1.1 Background

1.1.1 Organic Electronics

Since the invention of transistor in 1948, the solid-state electronics have been tremendously developed for about 50 years. The integration of the electronic circuits onto a single silicon chip enabled high-speed processing and storage of large amount of information. Photo emitting and detecting devices such as laser and photo diodes made of compound semiconductors enabled high-speed networking through the optical fiber cables. These key devices which play important roles in the present information-oriented society are mostly made of inorganic materials such as Si, III-V semiconductors and metals. On the other hand, in the field of electronics, organic materials have been used as passive components such as insulators and photoresists for the lithography.

Recently, however, there has been growing attention to the "organic electronics" where organic materials are used as active devices in the electronic circuits because of their practical advantages as well as academic interests. For example, since organic thin films are relatively soft and tolerant to the bending, novel applications such as flexible displays using organic electroluminescent (EL) devices[1,2] can be expected. Low-cost and low-temperature fabrications of active matrix displays would be realized by using organic field effect transistors (FETs)[3,4] in the driving circuits. In addition, the possibility of ultrahigh density data storage devices using organic ferroelectric thin films was recently demonstrated.[5] Because of these fascinating applications, the number of researchers in the field has drastically increased in the last a few years. So far, many research efforts were concentrated on the device fabrications and evaluations of their performance, which successfully demonstrated promising potential of organic thin film devices.[6–9] However, in order to fabricate practicable devices, further improvement would be required in terms of their effi-

ciency and durability. Since such device performance can be significantly affected by the microscopic structures and properties of the thin films, it would be of great importance to investigate such local information on a nanometer-scale.

In addition to these thin film devices, there has been proposed another promising application called "molecular electronics", where individual molecules work as active devices such as rectifiers and transistors. In 1974, Aviram and Ratner first proposed an idea of the molecular electronic device which functions as a rectifier.[10] Then in 1980s, Carter presented more comprehensive concept of molecular electronics.[11,12] Since the molecular devices have the size of single molecule, typically smaller than a few nanometers, they are expected to be the basic units of the next generation integrated circuits. Moreover, if the fabrication of the molecular electronic circuits using self-assembly is realized, it would be possible to drastically cut down the fabrication costs and improve the productivity of the integrated circuit. Although these ideas stimulated much scientific and technological interest, it was not until quite recently that chemical syntheses of such molecular devices were realized.[13–15] For example, Tour and co-workers succeeded in syntheses of molecular switches proposed by Aviram.[13,14] Aratani and co-workers synthesized an extremely large π-conjugated oligomers composed of porphyrine arrays, which are expected to be used as molecular wires.[15] However, in order to advance to the next stage for the realization of molecular integrated circuits, it is required to develop direct access tools to the molecular-scale electronic devices.

1.1.2 Scanning Probe Microscopy

As described above, there are strong demands for the direct access tools for the nanometer-scale or molecular-scale organic electronic devices. Scanning probe microscopy (SPM) is one of the most promising tools to realize these requirements. Among various kinds of SPMs, scanning tunneling microscopy (STM)[16] exhibits the highest spatial resolution with a quite simple setup. Thus the method has been intensively used for the investigations on the molecular electronic devices. So far, the conductivity of the single π-conjugated molecule was directly measured using STM and microwave frequency alternating current STM.[17] The single molecular switching was directly visualized by molecular-scale STM imaging at a low temperature.[18] Furthermore, an electromechanical amplifier was demonstrated using a single fullerene molecule mechanically pressed with an STM probe.[19,20]

In spite of these excellent results presented so far, there have been pointed out some problems on STM applications to the organic systems. In STM, the tip-sample distance regulation is made by detecting the tunneling current flowing between the

tip and the surface. Since most of the organic materials show very poor conductivity, organic systems which can be imaged or evaluated by STM are quite limited. Thus STM cannot be applied to the investigations on most of organic thin film devices or relatively large molecular electronic devices.

On the other hand, there is another major SPM technique called atomic force microscopy (AFM).[21] In AFM, since the tip-sample distance regulation is made by detecting the tip-sample interaction forces, it can be used for the investigations even on insulators. This feature opend a wide variety of AFM applications to the organic thin films and metal oxides. However, this technique also has some problems in its applications to the organic surfaces. In AFM, the tip is scanned in contact with the sample surface. Accordingly, if the sample is relatively soft such as polymers and biological samples, the surface will be damaged by the tip and the reproducible imaging is quite difficult. In addition, the true-atomic resolution AFM images can be obtained only in a liquid environment.

Recently significant advance has been made in dynamic force microscopy (DFM)[22,23] where the tip-sample interactions are detected by the mechanically vibrated cantilever. In DFM, the tip is scanned in intermittently contact or non-contact with the sample surface so that the lateral component of the interaction force is significantly reduced compared to that of AFM. Thus, even relatively soft materials can be imaged by DFM with nanometer-scale resolution. In addition, when DFM is used under ultrahigh vacuum (UHV) conditions, true-atomic resolution can be obtained even on insulating surfaces[24,25] which cannot be imaged by STM. Since organic materials are relatively soft and have poor conductivity, DFM should be quite suitable for the investigations on the surface structures of organic materials. Moreover, the molecular-resolution on insulating surface is essential for the future applications to molecular electronic devices because electronic devices should be insulated from the conductive substrates.

Another big advantage of DFM is its applications to the surface property measurements. For example, surface potential distribution can be mapped with bias modulation method which is called Kelvin probe force microscopy (KFM).[26] Furthermore, recently it was suggested that the surface mechanical property or electrical conductivity can be evaluated from the dissipation of the cantilever vibration energy induced by the tip-sample interactions.[27,28] So far these techniques have been mainly applied to the inorganic surfaces, demonstrating their atomic-scale resolutions.[29,30] However, the interpretation of the obtained images, especially of their atomic-scale contrasts, still remains controversial. In addition, there have been almost no reports on the molecular-scale surface property measurements of organic surfaces. Although there still remain a lot of issues to be established concerning these techniques, their

extremely high spatial resolution indicates a promising potential for the molecular-scale surface property measurements.

In spite of these distinctive features described above, DFM has not been well exploited to the characterization of organic materials. Two major reasons for this discrepancy are described as follows.

1. Although there are many advantages in DFM applications to the organic materials, most of them have never been experimentally demonstrated. In particular, there have been only a few reports on molecular-scale DFM imaging of organic surfaces. Thus it is still unclear what kind of information DFM can provide on organic materials and whether or not there are any problems specific to the organic surfaces.

2. Since DFM is still relatively new technique, there are many issues to be elucidated in terms of their imaging mechanisms. Thus the interpretations of the obtained images are often very difficult especially on its applications to the surface property measurements.

In order to make the best use of DFM for the investigations on organic materials, it is of great importance to solve these two problems.

1.2 Purpose

The purpose of this study is to advance the applications of DFM to the molecular-scale investigations on organic ultrathin films. In order to achieve this goal, the two problems pointed out in the previous section should be solved.

The first purpose is experimental demonstration of the possibilities and the problems of DFM applications to the organic thin films. DFM has mainly two distinctive advantages compared to the other SPM techniques. One of them is stable imaging ability of the relatively soft surfaces. In order to make use of this advantage, *in-situ* analyses of thermal phase transition processes of ferroelectric polymer thin films were performed. This is because the surfaces are expected to show fluid-like behavior during such phase transitions. Another advantage is true-atomic resolution on insulating surfaces. There are a lot of insulating organic systems which cannot be imaged by STM. Among them, typical cases are thin films on insulators and thin films with a thickness of larger than about 2 nm. In this study, DFM was applied to the molecular-scale imaging of such insulating surfaces.

The second purpose is further understanding of imaging mechanisms and development of molecular-scale surface property measurement techniques. These two things might appear to be quite different. However, they are strongly related to each

other. The tip-sample interaction forces contain information not only on the surface topography but also on the surface electrical, mechanical and chemical properties. Thus it is of great importance to detect these different force components separately and accurately, which will lead to the better understanding of topographic imaging and surface property measurements.

1.3 Structure of Thesis

This thesis is composed of the following seven chapters. The structure of the thesis is schematically shown in Fig. 1.1

In chapter 1, the background and the purpose of this study are described. The rapidly increasing needs for the molecular-scale investigation tools are pointed out. The distinctive advantages and the problems in DFM are discussed in terms of its applications to the organic thin films.

In chapter 2, the basic principles and the instrumentation of DFM are described. In particular, two major tip-sample distance regulation methods used in DFM are explained in detail. The instrumentation of energy dissipation measurement and surface potential measurement are also described.

In chapter 3, DFM applications to the *in-situ* analyses of thermal phase transitions were experimentally demonstrated on ferroelectric polymer thin films. The nano-scale structural and electrical changes during the thermal phase transition processes are directly visualized.

In chapter 4, the possibilities and the problems of FM-DFM applications to the molecular-scale investigations on insulating organic thin films were experimentally demonstrated.

In chapter 5, the dissipation mechanisms of the cantilever vibration energy were investigated in relation to the electrical interaction and the molecular fluctuation.

In chapter 6, the formation mechanisms of the molecular-scale contrasts in topography and dissipation were experimentally studied in relation to the chemical and mechanical properties of the organic surfaces.

In chapter 7, the conclusions of this study are summarized. Some proposals for the future works are also presented.

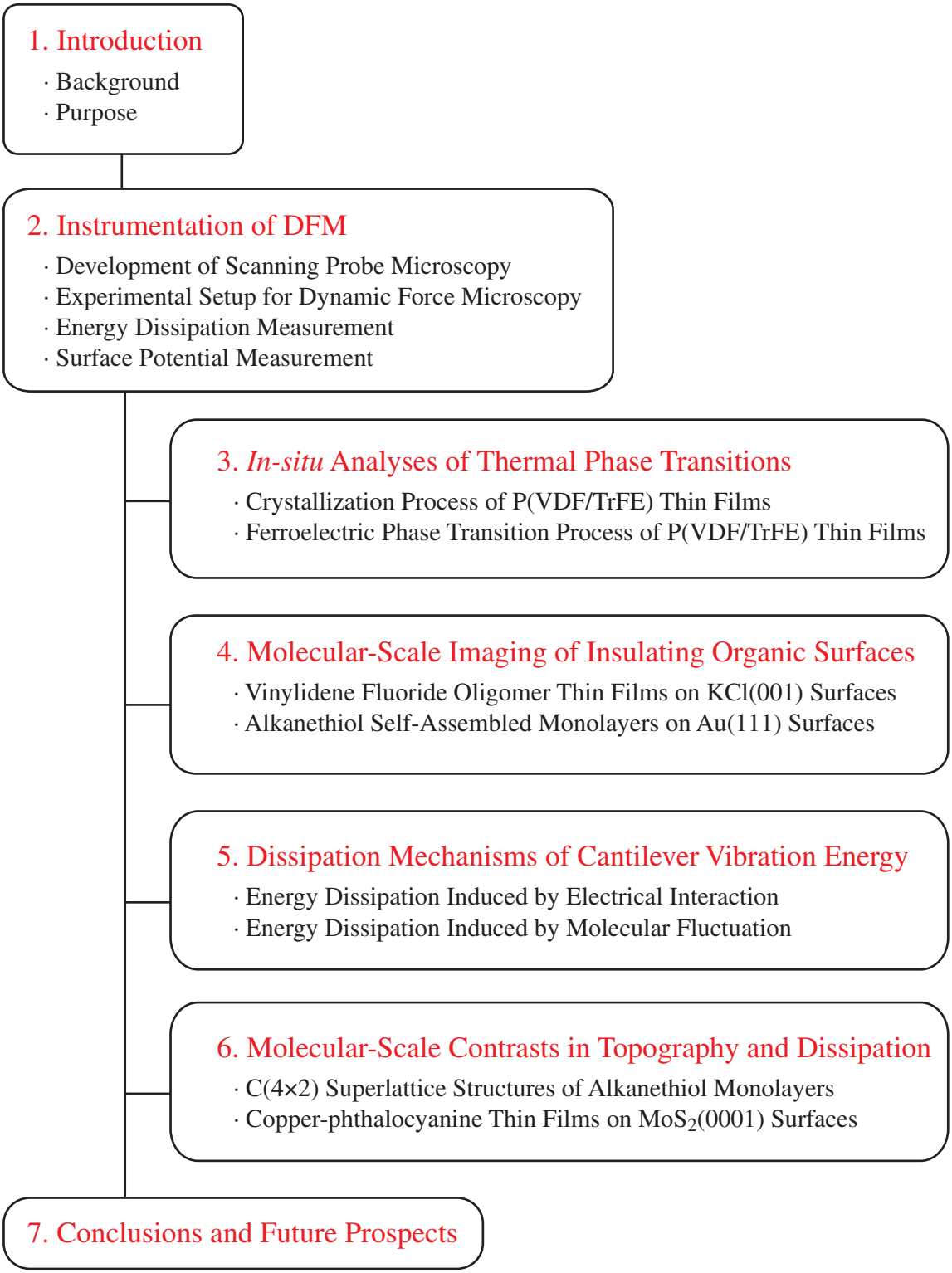

Figure 1.1: Structure of the thesis

Chapter 2

Instrumentation of Dynamic Force Microscopy

2.1 Development of Scanning Probe Microscopy

2.1.1 Scanning Tunneling Microscopy (STM)

In 1981, Binnig and Rohrer invented scanning tunneling microscopy (STM),[16] which allowed us to visualize atomic-scale structures directly in real-space. In STM, a sharp conductive tip is brought in close proximity of a conductive surface and laterally scanned. During the scan, the tunneling current flowing between the tip and the sample ($I_{\rm ts}$) is detected and kept constant by feedback electronics which controls the vertical position of the tip. Thus the surface height variations can be visualized from the tip trajectory during the scan.

Although the radius of the tip ($R_{\rm t}$) used in STM is much larger than the single-atomic scale, STM has achieved the highest spatial resolution in all SPMs. This can be understood from the strong distance dependence of $I_{\rm ts}$ which is described by

$$I_{\rm ts} = I_{\rm ts0} \exp(-2\kappa z_{\rm t}). \tag{2.1}$$

I_0 is a function of $V_{\rm ts}$ and the density of states in both the tip and the sample. $z_{\rm t}$ is the tip position with respect to the sample surface. κ is expressed by

$$\kappa = \frac{\sqrt{2m_{\rm e}\Phi_{\rm eff}}}{\hbar} \tag{2.2}$$

where $m_{\rm e}$ is the mass of the electron, $\Phi_{\rm eff}$ is the effective barrier height between the tip and the sample and $\hbar$ is the Planck's constant. For metals, $\Phi_{\rm eff} \simeq 4$ eV so that $\kappa = 0.1$ nm^{-1}, which means that 0.1 nm increase of $z_{\rm t}$ results in a current drop by an order of magnitude (Fig. 2.1(a)). Thus most of $I_{\rm ts}$ flows through the "front atom" that is closest to the sample (Fig. 2.1(b)). This is the most important reason for the extremely high spatial resolution of STM even with a relatively dull tip.

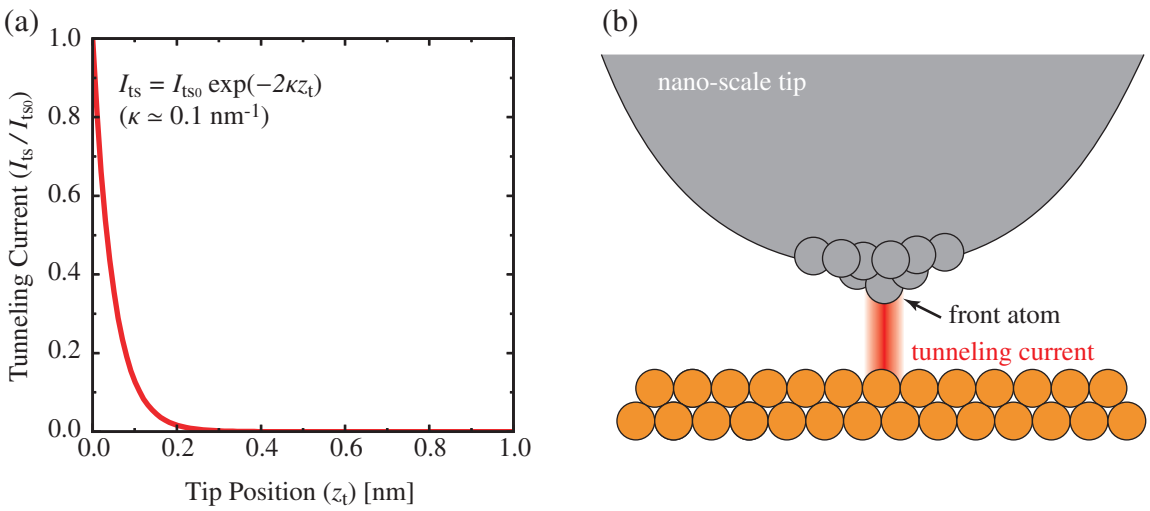

Figure 2.1: (a) Distance dependence of the tunneling current (I_{ts}) which flows between the tip and the sample. (b) A schematic model showing the tunneling current flowing between the tip and the sample. Due to the strong distance dependence of I_{ts}, most of it flows through the front atom that is closest to the sample, leading to the extremely high spatial resolution of STM.

So far, STM has been successfully applied to the studies on metals, semiconductors and molecular adsorbates on them. However, the utilization of the tunneling current significantly limits the range of the STM applications. STM cannot be used on the insulating surfaces such as polymers and metal oxides. STM cannot probe the interaction between the insulating materials.

2.1.2 Atomic Force Microscopy (AFM)

Basic Principle

In 1986, another probe technique referred to as atomic force microscopy (AFM) was invented by Binnig, Gerber and Quate,[21] which realized high-resolution imaging even on insulating surfaces. In AFM, a sharp tip is brought close to the surface and gently contacted on it. Then the interaction force acting between the tip and the sample (F_{ts}) is detected and its magnitude is kept constant while the tip is laterally scanned. The force detection is made by measuring the deflection of a cantilever that has a tip mounted at the end (Fig. 2.2).

Since the cantilever deflection induced by F_{ts} is generally much smaller than the length of the cantilever, the vertical displacement of the tip (Δz_t) shows linear dependence on F_{ts} as described by

$$\Delta z_t = \frac{F_{ts}}{k}, \tag{2.3}$$

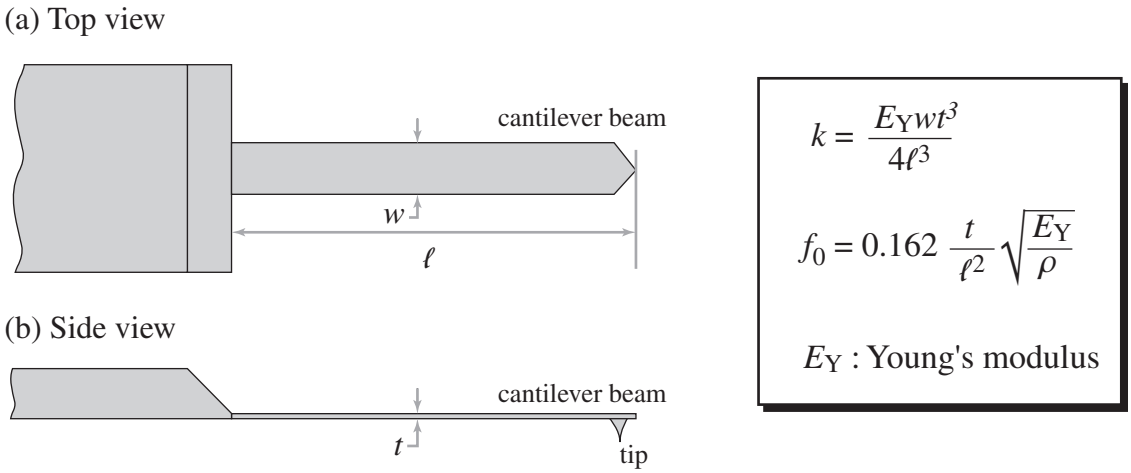

Figure 2.2: (a) Top view and (b) side view of the AFM force sensor which consists of the cantilever beam and a small tip mounted at the end.

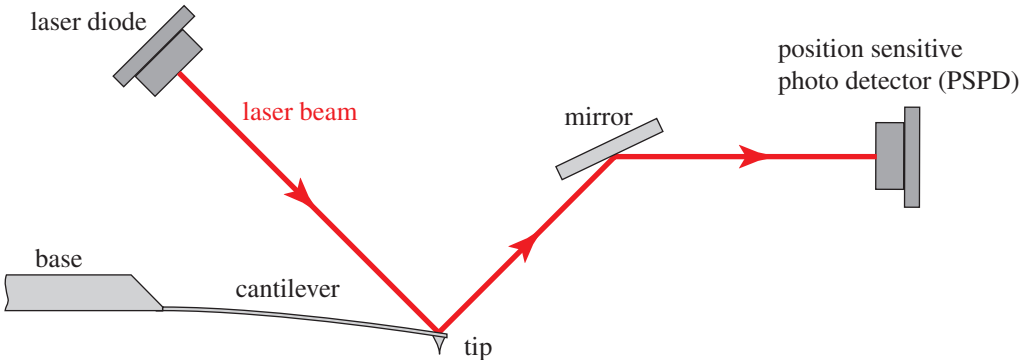

Figure 2.3: A schematic drawing of the setup to measure the cantilever deflection using laser beam deflection method.

where k is the spring constant of the cantilever.

Although many different methods for measuring Δz_t have been proposed, the one most commonly used is laser beam deflection method (Fig. 2.3). In this method, a focused laser beam is irradiated onto the backside of the cantilever and the reflected beam is detected by a position sensitive photo detector (PSPD) whose output signal (which is referred to as "deflection signal") represents the position of the laser spot irradiated onto it. Thus Δz_t is detected via the laser beam deflection.

Large Friction Force

In order to avoid the surface deformation, the cantilever should be much softer than the bonds between the bulk atoms in the tip and the sample. Inter-atomic spring constants in solids lie in a range from 10 N/m to 100 N/m, while in biological samples they can be as small as 0.1 N/m. Thus typical values for k in AFM are

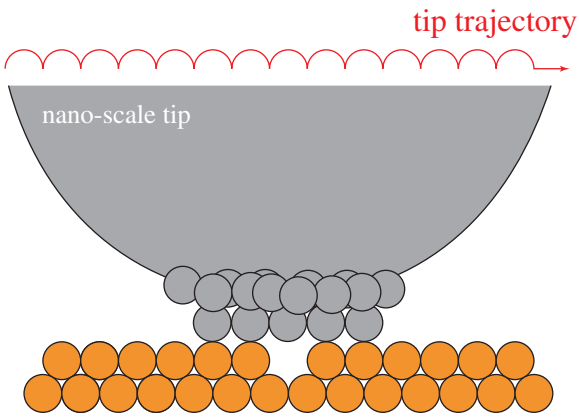

Figure 2.4: A schematic model to show the origin of the atomic-scale contrasts in AFM images.

0.01 – 5 N/m.

Using a soft cantilever and precisely controlling the tip position, the normal component of F_{ts} can be sufficiently reduced so as not to yield irreversible damage of the surface. However, to image surface topography by AFM, the tip has to be laterally scanned over the sample, which is inevitably accompanied by a considerable amount of friction force between the tip and the sample. This can be a serious problem for the applications to very soft materials such as polymers and biological samples. In particular, biological samples are often bound to the substrate so weakly that the sample is laterally dragged by the friction force of the tip.

Lattice Imaging

In 1987, Binnig *et al.* first presented atomic-scale AFM images of graphite surfaces.[31] Since then, many atomic-scale AFM images were demonstrated on a variety of surfaces including alkali halides[32,33] and organic materials.[34,35] However, these atomic-scale AFM images did not show atomic-scale point defects or non-periodic structures.[36] In addition, since the normal load for typical AFM measurements considerably exceeds the load limit of the single atom, the contact area should be larger than the single-atomic scale.[36] Figure 2.4 illustrates the formation mechanism of the atomic-scale contrasts in AFM images. If the surface has an atomic-scale periodic structure, the total interaction force shows atomic-scale variation when the tip is laterally scanned. This mechanism is obviously different from the "true-atomic resolution" realized in STM, where the interaction between the tip and the individual atom is directly detected. Therefore, the typical atomic-scale AFM images are referred to as "lattice images" and discriminated from the "true-atomic resolution images".

Jump-to-Contact

In order to achieve true-atomic resolution, the tip should be accurately positioned close proximity of the surface where the interaction between the front atom of the tip and the single atom of the surface predominantly contributes to the net interaction force. However, it cannot be realized by a typical AFM due to the surface adhesion which is referred to as "jump-to-contact." Figure 2.5 shows a typical distance dependence of F_{ts} and the deflection signal. As the tip approaches the surface, a sudden adhesion of the tip takes place at a certain threshold distance from the surface. In order to prevent this adhesion, following equation has to be met,

$$k > \left(\frac{\partial F_{\mathrm{ts}}}{\partial z_{\mathrm{t}}} \right)_{\mathrm{max}}. \tag{2.4}$$

This criterion suggests that using a very stiff cantilever may prevent the surface adhesion, which, however, gives rise to other problems such as surface damaging and low sensitivity to the interaction force.

The only exceptional results were reported on AFM experiments under liquid environment, where sub-nanometer scale resolution was achieved on calcite[37] or organic surfaces.[38,39] By immersing the tip and the sample, the solvent force significantly compensates the long-range attractive force acting between the tip and the sample so that the precise control of the tip position at the vicinity of the surface can be performed without jump-to-contact. However, it still remains impossible to obtain true-atomic resolution under ultrahigh vacuum (UHV) or ambient conditions.

2.1.3 Dynamic Force Microscopy (DFM)

Force Detection without Jump-to-Contact

In order to achieve true-atomic resolution by AFM, k should be large enough to avoid jump-to-contact and, at the same time, k should be small enough to attain a required force sensitivity. In 1987, Martin *et al.* invented a novel type of SPM referred to as dynamic force microscopy (DFM) to satisfy these contradictory requirements using a vibrating cantilever as a force sensor.[22]

The cantilever deflected towards the sample surface is pulled up by the restoring force of the cantilever spring. Thus even if Eq. (2.4) is not satisfied, the jump-to-contact can be avoided as long as the restoring force is larger than the attractive interaction force. This criterion is expressed by

$$F_{\mathrm{ts}} < kA, \tag{2.5}$$

where A is vibration amplitude of the cantilever. Thus, in DFM, the value for k

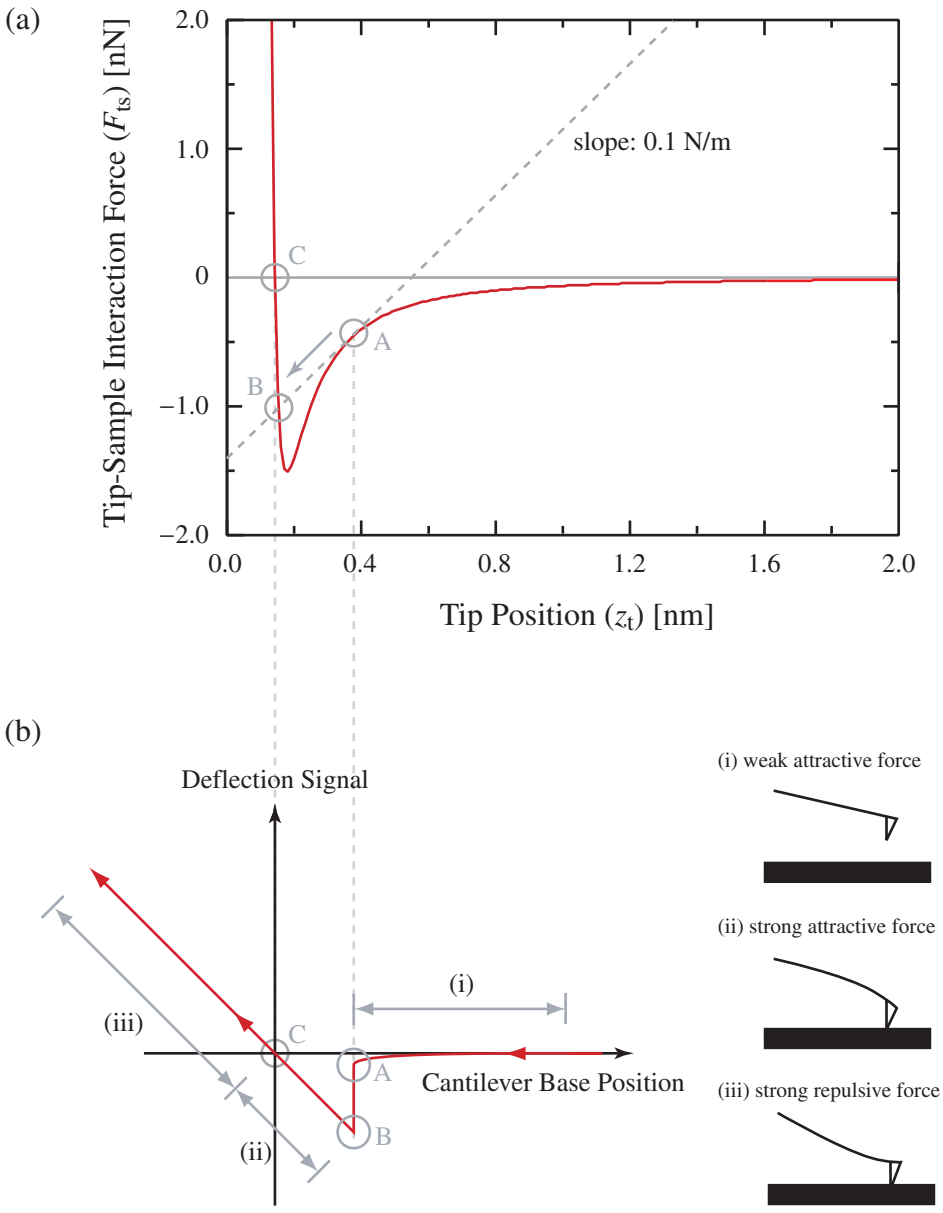

Figure 2.5: A typical distance dependence of (a) the tip-sample interaction force and (b) the deflection signal.

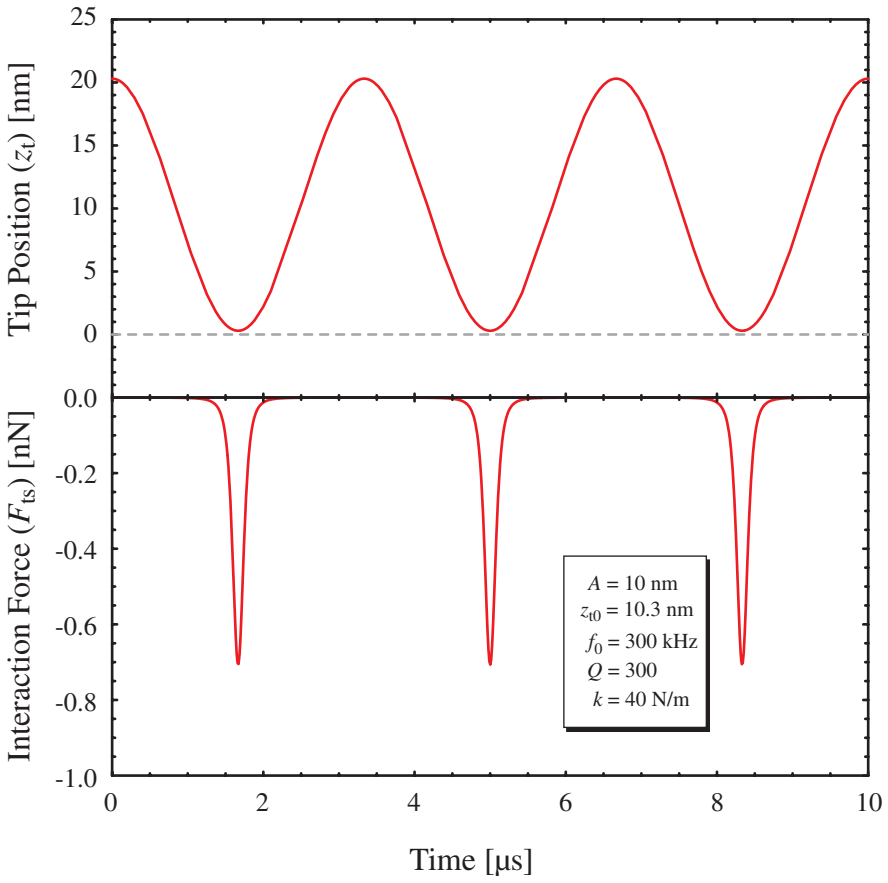

Figure 2.6: An example of (a) the tip motion and (b) the corresponding variations in $F_{\rm ts}$.

required to avoid the jump-to-contact varies depending on A. For typical DFM experiments, $A = 5 - 10$ nm and $k = 20 - 60$ N/m.

Although such a stiff cantilever is used, the force sensitivity of DFM can be much higher than that of AFM. The mechanism can be understood by taking account of the fundamental nature of the vibrating system. Even when the magnitude of $F_{\rm ts}$ is too small to induce a detectable dc deflection of the cantilever, it may still be able to significantly affect the cantilever motion if the force periodically exerts on the cantilever with a frequency near the cantilever resonance (f_0). This is the very situation where the vibrating cantilever used in DFM is placed. Namely, if the cantilever is driven at a frequency around f_0, $F_{\rm ts}$ also varies at the same frequency (Fig. 2.6). This periodically changing force synchronized with the cantilever motion causes a detectable amount of negative shift in the cantilever resonance frequency (Fig. 2.7). This resonance enhancement of the force sensitivity becomes more prominent when the Q-factor of the cantilever gets large. Under vacuum environments, Q-factor is significantly magnified so that the extremely high force sensitivity can be attained.

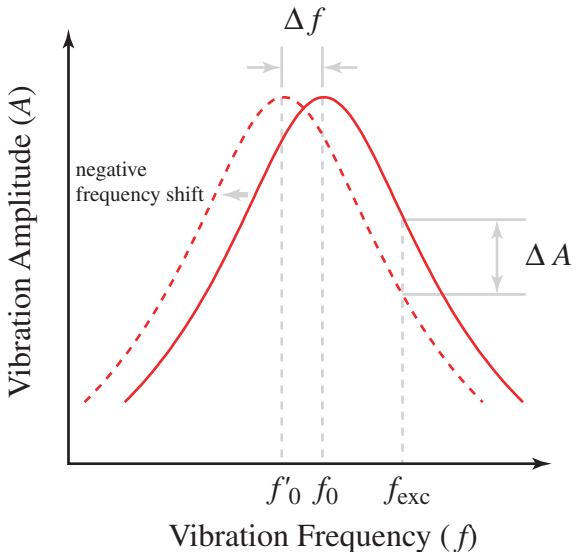

Figure 2.7: A schematic model of a typical cantilever resonance curve. When the tip approaches the surface, attractive tip-sample interaction force causes a negative shift of the resonance frequency.

For the typical micromachined cantilevers, Q is about $100 - 600$ in air whereas it can reach as large as $10,000 - 60,000$ under UHV conditions.

The frequency shift (Δf) induced by the tip-sample interaction is detected by either amplitude modulation (AM)[22] or frequency modulation (FM)[40] detection method. In the former case (AM-DFM), the cantilever is oscillated at a fixed frequency (f_{exc}) slightly higher than f_0 and the amplitude deviation (ΔA) caused by the negative frequency shift is detected. In the latter case (FM-DFM), the phase difference between the cantilever vibration and the excitation (ϕ) is kept at $-90°$ so that the cantilever is continuously driven at f_0. Thus Δf is obtained by measuring the deviation of the cantilever vibration frequency using a FM demodulator.

AM-DFM for Soft Materials

In 1987, AM detection method was first introduced by Martin *et al.* as a force detection method in the first DFM.[22] However, it was not until its first application to the low-modulus polymer by Zhong *et al.*[41] in 1993 that the method evoked enormous attention from the researchers in polymer and biological science. Since such soft materials cannot be imaged by typical AFM due to the large friction force between the tip and the sample, the researchers in those fields were really eager for the method which makes it possible.

Zhong *et al.* used AM-DFM in the intermittent-contact region, where the tip goes through the contact and the non-contact regimes within the each oscillation cycle.

And hence they named this operation mode "tapping mode". They avoided surface adhesion, using a very large amplitude ($A \simeq 100$ nm) oscillation. Therefore, in spite of the existence of surface adhesion layers (e.g. water and hydrocarbon molecules), a stable operation was possible even under an ambient condition. In addition, since the tip is in contact with the sample only in a fraction of the oscillation period, the lateral force acting between the tip and the sample is significantly reduced compared to the case of conventional AFM.

Although AM-DFM has been successfully applied to the soft materials, the method is not preferred to be used under vacuum environments where Q-factor becomes much higher than that for ambient conditions. Since Q-factor is directly connected with damping factor (γ) as expressed by $\gamma = m\omega_0/Q$, high Q-factor results in low γ and a low dissipation rate of the cantilever vibration energy. In AM-DFM, the change in $F_{\rm ts}$ is detected as that in A, which, however, takes considerably long time under vacuum conditions because of the low dissipation rate. The timescale of the amplitude response is described by[40]

$$\tau_{\rm AM} \simeq \frac{2Q}{\omega_0}, \tag{2.6}$$

where ω_0 is the angular frequency at the cantilever resonance. For the typical cantilever used in DFM, the order of $\tau_{\rm AM}$ becomes 0.1 sec, which is too long to obtain a realistic time response of the distance feedback regulation. Although it may be possible to acquire an image with a very slow scanning speed, the thermal drift of the tip and the sample would prevent the high-resolution imaging unless the DFM system is operated at a very low temperature.

FM-DFM for UHV Applications

In AM-DFM, Q-factor has to be small enough to achieve a required time response of A, whereas high Q-factor is desirable to enhance the force sensitivity. In 1991, Albrecht *et al.* found a way to combine the benefits of high Q-factor and high speed operation by introducing the FM detection method.[40] In FM-DFM, the change in $F_{\rm ts}$ is detected as that in the oscillation frequency of the cantilever. The oscillation frequency is controlled by the phase feedback circuit regulating the phase difference between the tip oscillation and the excitation voltage. Thus the time response of the cantilever frequency is determined by the settling time of the phase feedback circuit, which is much shorter than that of the amplitude deviation. In fact, the bandwidth of FM detection method is not limited by that of the phase feedback circuit but by that of the FM demodulator. However, the band width of the FM demodulator typically lies in the range of 1–10 kHz, which is still fast enough to be used as the feedback signal of the tip-sample distance regulation circuit.

Using FM detection method and working under UHV conditions, the force sensitivity of DFM was drastically improved without deteriorating the scanning speed. In addition, UHV environment allowed one to work with atomically clean surfaces, which was essential for the atomic- or molecular-scale studies. And finally, in 1995, true-atomic resolution was achieved by Giessibl[42] and by Kitamura and Iwatsuki,[43] where atomically-resolved FM-DFM images of Si(111)-7×7 surfaces were presented. Furthermore, in 1997, Bammerlin *et al.* imaged atomic-scale structures of NaCl(001) surfaces,[24] which first demonstrated the true-atomic resolution of FM-DFM on insulating surfaces. Subsequently, many atomically-revolved FM-DFM images were presented on semiconductors,[44–49] metals,[50,51] metal oxides[52] and alkali halides.[25] Moreover, true-molecular resolution was also achieved by FM-DFM on various organic surfaces.[53–60]

After these pioneering works, present studies on FM-DFM are categorized into following four parts;

1. improvement of its instrumentation,
2. elucidation of its imaging mechanism,
3. development of its related techniques,
4. exploitation of its applications.

The category (1) includes the improvement of the FM demodulator[61] and the force sensor.[62] The category (2) aims at the detailed understanding on the Δf versus distance curve,[63–71] contrast formation mechanisms[72–77] and the dissipation processes of cantilever vibration energy.[27,28,78–94] The category (3) includes development of surface property measurement methods[29] and surface modification methods.[95] The category (4) includes the applications to the organic[96–103] or magnetic materials[104] and operation under liquid,[105] ambient[105] and low temperature[106] environments.

Dynamic Mode AFM / Dynamic Force Microscopy

When the general classification of SPM is discussed, DFM is mostly regarded as one of the operation modes in AFM and referred to as "dynamic-mode AFM" as shown in Fig. 2.8(a). This is because in both AFM and DFM the tip-sample distance regulation is made by measuring the tip-sample interaction force. In addition, the force is detected from the deflection of the cantilever having a tip at the end. Thus the classification shown in Fig. 2.8(a) is well accepted and widely used.

However, a considerable number of researchers especially in the field of DFM often prefer to use "dynamic force microscopy" rather than "dynamic-mode AFM".

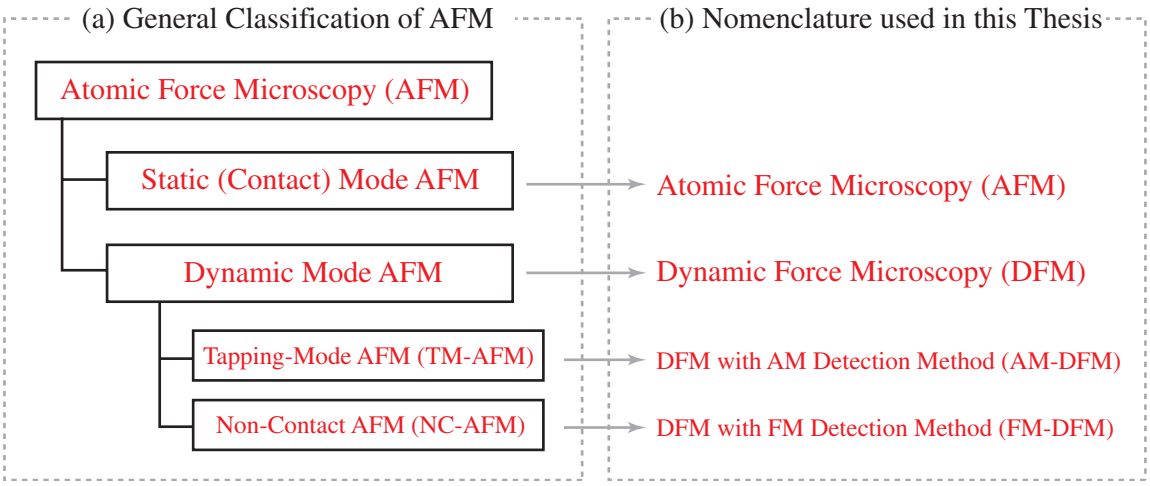

Figure 2.8: A typical classification of SPM and the nomenclature used in this thesis.

One obvious reason for this is that "DFM" is much simpler than "dynamic-mode AFM". Besides, the words "dynamic force" seems to be well representing the essence of this technique where the dynamically vibrating tip experiences the dynamically varying interaction force. The study described in this thesis was mainly focused on the DFM applications whereas other SPM techniques such as contact-mode AFM and STM were hardly used. Therefore, the terminology DFM was adopted in this thesis to represent this novel type of SPM technique.

Tapping and Non-contact / AM-DFM and FM-DFM

Im most cases, AM-DFM is referred to as "tapping-mode AFM" because in this method the tip is usually oscillated in the intermittent-contact region. However, recent study revealed that this method can also be operated in the non-contact regime where the cantilever is oscillated above the surface and the tip front atom does not suffer from the repulsive force from the surface. In addition, experimental studies revealed that such a operation at a relatively large separation from the surface will produce the highest resolution in AM-DFM.

The resonance frequency of the cantilever is negatively shifted only if the tip-sample interaction is attractive whereas the repulsive force leads to the positive frequency shift in the resonance curve. Since FM-DFM is usually operated by detecting the negative frequency shift, some researchers were really convinced that the cantilever is oscillated in the non-contact region during the FM-DFM imaging. Thus they started to call this method "non-contact AFM (NC-AFM)" and discriminated it from the "tapping-mode AFM" in terms of their closest tip position from the surface. However, subsequent studies revealed that the tip front atom

can experience the repulsive force even when the net tip-sample interaction force is attractive. Moreover, it was found that the atomic-scale contrasts in FM-DFM images is most likely to be originated from the short-range chemical interaction force between the tip front atom and the surface atom. In other words, the separation of these interacting two atoms should be around the chemical bonding length.

Although AM-DFM and FM-DFM were developed in a different way, both of them are reaching at the same tip-sample separation where the tip front atom is predominantly interacting with a single surface atom just underneath the tip position, which is crucial for the true-atomic resolution. Actually, even with AM-DFM, the true-atomic resolution was demonstrated on Si(111)-7×7 surfaces in 1996 by Erlandsson *et al.*[107] where a low Q-factor cantilever made of tungsten was used to prevent the slow time response of the amplitude deviation. As a result, it becomes unrealistic to differentiate these two methods in terms of their tip-sample separation. In addition, the words "tapping" and "non-contact" are so misleading that people may believe that the cantilever is really tapping the surface or in the non-contact region.

From such a point of view, the terminologies AM-DFM and FM-DFM were used in this thesis instead of generally used "tapping mode" and "non-contact mode" as shown in Fig. 2.8(b).

2.2 Experimental Setup for Dynamic Force Microscopy

2.2.1 Force Sensor

In most of the DFM setups, a microfabricated single silicon cantilever is used as a force sensor. The property of the cantilever is characterized by the following three parameters; spring constant (k), resonance frequency (f_0) and Q-factor of the cantilever resonance (Q).

In the case of rectangular-shaped cantilevers (Fig. 2.2), the spring constant is given by

$$k = \frac{E_{\mathrm{Y}} w t^3}{4\ell^3}, \tag{2.7}$$

where E_{Y}, w, t and ℓ are the Young's modulus of the cantilever material and width, thickness and length of the cantilever, respectively. k has to be small enough to allow detection of small forces and at the same time it should be large enough to meet Eq. (2.5) to avoid the jump-to-contact. The typical value of k ranges from 20 to 60 N/m.

The resonance frequency of the cantilever (f_0) is given by

$$f_0 = 0.162 \frac{t}{\ell^2} \sqrt{\frac{E_Y}{\rho}}, \tag{2.8}$$

where ρ denotes the mass density of the cantilever material. f_0 should be high enough to reduce the sensitivity to the mechanical vibration of the DFM system. In addition, the high resonance frequency is also desirable to enhance the force sensitivity and the time response of the force detection in DFM. The upper limit for f_0 is usually determined by the cutoff frequency of the measurement system for cantilever deflection. The typical values for f_0 are 50 – 400 kHz.

The quality factor (Q) of the cantilever resonance is directly related to the damping coefficient (γ) by the following equation,

$$Q = \frac{m\omega_0}{\gamma}, \tag{2.9}$$

where m stands for the effective mass of the cantilever. The damping of the cantilever vibration occurs due to both the intrinsic friction within the lever itself (γ_0) and the friction between the lever and the surrounding molecules (γ_m). The Q-factor measured under an UHV condition is mostly determined by γ_0 while the value is reduced by the existence of γ_m under ambient or liquid environments. For micromachined cantilevers, Q-factor is typically 10,000 – 60,000 in vacuum whereas it becomes 100 – 600 under ambient conditions and 1 – 6 under liquid environments. Since γ is reduced by decreasing the temperature, Q-factor can be enhanced working under low-temperature environments.

2.2.2 Measurement of Cantilever Deflection

There have been proposed various methods for cantilever deflection measurements. They can be classified into two categories such as optical and electrical methods. The former includes homodyne[108–110] and heterodyne[22,23] interferometries, laser beam deflection method,[111,112] laser diode feedback detection[113,114] and polarization detection system.[115,116] The latter includes tunneling detection method,[21] capacitance detection system,[117] piezoresistive[118] and piezoelectric[119,120] cantilever detection methods. Among them, the laser beam deflection method is most commonly used due to its high sensitivity and easy experimental setup as shown in Fig. 2.9(a).

In the laser beam deflection method, the focused laser beam is irradiated onto the backside of the cantilever and the reflected beam is detected by the position sensitive photo detector (PSPD). The PSPD is composed of two adjacent photo diodes (PD_A and PD_B). The laser beam is aligned so that the laser spot on the PSPD surface is positioned at the center of it (Fig. 2.9(b)).

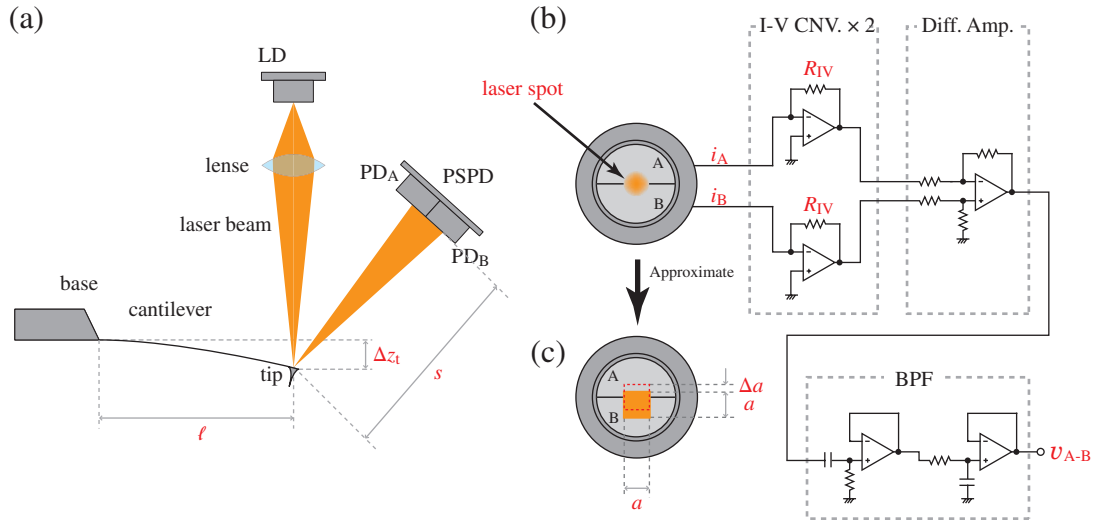

Figure 2.9: A schematic drawing of the experimental setup for cantilever deflection measurement using laser beam deflection method.

The cantilever displacement Δz_{t} induces the cantilever deflection $\Delta\theta$ as expressed by[121]

$$\Delta\theta = \frac{3}{2}\frac{\Delta z_{\mathrm{t}}}{\ell}. \tag{2.10}$$

This cantilever deflection gives rise to the laser beam deflection of $2\Delta\theta$. Thus the laser spot irradiated onto the PSPD is displaced by Δa as shown in Fig. 2.9(c), which is described by

$$\Delta a = 3\frac{s}{\ell}\Delta z_{\mathrm{t}}, \tag{2.11}$$

where s is the distance between the tip and the PSPD surface. The amplification factor β given by $\beta = 3s/\ell$ can be as large as 10^3, which significantly facilitates the detection of small cantilever displacement.

The photo induced currents (i_{A} and i_{B}) of the two PDs are independently detected by I-V converters and the detected signals are fed into a differential amplifier which produces the voltage signal proportional to the current difference ($i_{\mathrm{A-B}}$) between i_{A} and i_{B}. Then the undesirable frequency components are eliminated by the band pass filter (BPF) with a center frequency near the cantilever resonance. The displacement of the laser spot causes one of the photo diodes to collect more light than the other, leading to the deviation ($\Delta i_{\mathrm{A-B}}$) in $i_{\mathrm{A-B}}$. In the case of DFM, the cantilever displacement does not occur in a static manner but dynamically. On the other hand, the time response of the photo detector is limited by the discharging time of the junction capacitance (C_{j}) of the photo diodes through the load resistance

($R_{\rm IV}$). Thus, the frequency dependent gain damping ($\xi_{\rm PD}(\omega)$) and the phase delay ($\phi_{\rm pd}(\omega)$) have to be taken into account.

$$\Delta i_{\rm A-B} = \eta P_0 \xi_{\rm PD} \frac{3s}{\ell a} \Delta z_{\rm t}, \tag{2.12}$$

where η and P_0 are the efficiency of the light-to-current conversion and the averaged laser power, respectively. Note that the shape of the laser spot is assumed to be square with a dimension of $a \times a$ (Fig. 2.9(c)). Eq. (2.12) represents that $\Delta i_{\rm A-B}$ increases in proportion to the increase of $\Delta z_{\rm t}$. Assuming that $\eta = 0.3$ A/W, $P_0 = 100$ μW, $\xi_{\rm PD} = 0.1$, $s = 5$ cm, $\ell = 100$ μm and $a = 5$ mm, the cantilever deflection of $\Delta z_{\rm t} = 0.1$ nm generates the current variation of $\Delta i_{\rm A-B} \simeq 100$ pA.

2.2.3 Noises in Laser Beam Deflection Method

Load Resistance Johnson Noise

The resistor used in the I-V converter ($R_{\rm IV}$) produces the Johnson noise due to the agitation of the electrons. The mean square of the current noise equivalent to the Johnson noise is given by[121]

$$\langle \delta i_{\rm J}^2 \rangle = \frac{8 k_{\rm B} T B_{\rm BPF}}{R_{\rm IV}}, \tag{2.13}$$

where $k_{\rm B}$, T and $B_{\rm BPF}$ are Boltzmann constant, temperature and the band width of the BPF. If it is assumed that $T = 300$ K, $B_{\rm BPF} = 10$ kHz and $R_{\rm IV} = 100$ kΩ, the current noise becomes about 60 pA. Although this value is not necessarily negligible compared to the magnitude of the deflection to be detected, it can be usually neglected compared to the other dominant noise sources described later.

Laser Intensity Noise

Since the output of the semiconductor laser diode is easily fluctuated by the temperature variation of both the environment and the semiconductor laser chip. In order to maintain the output power constant, the laser diode is usually driven by an automatic power control (APC) circuit. In the APC circuit, the output power of the laser beam is detected with a photo diode and the detected signal is used for the feedback regulation of the output intensity. The magnitude of the laser intensity fluctuation (δP) is often characterized by the relative intensity noise ($\zeta_{\rm RIN}$) which is defined as

$$\zeta_{\rm RIN} \equiv \frac{\langle \delta P^2 \rangle}{P_0^2}. \tag{2.14}$$

Although the theory for the estimation of $\zeta_{\rm RIN}$ is quite complicated, a typical value for $\zeta_{\rm RIN}$ is given by[121] $\zeta_{\rm RIN} = 10^{-13} B_{\rm BPF}$.

The mean square of the effective current noise due to the laser intensity fluctuation is described by[121]

$$\langle \delta i_\ell^2 \rangle = \zeta_{\mathrm{RIN}} (\eta P_0 \xi_{\mathrm{PD}})^2 \frac{\Delta a}{a} = \zeta_{\mathrm{RIN}} (\eta P_0 \xi_{\mathrm{PD}})^2 \frac{3s}{\ell} \frac{\Delta z_{\mathrm{t}}}{a}. \tag{2.15}$$

Provided that $\eta = 0.3$, $B_{\mathrm{BPF}} = 10$ kHz, $P_0 = 100$ μW, $\xi_{\mathrm{PD}} = 0.1$, $a = 5$ mm, $s = 5$ cm, $\ell = 100$ μm and the maximum cantilever displacement is 10 nm, the current noise becomes about 5 pA, which is small enough to be neglected for most of the applications. Owing to $\Delta a \ll a$, the laser power intensity noise is mostly eliminated at the differential amplifier as a common mode noise.

Cantilever Thermal Brownian Noise

The thermally-induced Brownian motion of the cantilever is translated into photocurrent noise and its mean square value around the cantilever resonance is described by[121]

$$\langle \delta i_{\mathrm{t}}^2 \rangle = \left(\eta P_0 \xi_{\mathrm{PD}} \frac{3s}{\ell a} \right)^2 \frac{2 k_{\mathrm{B}} T B_{\mathrm{BPF}} Q}{\omega_0 k}. \tag{2.16}$$

When $k = 40$ N/m, $Q = 30,000$, and the other parameters are assumed to be the same as described above, the current noise is estimated to be 160 pA. Since the thermal Brownian motion is enhanced by a factor of Q at the cantilever resonance, it is usually the predominant noise source in the DFM experiments under vacuum conditions. Q-factor under ambient condition is typically 300 so that the equivalent current noise becomes 16 pA.

Photo Diode Shot Noise

The shot noise originated from the statistical irregularity of the photo-induced currents in the photo diodes is described by[121]

$$\langle \delta i_{\mathrm{s}}^2 \rangle = 2 e \eta B_{\mathrm{BPF}} P_0, \tag{2.17}$$

where e is the electron charge. Assuming the relevant parameters to be the same as described above, the current noise is estimated to be 310 pA, which is large enough to affect the cantilever deflection measurements.

Effective Cantilever Deflection Noise

Neglecting the contribution from the laser intensity noise, the effective cantilever deflection noise δz_t becomes

$$\delta z_\mathrm{t} = \frac{\sqrt{\langle \delta i_\mathrm{J}^2 \rangle + \langle \delta i_\mathrm{t}^2 \rangle + \langle \delta i_\mathrm{s}^2 \rangle}}{\Delta i_{\mathrm{A-B}} / \Delta z_\mathrm{t}} \tag{2.18}$$

$$= \sqrt{\frac{2k_\mathrm{B}TB_\mathrm{BPF}Q}{\omega_0 k} + \left(\frac{\ell a}{3s}\right)^2 \left[\frac{2eB_\mathrm{BPF}}{\eta P_0 \xi_\mathrm{PD}^2} + \frac{8k_\mathrm{B}TB_\mathrm{BPF}}{(\eta P_0 \xi_\mathrm{PD})^2 R_\mathrm{IV}}\right]} \tag{2.19}$$

Assuming that relevant parameters are the same as described above, the value for δz_t becomes about 0.4 nm, which is predominantly determined by the shot noise of the photo detector. Thus the corresponding noise density of the cantilever deflection signal around the resonance frequency ($n_\mathrm{z} \equiv \delta z_\mathrm{t}/\sqrt{B_\mathrm{BPF}}$) is about 4 pm/$\sqrt{\mathrm{Hz}}$.

Eq. 2.19 gives following fundamental directions to reduce the cantilever deflection noise. A high-speed photo detector, a band pass filter with a narrow bandwidth and low-temperature environment are desirable. Higher resonance frequency seems to be effective, which however may result in smaller ξ_PD. A stiff cantilever with a low Q-factor is desirable to suppress the deflection noise whereas it would reduce the sensitivity to the tip-sample interaction force. The laser power should be enlarged to reduce the noise as long as it does not interfere with the expected physical phenomena to be observed by DFM. Although the size of the laser spot on the PSPD is preferred to be small, it should be larger than the diffraction-limited spot size which is given by[121]

$$a_\mathrm{min} = \frac{2s\lambda}{\pi a_\mathrm{c}}, \tag{2.20}$$

where λ and a_c denote the wavelength of the laser beam and the beam spot size on the cantilever backside, respectively. Therefore, in order to reduce the noise, a_c has to be as large as possible. The effective noise is also reduced using a cantilever with a shorter length. However, it should be noted that the resonance frequency of the cantilever is also affected by the cantilever length (Eq. (2.8)).

2.2.4 Cantilever Excitation

In DFM, the cantilever is mechanically vibrated by a adjacent PZT actuator sandwiched with two electrodes (Fig. 2.10). The excitation voltage applied between them induces the piezoelectric vibration of the PZT actuator, which in turn gives rise to the vibration of the cantilever base. When the excitation voltage is assumed to be $v_\mathrm{exc} = V_\mathrm{exc}\cos(\omega t)$, the motion of the cantilever base is described by

$$z_\mathrm{b} = z_\mathrm{b0} + A_\mathrm{b}\cos(\omega t + \phi_\mathrm{b}). \tag{2.21}$$

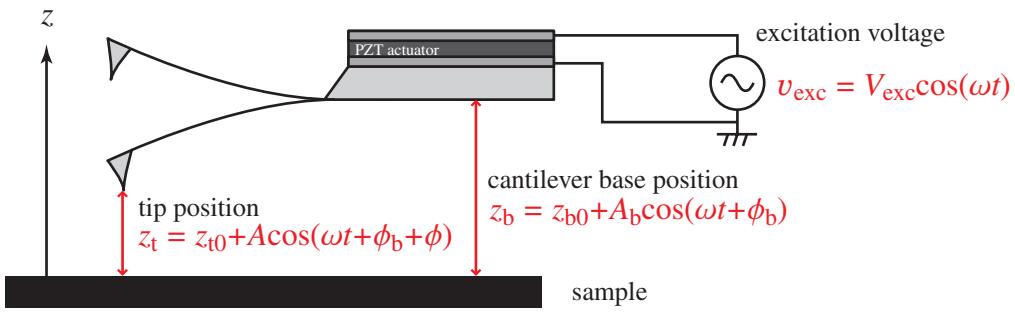

Figure 2.10: A schematic drawing of the setup for cantilever excitation. The cantilever is mechanically oscillated by the adjacent PZT actuator.

z_{b0} is the mean position of the cantilever base. A_b is the vibration amplitude of the cantilever base and given by

$$A_b = \frac{d_{33}}{t_{PZT}} V_{exc}, \tag{2.22}$$

where d_{33} and t_{PZT} are the piezoelectric constant and the thickness of the PZT actuator, respectively. ϕ_b is the phase delay of the cantilever base oscillation with respect to the excitation voltage, which is usually determined by the poling direction of the PZT so that $0°$ or $-180°$.

The vibration of the cantilever base induces the cantilever beam deflection. The resultant tip motion is obtained by solving the equation of motion which is given by

$$m\frac{\mathrm{d}z_t^2}{\mathrm{d}t^2} + \gamma\frac{\mathrm{d}z_t}{\mathrm{d}t} + k(z_t - z_b + d_{bt0}) = 0, \tag{2.23}$$

where d_{bt0} denotes the mean distance between the tip and the cantilever base. Assuming that the tip motion is sinusoidal, the tip position z_t is described by

$$z_t = z_{t0} + A\cos(\omega t + \phi_b + \phi), \tag{2.24}$$

where z_{t0} and A are the mean tip position and the amplitude of the tip vibration, respectively, while ϕ denotes the phase of the tip vibration with respect to the cantilever base motion. From Eq. (2.21), (2.23) and (2.24), A and ϕ are obtained as

$$A = \frac{QA_b}{\sqrt{Q^2(1-\omega^2/\omega_0^2)^2 + \omega^2/\omega_0^2}}, \tag{2.25}$$

$$\phi = \arctan\left[\frac{-\omega/\omega_0}{Q(1-\omega^2/\omega_0^2)}\right]. \tag{2.26}$$

From these equations, the frequency dependence of A and ϕ is plotted as shown in Fig. 2.11. The relevant parameters are defined as shown in this figure. At the

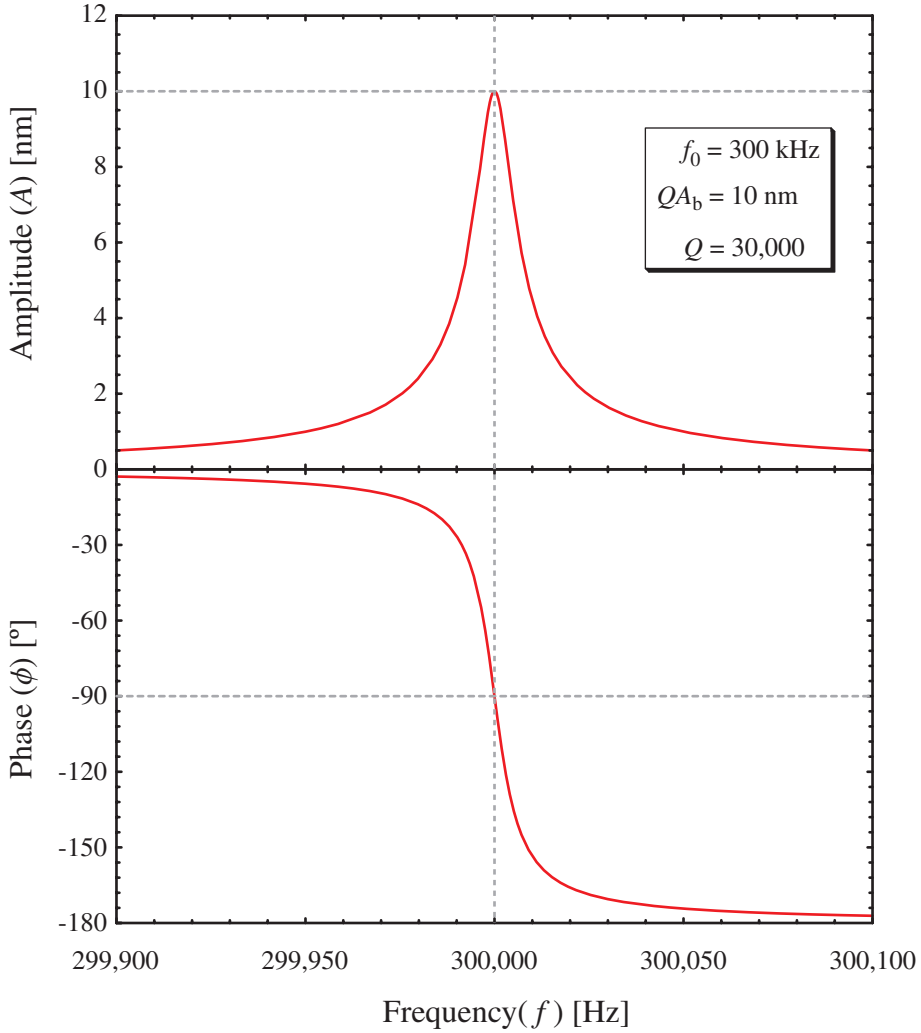

Figure 2.11: Frequency dependence of the amplitude (A) and the phase (ϕ) of the cantilever vibration plotted around the resonance frequency, which was calculated from Eq. (2.25) and (2.26). At resonance, A and ϕ become QA_b and $-90°$, respectively.

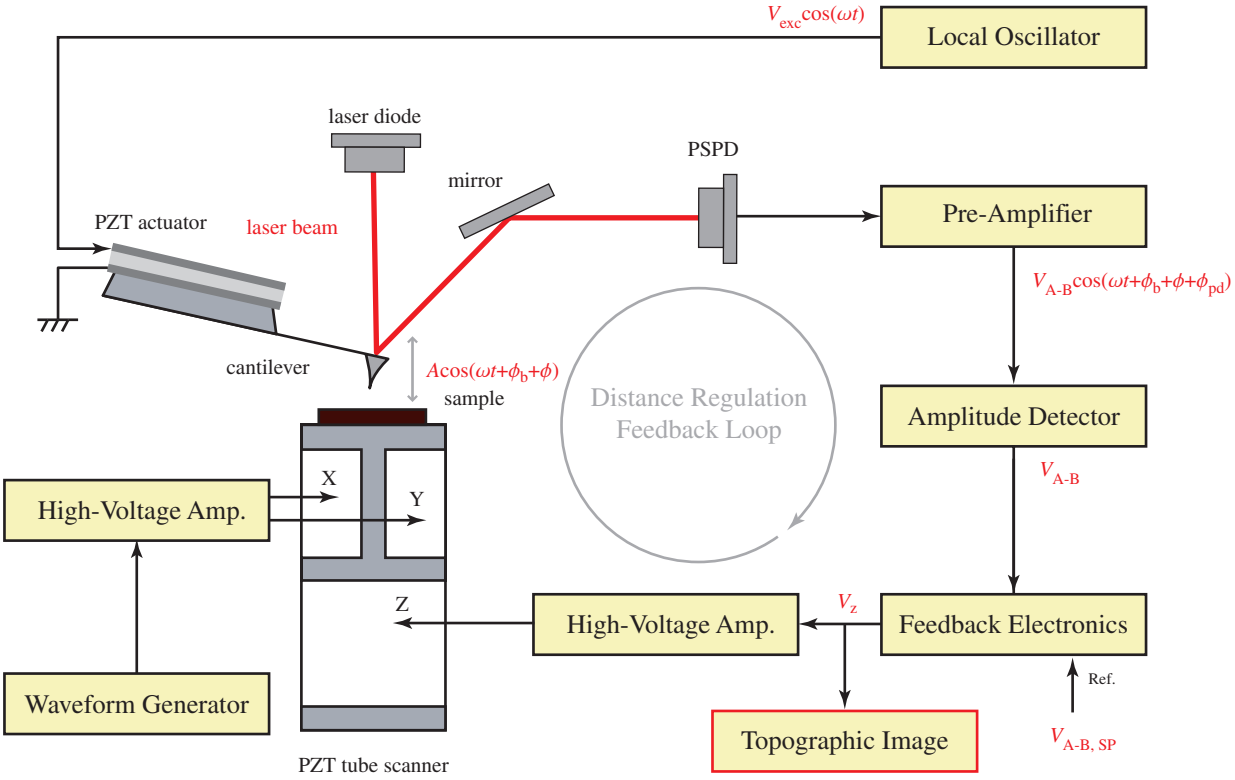

Figure 2.12: A schematic drawing of the experimental setup for AM-DFM.

resonance frequency, the vibration amplitude becomes its maximum and the value amounts to QA_b, which means that the vibration of the cantilever base induces Q times larger tip vibration at resonance. On the other hand, ϕ steeply varies from 0° to −180° around the resonance frequency and it becomes −90° just at the resonance.

2.2.5 DFM with AM Detection Method (AM-DFM)

Cantilever Excitation

Figure 2.12 shows a typical experimental setup for AM-DFM. In AM-DFM, the cantilever is oscillated at a fixed frequency with a fixed excitation amplitude, namely, f and V_{exc} are continuously fixed at the preset values during the AM-DFM imaging. Since the cantilever excitation voltage is totally free from the influence of the tip-sample interaction, the cantilever excitation can be stably performed even when there is a large variation in the tip-sample interactions. This feature facilitates the use of AM-DFM in intermittent-contact region, where the local variation in the viscoelasticity strongly affects the motion of the vibrating cantilever. Especially under ambient conditions, the surface would be covered with an adhesion layer comprised of the water and hydrocarbon molecules so that the cantilever motion may be severely disturbed by the meniscus force acting between the tip and the

adhesion layer. Therefore, AM-DFM is much more suitable for the operation in the intermittent-contact region under ambient conditions than FM-DFM which utilizes the cantilever deflection signal as a prototype for preparing the excitation signal.

Amplitude Detector

In AM-DFM, the amplitude of the cantilever vibration is detected by measuring the amplitude of the deflection signal ($V_{\mathrm{A-B}}$). The amplitude detection is mostly made by an RMS-DC converter or a lock-in amplifier. Although the former is simpler than the latter, its output voltage can be affected by the cantilever deflection in all frequency range unless the pre-amplifier is equipped with a band path filter with a sufficiently narrow bandwidth to reject undesirable frequency components contained in the deflection signal. This can be a problem when AM-DFM is combined with other modulation techniques such as Kelvin probe force microscopy (KFM) where another vibration mode is induced by an ac bias modulation voltage applied between the tip and the sample.

2.2.6 DFM with FM Detection Method (FM-DFM)

Cantilever Excitation

Figure 2.13 shows a typical experimental setup for FM-DFM. In FM-DFM, the cantilever is used as a resonator in a self-excitation circuit. The deflection signal is phase shifted (ϕ_{ps}), routed through an automatic gain control (AGC) circuit and fed back to the PZT actuator. The phase difference between the cantilever vibration and the excitation voltage (ϕ) is given by

$$\phi = -360^\circ - (\phi_{\mathrm{b}} + \phi_{\mathrm{pd}} + \phi_{\mathrm{ps}}). \tag{2.27}$$

Since ϕ_{b} and ϕ_{pd} are nearly constant, ϕ can be arbitrarily determined by adjusting ϕ_{ps}. In FM-DFM, ϕ_{ps} is adjusted so as to meet $\phi = -90^\circ$. Thus the cantilever is continuously oscillated at its resonance frequency during the FM-DFM imaging.

When ϕ rapidly changes beyond the time response of the phase feedback circuit, the cantilever oscillation is temporarily suspended because the condition for the self-oscillation is no longer satisfied. Such a sudden phase variation often takes place when the tip contacts with the surface adhesion layer. Thus, FM-DFM is not suitable for the applications under ambient conditions or in the intermittent-contact region.

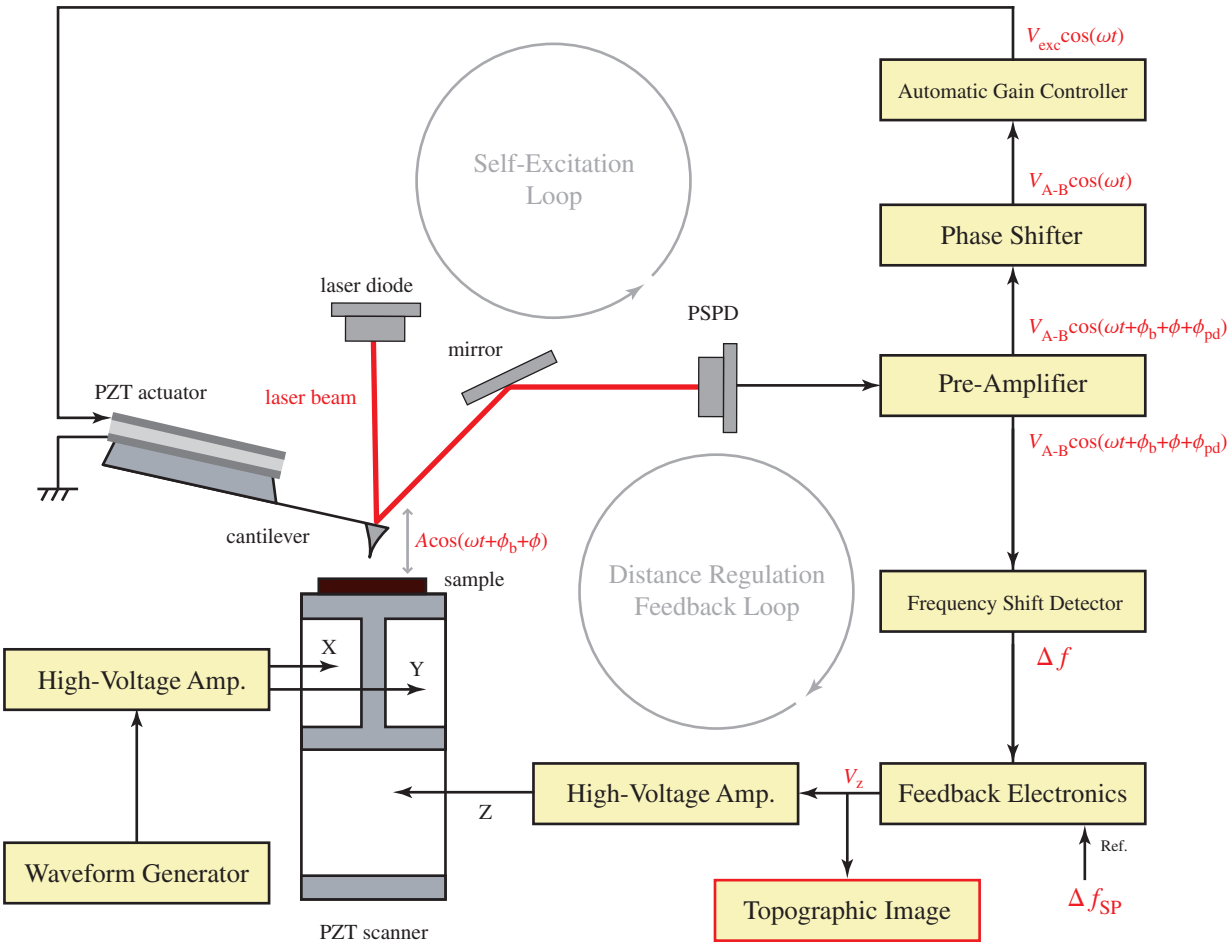

Figure 2.13: A schematic drawing of the experimental setup for FM-DFM.

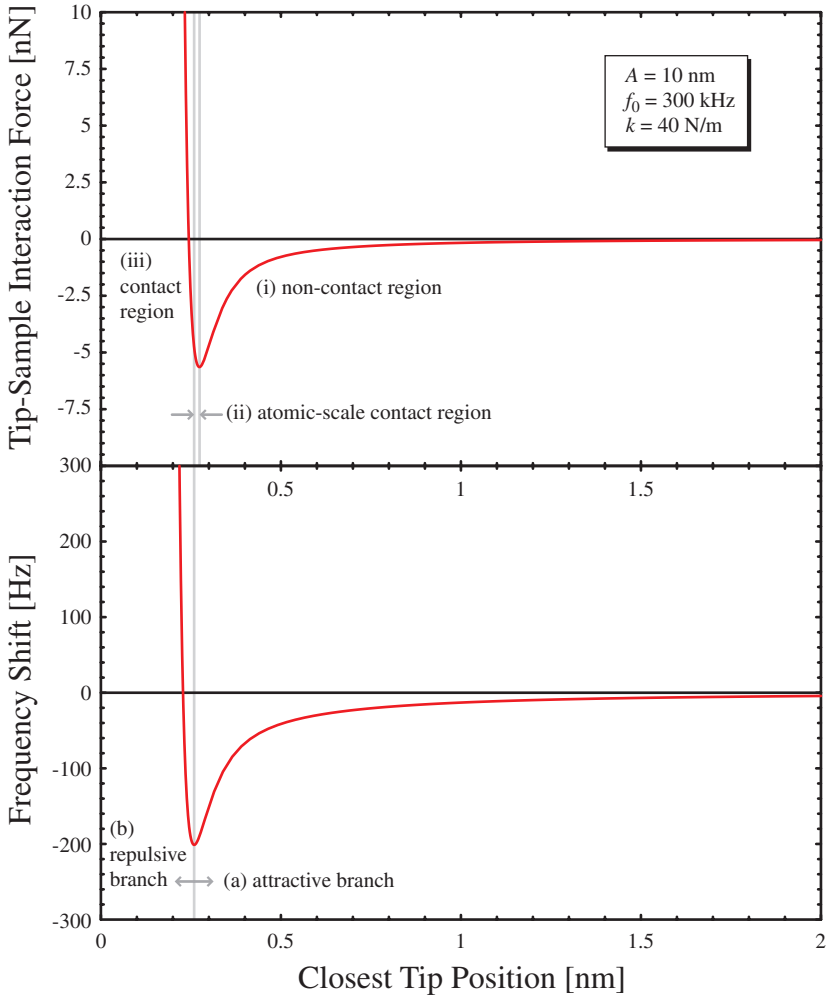

Figure 2.14: A typical distance dependence of the tip-sample interaction force and the corresponding frequency shift calculated with Eq. (2.29).

Distance Dependence of Frequency Shift

One of the most distinctive features of FM-DFM is precise control over the tip position in the non-contact and atomic-scale contact regions, which is essential to achieve the true-atomic resolution. In order to know the mechanism which realizes this feature, it is required to understand the distance dependence of the tip-sample interaction force and the resultant frequency shift.

If the vibration amplitude is relatively small (typically less than 1 nm), the gradient of the tip-sample interaction force can be approximated to be constant. In this case, the frequency shift induced by the tip-sample interaction (Δf) is given by

$$\Delta f = -\frac{f_0}{2k}\frac{\partial F_{\mathrm{ts}}}{\partial z_{\mathrm{t}}}. \tag{2.28}$$

Namely, Δf is directly proportional to the force gradient.

However, in most of the experimental conditions, the amplitude is in the range of 5 – 10 nm so that the small amplitude approximation cannot be applied. In that case, Δf is obtained by integrating the contribution of force gradient in the whole distance range of tip oscillation, which is given by[122]

$$\Delta f = -\frac{f_0}{2k}\int_{-A}^{A}\frac{\partial F_{\mathrm{ts}}(z_{\mathrm{t}}-z)}{\partial z_{\mathrm{t}}}\frac{\sqrt{A^2-z^2}}{\pi A^2/2}\mathrm{d}z. \tag{2.29}$$

Figure 2.14 shows a typical distance dependence of the tip-sample interaction force and the corresponding frequency shift calculated with Eq. (2.29). When the tip is in the non-contact region (Fig. 2.14(i)), the attractive interaction force causes a negative frequency shift. As the tip-sample separation is reduced, the tip front atom begins to suffer from a weak repulsive interaction force at the closest position to the surface. Even in such an atomic-scale contact region (Fig. 2.14(ii)), the tip is still in the attractive branch (Fig. 2.14(a)) of the frequency shift curve because of the background long-range attractive interaction force. On further approaching, the frequency shift turns to show an inverse dependence on the tip-sample distance (Fig. 2.14(b)). In such a contact region (Fig. 2.14(iii)), a relatively strong repulsive force may give rise to an irreversible change in the atomic-scale structures of the tip and the surface so that the high-resolution imaging becomes nearly impossible.

In general, FM-DFM is operated in the attractive branch of the frequency shift curve where the cantilever resonance frequency is negatively shifted by reducing the tip-sample separation. Thus, as long as FM-DFM is stably operated, the tip is surely in the non-contact or atomic-scale contact regions. This feature is particularly important for controlling the tip position at the close vicinity of the sample surface without surface damaging. Owing to such an excellent controllability of the tip position, FM-DFM can realize an extremely high spatial resolution.

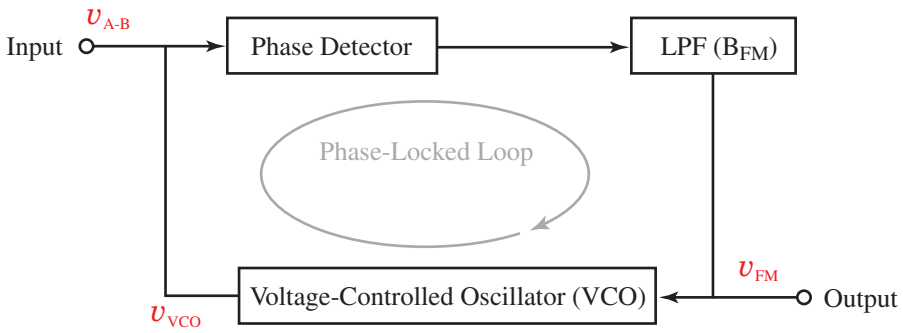

Figure 2.15: A schematic block diagram of the phase-locked loop (PLL) circuit for frequency shift detection.

Frequency Shift Detector

The frequency shift detection is mostly made by a phase-locked loop (PLL) circuit (Fig. 2.15). In the PLL circuit, the phase difference between the deflection signal ($v_{\text{A}-\text{B}}$) and the output signal of the voltage-controlled oscillator (VCO) (v_{VCO}) is detected by a phase detector. The output signal of the PLL circuit (v_{FM}) is obtained by averaging the detected signal with a low-pass filter. v_{FM} is also used as the input signal of the VCO which outputs a signal whose frequency is proportional to v_{FM}. Since this feedback-loop circuit works to cancel out the frequency difference between v_{VCO} and $v_{\text{A}-\text{B}}$, v_{FM} varies in proportion to the frequency of $v_{\text{A}-\text{B}}$.

2.3 Energy Dissipation Measurement

2.3.1 Estimation of Energy Dissipation

Energy Dissipation of Freely Oscillating Cantilever

The cantilever motion driven by a PZT actuator is described by the equation of motion (Eq. (2.23)). Assuming that the alternating terms of z_{b} (Δz_{b}) and z_{t} (Δz_{t}) are given by

$$\Delta z_{\text{b}} = A_{\text{b}} \cos(\omega t), \tag{2.30}$$

$$\Delta z_{\text{t}} = A \cos(\omega t + \phi) \equiv A \cos(\omega t - \varphi), \tag{2.31}$$

the equation of motion is rewritten as

$$m\frac{\mathrm{d}^2 \Delta z_{\text{t}}}{\mathrm{d}t^2} + \gamma \frac{\mathrm{d}\Delta z_{\text{t}}}{\mathrm{d}t} + k\Delta z_{\text{t}} = kA_{\text{b}} \cos(\omega t). \tag{2.32}$$

Note that φ is defined as $\varphi \equiv -\phi$. The first and the third terms in the left hand side of this equation are the inertial force and the restoring force of the cantilever

spring, respectively. These two force components are conservative and have nothing to do with energy dissipation process while other two force components are relevant to the energy dissipation process of the vibrating system.

The external force $kA_\mathrm{b}\cos(\omega t)$ provides some energy to the vibrating cantilever and the input power averaged over one period of the cantilever oscillation (P_in) is given by,

$$P_\mathrm{in} = \frac{1}{T}\int_0^T kA_\mathrm{b}\cos(\omega t)\frac{\mathrm{d}z_\mathrm{t}}{\mathrm{d}t}\mathrm{d}t \tag{2.33}$$

$$= \frac{1}{2}kAA_\mathrm{b}\omega\sin(\varphi). \tag{2.34}$$

The second term in the left hand side of Eq. (2.32) is originated from the internal and external viscosity, which results in the dissipation of the cantilever vibration energy. Using $\gamma = m\omega_0/Q$ and $k = m\omega_0^2$, the mean power for this energy loss is obtained as,

$$P_0 = \frac{1}{T}\int_0^T \gamma\left(\frac{\mathrm{d}z_\mathrm{t}}{\mathrm{d}t}\right)^2\mathrm{d}t \tag{2.35}$$

$$= \frac{kA^2\omega^2}{2Q\omega_0}. \tag{2.36}$$

Although this dissipation contains contributions from the friction force between the cantilever and the surrounding molecules, it is often referred to as "intrinsic dissipation" in order to discriminate it from the energy dissipation induced by the tip-sample interactions.

Energy Dissipation Induced by Tip-Sample Interactions

When the tip approaches the sample surface, the vibration energy of the cantilever is partially dissipated by the tip-sample interactions. The mean power of this dissipation (P_ts) is given by

$$P_\mathrm{ts} = P_\mathrm{in} - P_0 \tag{2.37}$$

$$= \frac{\pi kA^2 f}{Q}\left(\frac{QA_\mathrm{b}}{A}\sin(\varphi) - \frac{f}{f_0}\right). \tag{2.38}$$

Since $\omega \simeq \omega_0$, P_0 and P_ts can be approximated as

$$P_0 = \frac{\pi kA^2 f_0}{Q}, \tag{2.39}$$

$$P_\mathrm{ts} = P_0\left(\frac{QA_\mathrm{b}}{A}\sin(\varphi) - 1\right). \tag{2.40}$$

2.3.2 Energy Dissipation Measurement with AM-DFM

Basic Principle

In AM-DFM, $A_{\rm b}$ and f are always fixed, and A is kept constant by the distance feedback regulation. Thus the energy dissipation induces the variation in ϕ in Eq. (2.40). $QA_{\rm b}$ is equal to the cantilever vibration amplitude at the resonance frequency without any tip-sample interactions (A_0). Thus from Eq. (2.40), $P_{\rm ts}$ is given by

$$P_{\rm ts} \;=\; P_0 \left(\frac{A_0}{A} \sin(\varphi) - 1 \right). \tag{2.41}$$

This equation implies that if there is no energy dissipation (i.e., $P_{\rm ts} = 0$), φ should be constant and given by

$$\varphi = \arcsin \left(\frac{A}{A_0} \right). \tag{2.42}$$

In other words, it is only when the energy dissipation varies that the phase variation is observed during AM-DFM imaging. The only exceptional phase variation takes place when the tip moves from the attractive regime to the repulsive one. Since $\sin(\varphi)$ is symmetrical to $\varphi = 90°$, the symmetric phase jumps between the attractive phase ($\varphi > 90°$) and the repulsive phase ($\varphi < 90°$) is allowed even when there is no energy dissipation. Except for these discontinuous phase jumps, the phase variation is directly related to the energy dissipation and its magnitude can be quantitatively estimated with Eq. (2.41).

Experimental Setup

Figure 2.16 shows a typical experimental setup for the dissipation imaging with AM-DFM which is the method to record the phase variation during the AM-DFM imaging. The phase difference between the excitation signal and the deflection signal is detected by a phase detector. Then the output signal proportional to the phase difference $\phi_{\rm b} + \phi + \phi_{\rm pd}$ is two-dimensionally mapped to obtain a phase image. The discontinuous phase variation is mostly due to the above mentioned phase jumps around $\varphi = 90°$ while gradual phase variation represents the energy dissipation variation. In the case of AM-DFM operated in the intermittent-contact region, the energy dissipation is closely related to the viscoelastic property of the sample surface.

2.3.3 Energy Dissipation Measurement with FM-DFM

Basic Principle

In FM-DFM, φ is kept at 90° using a self-excitation circuit and f is kept constant to establish the tip-sample distance regulation. In terms of $A_{\rm b}$ and A, there are

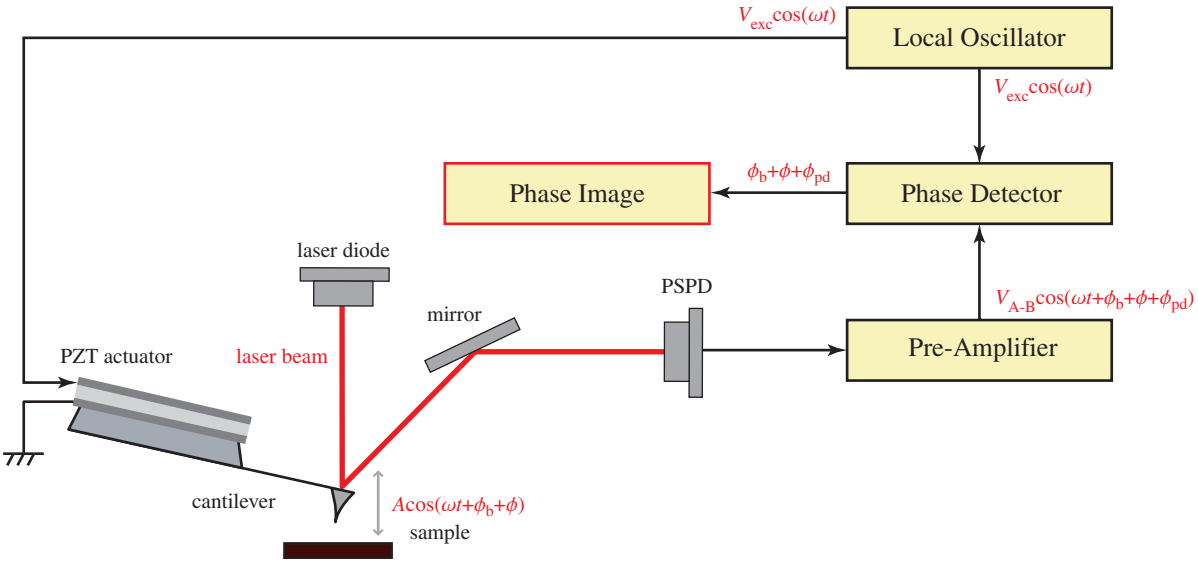

Figure 2.16: The experimental setup for the dissipation imaging with AM-DFM.

two different treatments, namely, constant excitation mode and constant amplitude mode.

In constant excitation mode, A_b is fixed while A varies due to the dissipative tip-sample interactions. From Eq. (2.40) and $\varphi = 90°$, P_{ts} is given by

$$P_{ts} = P_0 \left(\frac{A_0}{A} - 1 \right). \tag{2.43}$$

This equation shows that the variation in P_{ts} is inversely proportional to A.

In constant amplitude mode, A_b is feedback-controlled so as to keep A constant and hence the changes in A_b represent the variation in energy dissipation. From Eq. (2.40), the useful expression for P_{ts} is given by

$$P_{ts} = P_0 \left(\frac{A_b}{A_{b,0}} - 1 \right) = P_0 \left(\frac{V_{exc}}{V_{exc,0}} - 1 \right), \tag{2.44}$$

where $A_{b,0} = A/Q$ and $V_{exc,0}$ are defined as the values for A_b and $V_{exc,0}$ measured without any tip-sample interactions, respectively. In this case, the energy dissipation is directly proportional to the excitation amplitude V_{exc}.

Experimental Setup

Figure 2.17 shows a typical experimental setup for the dissipation measurement with FM-DFM. The deflection signal is fed into the amplitude limiter which regulates the signal amplitude to be constant (V_{lim}). Then the output signal is phase shifted, amplified and fed back to the PZT actuator. In constant excitation mode, the gain factor of the variable gain amplifier (VGA) is manually controlled and fixed during

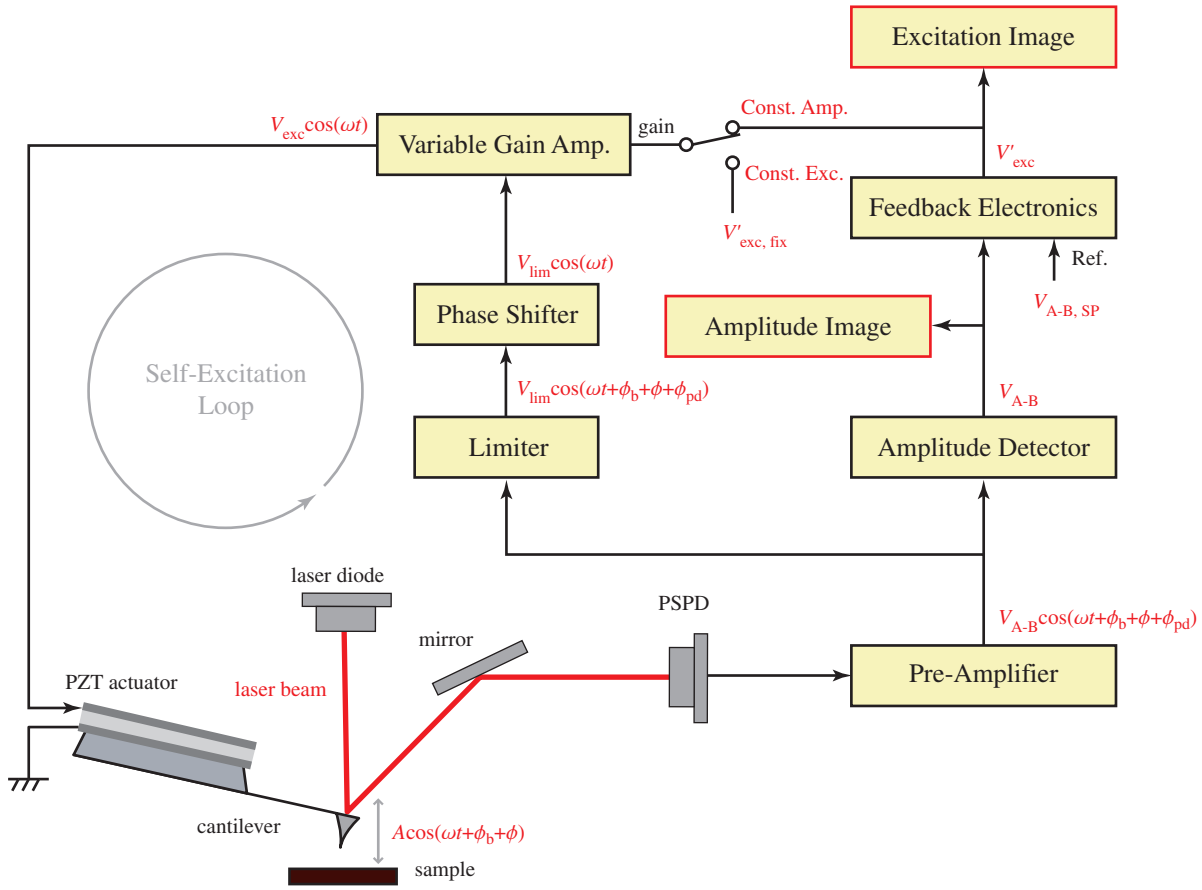

Figure 2.17: The experimental setup for the dissipation imaging with FM-DFM. In constant excitation mode, A_b is fixed while A can be varied by the dissipative tip-sample interactions. In constant amplitude mode, A is kept constant by adjusting V_{exc} and the changes in V_{exc} represent the variation in energy dissipation.

the FM-DFM imaging. On the other hand, the amplitude of the deflection signal ($V_{\mathrm{A-B}}$) is evaluated by the amplitude detector and two-dimensionally mapped to produce an amplitude image showing the dissipation variation during the FM-DFM imaging. In constant amplitude mode, the amplitude signal is also fed into the feedback electronics which controls the gain factor of VGA (V'_{exc}) so as to make $V_{\mathrm{A-B}}$ equal to the preset value of $V_{\mathrm{A-B,SP}}$. In this setup, V'_{exc} is proportional to V_{exc} and A_{b}. Thus the two-dimensional map of V'_{exc}, namely, excitation image represents the dissipation variation during the FM-DFM imaging.

Although energy dissipation can be measured in both constant excitation mode and constant amplitude mode, the latter is more desirable for the quantitative dissipation measurement and accurate tip-sample distance regulation. In constant excitation mode, the dissipative tip-sample interaction causes the amplitude damping, which, however, reduces the amount of the negative frequency shift. Then, due to the distance feedback regulation, the tip-sample distance will be reduced until the increasing attractive interaction compensates the influence of amplitude damping. Therefore, the topographic image taken in constant excitation mode is inevitably involved with such a topographic artifact unless there is no energy dissipation variation. In addition, the interpretation of the contrasts in the amplitude image is not straightforward because it does not taken with a constant tip-sample separation. On the other hand, the constant amplitude regulation allows one to detect the conservative and dissipative interaction forces more independently although the separation is not perfect in some cases.

2.4 Surface Potential Measurement

The tip-sample interaction force (F_{ts}) contains different force components such as van der Waals force (F_{vdW}), electrostatic force (F_{es}) and chemical interaction force (F_{chem}). Since an experimentally measured value for F_{ts} always represents the whole sum of these different components, it is impossible to deduce the magnitude of each component directly from the value itself. However, it becomes possible if the magnitude of a certain force component can be independently modulated and if the modulated force can be separately detected. All force components depend on the tip-sample separation while F_{es} also depends on the tip-sample potential difference (V_{ts}) as described by

$$F_{\mathrm{es}} = \frac{1}{2}\frac{\partial C_{\mathrm{ts}}}{\partial z_{\mathrm{t}}} V_{\mathrm{ts}}^2, \tag{2.45}$$

where C_{ts} is the capacitance between the tip and the sample. Thus F_{es} can be modulated simply by applying an ac bias modulation voltage between the tip and

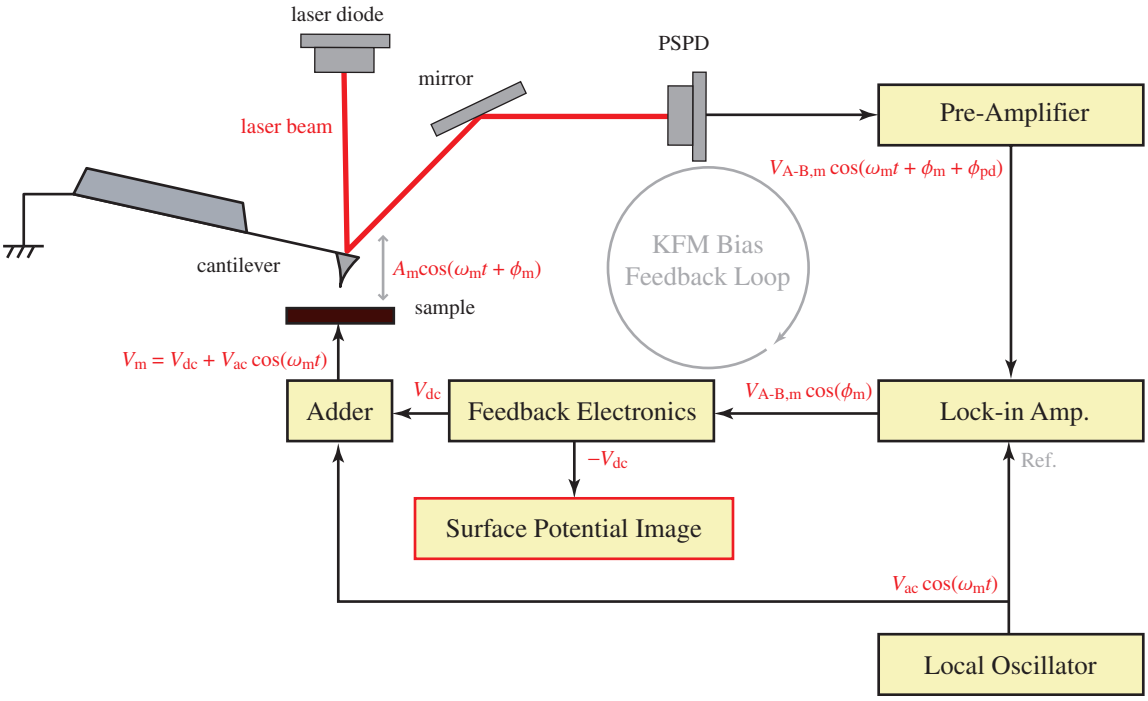

Figure 2.18: A typical experimental setup for KFM with AM detection method (AM-KFM). The distance regulation is made by AM detection method while the modulated electrostatic force is detected directly from the cantilever deflection signal.

the sample.

In order to image surface potential distribution with a high spatial resolution, the tip-sample distance should be accurately controlled simultaneously with the detection of the modulated F_{es}. This complexity gave rise to a number of different types of surface potential measurement methods. Among them, Kelvin probe force microscopy (KFM), which was first introduced by Nonnenmacher *et al.*,[26] probably is the most widely used technique. In KFM, the tip-sample distance regulation can be made by either AM detection method or FM detection method. Hereafter in this section, the basic principle and the experimental setup of KFM are described for each of these two operation modes.

2.4.1 KFM with AM Detection Method (AM-KFM)

Figure 2.18 shows a typical experimental setup for KFM with AM detection method (AM-KFM). The tip is electrically grounded while the sample is biased with a modulation voltage (V_m) which is given by

$$V_m = V_{dc} + V_{ac}\cos(\omega_m t), \tag{2.46}$$

where $V_{\rm dc}$ is the dc component of $V_{\rm m}$ while $V_{\rm ac}$ and $\omega_{\rm m}$ are the amplitude and the frequency of the ac component of $V_{\rm m}$, respectively. From Eq. (2.45) and (2.46), $F_{\rm es}$ is given by

$$\begin{aligned} F_{\rm es} &= \frac{1}{2}\frac{\partial C_{\rm ts}}{\partial z_{\rm t}}(V_{\rm m}+V_{\rm CPD})^2 && (2.47)\\ &= \frac{1}{2}\frac{\partial C_{\rm ts}}{\partial z_{\rm t}}[(V_{\rm dc}+V_{\rm CPD})^2+2(V_{\rm dc}+V_{\rm CPD})V_{\rm ac}\cos(\omega_{\rm m}t) \\ &\quad +V_{\rm ac}^2\cos^2(\omega_{\rm m}t)], && (2.48)\end{aligned}$$

where $V_{\rm CPD}$ is the contact potential difference (CPD) between the tip and the sample. $V_{\rm CPD}$ between two materials depends on a variety of parameters such as work function (Φ), adsorption layers, oxide layers, dopant concentration in semiconductors and so on. In a simplest model, $V_{\rm CPD}$ is expressed by

$$V_{\rm CPD}=\frac{\Phi_t-\Phi_s}{e}, \tag{2.49}$$

where Φ_t and Φ_s are the work function of the tip and the sample, respectively, including the changes due to the adsorption layers on the surface.

From Eq. (2.48), $\omega_{\rm m}$ component of $F_{\rm es}$ ($(F_{\rm es})_{\rm m}$) is given by

$$(F_{\rm es})_{\rm m}=\frac{\partial C_{\rm ts}}{\partial z_{\rm t}}(V_{\rm dc}+V_{\rm CPD})V_{\rm ac}\cos(\omega_{\rm m}t). \tag{2.50}$$

This force component induces the cantilever deflection at the frequency of $\omega_{\rm m}$. In AM-KFM, the $\omega_{\rm m}$ component of the deflection signal is detected by a lock-in amplifier and routed for the feedback electronics which controls $V_{\rm dc}$ so as to cancel out $(F_{\rm es})_{\rm m}$. Consequently, $V_{\rm dc}+V_{\rm CPD}$ becomes nearly zero in a steady state so that the surface potential image can be obtained by recording $-V_{\rm dc}$ as a two-dimensional map.

In AM-KFM, the cantilever is mechanically vibrated near the resonance frequency to perform the tip-sample distance regulation whereas the cantilever is also driven by a modulated electrostatic force to perform the bias feedback regulation. In order to avoid the interference between the distance regulation and the bias regulation, $\omega_{\rm m}$ should be carefully selected. Firstly, $\omega_{\rm m}$ should be higher than the cutoff frequency of the distance regulation ($\omega_{\rm c}$), which typically lies in the range of 100 – 500 Hz. Secondly, $\omega_{\rm m}$ should be sufficiently apart from the first resonance (ω_0) of the cantilever so as not to affect the amplitude of the mechanically driven oscillation.

In most cases, $\omega_{\rm m}$ is selected to meet $\omega_{\rm c} \ll \omega \ll \omega_0$. In that case, since the cantilever is driven at an off-resonance frequency by a modulated electrostatic force, k has to be small (typically 1 – 5 N/m) enough to achieve a sufficient force sensitivity. For such a relatively soft cantilever, the resonance frequency is relatively low (typically 10 – 100 kHz). Thus typical values for $\omega_{\rm m}$ are 1 – 20 kHz.

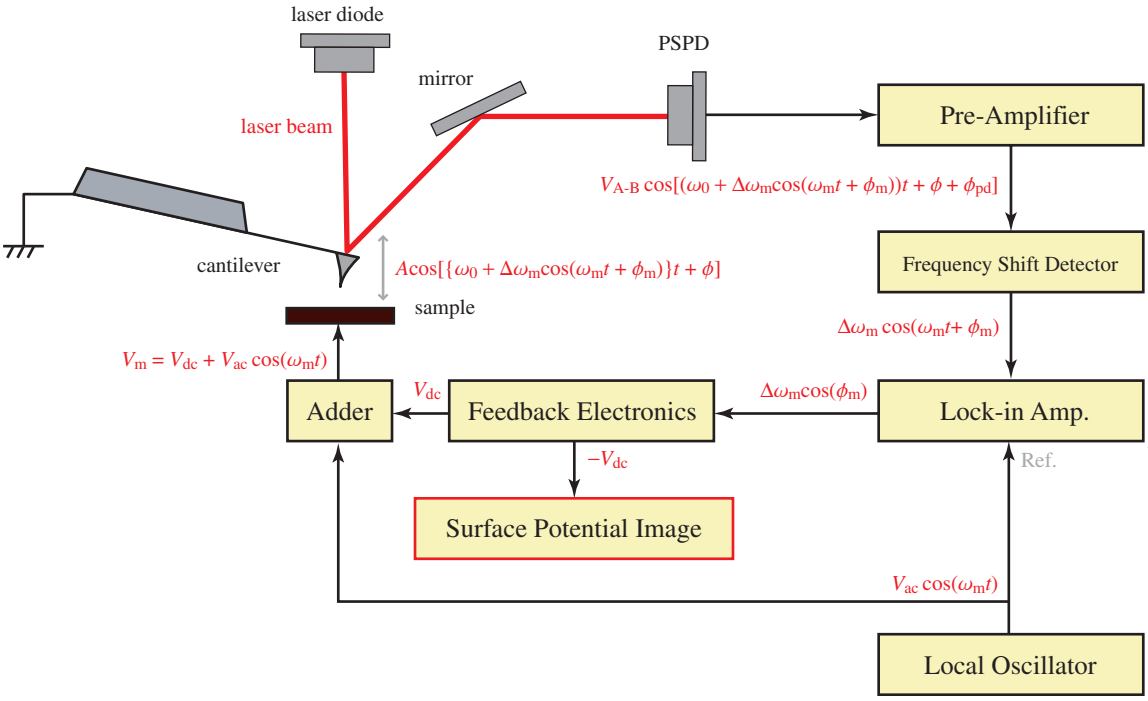

Figure 2.19: A typical experimental setup for KFM with FM detection method (FM-KFM). The distance regulation is made by FM detection method while the modulated electrostatic force is detected from the output signal of the frequency shift detector.

2.4.2 KFM with FM Detection Method (FM-KFM)

Figure 2.19 shows a typical experimental setup for KFM with FM detection method (FM-KFM).[29] The main difference between AM-KFM and FM-KFM is the detection method of $(F_{es})_m$. In FM-KFM, $(F_{es})_m$ is detected from the output signal of the frequency shift detector using a lock-in amplifier. Although it is possible to detect $(F_{es})_m$ directly from the deflection signal as performed in AM-KFM, this method is rarely used in FM-KFM. Since FM-KFM is usually operated in the non-contact or atomic-scale contact regions, the cantilever has to be relatively stiff (typically 20 – 60 N/m) in order to avoid the jump-to-contact. Accordingly, the force sensitivity of the cantilever deflection is insufficient for most of the applications. Instead, the force sensitivity of Δf is good enough to be used for the detection of $(F_{es})_m$. In particular, the force sensitivity is significantly improved under vacuum conditions owing to the enhancement of the Q-factor.

In FM-KFM, ω_m is usually determined by the bandwidth of the frequency shift detector (typical 1 – 10 kHz). Thus typical values for ω_m are 1 – 4 kHz.

Chapter 3

In-situ Analyses of Thermal Phase Transitions

3.1 Introduction

AM-DFM is quite tolerant to the drastic change of the tip-sample interaction force because the cantilever is continuously vibrated at a fixed frequency with a constant excitation voltage. In order to make the best use of this advantage, AM-DFM was applied to the *in-situ* analyses of thermal phase transition processes of polymer thin films. During such processes, the surface becomes so unstable that it cannot be imaged by a conventional AFM where the tip is scanned in contact with the sample surface. For example, during the crystallization process, the surface is dynamically moving due to the molecular motion involved with the amorphous-to-crystal transition. Simmilarly, during the melting and recrystallization process, the surface shows fluid-like behavior due to the transition between the solid phase and the liquid phase.

Although AM-DFM is expected to be one of the most promising tools for the direct investigations on thermal phase transitions of polymers, there have been only a few reports on such applications.[123,124] Therefore, there still remain many important applications to be experimentally demonstrated. In this chapter, the nano-scale structural changes of ferroelectric polymer thin films were directly visualized using a variable-temperature AM-DFM (VT-AM-DFM) during various thermal phase transition processes such as crystallization, ferroelectric phase transition, and melting and recrystallization processes. In addition, a variable-temperature AM-KFM (VT-AM-KFM) was employed to measure the temperature dependence of both surface potential and film thickness during the ferroelectric phase transition process.

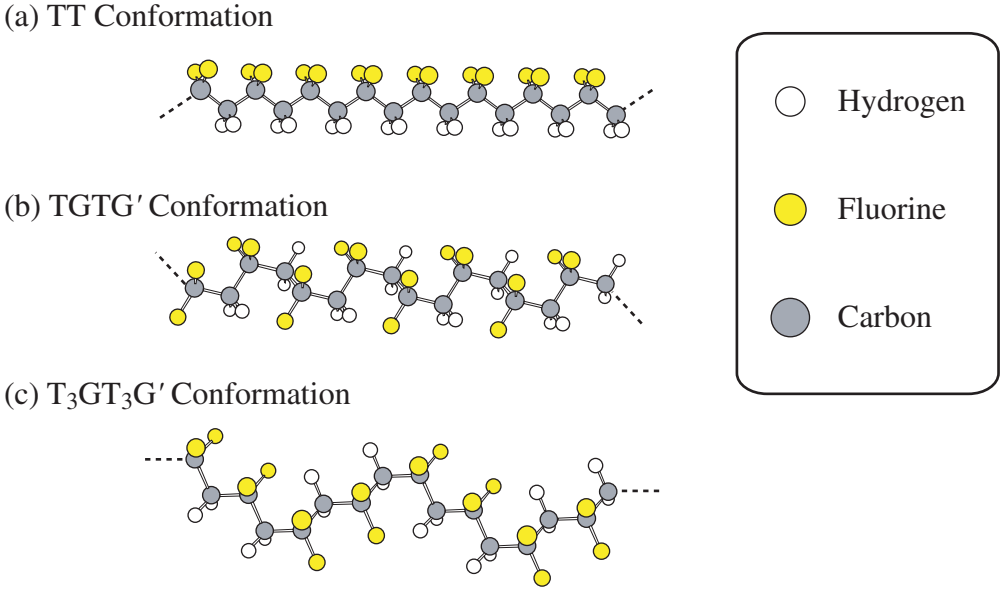

Figure 3.1: Schematic drawings of three different conformations of PVDF. (a) TT conformation. (b) TGTG′ conformation. (c) T_3GT_3G' conformation (T: *trans*, G: *gauche*).

3.2 P(VDF/TrFE) Thin Films on HOPG Surfaces

3.2.1 Polyvinylidene Fluoride

Polyvinylidene fluoride (PVDF: CH_3-$(CH_2CF_2)_n$-CH_3) has good mechanical strength and excellent tolerance to the heat and chemicals. Thus the polymer had been mostly used as a coating material for the mechanical and electrical parts. However, since the first demonstration of its piezoelectricity in 1969,[125] PVDF has started to be intensively studied as a ferroelectric polymer material.

The molecular chain of PVDF can take three different conformations as shown in Fig. 3.1, namely, TT, TGTG′ and T_3GT_3G' (T: *trans*, G: *gauche*) conformations. In addition when the polymers are crystallized, their molecular chains are packed in parallel or antiparallel to each other. Thus depending on these conformations and packing forms, PVDF is expected to show six different crystal forms as shown in Fig. 3.2. Among them, the existence of five crystal forms except for the form VI have been experimentally confirmed although in most cases PVDF shows the form II or form I.

In the molecular chains, each VDF unit (-CH_2CF_2-) has a large electric dipole

moment (2.1 debye/monomer)* between the hydrogen and fluorine pairs due to the difference in electronegativity. When the molecular chains take parallel packing forms, the polymer crystal shows some spontaneous polarization corresponding to the overall vector sum of the dipole moments. Thus the form I, III and IV exhibit order-disorder type ferroelectricity. Among these three ferroelectric crystal forms, the form I shows the strongest ferroelectricity because the dipole moments of all VDF units are aligned in one direction in this crystal form. However, the most stable crystal form of PVDF at room temperature is not the ferroelectric phase but the paraelectric phase of form II. Therefore, in order to utilize PVDF as ferroelectric material, it is required to transform the crystal form from the form II to form I by some special preparation processes such as uni-axial drawing, annealing and applying strong electric field.

3.2.2 Copolymer of Vinylidene Fluoride and Trifluoroethylene

In contrast to PVDF, the copolymers of VDF and trifluoroethylene (P(VDF/TrFE)) with VDF content of 12 – 82% are directly crystallized into the ferroelectric phase at room temperature without any special preparations.[126] Thus the ferroelectric phase crystal of P(VDF/TrFE) can be easily obtained by spin-coating or cast method. In particular, when the VDF content is within the range of 50 – 80%, the copolymers show remarkably strong ferroelectric nature such as abnormal dielectric behavior around the Curie temperature (T_C). The ferroelectric phase P(VDF/TrFE) takes quite similar crystal form to the form I of PVDF though the lattice constants are a little expanded along the a-axis and b-axis.[127] Hereafter the ferroelectric phase crystal form of P(VDF/TrFE) will be also referred to as form I.

The structural changes during the thermal phase transitions of P(VDF/TrFE) have been extensively studied by X-ray and electron beam diffraction methods and infrared and Raman absorption spectroscopies. For instance, Koga *et al.* presented the phase diagram of P(VDF/TrFE) crystal structures as a function of the VDF content and temperature[128] as shown in Fig. 3.3. When the form I crystal of P(VDF/TrFE) was heated beyond T_C, the crystal form is changed into so-called "rotator-phase" where the molecular chains are hexagonally packed taking the conformation of TT, TG and TG′ random combinations.[129,130] In this phase, the molecular chain suffers from a rotational fluctuation along its molecular axis so that the crystal shows no net polarization and exhibits paraelectric behavior. The crystal forms of ferroelectric and paraelectric phases are schematically depicted in Fig. 3.4

*For example, $BaTiO_3$ shows about 3.1 debye per unit cell at room temperature.

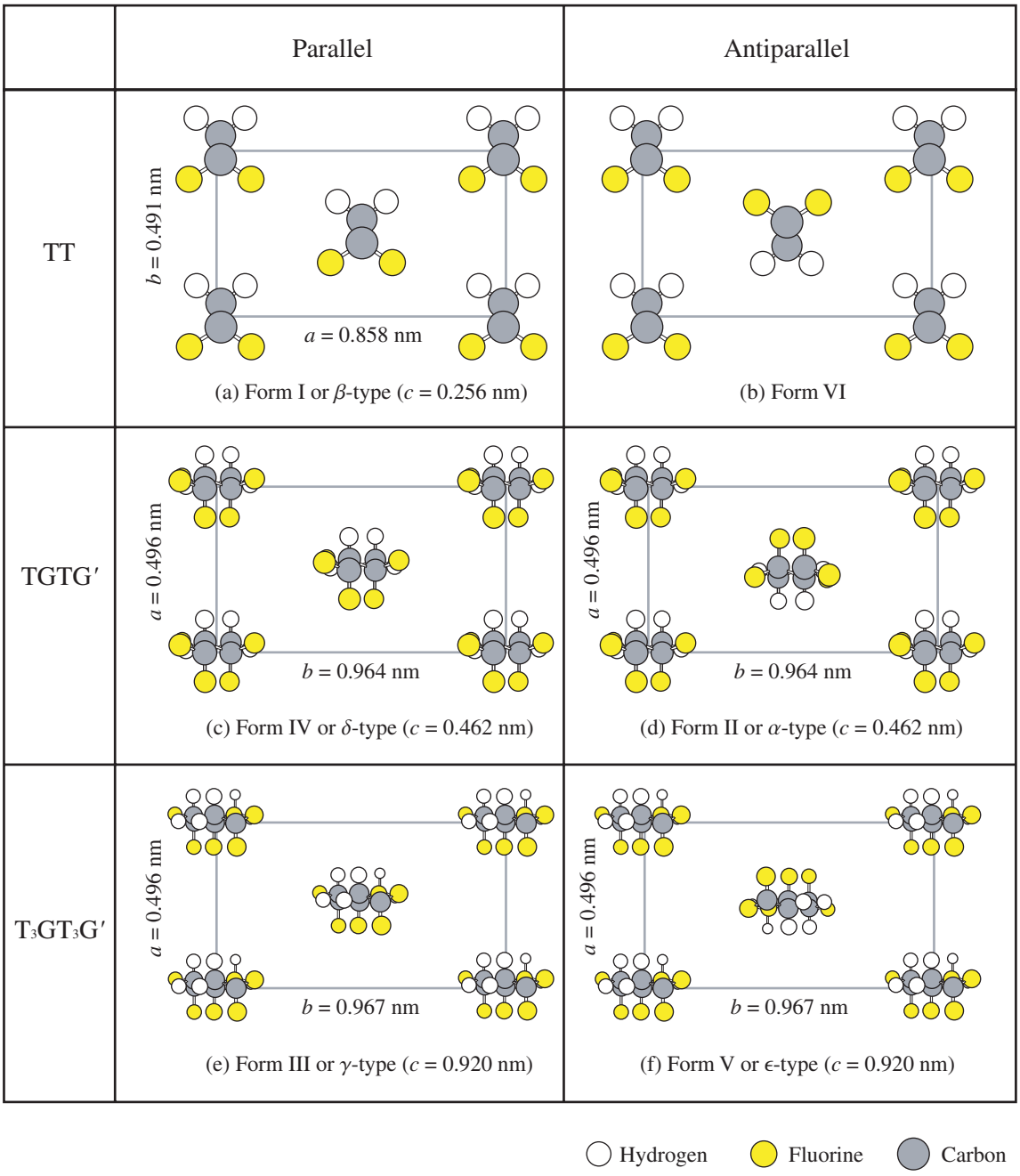

Figure 3.2: Schematic drawings of six different crystal forms of PVDF. (a) Form I (β-type). (b) Form VI. (c) Form IV (δ-type). (d) Form II (α-type). (e) Form III (γ-type). (f) Form V (ε-type).

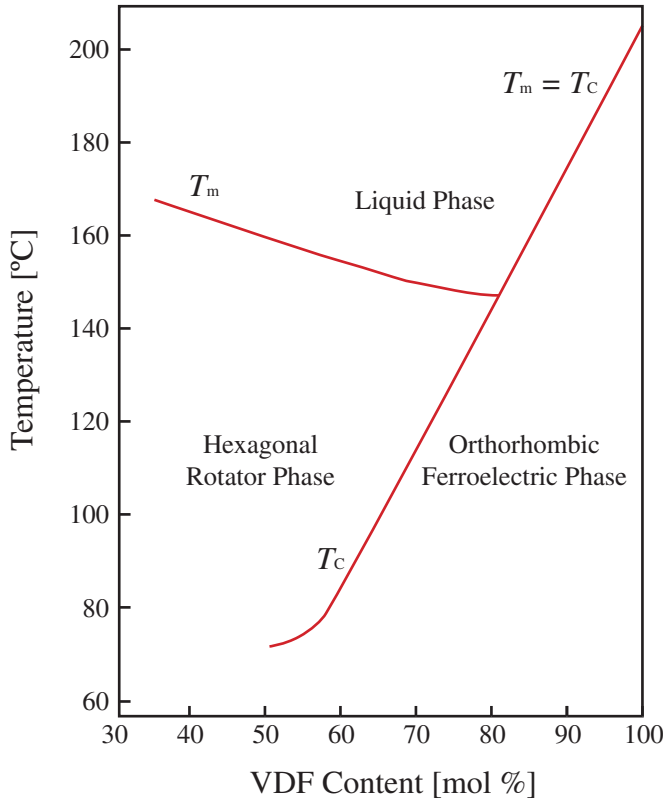

Figure 3.3: Phase diagram of P(VDF/TrFE) crystal structures which was proposed by Koga *et al.*[128]

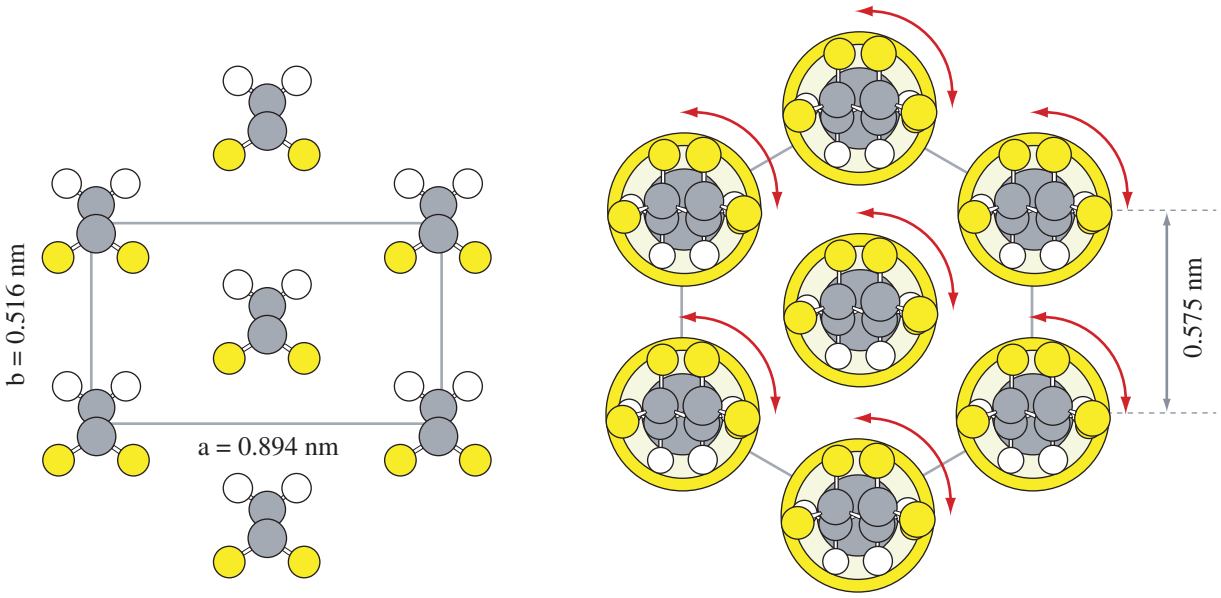

(a) Ferroelectric Phase (Orthorhombic Structure)

(b) Rotator Phase (Hexagonal Structure)

Figure 3.4: The crystal structures of (a) ferroelectric phase and (b) paraelectric rotator phase of P(VDF/TrFE).

The crystallinity of the P(VDF/TrFE) is drastically improved by annealing at a temperature between T_C and melting point (T_m).[131] In general, the crystallinity of single component polymers is better than that of its related copolymers. However, in the case of P(VDF/TrFE), its crystallinity is much better than that of PVDF. As a result, the copolymer shows better characteristics in terms of its ferroelectric properties such as piezoelectricity and pyroelectricity.

3.2.3 P(VDF/TrFE) Thin Films on HOPG Surfaces

Recently, Bune *et al.* revealed that the P(VDF/TrFE) thin film can maintain its ferroelectricity even when its thickness is reduced to 3 – 4 nanometers.[132] This result opened a wide variety of future applications to the organic thin film devices. As the film thickness is reduced, the effects of film/substrate and film/air interfaces are getting more and more evident. Therefore, in order to realize the practicable thin film devices of P(VDF/TrFE), it would be of great importance to elucidate the local structural and electrical properties of P(VDF/TrFE) thin films. Although the bulk materials of P(VDF/TrFE) were already studied in detail, the properties in thin film state have rarely understood yet.

The sample used in this study was the P(VDF/TrFE) thin film spin-coated on HOPG surface. The VDF content of the copolymer was 73%. The copolymer of this VDF content shows ferro-to-paraelectric phase transition at about 100 – 120°C during the heating process while para-to-ferroelectric phase transition occurs at about 80 – 90°C during the cooling process.[127] The melting point (T_m) of the copolymer is about 150°C. Note that these values for the Curie points (T_C) and T_m were reported on the samples in a bulk state. Namely, T_C and T_m for the P(VDF/TrFE) thin films have not been clarified yet.

So far, the structural and electrical properties of the sample were intensively studied by Chen *et al.*[5,133–136] They investigated the dependence of the surface morphology and the film crystallinity on the annealing temperature using AFM.[5] The result revealed that the appropriate annealing condition is 140°C for 2h. They found that the sample prepared with this condition is composed of some "rod-like grains" as shown in Fig. 3.5 although the formation mechanism of the grains still remains unclear.

They also studied the electrical property of the sample using piezoelectric response imaging,[134–136] which revealed the alignment of the electric dipole moments within the film (Fig. 3.6). The dipoles near the film/substrate interface are somehow aligned in the negative direction by the film/substrate interaction and cannot be "switched" by applying the electric field between the conductive AFM tip and

Figure 3.5: The AM-DFM image of the P(VDF/TrFE) thin film annealed at 140°C for 2 h (1 μm $\times$ 1 μm).

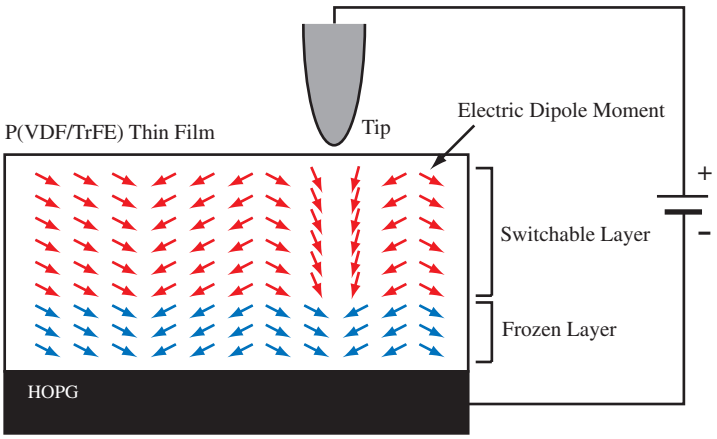

Figure 3.6: A schematic model showing the alignment of the electric dipole moments within the P(VDF/TrFE) thin film annealed at 140°C for 2 h.[134–136]

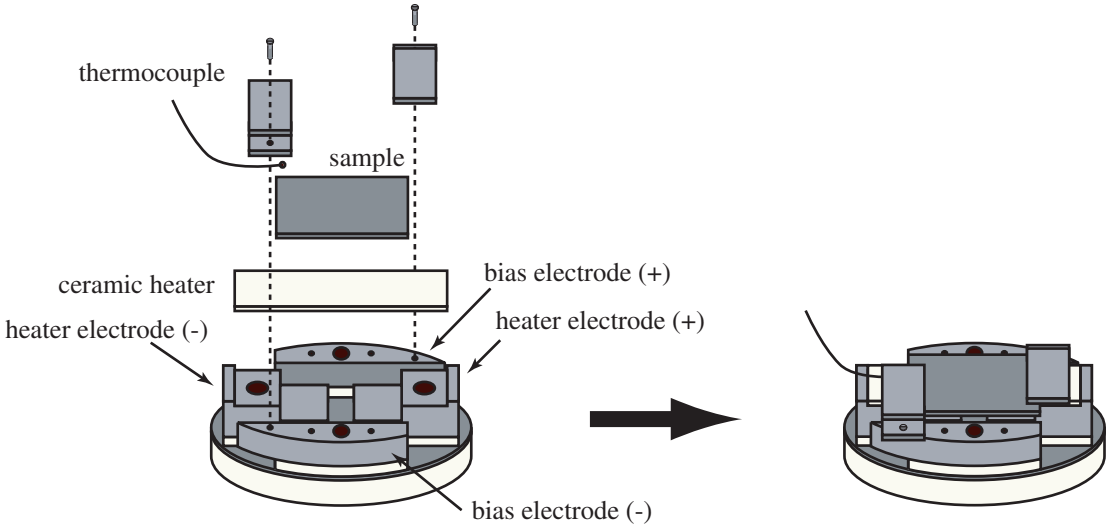

Figure 3.7: The schematic drawing of the sample holder for the VT-DFM. The film temperature is measured with a thermocouple sensor and controlled by heating a small ceramic heater which is in contact with the backside of the sample.

the HOPG substrate. And hence they referred to this quenched layer as "frozen layer". Therefore, the post-annealed sample always shows negative surface potential with respect to the HOPG substrate. On the other hand, the dipoles in the rest part of the film ("switchable layer") can be switched by an external electric field. In view of its applications to the organic thin film devices such as ultrahigh-density data storage media, the temperature dependence of the electric dipole moments has to be elucidated. This is one of the major motivations for the *in-situ* AM-KFM measurements described in this chapter.

3.3 Experimental

3.3.1 Experimental Setup

All the experiments described in this chapter were performed under ambient conditions with a commercially available variable-temperature DFM (VT-DFM) system (JEOL: JSPM-4200). Figure 3.7 shows a schematic drawing of the sample holder for the VT-DFM system. The sample was heated with a small ceramic heater which was in contact with the backside of the graphite substrate. The thermocouple sensor was directly attached to the sample surface, in order to measure the surface temperature of the film accurately. The temperature control was made by a PID feedback controller (Shimaden: FP21). The sample was fixed with the two metal fittings which also make the electrical connection between the sample and the bias electrode. The whole DFM unit was covered with a glass bell jar in order to pre-

vent the disturbance due to the air convection during the heating and the cooling processes.

The Si cantilever (Olympus) with a resonance frequency of about 300 kHz and a nominal spring constant of 20 N/m was used for the AM-DFM imaging. The typical Q-factor measured under an ambient condition was about 300. During the AM-DFM imaging, the tip and the sample were electrically grounded. The tip-sample distance regulation was made in constant amplitude mode. As an amplitude detector, a single-chip RMS-to-DC converter equipped with the JSPM-4200 was used without any modifications.

The gold-coated Si cantilever (Olympus) with a resonance frequency of about 24 kHz and a nominal spring constant of 1.7 N/m was used for the AM-KFM imaging. The ac and dc bias voltage were applied between the tip and the sample during the AM-KFM imaging. The amplitude and the frequency of the ac bias modulation voltage were 2.8 $V_{p\text{-}p}$ and 4 kHz, respectively. Due to the bias modulation, the electrostatic force and the resultant cantilever deflection were modulated at the same frequency. Then the modulated deflection signal was detected by a lock-in amplifier (NF: 5610B). The KFM bias feedback regulation was made using a proportional feedback controller equipped with JSPM-4200.

3.3.2 Sample Preparation

The molecules used in this experiment were P(VDF/TrFE) with 73% VDF content. The copolymer shows ferro-to-paraelectric phase transition at about 100 – 120°C during the heating process while para-to-ferroelectric phase transition occurs at about 80 – 90°C during the cooling process.[127] The melting point (T_m) of the copolymer is about 150°C. Note that these values for the Curie points (T_C) and T_m were reported on the samples in a bulk state.

After P(VDF/TrFE) powder was dissolved in methylethylketone, the solution (5 mg/ml) was deposited onto a freshly cleaved graphite substrate using spin-coating method. The thickness of the film ranged from 20 to 50 nm depending on the spin-coating conditions. The obtained thin film was crystallized by annealing at 140°C for 2 h. As for the *in-situ* imaging of the crystallization process, the annealing treatment was performed under an ambient condition and the structural changes during this annealing process were directly visualized by AM-DFM. As for the other experiments, the sample was annealed under a vacuum condition and the post-annealed sample was used for the AM-DFM and AM-KFM experiments.

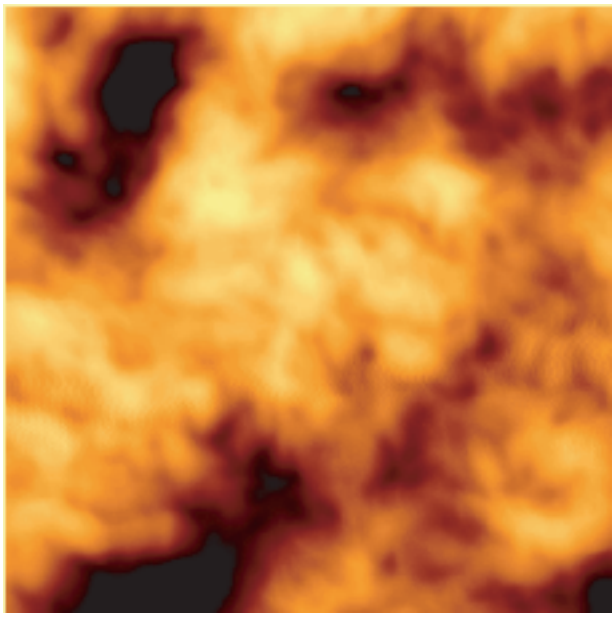

Figure 3.8: The AM-DFM image of the P(VDF/TrFE) thin film just after the spin-coating (1 μm $\times$ 1μm). The image was taken with a relatively strong tip-sample interaction force (Hard-Force Imaging).

3.4 Crystallization Process of P(VDF/TrFE) Thin Films

Heating Process

Figures 3.8 shows an AM-DFM image of the copolymer thin film immediately after the spin-coating. The image was taken with a relatively strong tip-sample interaction force (hard-force imaging). This image is rather obscure and no distinctive structures can be observed. No reproducibility could be obtained under this condition, probably because the film was deformed by the strong tip-sample interaction force. The same sample was imaged with relatively weak tip-sample interaction force (light-force imaging) as shown in Fig. 3.9(a). The image clearly reveals that the as-deposited film consists of closely packed spherical grains with diameters of 20 – 50 nm. These results suggested that most of the film is covered with amorphous regions which are too soft to be imaged by hard-force imaging. In other words, it was found that even such a very soft surface can be imaged by light-force imaging. Therefore, light-force imaging was used to image the film at the beginning of the heating process.

Figure 3.9 shows a series of AM-DFM images obtained in the heating process from room temperature (25°C) to the annealing temperature (140°C). While the film was heated from 25°C to 100°C, adjacent small grains gradually formed clusters.

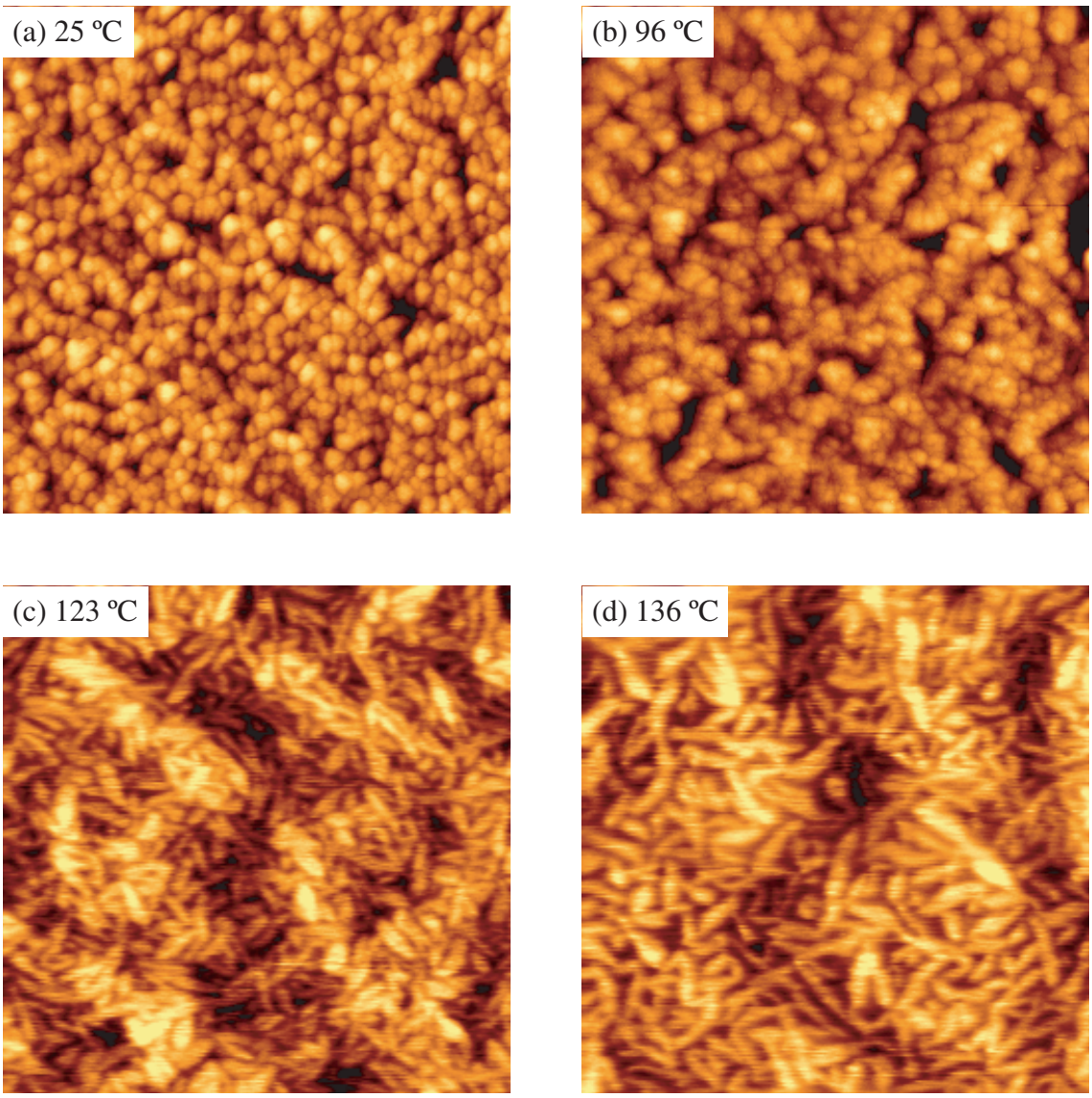

Figure 3.9: The AM-DFM images of the P(VDF/TrFE) thin film taken during the heating process at (a) 25°C, (b) 96°C, (c) 123°C and (d) 136°C (1 μm $\times$ 1μm).

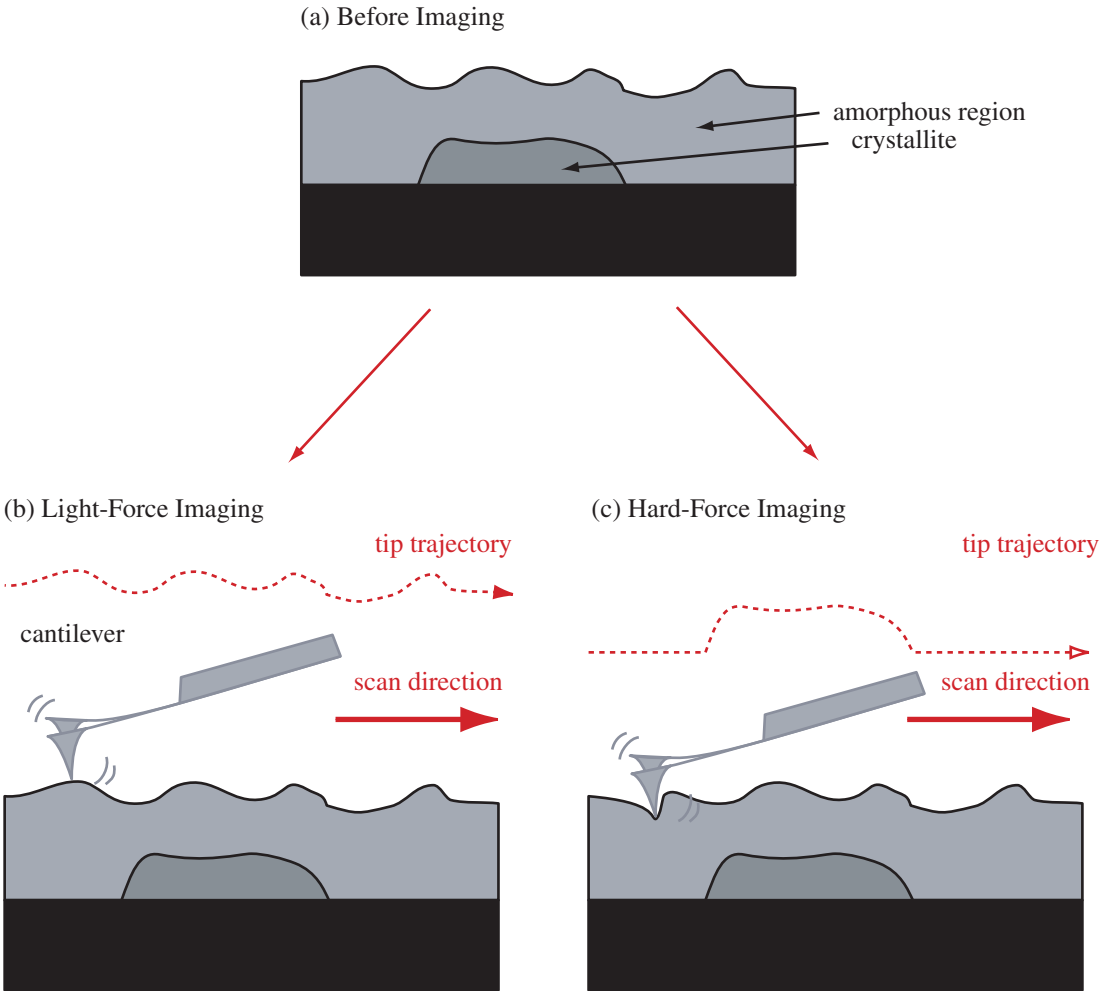

Figure 3.10: A schematic model showing the difference between light-force imaging and hard-force imaging.

Some spherical grains could be still observed in the clusters as shown in Fig. 3.9(b).

However, in the temperature range between 100°C and 130°C, it became even more difficult to image the real surface morphology by light-force imaging. Instead, hard-force imaging became more useful for revealing the structure of underlying crystallites, as shown in Fig. 3.9(c). The imaging mechanism can be explained as follows (Fig. 3.10). Using light-force imaging, the surface morphology can be imaged even on a very soft surfaces such as amorphous polymers as shown in Fig. 3.10(b). Since the structure couldn't be observed by light-force imaging, the image should represent not the surface morphology but the surface stiffness variation. In this experiment, the film is composed of a single molecular species so that the observed stiffness variation is ascribed to the difference in the molecular packing arrangements, namely, the crystallinity. In general, there is large difference in the stiffness between the amorphous polymer and the crystal one. Therefore, the grains observed

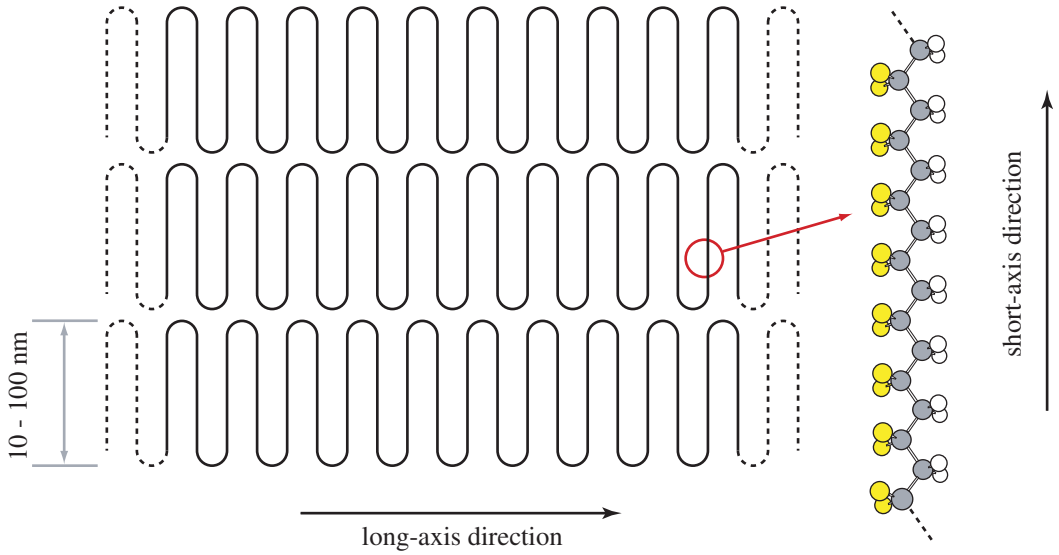

Figure 3.11: A schematic model showing the lamella structure of P(VDF/TrFE).

in Fig. 3.9(c) corresponds to the small crystallites hidden under a amorphous layer as shown in Fig. 3.10(c).

The temperature range where the light-force imaging became unstable was well corresponds to the reported value for T_C in the heating process (100 – 120°C). In addition, it was reported that the crystallinity of P(VDF/TrFE) is drastically improved when it is annealed at a temperature between the T_C and T_m. From these results, it was suggested that the crystallization process of the P(VDF/TrFE) thin film takes place when the temperature is elevated over T_C. During the crystallization process, the surface structure should be continuously changing so that no surface information can be obtained by light-force imaging. Thus the hard-force imaging was used above this temperature range to visualize the structural changes of the underlying crystallites.

In the temperature range between 130°C and 140°C, some crystallites coalescent into the rod-like grains with a width of 20 – 40 nm as shown in Fig. 3.9(d). The grain showed not a "round-shaped" structure but a "rod-like" structure. Such an anisotropic crystal growth can be explained It is known that the P(VDF/TrFE) with this VDF content is crystallized into the lamella structure (Fig. 3.11) after the annealing treatment at a temperature between T_C and T_m. In addition, the grain showed anisotropic growth, making up a "rod-like" grain. Thus it was suggested that the grain is composed of the lamella structure with the molecular axis oriented in the short-axis direction of the rod-like grain.

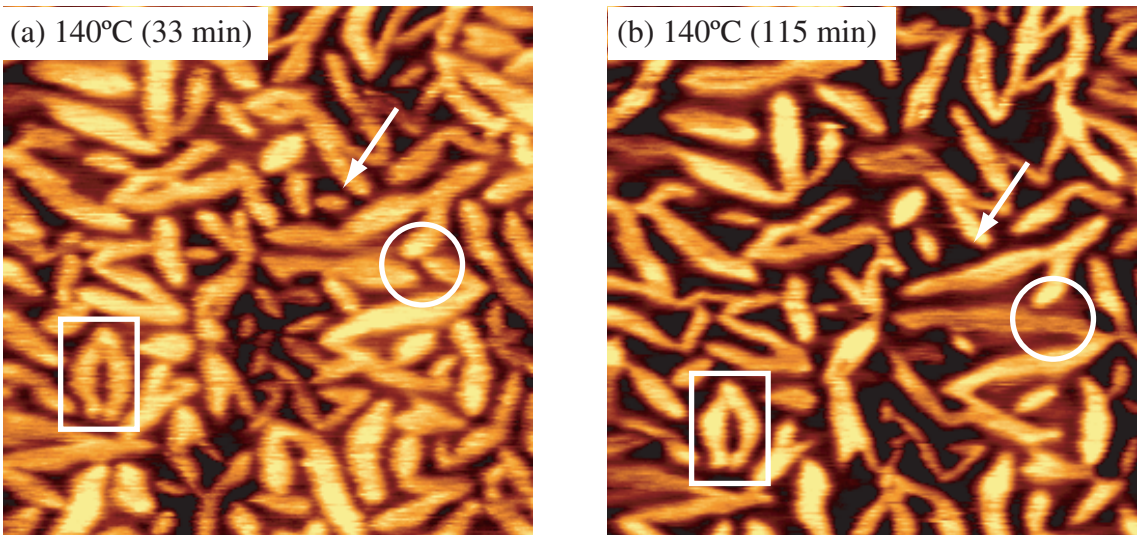

Figure 3.12: The AM-DFM images of the P(VDF/TrFE) thin film taken after annealing at 140 °C for (a) 33 min and (b) 115 min (1 μm $\times$ 1μm).

Annealing Process

Figures 3.12(a) and 3.12(b) show the AM-DFM images of the P(VDF/TrFE) thin film obtained during the annealing process at 140°C for 2 h. In the first stage of the heating process, it was very difficult to image the same area because the surface morphology had no evident structural feature which could be used as a landmark to identify the area. However, the grains formed during the heating process had distinct features which could be used as landmarks. Thus, as for the annealing and cooling processes, almost the same area was imaged based on the landmark grain which is surrounded by a white square in Fig. 3.12.

While the film was annealed at 140°C, some of the small grains disappeared as indicated by the white arrow in Fig. 3.12. At the same time, relatively large grains started to combine with neighboring ones as indicated by the white circle in Fig. 3.12. This tendency continued until about 50 min past from the beginning of the annealing process, while little change was observed during the remaining 70 min of the annealing time. These results revealed that the melting of the smaller grains and the coalescence of the larger grains simultaneously take place during the annealing process.

Cooling Process

Figures 3.13(a) and (b) show the AM-DFM images of the copolymer film obtained in the cooling process. During the cooling process, the grains grew in the width until about 110°C as shown in Fig. 3.13(a). As a general crystal growth mechanism of

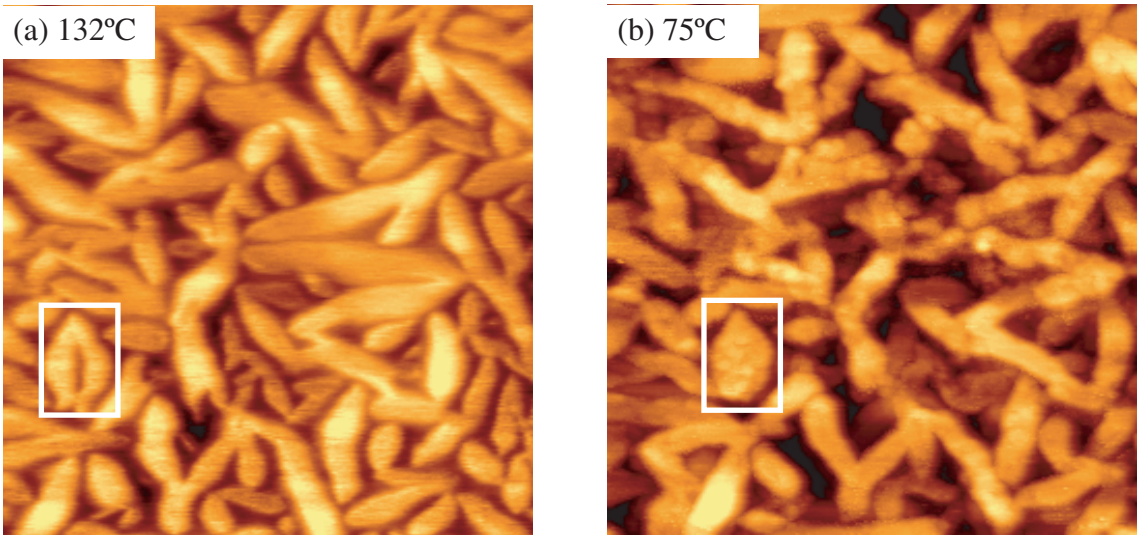

Figure 3.13: The AM-DFM images of the P(VDF/TrFE) thin film taken in the cooling process at (c) 132 °C and (d) 75 °C (1 μm × 1μm).

the linear-chain polymers, Hikosaka proposed sliding diffusion mechanism.[137] As for the P(VDF/TrFE), this mechanism is explained as follows.[138–141] In the ferroelectric phase, the chain sliding in the molecular axis direction is prohibited by the large potential barrier due to the steric hindrance. In the paraelectric phase, the potential barrier is significantly reduced due to the rotational fluctuation along the molecular chain (Fig. 3.4(b)). Thus the crystal grows in the c-axis (molecular axis) direction due to the sliding diffusion at the temperature range between T_{C} and T_{m}. Therefore, the observed expansion in the grain width confirmed that the molecular axis is oriented in the short-axis direction of the rod-like grain.

Little change was observed in the temperature range from 110°C to 85°C. However, fine structures gradually appeared in the grains from 85°C to 70°C as shown in Fig. 3.13(b). This temperature approximately corresponds to T_{C} reported on the bulk copolymer. Figure 3.14 shows more magnified images obtained before and after this structural change. The origin of this phenomenon will be discussed in the next section in relation to the ferroelectric phase transition. After this drastic change, little change was observed during the rest of the cooling process.

Crystallization Process

From the results obtained in this section, the structural changes during the crystallization process are summarized as follows. The as-deposited film is composed of some spherical amorphous grains with a diameter of 20 – 50 nm (Fig. 3.9(a)). When the film is heated, they coalescent into larger grains (Fig. 3.9(b)). As the

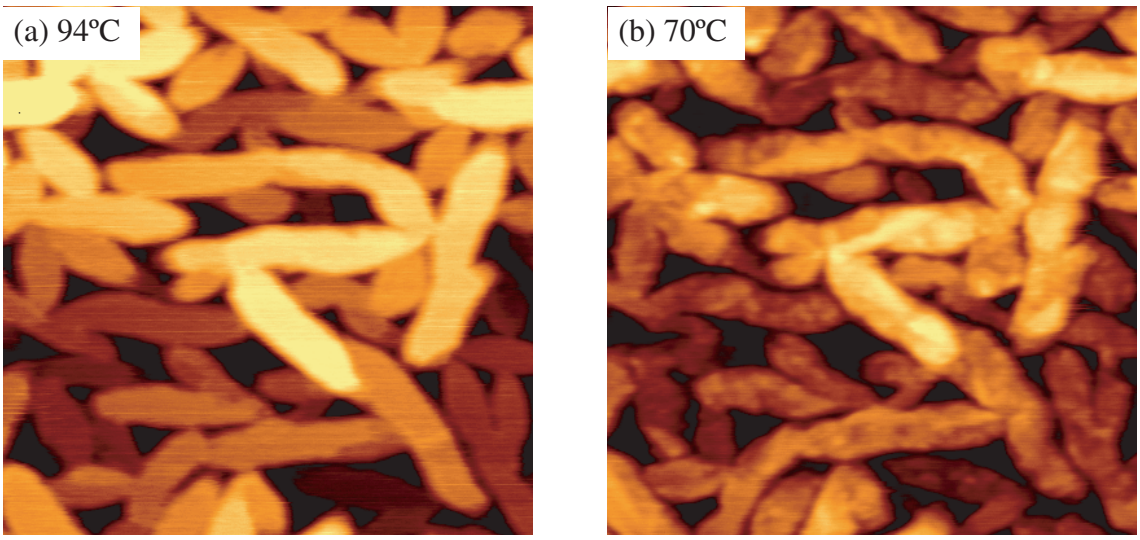

Figure 3.14: The AM-DFM images of P(VDF/TrFE) thin film obtained (a) above (94 °C) and (b) below (70 °C) T_C in the cooling process (800 nm × 800 nm).

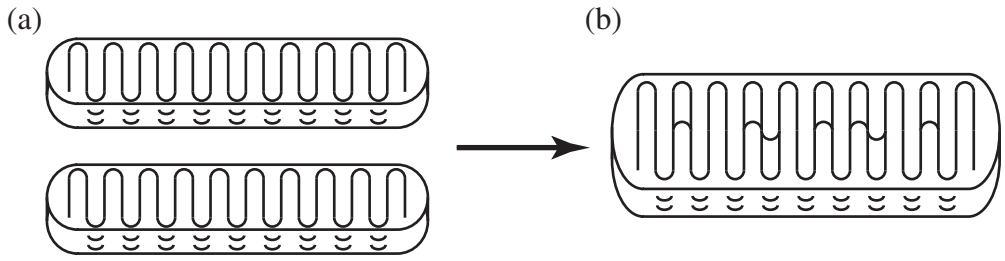

Figure 3.15: A schematic model of showing the inner structure of the rod-like grains.

temperature exceeds T_C, the copolymers start to crystallize into the rod-like grains from the film/substrate interface (Fig. 3.9(c)). The grain is composed of the lamella crystal as schematically depicted in Fig. 3.15(a). Then further heating makes some of the rod-like grains coalescent into thicker grains (Fig 3.9(d)). In this process, some of the molecular chains in one grain should penetrate into the other one due to the sliding diffusion (Fig. 3.15(b)). Such a diffusion process makes the domain boundary with in the rod-like grains relatively ambiguous. During the annealing, smaller grains are eliminated due to the melting (Fig. 3.12). During the subsequent cooling process the grain width expands because of the sliding diffusion (Fig. 3.13). This sliding diffusion further makes the above mentioned domain boundary more and more ambiguous.

3.5 Ferroelectric Phase Transition Process of P(VDF/TrFE) Thin Films

3.5.1 AM-DFM Imaging

In this experiment, the post-annealed sample was heated up to just below T_m and then cooled down to the room temperature. During the heating and cooling processes, the surface structures were directly imaged by AM-DFM. Judging from the results described in the previous section, it is expected that the topmost surface morphology would become quite unstable near T_m. Thus in this experiment, hard-force imaging was used to visualize the structural changes of the rod-like grains.

Figure 3.16 shows a series of AM-DFM images acquired during the heating and cooling process. One of the rod-like grains surrounded by a white square in Fig. 3.16 was used as a landmark to confirm the fact that approximately the same area of the film was imaged. Little change in structure was found until 120°C. However, when the temperature exceeded 120°C, the fine structures suddenly disappeared and the grains apparently turned smooth as shown in Fig. 3.16(b). The more magnified AFM images obtained before and after this drastic change are shown in Fig. 3.17. On further heating, the rod-like grains started melting as shown in Fig. 3.16(c). At 151°C the melting process almost came to the end as shown in Fig. 3.16(d).

The cooling process was started at this temperature right before the film would thoroughly melt in order to image the recrystallization process of the same region based on the landmark grain. As the temperature was decreased, similar structures to the ones observed before the melt reappeared as shown in Fig. 3.16(e). The fine structures gradually reappeared in the rod-like grains from 85°C to 70°C as shown in Fig. 3.16(f).

The disappearance and the appearance of the fine structures in the rod-like grains occurred at almost the same temperatures as T_C of the bulk copolymer, which strongly suggested these structural changes are related to the ferroelectric phase transitions. Thus the observed structural change should be caused by the crystal form transition between the ferroelectric phase and the rotator phase (Fig. 3.4).

Since the specific volume of the rotator phase is larger than that of the ferroelectric phase,[127] the copolymer is subject to about 20% contraction at the para-to-ferroelectric phase transition in the cooling process. When the rod-like grain is initially formed at an elevated temperature, the copolymer is in the rotator phase (Fig. 3.18(a)). As the grain is cooled below T_C, the grain will be separated into the fine granular structures because of the contraction (Fig. 3.18(b)). As a result,

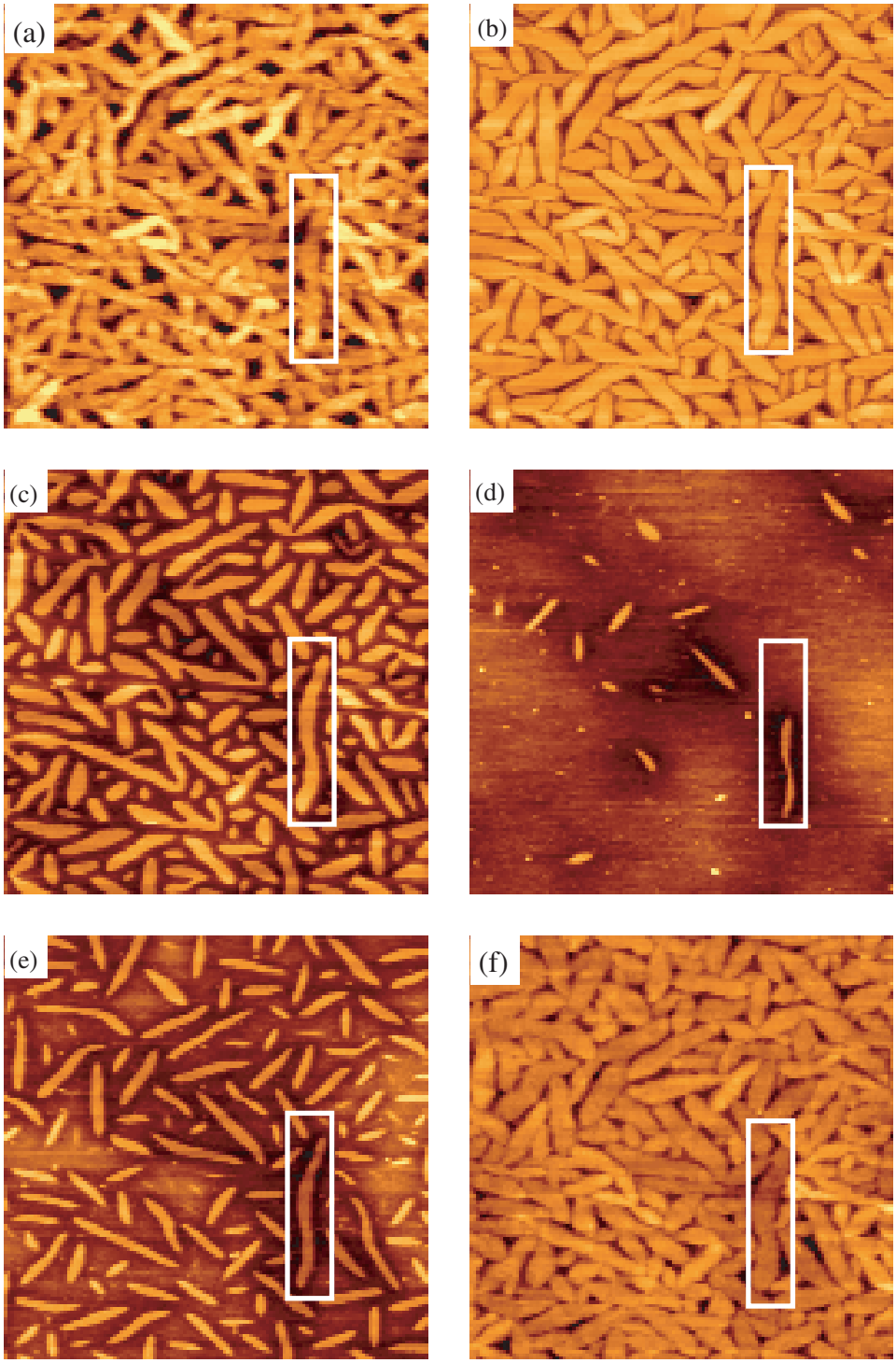

Figure 3.16: A series of AM-DFM images of the P(VDF/TrFE) film (2 μm $\times$ 2 μm) obtained at (a) 43°C, (b) 124°C, (c) 146°C and (d) 151°C in the heating process, and obtained at (e) 147°C and (f) 26°C in the cooling process.

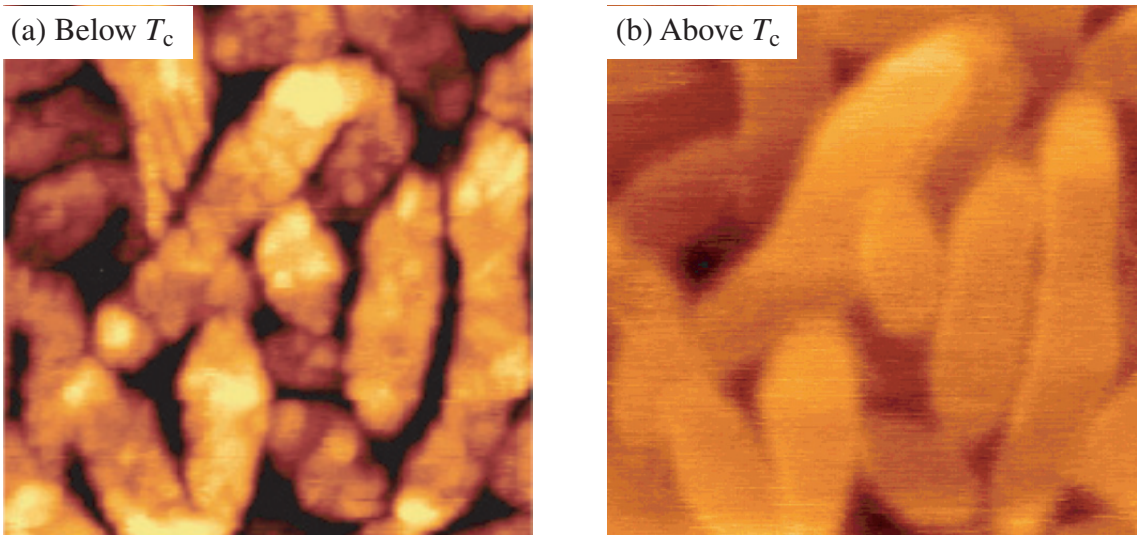

Figure 3.17: AM-DFM images of the P(VDF/TrFE) film (400 nm × 400 nm) obtained (a) below (25°C) and (b) above (123°C) T_C in the heating process.

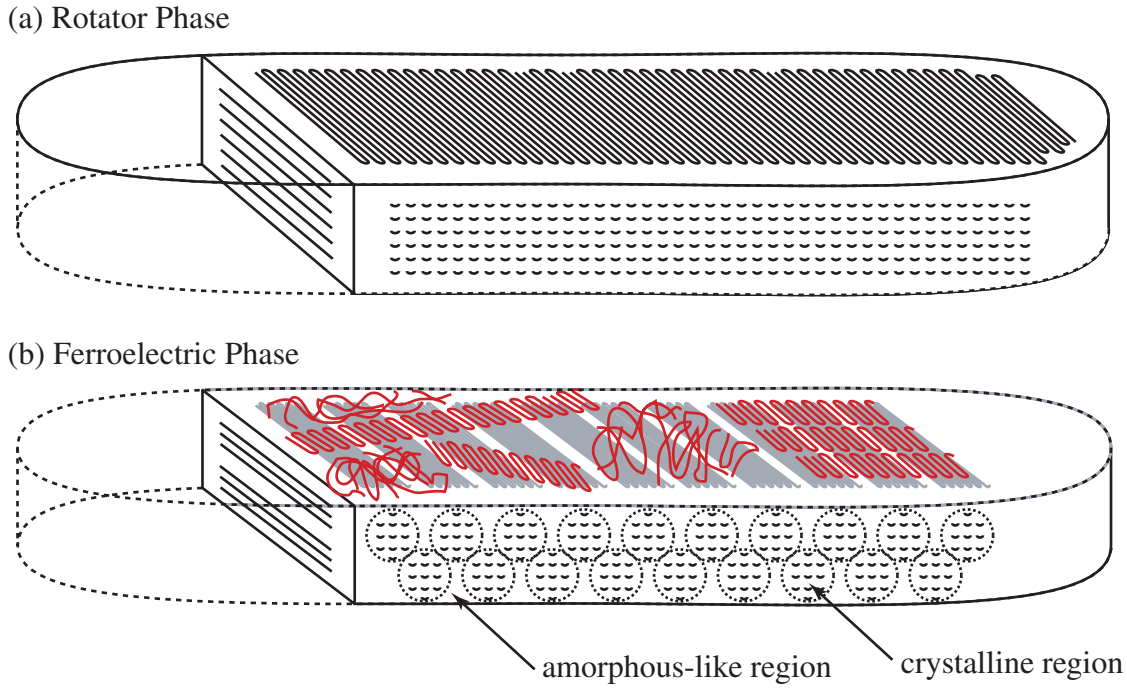

Figure 3.18: A schematic model of the rod-like grain in (a) rotator phase and (b) ferroelectric phase.

there exist both densely packed crystalline regions and loosely packed amorphous-like regions within the rod-like grain. In this process, the quenching effect at the film/substrate interface may play an important role. This is because if the grain is totally free from external binding forces, the overall grain structure would suffer from the contraction (or the expansion) at the ferroelectric phase transition but the grain should not be divided into fine structures.

On the other hand, another structural change is expected at the ferroelectric phase transition. In the rotator phase, molecular chains are relatively extended due to the sliding diffusion. In general, such an extended chain structure is relatively unstable if the molecule independently exist. However, if the molecule is embedded in the closely-packed polymer crystal, the molecule is stabilized due to the van der Waals interaction with the adjacent molecular chains. Therefore, the extended folding within the rod-like grain is maintained even after the transition from the rotator phase to ferroelectric phase. On the other hand, if the molecule is at the topmost surface of the grain, the van der Waals interaction should be much smaller than that for the one embedded in the grain. Therefore the extended molecular chain at the grain surface cannot be maintained at the para-to-ferroelectric phase transition. Instead, it will suffer from the transition into a lamella structure with a shorter folding period (Fig. 3.18(b)). Otherwise, they will be quenched before completing the transition, making up some small amorphous grains on the surface (Fig. 3.18(b)). Such small lamella crystallites and amorphous grains are probably ascribed to the observed fine structures on the rod-like grains.

3.5.2 AM-KFM Measurements

In order to measure the potential difference between the copolymer thin film and the HOPG substrate by AM-KFM, the scanning area was selected such that both regions should be simultaneously imaged. Figures 3.19(a) and (b) show examples of a topographic image and a surface potential image of such an area, respectively. These images were simultaneously obtained at 105°C in the heating process. The film thickness and the film/substrate potential difference were estimated from the cross-sectional plots of these images as shown in Fig. 3.19(c) and (d), respectively.

Figures 3.20(a) and (b) show the temperature dependence of the surface potential difference and the thickness of the film, respectively, in the heating process. The dotted line in each figure indicates the temperature of the disappearance of the fine granular structures, namely, T_C. Both of the potential difference and the thickness also drastically changed around this temperature. The surface potential of the film still increased gradually as the sample was heated above this temperature.

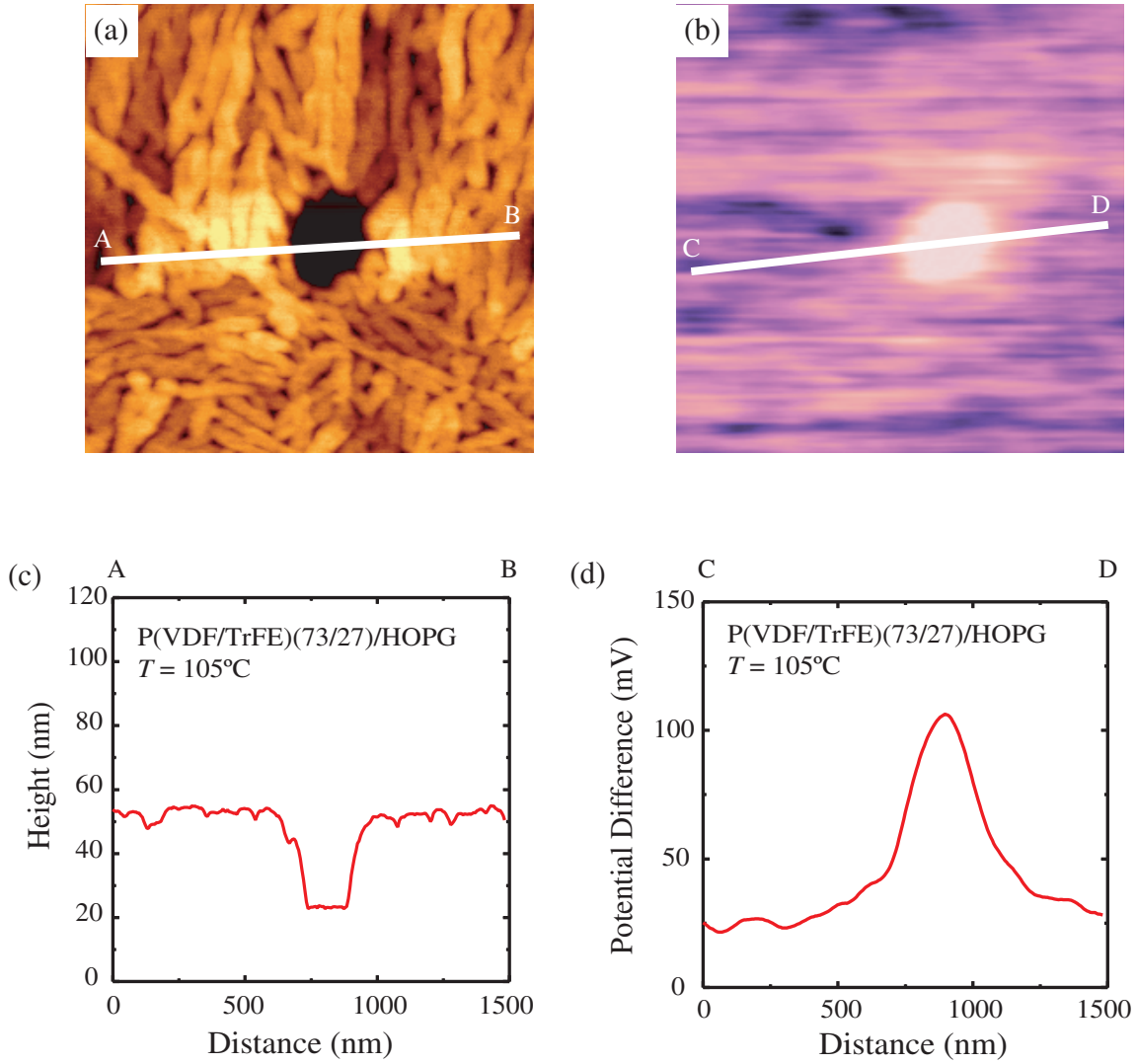

Figure 3.19: Examples of (a) a topographic image and (b) a surface potential image of the P(VDF/TrFE) film, which were simultaneously obtained by AM-KFM at 105°C (1.5 μm × 1.5 μm). Cross-sectional plots measured along the white lines (c) A – B and (d) C – D.

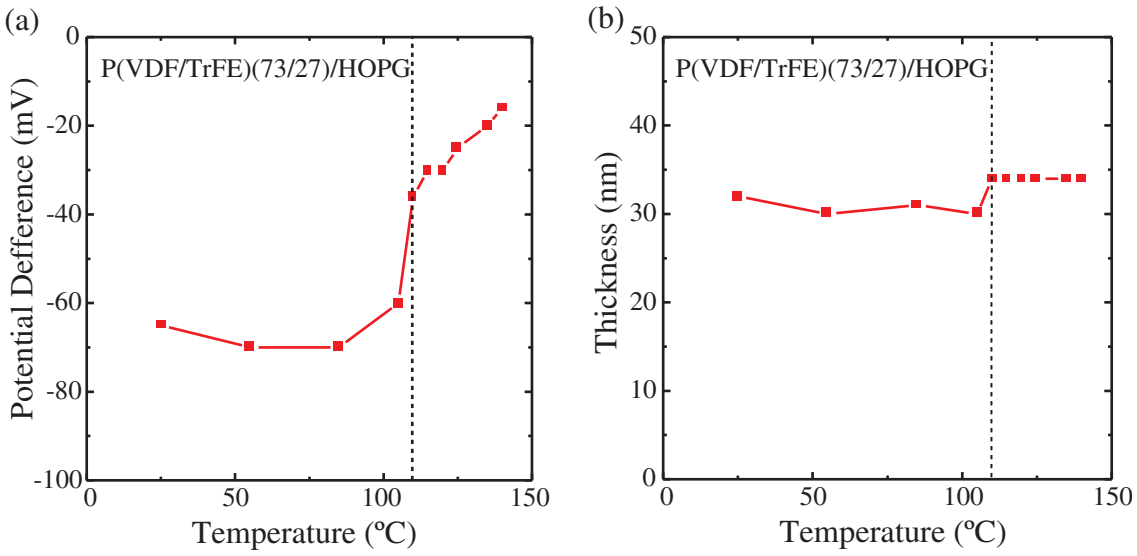

Figure 3.20: The temperature dependence of (a) the potential difference between the film and the substrate and (b) the thickness of the film. These profiles were obtained from the cross-sectional plots of the several AM-KFM images taken in the heating process.

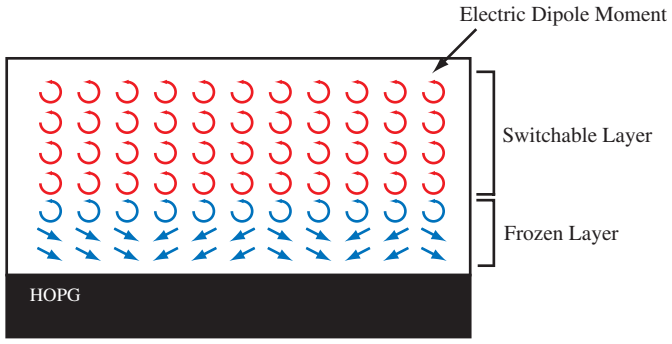

Figure 3.21: A schematic model showing the alignment of the electric dipole moments within the P(VDF/TrFE) thin film in rotator phase.

Chen *et al.* suggested that the negative surface potential of the copolymer films with respect to the HOPG substrate is attributed to the dipoles which were aligned by some interaction with the substrate surface (Fig. 3.6). The result obtained in this experiment is consistent with the explanation that most of the aligned dipoles were disordered around T_C because of the ferro-to-paraelectric phase transition (Fig. 3.21). Furthermore, the gradual increase of the potential observed above T_C could be explained by the persistent dipoles located near the substrate surface. These dipoles might have still remained aligned due to the stronger interaction.

The measured thickness of the film was also changed by 13% from about 30 nm to 34 nm at T_C as shown in Fig. 3.20(b). This result can be also explained by the crystal form transition from ferroelectric phase to rotator-phase. So far, an X-ray diffraction study showed that the copolymer expands by 12% in the direction perpendicular to the molecular axis at T_C in the heating process,[127] which corresponds well to the observed result in our experiments.

3.6 Summary

In this chapter, the AM-DFM applications to the *in-situ* analyses of thermal phase transitions were experimentally demonstrated on ferroelectric polymer thin films.

Demonstration of *In-situ* Analyses of Thermal Phase Transitions

It was demonstrated that a variable-temperature AM-DFM is quite useful for the direct investigations on various thermal phase transitions of polymer thin films.

1. The AM-DFM images revealed the crystallization process of P(VDF/TrFE) thin films on a nanometer-scale. The result first demonstrated the *in-situ* AM-DFM imaging of crystallization process at an elevated temperature.

2. The AM-DFM images revealed the structural changes during the ferroelectric phase transition process of P(VDF/TrFE) thin films on a nanometer-scale. The result first demonstrated the *in-situ* AM-DFM imaging of ferroelectric phase transition process.

3. The AM-KFM images revealed the temperature dependence of the surface potential of P(VDF/TrFE) thin films during the ferroelectric phase transition process. The result first demonstrated the *in-situ* AM-KFM measurements during the thermal phase transition process.

Light-Force Imaging and Hard-Force Imaging

It was revealed that AM-DFM can provide different types of information on the sample using light-force imaging and hard-force imaging. In order to visualize thermal phase transition processes of polymers, it is essential to choose these two operation modes appropriately.

1. Using light-force imaging, the topmost surface morphology can be imaged even on an extremely soft surface. Thus the structural changes of amorphous polymer surfaces can be imaged.

2. Using hard-force imaging, surface stiffness variation can be mapped. In the crystallization process, the crystallites formed under an amorphous layer can be imaged. In the melting and recrystallization processes, the solid phase grains embedded in the liquid phase polymers can be imaged.

Chapter 4

Molecular-Scale Imaging of Insulating Organic Surfaces

4.1 Introduction

One of the most distinctive features of FM-DFM is capability of imaging insulating surfaces with true-atomic resolution.[24] Since most of the organic materials are insulating, FM-DFM applications to the organic systems are particularly important. In 1997, Fukui *et al.* presented molecular-scale images of formate ions adsorbed on TiO_2(110)-(1×1) surface,[53] which was the first demonstration of the true-molecular resolution imaging of FM-DFM. Since then, many molecular-resolution images were reported on the different organic systems.[53–60,96] However, most of these previous works were performed on the conductive organic surfaces whose structures and properties had already been characterized by STM. The only one exceptional result was presented by Kitamura *et al.* in 1998, where molecularly-resolved FM-DFM images were obtained on the bulky polypropylene films. Other than this result, there have been no reports on FM-DFM imaging of insulating organic surfaces. Namely, FM-DFM imaging of insulating organic thin films have never been performed so far. Therefore, it is still unclear what kinds of insulating organic thin films can be imaged by FM-DFM and whether there are any problems specific to such applications.

In this chapter, the possibilities and the problems of FM-DFM applications to the molecular-scale investigations on the insulating organic thin films were experimentally demonstrated. The most typical organic thin films which cannot be imaged by STM are those formed on the insulating substrates. In this experiment, the epitaxial growth process of the ferroelectric oligomer thin films deposited on alkali halides were investigated on a molecular-scale. On the other hand, even if the substrate is conductive, STM investigations on the relatively thick (typically > 2 nm) films are impossible. In this experiment, FM-DFM imaging was performed on the alkanethiol monolayers composed of the relatively longer-chain molecules.

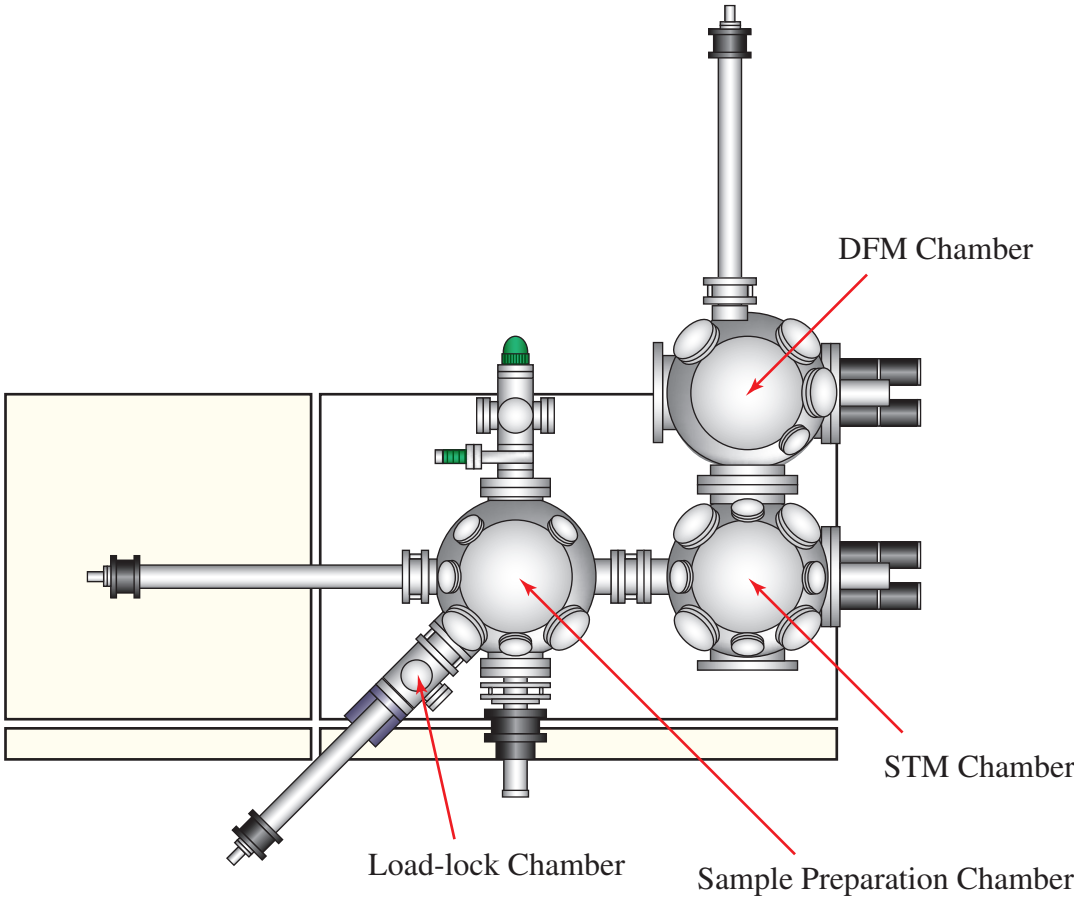

Figure 4.1: Schematic drawing of UHV-SPM system used in this experiment. The system is composed of four chambers; load-lock chamber, sample preparation chamber, STM chamber and DFM chamber.

4.2 Experimental

All the experiments described in this chapter were performed under UHV conditions with a commercially available UHV-SPM system (JEOL: JSTM/AFM-4500XT). Figure 4.1 shows a schematic drawing of the UHV-SPM system, which is composed of four chambers; a load-lock chamber, a sample preparation chamber, an STM chamber and a DFM chamber. The load-lock chamber is evacuated by a turbo molecular pump and a rotary pump. Each of the sample preparation chamber and the STM chamber is equipped with a sputtering ion pump and a titanium sublimation pump. The DFM chamber is directly connected to the STM chamber and has no pumping system. The base pressure in these chambers is usually maintained at a pressure of better than 5×10^{-7} Pa.

The highly-doped n-Si cantilever (Nanosensors: NCH) with a resonance frequency of about 300 kHz and with a nominal spring constant of 40 N/m was used

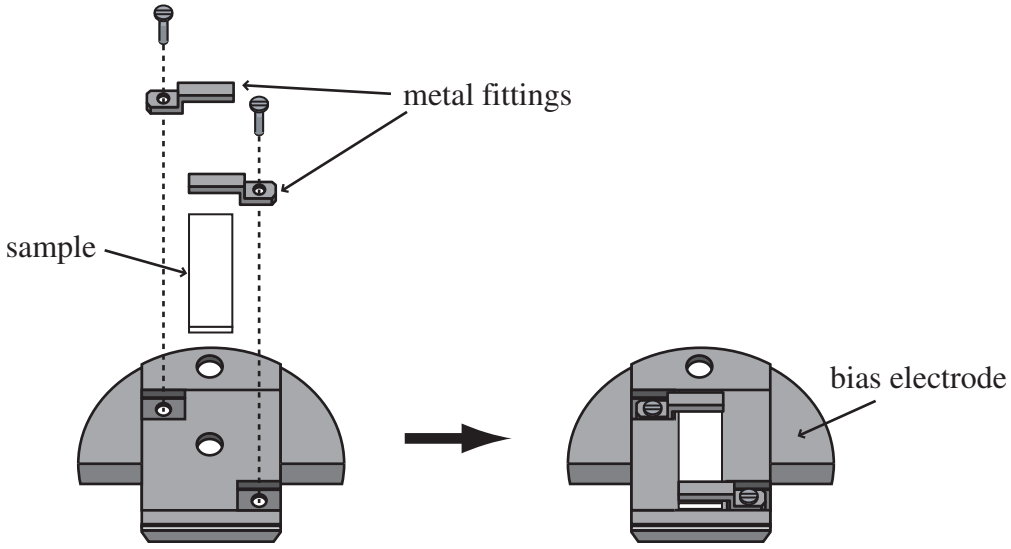

Figure 4.2: Schematic drawing of the sample holder for the UHV-SPM system.

for both FM-DFM and FM-KFM. The typical Q-factor measured under an UHV condition was 30,000. The resistivity of the cantilever was 0.01 – 0.025 Ωcm. In order to reduce the contamination on the tip apex, the cantilevers were annealed at 150°C for several hours in the sample preparation chamber before use. The cantilever was vibrated in constant excitation mode. The tip-sample distance regulation was made in constant frequency shift mode. As a frequency shift detector and an amplitude detector, a single-chip PLL circuit and a single-chip RMS-to-DC converter equipped with the JSTM/AFM-4500XT were used.

Figure 4.2 shows the schematic drawing of the sample holder used in this experiment. Since all the parts of this holder are made of metal, it has uniform electrical potential determined by the sample bias voltage. In this experiment, both the tip and the sample bias were continuously grounded during the FM-DFM imaging. As for the gold substrates, they are electrically connected to the sample bias electrode through the metal fittings. Thus the potential of the substrate can be controlled by changing the bias voltage. On the other hand, alkali halide substrates are purely insulating and hence their potential cannot be directly controlled. In this case, the sample holder itself will serve as an opposite electrode with respect to the tip.

During the FM-KFM imaging, the ac and dc bias voltages were applied between the tip and the bias electrode. The amplitude and the frequency of the ac bias modulation voltage were 7 $V_{p\text{-}p}$ and 2 kHz, respectively. Due to the bias modulation, the electrostatic force and the resultant frequency shift were modulated at the same frequency. Then the modulated frequency shift was detected using a lock-in amplifier (NF: 5610B). The KFM bias feedback regulation was made using a home-built

feedback electronics.

4.3 Vinylidene Fluoride Oligomer Thin Films on KCl(001) Surfaces

4.3.1 Vinylidene Fluoride Oligomer

PVDF and P(VDF/TrFE) have been used for the practical applications such as pyroelectric sensors and electromechanical tansducers. Nevertheless, there have been pointed out some problems for the future applications to the ultrathin film devices. For example, in general, polymer thin films are formed by relatively easy methods such as spin-coating and cast method. However, it is very difficult to precisely control the film thickness with these techniques. Although layer-by-layer growth of P(VDF/TrFE) thin films was recently demonstrated by Bune *et al.* using Langmuir-Blodgett technique,[142] those films obtained by such a wet process often contains many impurities and water molecules. The problem is that polymer thin films cannot be obtained by dry processes such as vacuum deposition and molecular beam epitaxy due to the thermal decomposition of the molecules.

The oligomer of VDF is one of the possible solutions for this problem. Since VDF oligomer thin films can be prepared by dry processes with a precise control of their thickness, some research groups have recently begun to study fundamental properties of this material.[143–146] For example, Yoshida *et al.* investigated thin films of $(CF_3)_2CF$-$(CH_2CF_2)_{10}$-I, which revealed the dependence of molecular orientations on substrate temperature during the vacuum deposition process.[143] Herman *et al.* prepared CCl_3-$(CH_2CF_3)_n$-Cl thin films and examined the effect of molecular length on their crystal structure.[144,145]

The VDF oligomer used in this study was CF_3-$(CH_2CF_2)_{17}$-I. Figure 4.3 shows molecular conformations and packing arrangements of the VDF oligomers in the form I and form II. Since the molecules have linear structure compared to other VDF oligomers synthesized so far, they are relatively easy to crystallize into the form I crystal with all-*trans* conformation. In fact, this molecule is the only VDF oligomer whose ferroelectricity have been experimentally demonstrated.[147]

So far, Noda *et al.* performed detailed X-ray diffraction studies on the crystal structures and molecular orientations of VDF oligomer thin films deposited on alkali halides.[146] In particular, they reported that VDF oligomer thin films deposited on KCl(001) surfaces show clear epitaxial growth with their molecular axes oriented in the KCl$\langle 110 \rangle$ directions. The film is composed of characteristic superlattice structures as shown in Fig. 4.4, reflecting the four-fold symmetry of the KCl(001) surface.

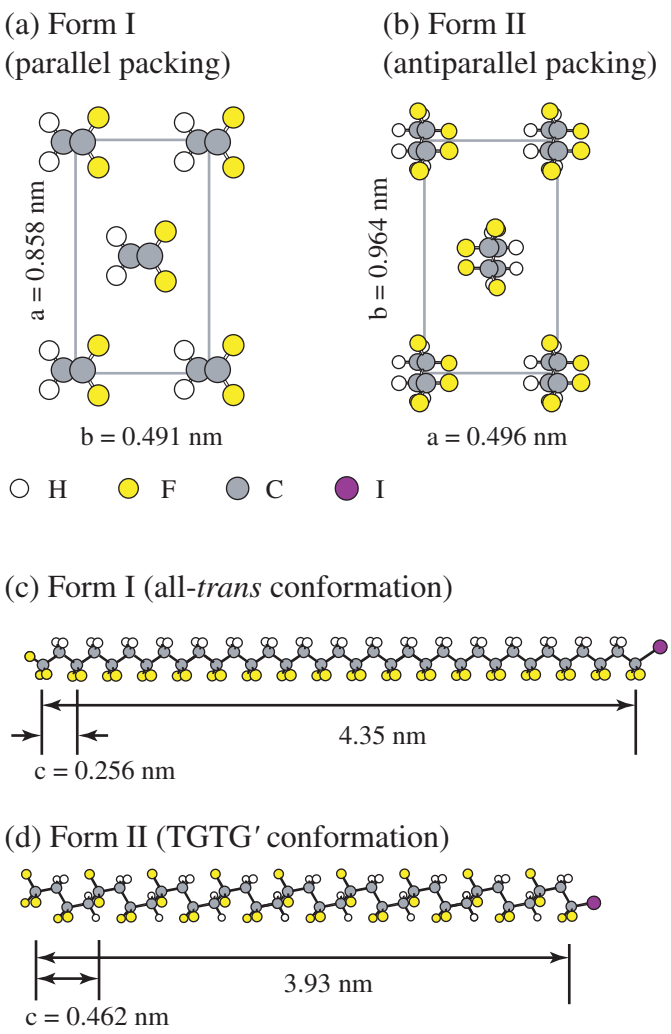

Figure 4.3: Schematic models of VDF oligomer crystals in the form I (a, c) and in the form II (b, d).

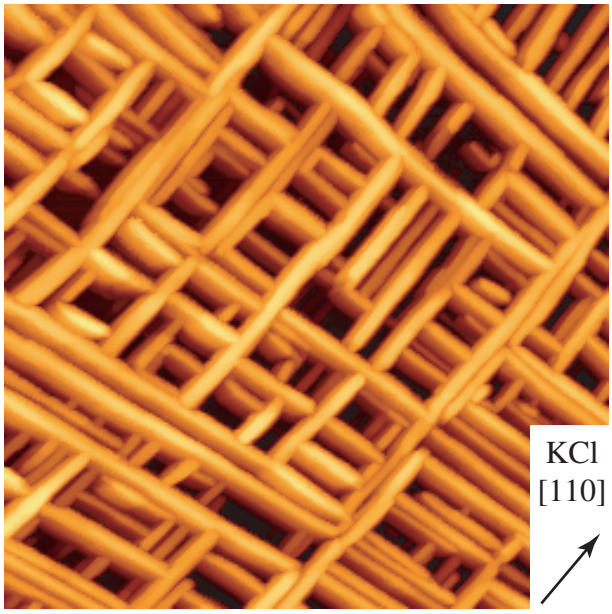

Figure 4.4: AM-DFM image of VDF oligomer thin film deposited on KCl(001) surface (8 μm $\times$ 8 μm). The film thickness was about 40 nm.

Hereafter this superlattice structure is referred to as a "rod-like structure".

Epitaxial growth process of such molecular superstructures are of great importance in view of its applications to the molecular orientation control. In particular, alkali halide substrates have been often used for making molecular thin films with high crystallinity and well-controlled molecular orientations.[148–152] For example, Shimada *et al.* demonstrated fabrication of the molecular nano-structures by taking advantage of molecular epixtaxy on alkali halides.[153] Although these epitaxial growth processes have been explained by electrostatic and van der Waals interactions between the films and the substrates, the molecular-scale description of the growth mechanisms have not been obtained yet.

The VDF oligomer has many excellent features for the applications to organic thin film devices. In order to realize such applications, it is essential to elucidate their fundamental properties in a thin film state. In this study, in order to reveal the epitaxial growth process of the VDF oligomers on KCl(001) surfaces, the initial stage of the film growth process was investigated by FM-DFM on a molecular-scale.

4.3.2 Sample Preparation

The VDF oligomer thin films were epitaxially grown on a freshly cleaved KCl(001) surfaces by vacuum deposition at a substrate temperature of 60°C. The deposition rate was about 0.1 nm/min, which was monitored using a quartz oscillator. The estimated thickness of the films were less than a few molecular layers. Immediately

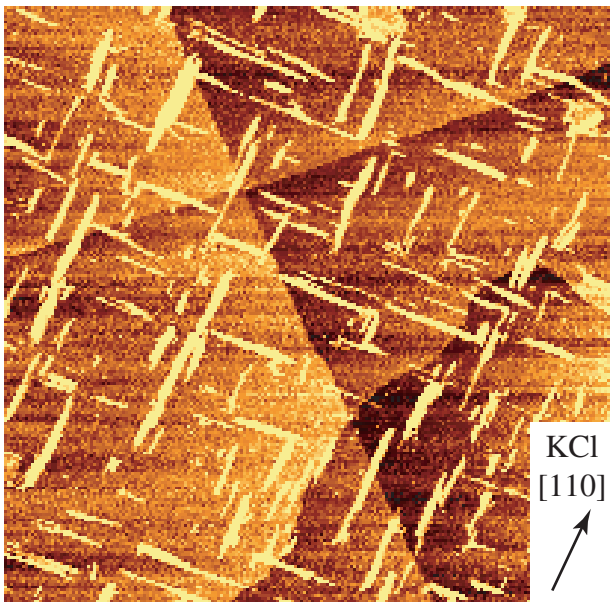

Figure 4.5: FM-DFM image of VDF oligomer thin film deposited on KCl(001) surface (2 μm $\times$ 2 μm, $\Delta f = -5$ Hz, $A_{\text{p-p}} = 15$ nm). The film thickness was a few monolayers.

after the deposition, the sample was transferred from the deposition chamber to the UHV-FM-DFM chamber through the air.

4.3.3 Results and Discussion

Rod-like Grains

In order to investigate the initial stage of the epitaxial growth process, VDF oligomer thin films with a thickness of less than a few monolayers were prepared. Figure 4.5 is a typical FM-DFM image of the sample, showing some nuclei of the rod-like structures seen in Fig. 4.4. Hereafter these nuclei are referred to as "rod-like grains". Since the two atomic steps found in this image are nearly perpendicular to each other, they should be oriented in the KCl$\langle 100 \rangle$ directions. Therefore, the image revealed that the rod-like grains grow in the KCl$\langle 110 \rangle$ directions, which well confirmed the result reported by Noda *et al.*[146]

Stripe Structures

Figure 4.6(a) is an FM-DFM image of some of the rod-like grains seen in Fig. 4.5. This figure shows that each rod-like grain consists of some stripes oriented in the KCl$\langle 110 \rangle$ directions. Figures 4.6(b) and (c) are cross-sectional plots of the bright lines A – B and C – D indicated in Fig. 4.6(a), respectively. The plot A – B shows that the distance between two neighboring molecular layers is about 0.43 nm,

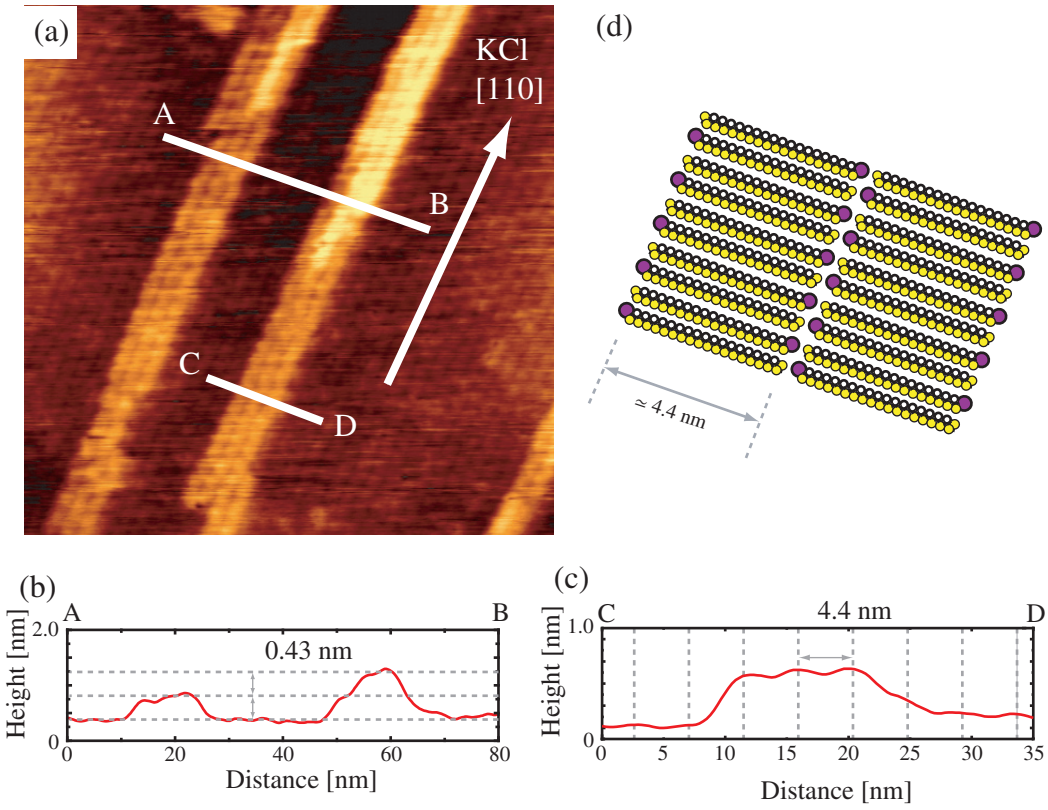

Figure 4.6: (a) FM-DFM image of a VDF oligomer thin film with a thickness of a few monolayers on a KCl(001) surface (150 nm × 150 nm, $\Delta f = -20$ Hz, $A_{\text{p-p}} =$ 15 nm). (b, c) Cross-sectional plots measured along the bright lines A – B and C – D. (d) A schematic model of the observed stripe structures.

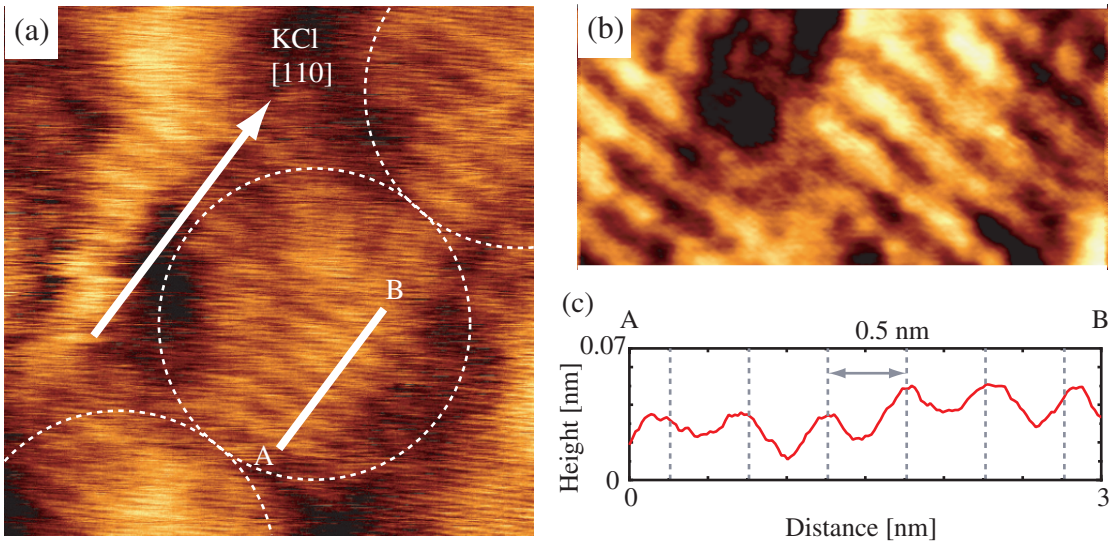

Figure 4.7: (a) FM-DFM image of one of the rod-like grains seen in Fig. 4.5(b) (10 nm × 10 nm, $\Delta f = -60$ Hz, $A_{\text{p-p}} = 15$ nm). (c) A more magnified FM-DFM image taken on a rod-like grain (4 nm × 2 nm, $\Delta f = -60$ Hz, $A_{\text{p-p}} = 15$ nm). (b) A cross-sectional plot measured along the bright line A – B indicated in (a).

which is close to the half unit cell length of the crystal form I in the a-axis direction ($a/2 = 0.429$ nm, see Fig. 4.3(a)). In addition, the plot C – D shows that the distance between two adjacent stripes is about 4.4 nm, which corresponds well to the molecular length of VDF oligomer in all-*trans* conformation (4.35 nm, see Fig. 4.3(c)). From these results, the molecular arrangements within the rod-like grains can be described as shown in Fig. 4.6(d). Namely, the film consists of the form I crystal with the a-axis perpendicular to the surface while the b-axis (polar axis) is oriented in the KCl⟨110⟩ directions.

Figure 4.7(a) is a molecularly-resolved FM-DFM image taken on one of the rod-like grains. Figure 4.7(b) is a more magnified image of the rod-like grain, which clearly shows individual molecular chains. Figure 4.7(c) is a cross-sectional plot measured along the bright line A – B indicated in Fig. 4.7(a). This plot shows that the distance between two neighboring molecules is about 0.5 nm, which roughly equals to the unit cell length of the crystal form I in the b-axis direction ($b = 0.491$ nm, see Fig. 4.3(a)). This result also confirms the above-mentioned structural model of the rod-like grains (Fig. 4.6(d)). Besides the molecular features, some height corrugation was found in this image as indicated by the white circles. The origin of this corrugation will be discussed later.

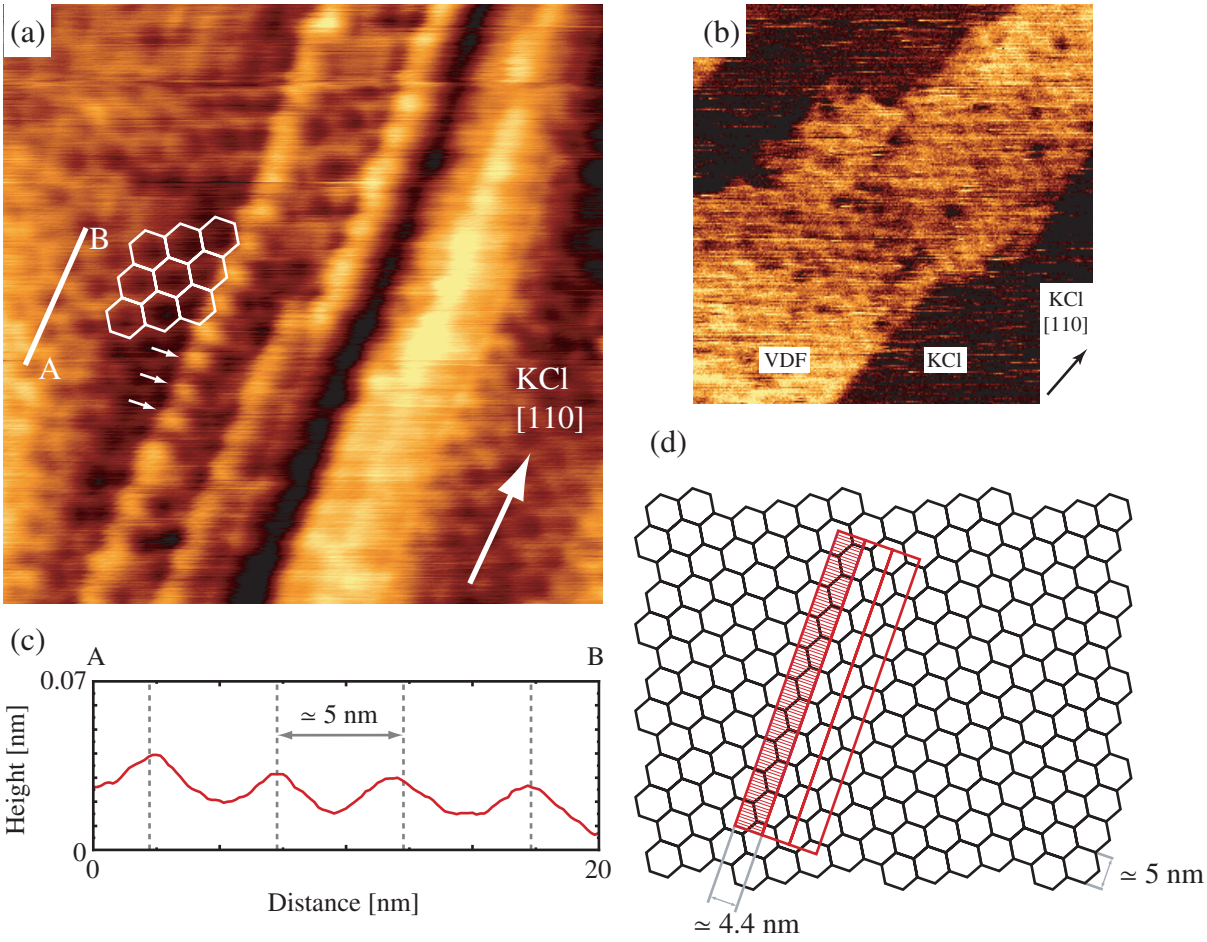

Figure 4.8: (a) FM-DFM image of the stripe structures and the underlying honeycomb-like structures (80 nm × 80 nm, $\Delta f = -20$ Hz, $A_{\text{p-p}} = 15$ nm). (b) FM-DFM image of a sub-monolayer film (100 nm × 100 nm, $\Delta f = -15$ Hz, $A_{\text{p-p}} = 15$ nm). (c) The cross-sectional plot measured along the bright line A–B indicated in (a). (d) A schematic model showing the relative position of the stripe structures with respect to the underlying honeycomb-like structures.

Honeycomb-like Structures

Figure 4.8(a) is an FM-DFM image of a VDF oligomer thin film in the more initial stage of the epitaxial growth, showing a few stripe structures and an underlying molecular layer composed of "honeycomb-like" structures as indicated by white hexagonals. The FM-DFM image of a sub-monolayer (Fig. 4.8(b)) revealed that the underlying molecular layer corresponds to the first monolayer at the film-substrate interface. These results suggest that the KCl(001) surface is totally covered with the honeycomb-like structures at the beginning of the epitaxial growth, and then the stripe structures are formed on top of the first layer. Since the honeycomb-like structure was found only in the first layer, it was likely to be caused by some interactions between the molecules and the substrate. Figure 4.8(c) is a cross-sectional plot measured along the bright line A–B indicated in Fig. 4.8(a). The plot showed that the period of the honeycomb-like structure in KCl[110] direction is about 5 nm.

It was found that the stripe structure consisted of a series of bright spots as shown by some white arrows indicated in Fig. 4.8(a). This result suggested that the molecules tend to adsorb on the preferred sites in the honeycomb-like structure. In fact, similar height variation was found even in the more tightly packed stripe structure as shown in Fig. 4.7(a) indicated by white circles. From Fig. 4.8(a), the relative position of the stripe structure with respect to the underlying honeycomb-like structure was depicted in Fig. 4.8(d). As shown in this structural model, it was revealed that the stripe structure grows along the zigzag line of the honeycomb-like structure oriented in KCl[110] direction.

Imaging Mechanism of Honeycomb-like Structure

Figure 4.9 is the FM-DFM image of the honeycomb-like structure taken on a smaller scale. The image clearly showed three different contrasts within the hexagonal unit of the honeycomb-like structure as indicated by the bright arrows (i)−(iii). However, the molecular arrangements within the honeycomb-like structures could not be imaged in this experiment. Since a lateral resolution of 1 nm can be mostly achieved by FM-DFM, the resolution for the image seems to be much lower than expected.

This low spatial resolution seems to be strongly related to the variations in the electrostatic tip-sample interactions. The tip-sample interaction force mainly consists of three components such as van der Waals force (F_{vdW}), chemical interaction force (F_{chem}) and electrostatic force (F_{es}). Since F_{vdW} is dependent only on the tip-sample distance, this force component does not prevent the high-resolution imaging if the surface is sufficiently flat. Although F_{chem} on the iodine atom located at the

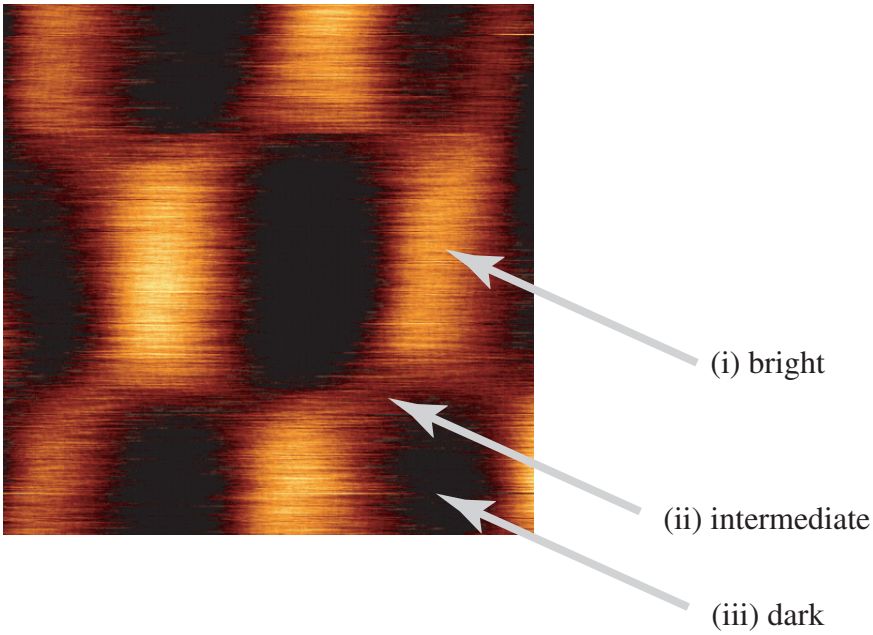

Figure 4.9: FM-DFM image of the honeycomb-like structure (10 nm × 10 nm, $\Delta f = -20$ Hz, $A_{\text{p-p}} = 15$ nm).

end of the molecule may be different from that on the main molecular chain, the variation is not likely to prevent the high-resolution imaging. This is because true-molecular resolution was successfully obtained on the higher molecular layers as shown in Fig. 4.7. On the other hand, if there is large surface potential variation on the surface, F_{es} would significantly affect the image resolution due to its relatively long interaction range.

Since the low resolution was found only at the very interface between the film and the substrate, the charge transfer at the interface should be ascribed to the surface potential distribution. In particular, the chemically reactive iodine site may have a different electrostatic potential from that of the main molecular chain. Therefore, the result suggested that the bright spots indicated by the arrow (i) in Fig. 4.9 corresponds to the sites of the iodine atoms while the dark spots indicated by the arrow (iii) represents the main molecular chain. The intermediate contrast indicated by the arrow (ii) reflects the electrostatic interaction from the adjacent two iodine sites.

Amplitude Variations

Figure 4.10(a) is the FM-DFM image taken on the sub-monolayer of VDF oligomers, showing the KCl(001) surface and the first and the second molecular layers (MLs). The amplitude variation of the cantilever vibration during the FM-DFM imaging

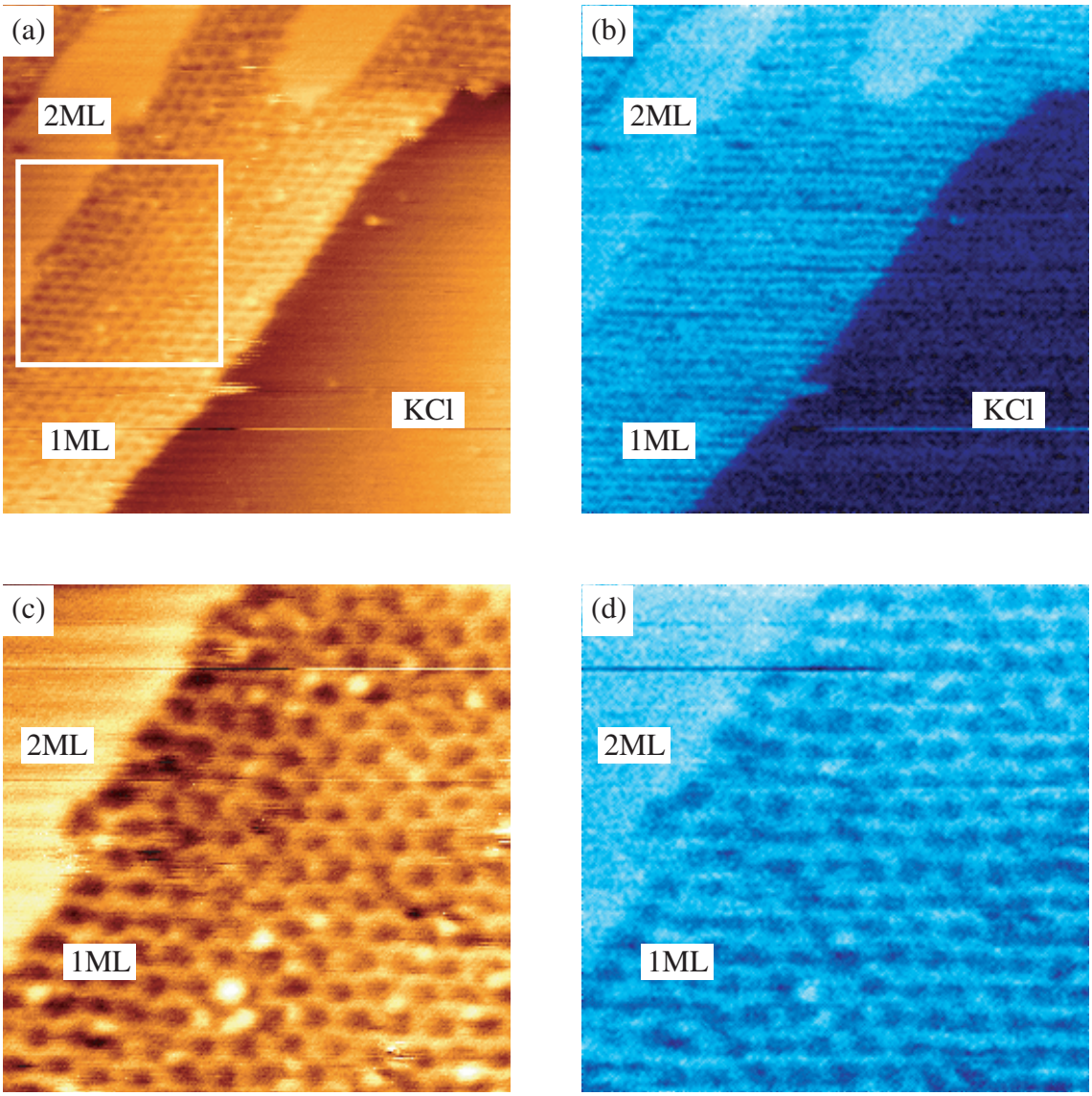

Figure 4.10: (a) Topographic and (b) amplitude images of VDF oligomer thin films on KCl(001) surface (150 nm × 150 nm, $\Delta f = -15$ Hz, $A_{\text{p-p}} = 15$ nm). (c) Topographic and (d) amplitude images of the area indicated by a white square in (a) (60 nm × 60 nm, $\Delta f = -15$ Hz, $A_{\text{p-p}} = 15$ nm).

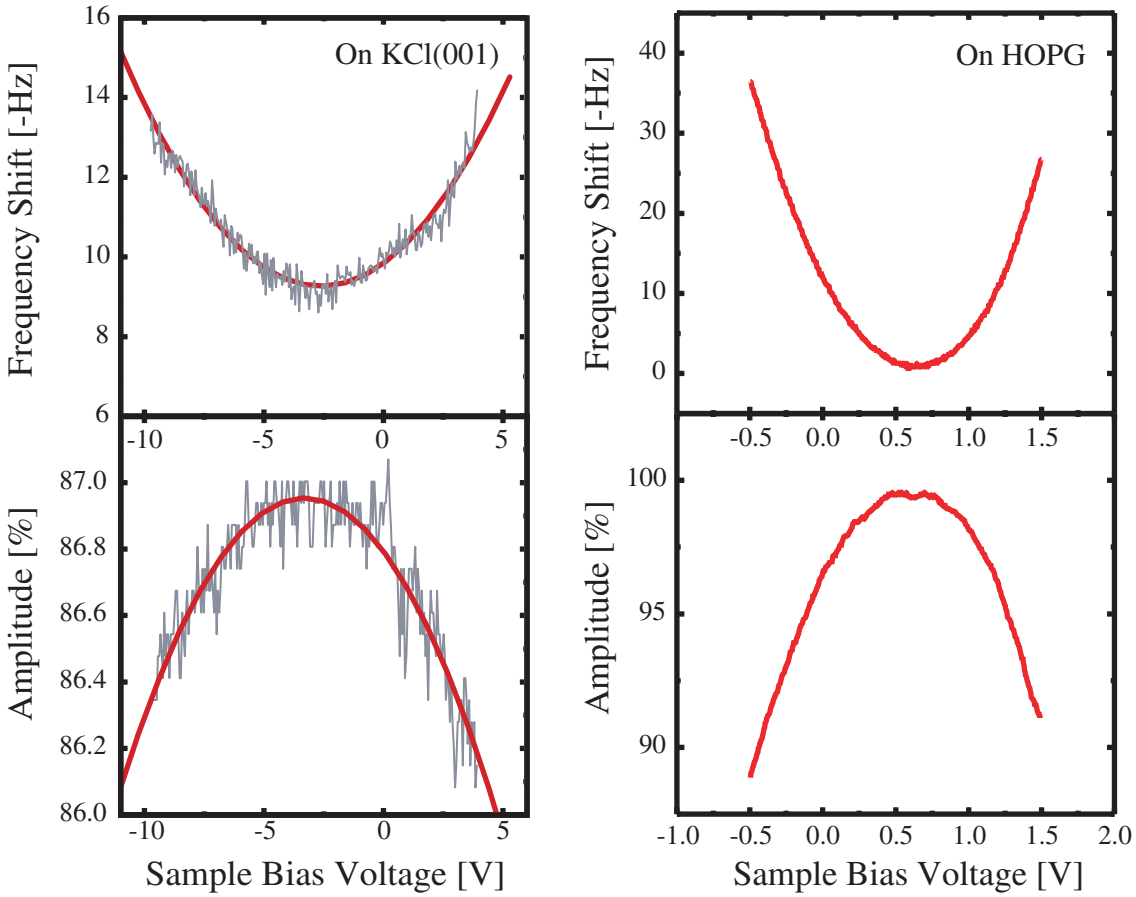

Figure 4.11: Bias dependence of the frequency shift and the vibration amplitude measured on (a) KCl(001) surface and (b) HOPG surface. (a) the gray line is the plot of the raw data and the red line represents the fitted profile as a quadratic curve. (b) the red line is the plot of the raw data.

was simultaneously recorded as shown in Fig. 4.10(b). Note that the brighter contrast corresponds to the larger amplitude. The amplitude image revealed that the amplitude damping on the KCl(001) surface is larger than that on the VDF oligomers while the damping on the first ML is larger than that on the second ML. Figure 4.10(c) and (d) shows the topographic and amplitude images taken on the area indicated by a white square in Fig. 4.10(a). From the amplitude image, it was found that the amplitude varies depending on the relative tip position with respect to the honeycomb-like structure.

Such an amplitude damping takes place if there is any tip-sample potential difference (V_{ts}). Figure 4.11(a) and (b) are the bias dependence of the frequency shift and the amplitude measured on KCl(001) and HOPG surfaces, respectively. The frequency shift showed quadratic dependence on V_{ts}, reflecting the quadratic bias dependence of electrostatic force (F_{es}). It was found that the amplitude is damped

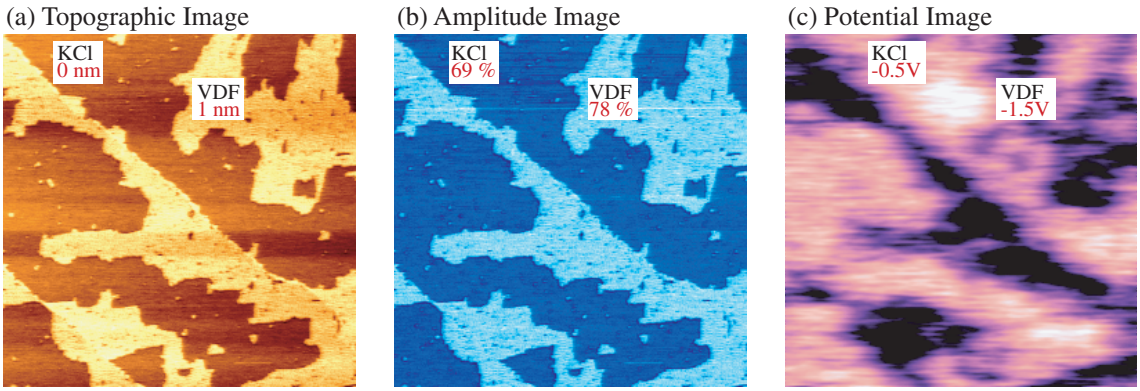

Figure 4.12: FM-KFM images of the sub-monolayer of VDF oligomers on KCl(001) surface. (a) Topographic image. The height of the KCl(001) surface was assumed to be 0 nm. (b) Amplitude image. The amplitude of the freely oscillating cantilever was assumed to be 100%. (c) Surface potential image. The tip potential was assumed to be 0 V. (500 nm $\times$ 500 nm, $\Delta f = -10$ Hz, $A_{\text{p-p}} = 15$ nm)

with increasing V_{ts} and the dependence is well fitted as a quadratic curve. In the case of KCl(001) surface, since the thickness of the sample was about 0.5 mm, the bottom electrode was located far below the tip position. Thus the observed bias dependence was relatively weak. However, when the bias curve was measured on a conductive surface such as HOPG, the bias dependence was much stronger as shown in 4.11(b). These bias curves revealed that the amplitude variation can be induced by the surface potential variation.

In FM-DFM operated in constant excitation mode, the magnitude of the amplitude damping signifies the dissipation of the cantilever vibration energy. The detailed discussions on the energy dissipation induced by the electrical interaction will be presented in the chapter 5.

Surface Potential Measurement

Using FM-KFM, it is possible to obtain topographic and surface potential images at the same time. In addition to these two images, the amplitude variation was also recorded during the FM-KFM imaging of the sub-monolayer of VDF oligomers as shown in Fig. 4.12. The surface potential image (Fig. 4.12(c)) revealed that the KCl(001) surface has about 1 V higher potential than that of the monolayer. However, the image contrast was not so clear compared to those of topographic and amplitude images. In this experiment, the bottom electrode was separated from the tip by the insulating KCl substrate with a thickness of about 0.5 mm. Thus the electric field was not well concentrated at the vicinity of the tip apex, which lead to such a low spatial resolution of the surface potential image. In that sense,

the electrostatic force detected by the cantilever was not localized but was averaged over some area of the sample surface. Although the qualitative potential relationship between the film and the substrate in the observed potential image should be correct, the quantitative analyses would be impossible in such a situation.

The amplitude image (Fig. 4.12(b)) showed that the amplitude on the film was larger than that on KCl(001) surface. Since the bias feedback regulation minimizes the electrostatic tip-sample interaction force, the amplitude variation was expected to be suppressed during the KFM imaging. However, the result revealed that such a bias compensation does not work well in the case of insulating surface. In order to cancel out the electrostatic interaction, the surface potential variation within the lateral extent of electric field between the tip and the surface should be negligible and the vertical extent of the potential variation should be much smaller than the tip-sample separation. In this experiment, it was impossible to meet these conditions due to the following reasons. First, there was large electric dipole moment within each molecule comprising the monolayer. Secondly, the ionic KCl(001) surface has periodic potential variation on a atomic-scale. Thirdly, the sample was purely insulating so that some stray charges might be trapped on the surface. Fourthly, the electric field was not well localized at the tip apex because of the large separation between the tip and the bottom electrode. And finally, even if the dc term of the electrostatic force could be canceled out, the remaining ac term of the bias modulation voltage would induce some electrostatic interaction.

From the topographic image (Fig. 4.12(a)), it was found that the VDF oligomer was imaged as 1 nm higher than the KCl(001) surface, which was about twice as large as the value expected from the crystal structure. The electrostatic interaction induces both negative frequency shift and amplitude damping as shown in Fig. 4.11. The topographic artifacts in FM-DFM images can be induced not only by the additional frequency shift due to the electrostatic interaction but also by the amplitude variations because the frequency shift is strongly dependent on the vibration amplitude. Therefore, the observed topographic artifact should be caused by the remaining variations in the electrostatic interaction force which could not be compensated by KFM bias feedback regulation.

Structural Model of Honeycomb-like Structure

Figure 4.13(a) shows a possible schematic model showing the inner structure of the honeycomb-like structure. Hereafter, the reasons which supports this structural model are described. Note that the KCl[110] and KCl[$1\bar{1}0$] directions are assumed as shown in Fig. 4.13(a).

The two opposite sides of the hexagonal unit of the honeycomb-like structure

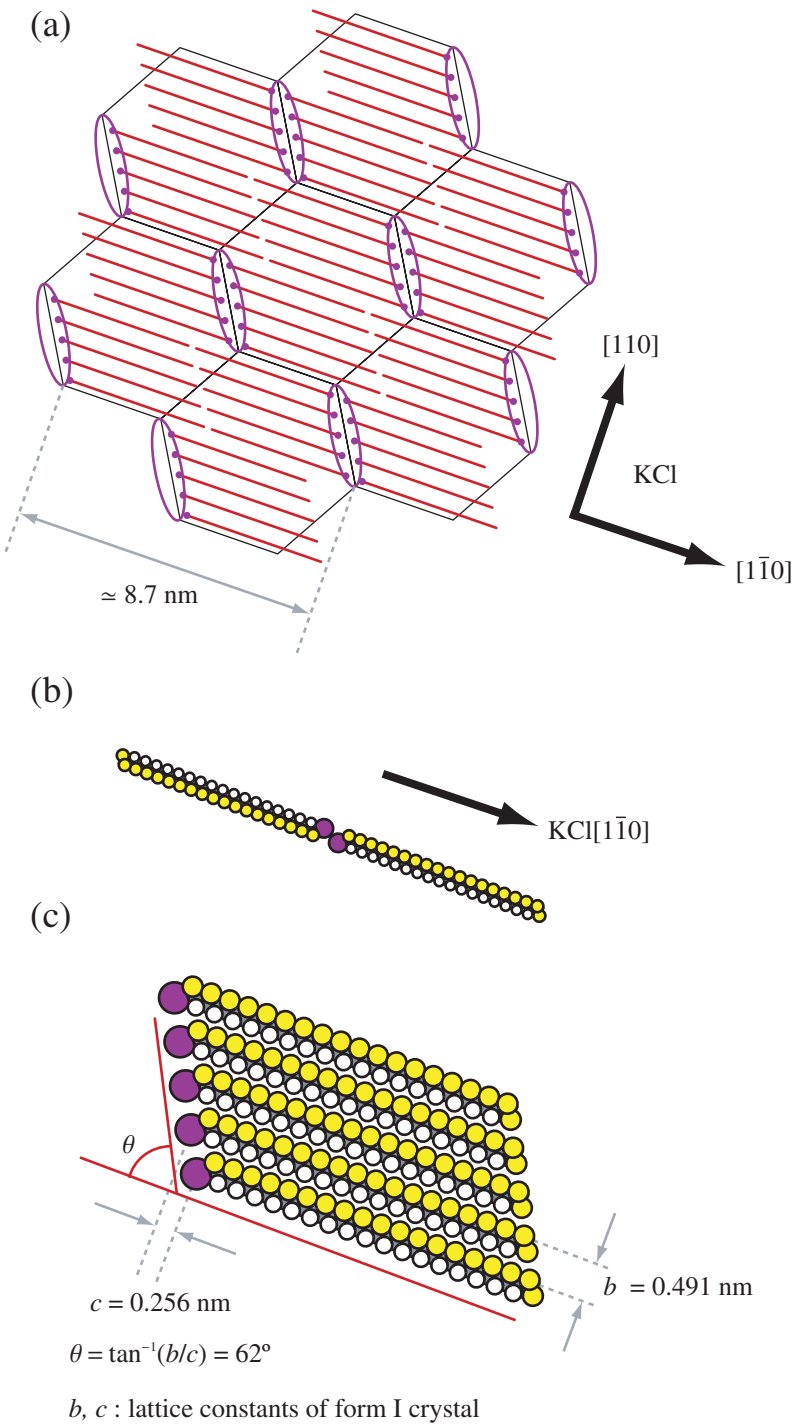

Figure 4.13: (a) A schematic model showing the inner structure of the honeycomb-like structure. (b) Basic unit of the honeycomb-like structure. (c) Packing arrangements within the honeycomb-like structure.

is separated by about 5 nm. Thus the repeating period in the KCl[$1\bar{1}0$] direction is about 8.7 nm (Fig. 4.13(a)). Since the length is twice as large as the molecular length in the all-*trans* conformation, the basic unit of the honeycomb-like structure should be composed of the two molecules with antiparallel orientations as shown in Fig. 4.13(b).

Since the rod-like grain shows clear epitaxial growth on the KCl(001) surface, the molecules in the honeycomb-like structure should have the same crystallographic structure and orientation as those in the rod-like grains. Namely, b-axis (polar axis) of the molecule should be oriented in the KCl[110] direction.

The lattice constant of the form I crystal in the b-axis direction is 0.491 nm while the repeating period of KCl(001) surface in the KCl[110] direction is 0.445 nm. Assuming that the $0.445n = 0.491(n-1)$, n becomes 10.67. Thus the first layer formed on the KCl(001) surface should have a repeating period of $0.445 \times 11 = 4.90$ nm in the [110] direction, which well agrees to the period of the honeycomb-like structure in KCl[110] direction (about 5 nm, see Fig. 4.8). Therefore, there should be 10 molecules within one repeating unit of the honeycomb-like structure in KCl[110] direction.

As discussed before, the bright spots seen in the honeycomb-like structure should correspond to the adsorption sites of the iodine atoms. In Fig. 4.13(a) the iodine atoms are indicated by some oval-shaped lines. In this model, the angle between the row of iodine atoms and the molecular chain (θ) becomes about 60°. In order to avoid the steric hindrance between the iodine atoms, two adjacent molecules will be packed with their molecular position in c-axis (main chain) direction shifted by a lattice constant ($c = 0.256$ nm) with each other (Fig. 4.13(c)). Thus the angle θ is given by $\theta = \tan^{-1}(0.491/0.256) \simeq 62°$, which is close to the above mentioned angle of 60°.

In the packing arrangement shown in Fig. 4.13(c), the molecules are stabilized by the inter-molecular van der Waals interaction. However, since the iodine adsorption sites are expected to have different potential from that of the main molecular chain, the electrostatic repulsion will increase the total energy of the system. Thus when the number of the molecules is increased, the instability due to the electrostatic repulsion will exceed the stabilization owing to the van der Waals interaction. In the case of the observed honeycomb-like structure, the molecules are packed as shown in Fig. 4.13(c) due to the van der Waals stabilization if the number of the molecules is less than five. Then the next molecule will be adsorbed on the shifted position in c-axis direction so as to make the distance between the iodine adsorption sites maximized. This is the driving force to make up the hexagonal arrangement of the iodine adsorption sites as shown in Fig. 4.13(a).

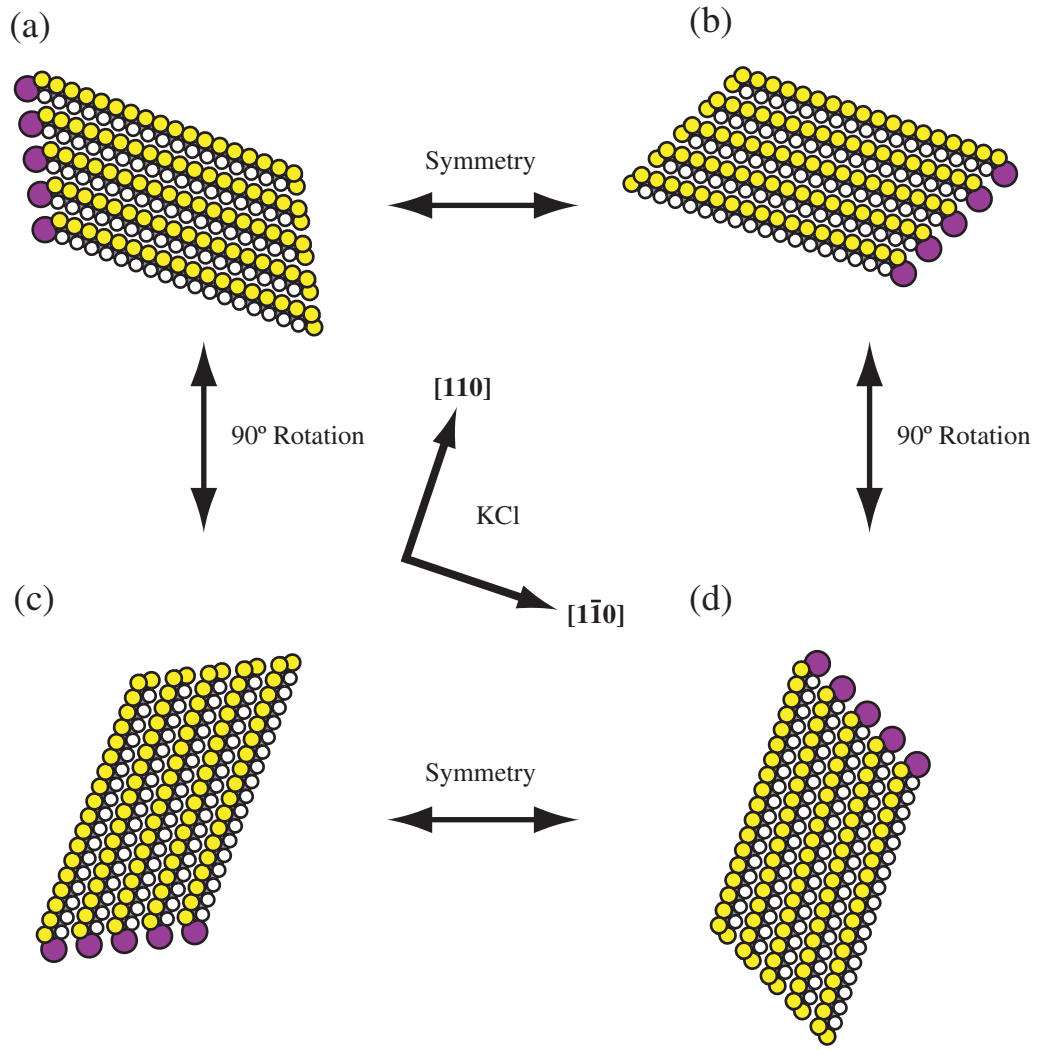

Figure 4.14: A schematic models of the four different packing arrangements in the honeycomb-like structure.

Domains of Honeycomb-like Structure

Four packing arrangements with different orientations are conceivable in the honeycomb-like structure as shown in Fig. 4.14. The one shown in 4.14(a) corresponds to that shown in Fig. 4.13(c). Another arrangement shown in 4.14(b) is mirror-symmetrical to the one shown in 4.14(a) with respect to the KCl[110] direction. Reflecting the four-fold symmetry of KCl(001) surface, there should be other two arrangements shown in 4.14(c) and (d) whose orientations are rotated by 90° from those shown in 4.14(a) and (b), respectively.

Corresponding to these four different packing arrangements, four different domains of honeycomb-like structure are conceivable as shown in Fig. 4.15. For example, Fig. 4.16(a) is an FM-DFM image taken on a domain boundary of two

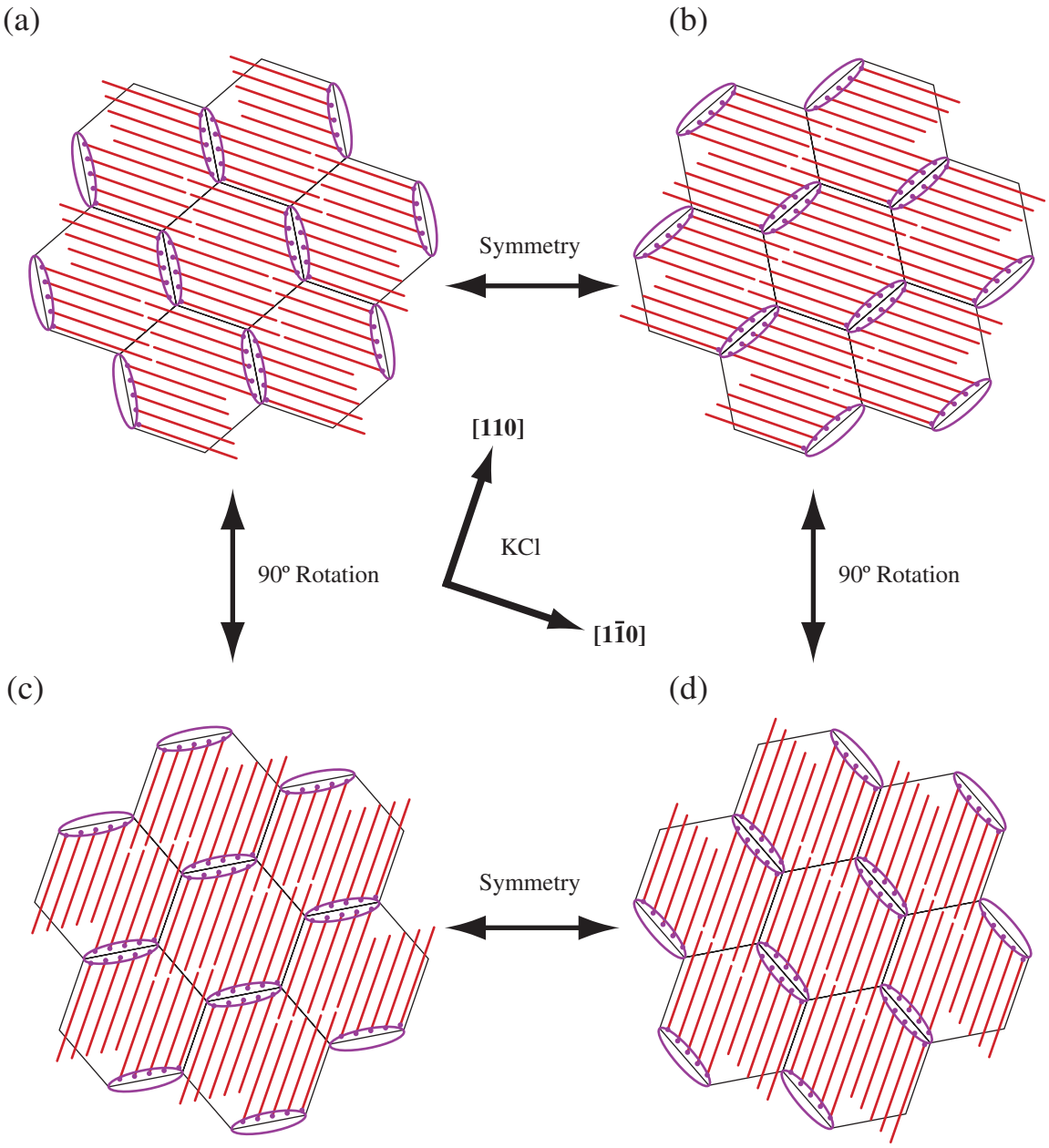

Figure 4.15: A schematic models showing the four different domains of the honeycomb-like structure.

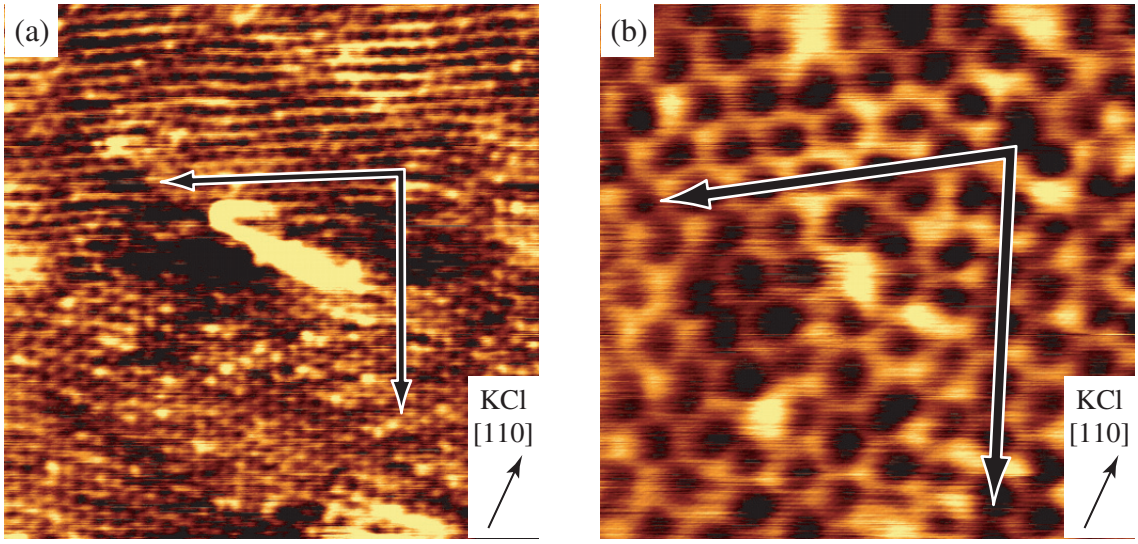

Figure 4.16: FM-DFM images of a VDF oligomer monolayer on KCl(001) surface. (a) 150 nm × 150 nm, $\Delta f = -20$ Hz, $A_{\text{p-p}} = 15$ nm. (b) 50 nm × 50 nm, $\Delta f = -20$ Hz, $A_{\text{p-p}} = 15$ nm.

different honeycomb-like structures. Their orientations are different by about 90° as indicated by two black arrows, reflecting the four-fold symmetry of the KCl(001) surface. Since the rod-like grains are formed on the honeycomb-like structures, the subsequent epitaxial growth directions of the rod-like structures might be determined by the orientations of the underlying domains. Figure 4.16(b) is a more magnified image of the domain boundary, which shows that the honeycomb-like structures at the very domain boundary is a little distorted. Thus the difference in orientation of the two domains is slightly deviated from 90° as shown by black arrows.

Second Molecular Layer

In the FM-DFM image shown in Fig. 4.17(a), some stripe structures along the KCl[110] direction are observed. The distance between the two adjacent stripes was about 4.4 nm, which corresponds to the molecular length in all-*trans* conformation. Thus the inner structure of the stripes should be the same as the one shown in Fig. 4.6(d). Figure 4.17(b) is the FM-DFM image taken on the same structure with a larger frequency shift ($\Delta f = -60$ Hz), which showed the individual molecules closely packed with an inter-molecular distance of about 0.5 nm. However, the stripes with a period of 4.4 nm found in Fig. 4.17(a) were not clearly seen in this image.

When the honeycomb mesh was put on the image shown in Fig. 4.17(b), the iodine adsorption sites well agreed to the bright contrasts in the image. This result suggested that the image was taken on the second ML formed on top of the

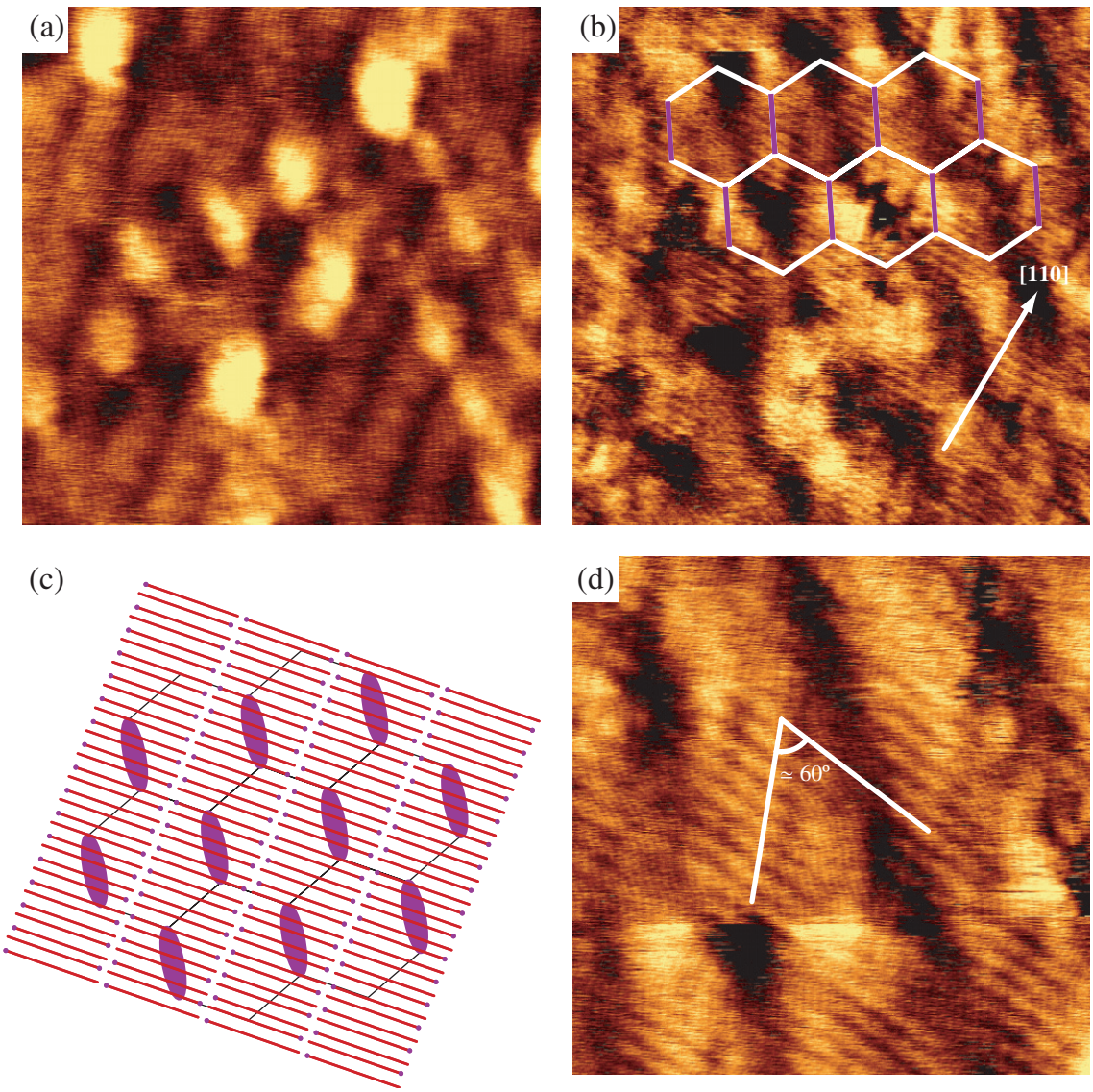

Figure 4.17: FM-DFM images of a VDF oligomer thin film on KCl(001) surface with a thickness of 2 MLs. (a) 40 nm × 40 nm, $\Delta f = -20$ Hz, $A_{\text{p-p}} = 15$ nm. (b) 25 nm × 25 nm, $\Delta f = -60$ Hz, $A_{\text{p-p}} = 15$ nm. (c) A schematic model showing the relative positions of the molecules in the second layer with respect to the underlying honeycomb-like structure. (d) 15 nm × 15 nm, $\Delta f = -60$ Hz, $A_{\text{p-p}} = 15$ nm.

honeycomb-like structure as shown in Fig. 4.17(c). When the frequency shift is relatively small, namely, the tip position is relatively distant from the surface, the molecular rows are observed due to the van der Waals interaction between the tip and the second ML. As the frequency shift is increased and the tip is approached close to the surface, the molecular-scale structure is imaged owing to the short-range chemical interaction between the tip and the molecules in the second ML while the electrostatic interaction between the tip and the iodine adsorption sites results in the large scale image corrugations. Therefore, the true topographic corrugation of second layer (molecular rows) are not clearly observed when the frequency shift is increased. This result indicated that such a long-range electrostatic interaction will affect the image contrast of the FM-DFM image taken even on the second ML.

Figure 4.17(d) is the FM-DFM image taken on the same area with a smaller scanned area, which clearly shows molecular-scale arrangements within the stripe structures. As indicated in this image by white lines, the angle between the c-axis (main chain) direction and the row-like bright contrasts found in the image was about 60°, which well agreed to the expectation from the model shown in Fig. 4.13(c). Thus the result also strongly supported the structural model shown in Fig. 4.17(c).

Third Molecular Layer

The FM-DFM image shown in Fig. 4.18(a) shows some rod-like grains, which is similar to those found in the image shown in Fig. 4.6(a). Figure 4.18(b) shows the FM-DFM image taken on the area indicated by the white square in Fig. 4.18(a). In this image, some stripe structures along the KCl[$1\bar{1}0$] direction are observed, representing the molecular rows. The FM-DFM image shown in Fig. 4.18(c) was taken on the same area with a smaller scanned area, which clearly showed some protrusions hexagonally arranged with a separation of about 5 nm. A more high-resolution image of this structure (Fig. 4.18(d)) revealed the molecular packing arrangements within the structure.

From the orientation of the molecular axis, this molecular layer is formed on top of the honeycomb-like structure depicted by the model shown in Fig. 4.15(c) or (d). For example, when the hexagonal mesh corresponding to the model shown in Fig. 4.15(c) is put on the image in Fig. 4.18(c), the bright contrasts well agree to the iodine adsorption sites. The corrugation corresponding to the honeycomb lattice is smaller than that observed in Fig. 4.17. In addition, the bright contrast representing the row of the iodine atoms could not be imaged on this molecular layer. Thus this molecular layer should be higher than the second layer. In this experiment, three different structures were found in the two-dimensionally grown

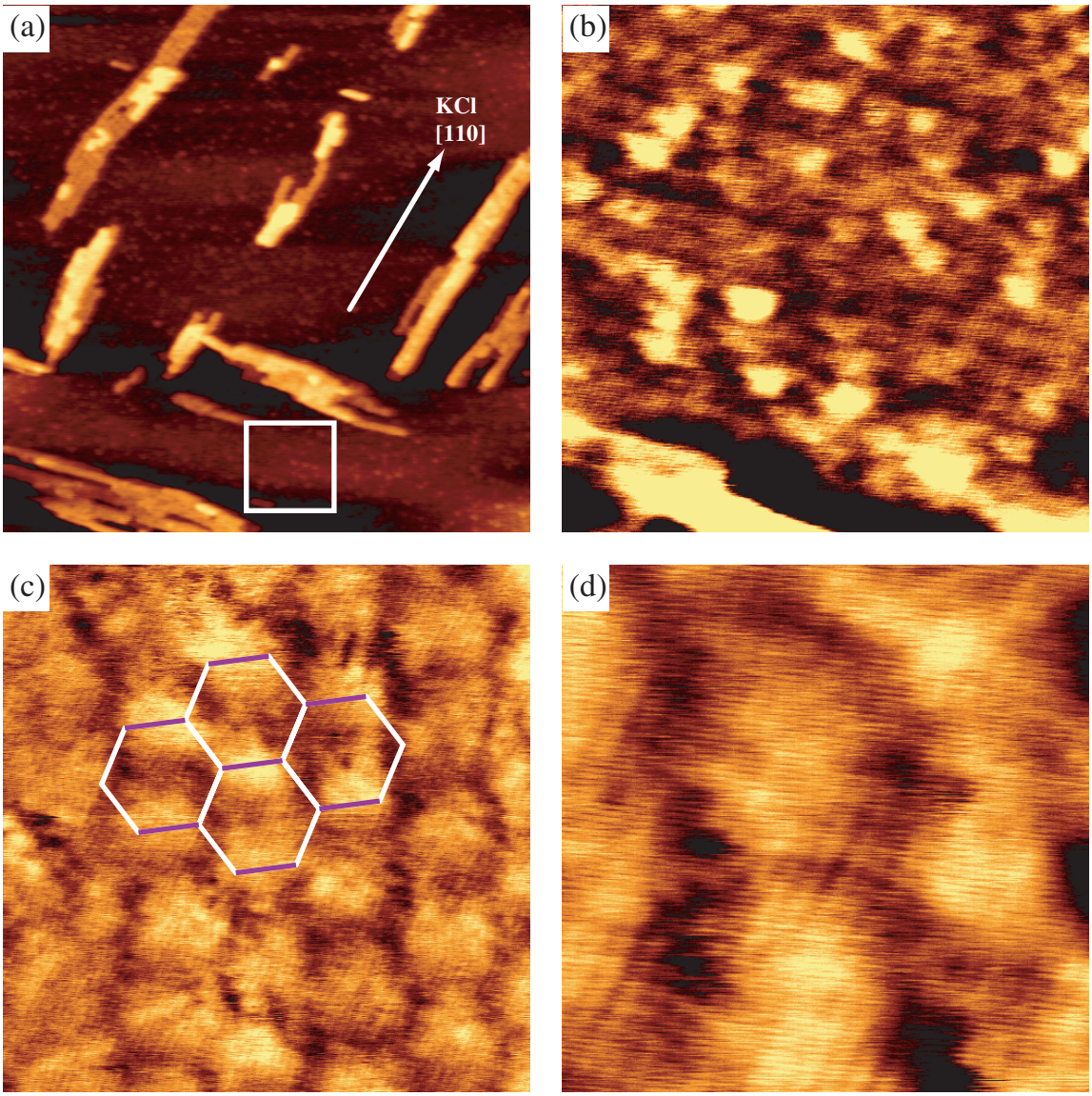

Figure 4.18: FM-DFM images of a VDF oligomer thin film on KCl(001) surface with a thickness of 3 MLs. (a) 300 nm × 300 nm, $\Delta f = -10$ Hz, $A_{\text{p-p}} = 15$ nm. (b) 50 nm × 50 nm, $\Delta f = -20$ Hz, $A_{\text{p-p}} = 15$ nm. (c) 25 nm × 25 nm, $\Delta f = -60$ Hz, $A_{\text{p-p}} = 15$ nm. (d) 10 nm × 10 nm, $\Delta f = -60$ Hz, $A_{\text{p-p}} = 15$ nm.

molecular layers; honeycomb-like structure, the second layer (Fig. 4.17) and the one shown in Fig. 4.18. Thus the image shown in Fig. 4.18 should be taken on the third ML.

Epitaxial Growth Process

From the results obtained in this experiment, the epitaxial growth process of VDF oligomer thin films can be described as follows.

Some islands of the honeycomb-like structures are first formed on the KCl(001) surface (Fig. 4.8(b)). There are some different kinds of honeycomb-like structures in terms of their orientations (Fig. 4.16). These islands two-dimensionally grow until the KCl(001) surface is totally covered reflecting the high surface energy of the KCl(001) surface.

Then the molecules deposited onto the first layer are adsorbed on the preferred sites in the honeycomb-like structures, making some stripe structures (Fig. 4.8(a)). The second and third MLs are also two-dimensionally grown to form the super-structures as shown in Fig. 4.17 and Fig. 4.18. Such a two-dimensional growth even in the third ML suggested the strong influence of the long-range electrostatic interaction between the molecules and the KCl(001) surface.

On the third layer, the molecules show three-dimensional growth forming some rod-like grains in the crystal form I (Fig. 4.6(a)). After that, some of the rod-like grains grow beyond other grains making a large rod-like structures (Fig. 4.4) Therefore, the growth direction of the rod-like grain is determined by the orientation of the underlying honeycomb-like structure at the very interface between the film and the substrate.

4.4 Alkanethiol Self-Assembled Monolayers on Au(111) Surfaces

4.4.1 Alkanethiol Self-Assembled Monolayers

In 1983, Nuzzo and Allara demonstrated that the dialkyldisulfides (RS-SR) are spontaneously organized into highly ordered monolayer on gold substrates.[154] Since then, such spontaneous organization processes called "self-assembly" have been intensively studied on various combinations of molecular species and substrates such as organosilicon compounds on hydroxylated surfaces (SiO_2/Si, Al_2O_3/Al and glass)[155–166] and organosulfur compounds on noble metals (gold, silver, platinum and copper).[167–179] Among them, alkanethiol self-assembled monolayers (SAMs) on Au(111) surfaces are the most well-studied system due to the simple structure of

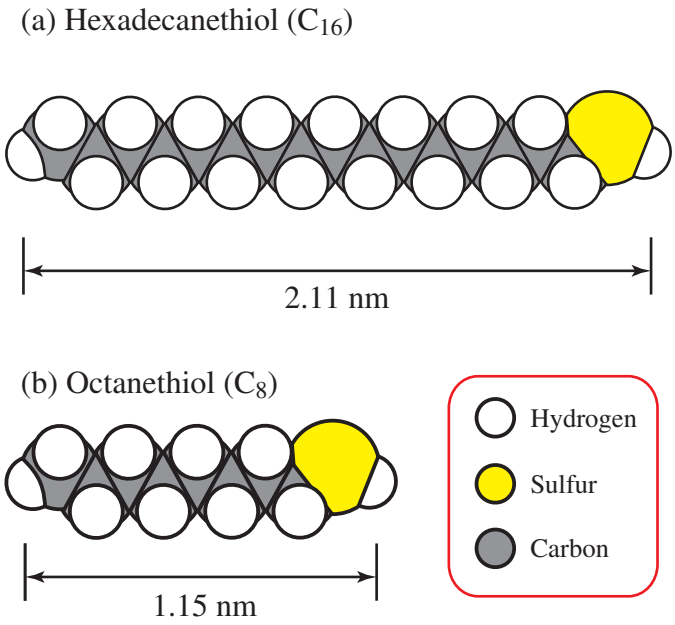

Figure 4.19: Schematic models of alkanethiol molecules used in this experiment. (a) Hexadecanethiol (C_{16}). (b) Octanethiol (C_8).

the molecules and easy preparation process of Au(111) surfaces.

Alkanethiol molecule (C_n; CH_3-$(CH_2)_{n-1}$-SH) is composed of a main alkyl chain and methyl (-CH_3) and thiol (-SH) end groups at the both ends of the molecule. Figure 4.19 shows the molecular structures of the alkanethiols used in this experiment such as hexadecanethiol (C_{16}) and octanethiol (C_8). Alkanethiols have such simple structures that they can be regarded as good prototypes for many other kinds of organosulfur compounds with different functional groups and repeating units of molecular chains. On the other hand, clean Au(111) surfaces can be easily obtained by flame annealing of a gold single crystal or simple vacuum deposition onto a mica or a glass substrate. Figure 4.20 shows a typical STM image of a clean Au(111) reconstructed surface showing clear features of 22 $\times\sqrt{3}$ structures. Since gold has no stable oxides, the surface can stably exist even under ambient conditions. Due to these reasons, alkanethiol SAMs on Au(111) surfaces have been often used as model systems for the investigations on self-assembling processes.

Alkanethiol SAMs are usually formed by immersing the clean gold substrates into the dilute (typically 1 mM) solution of alkanethiols at room temperature. The immersion time varies from several minutes to a few days. During the immersion molecules are chemisorbed onto the Au(111) surface making up a highly ordered molecular monolayer.

So far, molecular conformations and packing arrangements within the monolayer have been intensively studied by a variety of techniques. Studies using reflectance in-

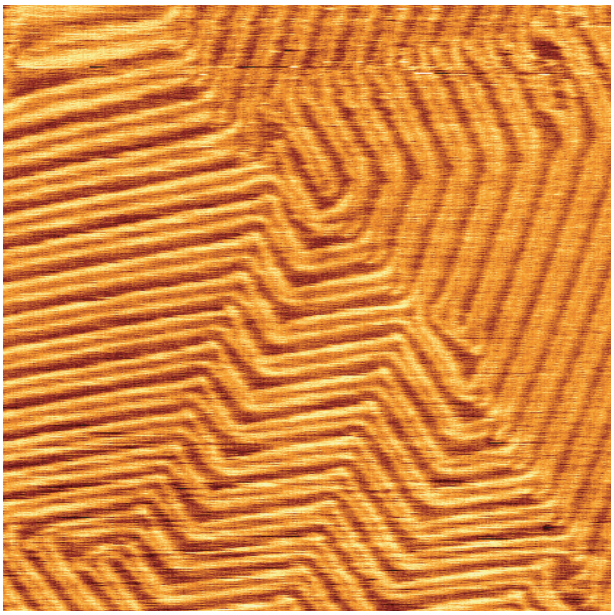

Figure 4.20: A typical STM image of a clean Au(111) surface formed on a mica substrate showing $22 \times \sqrt{3}$ structures (120 nm $\times$ 120 nm, $I_t = 10$ pA, $V_t = -0.6$ V).

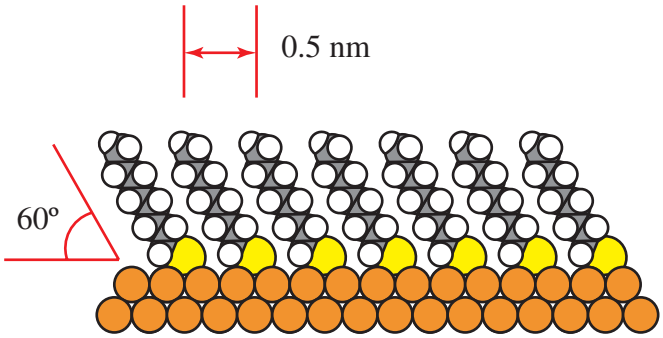

Figure 4.21: Schematic drawing of alkanethiol monolayer formed on Au(111) surface. It was assumed that the molecule is adsorbed onto the hollow site of the Au(111) surface although it still remains controversial.

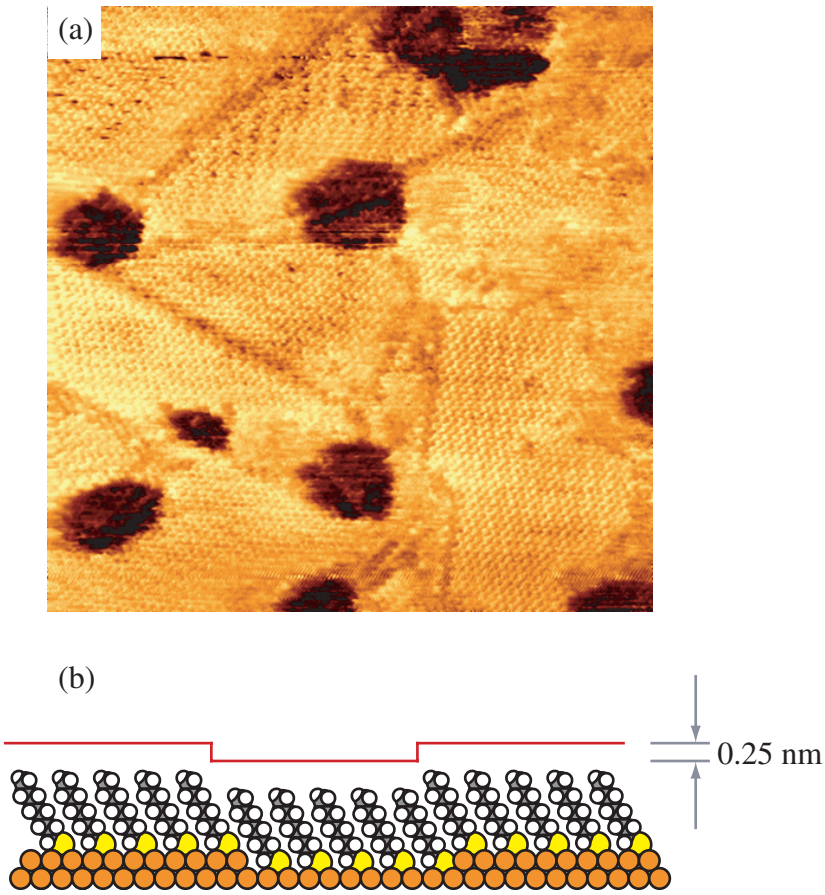

Figure 4.22: (a) A typical STM image of octanethiol (C_8) SAM formed on Au(111) surface showing some depressions and domain boundaries (30 nm × 30 nm, I_t = 10 pA, V_t = −0.6 V). (b) Schematic drawing of the etch pits seen in the STM image of C_8 SAM. The depth of the depression is about 0.25 nm which corresponds to the single atomic step of Au(111) surface.

frared (IR) spectroscopy revealed that the molecules take all-*trans* conformation with their molecular axes tilted by about 30° from the surface normal.[168,169] Transmission electron diffraction measurements showed that the molecules in the monolayer are hexagonally packed to form $(\sqrt{3} \times \sqrt{3})$R30° overlayer of Au(111) surface with inter-molecular distance of about 0.5 nm.[175] Figure 4.21 shows schematic drawing of alkanethiol monolayer formed on Au(111) surface.

Although these traditional spectroscopic methods have been successfully used to reveal "averaged" microscopic structures of alkanethiol monolayers, precise description of local structures such as molecular-scale domain boundaries and defect distributions cannot be directly obtained by these methods. On the other hand, since STM has true-atomic resolution in real space, it has been often used for the molecular-scale investigations on the alkanethiol monolayers.[180–184] Figure 4.22(a) shows typical STM image taken on octanethiol (C_8) SAM on Au(111) sur-

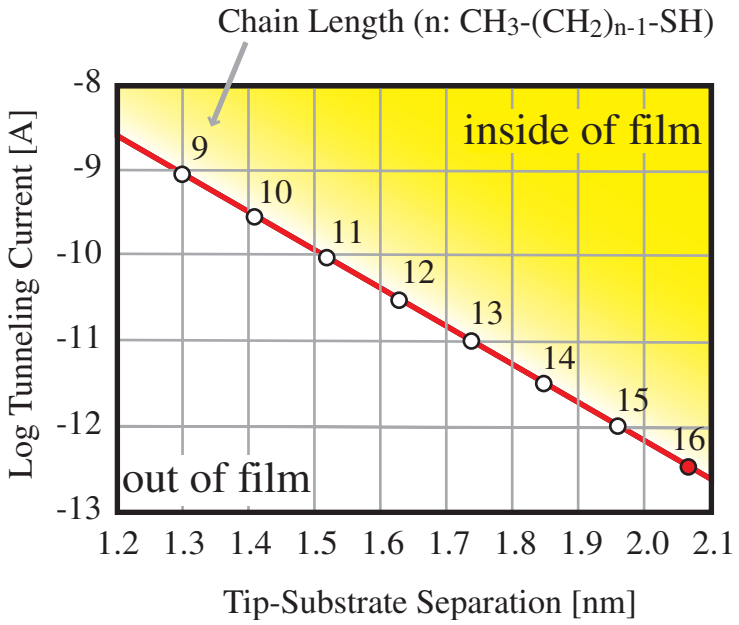

Figure 4.23: The semilogarithmic plot of the tunneling current vs. tip-substrate separation for STM imaging of alkanethiol SAMs with a 1 V bias voltage.[185,186] The solid line represents the tunneling current required to be detected in order to image without touching the surface.

face, which reveals molecular packing arrangements, domain boundaries and round-shaped depressions. Widrig *et al.* first presented molecularly-resolved STM images of alkanethiol SAMs, showing hexagonally-packed $(\sqrt{3}\times\sqrt{3})$R30° structures.[180] Schönenberger *et al.* investigated origin of the depressions found in the STM images of alkanethiol monolayers,[184] which revealed that the depressions are formed by the etching of gold surface as shown in Fig. 4.22(b).

In spite of these excellent results obtained so far, STM applications to the alkanethiol SAMs are limited to the ones composed of shorter-chain (typically $n < 14$) molecules. Figure 4.23 shows the semilogarithmic plot of the tunneling current vs. tip-substrate separation for STM imaging of alkanethiol SAMs with a 1 V bias voltage.[185,186] The solid line represents the tunneling current required to be detected in order to image without touching the surface. In the case of C_{16} SAMs, the tunneling current less than 0.3 pA has to be detected and kept constant, which is very difficult for most of the conventional STMs.

Although contact-mode AFM can be used for the investigations on longer-chain (typically $n > 14$) SAMs, it is very difficult to obtain true-molecular resolution images using this method. So far, some molecular-scale contact-mode AFM images of alkanethiol monolayers have been reported.[187,188] However, these AFM images did not present the molecular-scale arrangements at the domain boundaries or distri-

bution of the point defects. Therefore, there has been lack of information on the microscopic properties of longer-chain SAMs.

FM-DFM operated under UHV condition is the most promising solution for this problem because this technique can provide true-atomic resolution even on insulating surfaces.[24] So far, Uchihashi *et al.* reported molecularly-resolved FM-DFM images of nonanethiol (C_9) monolayers.[58] Aside from this result, there have been reported no results on FM-DFM imaging of alkanethiol monolayers. Namely, molecular-resolution have never been experimentally demonstrated on longer-chain SAMs. In addition, FM-DFM studies on the chain-length dependence of the SAMs have never been presented. In this study, FM-DFM was applied to the molecular-scale investigations both on shorter- and longer-chain SAMs formed on Au(111) surfaces. Then the chain-length dependence of the imaging conditions was discussed in detail.

4.4.2 Sample Preparation

The Au(111) surface was prepared by evaporating gold onto the freshly cleaved mica substrate. Before the evaporation, the mica substrate was annealed at 500°C for 24 h. The thickness of the gold thin film was about 100 nm, which was measured with a quartz deposition monitor. 1-octanethiols and 1-hexadecanethiols were purchased from Aldrich Chemical Co., Ltd. and used without any special treatment. The alkanethiol SAM was prepared by immersing the gold substrate in 1 mM ethanol solution for 24 h. After the immersion, the sample was rinsed with the pure ethanol for a few seconds and was dried in the pure N_2 flow. Then the sample was annealed in air at 70°C for 2 h in order to reduce the surface contamination. Immediately after these preparation processes, the sample was transferred into the UHV chamber for FM-DFM imaging.

4.4.3 Results and Discussion

Closely Packed Domains of Alkanethiol SAMs

Figure 4.24(a) is an FM-DFM image of the C_8 SAM formed on the Au(111) surface, showing some round-shaped depressions. The depth of the depressions estimated from the cross-sectional plot of the FM-DFM image was about 0.25 nm, which corresponds to the single atomic step of the Au(111) surface. The result confirmed that the depressions were formed by the gold etching[183,184] during the SAM formation process. Figure 4.24(b) shows an FM-DFM image taken on the same sample with a smaller scanned area. Although the image is a little distorted, the upper and lower parts of this image shows some stripe structures with a repeating period of about

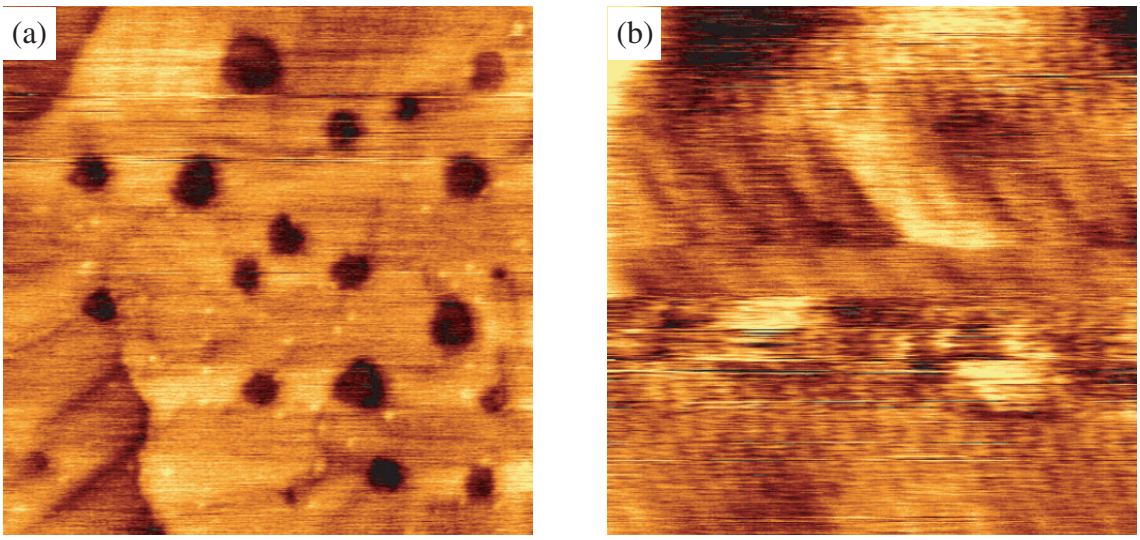

Figure 4.24: FM-DFM images of the octanethiol (C_8) SAM on Au(111) surface. (a) 120 nm × 120 nm FM-DFM image showing some depressions ($\Delta f = -40$ Hz, $A_{\text{p-p}}$ = 15 nm). (b) 10 × 10 nm FM-DFM image showing stripe structures in the upper and lower parts ($\Delta f = -40$ Hz, $A_{\text{p-p}} = 15$ nm).

0.45 nm.

When the molecules are closely packed to form $(\sqrt{3} \times \sqrt{3})$R30° structure, the inter-molecular distance between the nearest neighboring molecules becomes about 0.5 nm. Thus the repeating period of the molecular rows becomes about 0.43 nm. Since the length is close to the period of the molecular-scale contrasts found in Fig. 4.24(b), the observed structure should correspond to $(\sqrt{3} \times \sqrt{3})$R30° structure of C_8 monolayer.

Figure 4.25(a) is an FM-DFM image of the C_{16} SAM formed on Au(111) surface. In this image, both depressions and hexagonally packed individual molecules are simultaneously observed, revealing that true-molecular resolution can be achieved even on the longer-chain SAMs. Figure 4.25(b) is an FM-DFM image taken on the same sample with a smaller scanned area. Figure 4.25(c) is a cross-sectional plot measured along the bright line A−B indicated in Fig. 4.25(b). The plot shows that the distance between the nearest neighboring molecules is about 0.5 nm, which corresponds to the lattice constant of $(\sqrt{3} \times \sqrt{3})$R30° structure on Au(111) surface.

When the C_8 SAMs were imaged with a relatively large frequency shift ($|\Delta f| >$ 40 Hz), the imaging conditions such as vibration amplitude and frequency shift were quite unstable so that the high resolution was hard to achieve. On the other hand, the imaging conditions during the imaging of C_{16} SAMs were stable enough to obtain the clear molecularly-resolved images. These results suggested that the imaging conditions on the longer-chain SAMs are more stable than those on the

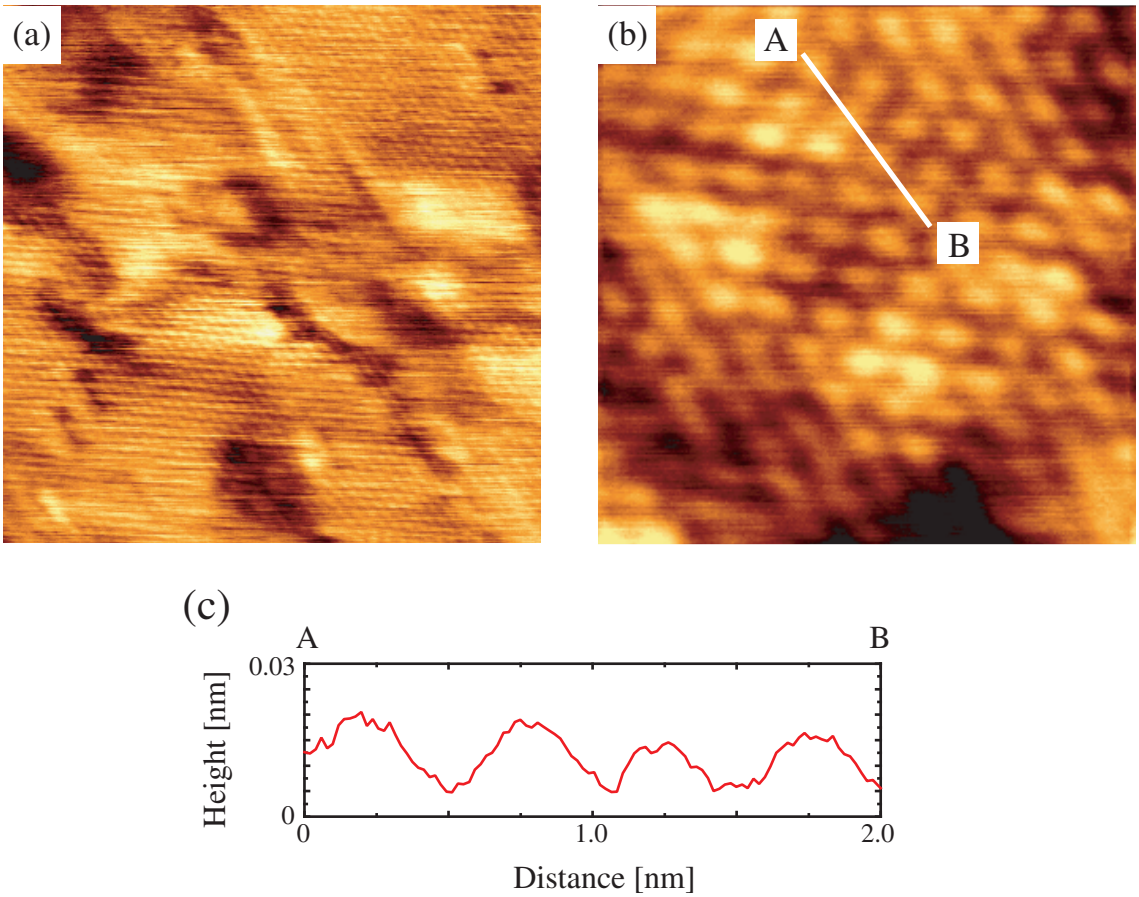

Figure 4.25: FM-DFM images of the hexadecanethiol (C_{16}) SAM on Au(111) surface. (a) 20 nm × 20 nm FM-DFM image showing some etch pits and domain boundaries ($\Delta f = -50$ Hz, $A_{\text{p-p}} = 15$ nm). (b) 5 nm × 5 nm FM-DFM image showing $(\sqrt{3} \times \sqrt{3})$R30° lattice structure ($\Delta f = -70$ Hz, $A_{\text{p-p}} = 15$ nm). (c) The cross-sectional plot measured along the bright line A – B indicated in (b).

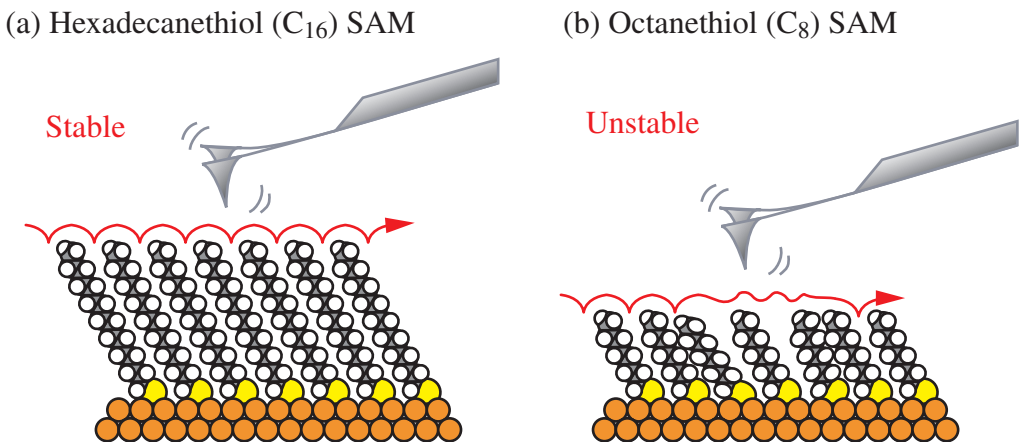

Figure 4.26: A schematic model showing the FM-DFM imaging of (a) the C_{16} SAM and (b) the C_8 SAM. The molecules in the C_8 SAM are easily displaced by the tip-sample interaction force because they are relatively loosely bound by the surrounding molecules. Such a molecular fluctuation results in the unstable imaging conditions, preventing the high-resolution imaging.

shorter-chain SAMs.

So far, Porter *et al.* performed a study using ellipsometry, infrared absorption and electrochemical measurements and revealed that the molecular ordering of the SAMs are improved with increasing chain length.[168] They also pointed out that the degree of ordering drastically changes at the chain length from C_6 to C_{12}. Another study using AFM suggested that the longer-chain (C_{18}) SAMs are able to withstand a greater tip-sample interaction force than shorter-chain (C_5) SAMs.[187]

From these results reported so far, the observed chain length dependence of the imaging conditions can be explained as follows (Fig. 4.26). The van der Waals interaction between the alkyl chains gets stronger when the chain length is increased. Thus the molecules in the longer-chain SAMs are more tightly bound by the surrounding molecules and rigid enough to withstand a larger tip-sample interaction force (Fig. 4.26(a)). In the case of shorter-chain SAMs, the molecules are loosely bound by the other molecules so that they are more easily displaced by the tip-sample interaction force. Such a tip-induced molecular fluctuation will result in the unstable imaging conditions, preventing the high-resolution imaging (Fig. 4.26(b)).

Low-Density Phase of Alkanethiol SAMs

Several studies using low-energy electron diffraction (LEED), helium-atom diffraction, and STM revealed the existence of the stripe structures referred to as $p \times \sqrt{3}$ structures[180,189,190] in relatively shorter-chain (C_4 to C_{12}) SAMs, where p varies depending on the sample preparation process. The structure is formed in the domains

with relatively low molecular density. Such a less-dense SAM can be prepared by either annealing of densely-packed monolayers,[191] adequate dosing in gas phase deposition,[192] or immersion in solution for short periods only.[190] In our experiment, the closely-packed structures of C_8 SAMs were changed into less-dense stripe structures after an annealing treatment at 80°C for 2 h in UHV.

Figure 4.27(a) is an FM-DFM image of the annealed sample showing many stripe structures and domain boundaries. In addition, it is recognized that each stripe consists of a pair of bright lines as shown in Fig. 4.27(b). Figure 4.27(c) is the cross-sectional plot of the bright line A – B indicated in Fig. 4.27(b). The period of the stripe structure is estimated to be about 2 nm, which is roughly 7 times as large as the lattice constant of Au(111) surface. Furthermore, a molecularly-resolved FM-DFM image was successfully obtained as shown in Fig. 4.27(d). The image shows that each bright line consists of bright dots. Figure 4.27(e) is the cross-sectional plot measured along the bright line C – D indicated in Fig. 4.27(d). This plot shows that the distance between the two adjacent bright dots is about 0.5 nm, which corresponds well to the lattice constant of $(\sqrt{3} \times \sqrt{3})$R30° structure on Au(111) surface. These results suggest that the stripe structures observed here should be 7 $\times\sqrt{3}$ structures.

There have been some reports on STM observations of $p \times \sqrt{3}$ structures of alkanethiol SAMs.[190,191,193,194] In particular, Poirier *et al.* reported very similar stripe structures to the result obtained in this experiment.[190] In these articles, some of them reported $p \times \sqrt{3}$ structures in which the length of p times the lattice constant of the gold substrate (a) corresponds to the length of molecules or the twice of it.[191,193] The others reported the stripe structures in which the length of $p \times a$ agreed to neither the molecular length nor the twice of it.[190,194] In the former case, the observed $p \times \sqrt{3}$ structures are explained by "head-to-head model" or "head-to-tail model", in which the molecules take parallel orientation to the substrate surface. In the latter case, although the detailed structural model have not been given, the molecules are said to have larger tilt angle from the surface normal compared to that in $(\sqrt{3} \times \sqrt{3})$R30° structure.

In our experiments, since the observed period of the stripe structure (about 2 nm) was slightly shorter than the twice of the molecular length (1.15 nm), the stripe structures should be composed of basic units containing two molecules with their molecular chains almost parallel to the gold substrate. Figure 4.28 shows one of the possible model of the molecular arrangements within the stripe structure observed in this experiment. In this model, the angle between the row of the sulfur atoms and the molecular chain is assumed to be 100° based on the image shown in Fig. 4.27(d).

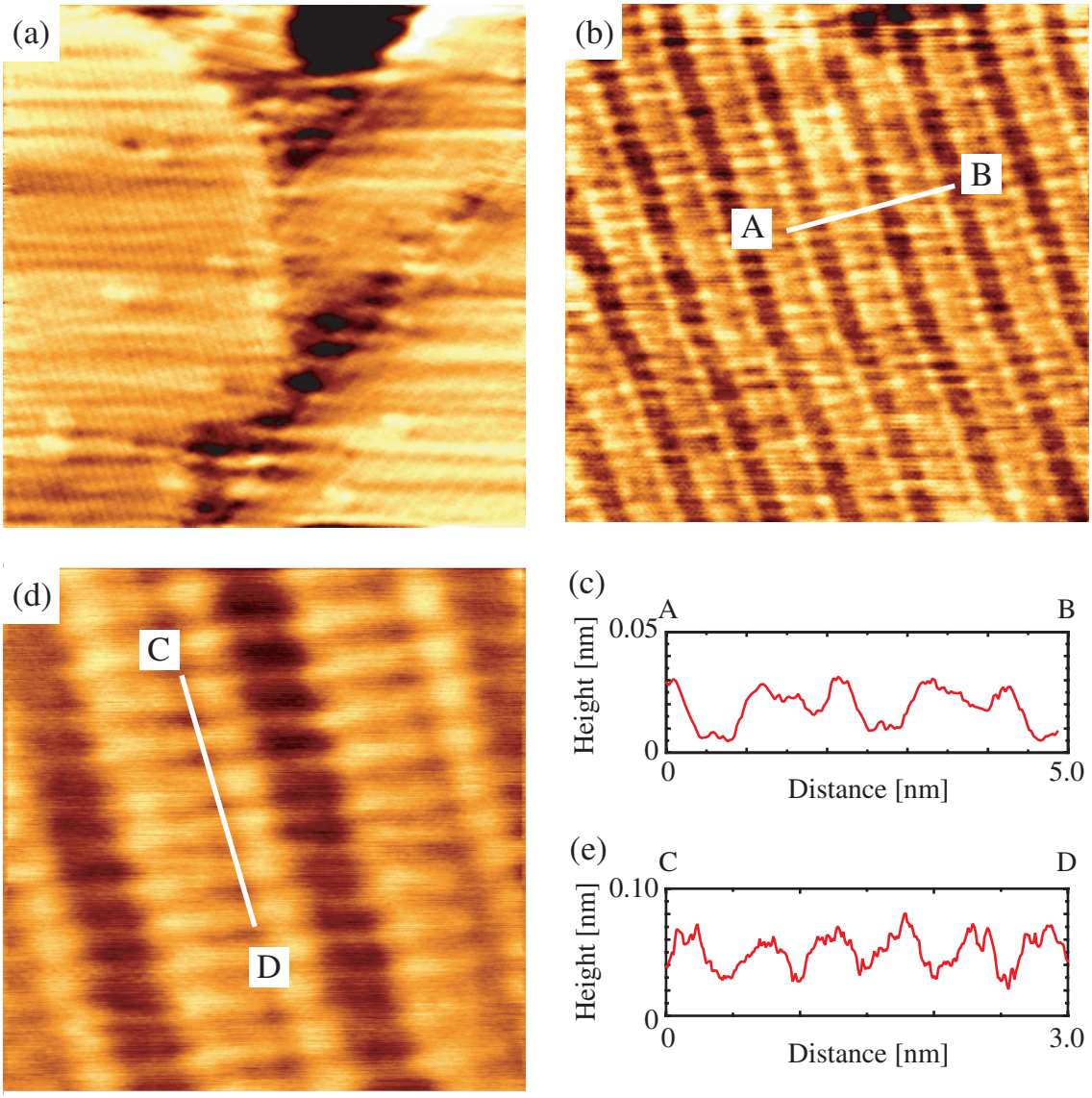

Figure 4.27: FM-DFM images of octanethiol monolayer. (a) 60 nm × 60 nm FM-DFM image showing many stripe structures and domain boundaries ($\Delta f = -40$ Hz, $A_{\text{p-p}} = 15$ nm). (b) 15 × 15 nm FM-DFM image showing that each stripe consists of two bright lines ($\Delta f = -40$ Hz, $A_{\text{p-p}} = 15$ nm). (c) The cross-sectional plot measured along the bright line A – B indicated in (b). (d) 6 nm × 6 nm FM-DFM image showing each bright line consist of bright dots ($\Delta f = -40$ Hz, $A_{\text{p-p}} = 15$ nm). (e) The cross-sectional plot measured along the bright line C – D indicated in (d).

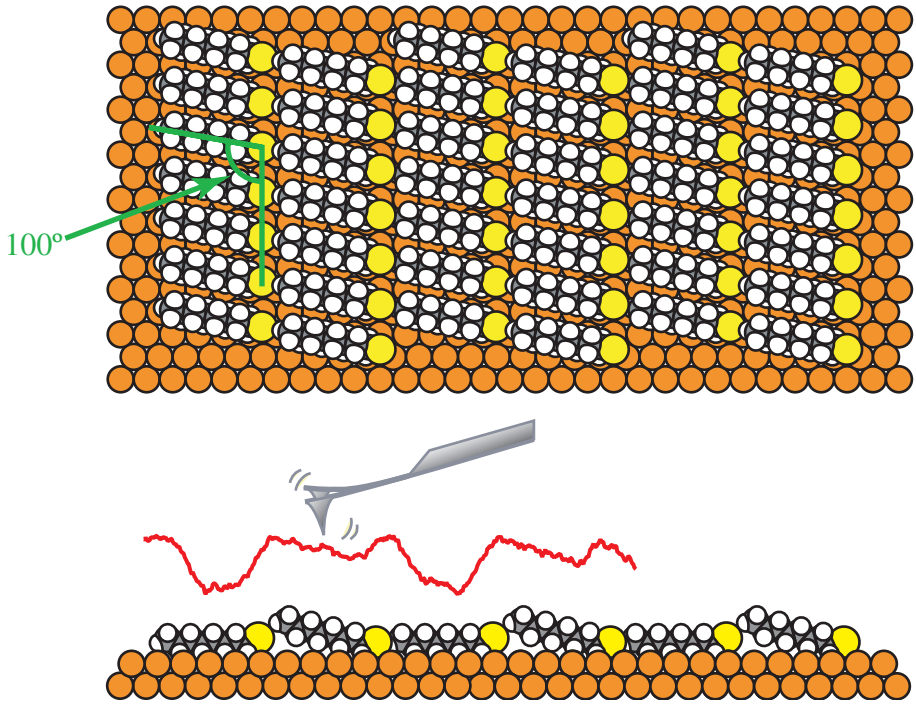

Figure 4.28: A schematic model showing the molecular arrangements in the $p \times \sqrt{3}$ structure observed in this experiment.

The high-resolution imaging of the shorter-chain SAMs in $(\sqrt{3} \times \sqrt{3})$R30° structure was rather difficult due to the molecular fluctuation induced by the tip-sample interactions (Fig. 4.24(b)). On the other hand, the shorter-chain SAMs in $p \times \sqrt{3}$ structure was easily imaged with true-molecular resolution (Fig. 4.27(d)). These results suggested that the molecules in the parallel orientation to the gold surface is tightly bound by the interaction with the substrate so that they can withstand the relatively strong tip-sample interaction force.

4.5 Summary

In this chapter, the possibilities and the problems of FM-DFM applications to the molecular-scale investigations on insulating organic thin films were experimentally demonstrated.

Demonstration of True-Molecular Resolution

It was demonstrated that the true-molecular resolution can be achieved by FM-DFM even on insulating organic surfaces.

1. Molecularly-resolved FM-DFM images of VDF oligomer thin films on KCl(001) surfaces were presented. The result first demonstrated the true-molecular

resolution on organic thin films formed on insulating substrates.

2. Molecularly-resolved FM-DFM images of longer-chain SAMs were presented. The result first demonstrated the true-molecular resolution on relatively thick (> 2 nm) organic thin films.

Problems in High-Resolution Imaging

Some specific situations where high-resolution was hard to achieve were found in this experiment.

1. It was difficult to achieve high-resolution on the first monolayer of VDF oligomers formed on KCl(001) surface while the second or higher MLs were successfully imaged with molecular-resolution. The result suggested that in the applications to purely insulating surfaces, large surface potential variation can prevent the high-resolution imaging.

2. It was difficult to obtain high-resolution images of shorter-chain SAMs due to the unstable imaging conditions (i.e. Δf and A) while molecular-resolution was stably obtained on longer-chain SAMs. The result suggested that in the applications to loosely-packed molecular layers, the tip-induced molecular fluctuation can prevent the high-resolution imaging.

Chapter 5

Dissipation Mechanisms of Cantilever Vibration Energy

5.1 Introduction

The results obtained in the previous chapter demonstrated that molecularly-resolved FM-DFM images can be obtained even on the insulating organic surfaces. However, some specific situations where high-resolution was hard to achieve were also found in the experiments. In the case of VDF oligomers on KCl(001) surfaces, it was difficult to obtain molecular-resolution at the very interface between the film and the substrate due to the large electrostatic interaction. In this case, the vibration amplitude of the cantilever showed large variation depending on the tip position with respect to the underlying honeycomb-like structure. On the other hand, the shorter-chain alkanethiol SAMs were also hard to image on a molecular-scale due to the molecular fluctuation induced by the tip-sample interaction. In this case, the imaging conditions such as vibration amplitude and frequency shift became unstable when the tip was positioned at the close vicinity of the sample surface. These results indicated that the observed inaccessibility to the high-resolution may be ascribed to the amplitude variation during the FM-DFM imaging.

Since the distance dependence of the frequency shift is significantly affected by the vibration amplitude, the tip-sample distance regulation can be severely disturbed by such an amplitude variation. In the previous chapter, the cantilever was vibrated in constant excitation mode so that the amplitude was varied by the dissipative tip-sample interactions. In this chapter (and also in the next chapter), in order to suppress such an undesirable amplitude variation, constant amplitude mode was employed. In this excitation mode, the amplitude damping caused by the dissipative tip-sample interaction is compensated by increasing the cantilever excitation amplitude. Thus the conservative and dissipative interaction forces are almost independently detected as an increase of the frequency shift and the excita-

tion amplitude, respectively.

The results obtained in the previous chapter suggested that the cantilever vibration energy can be dissipated by the electrical tip-sample interactions. In addition, it was indicated that the energy dissipation is also induced by the molecular fluctuations if the surface is not rigid enough to endure the tip-sample interaction force. Although electrical interactions and molecular fluctuations can be a serious problem in the high-resolution FM-DFM imaging, the results implied that the magnitude of the energy dissipation may be related to the electrical and mechanical properties of the surface. Therefore, if the relationship is elucidated, it may become possible to evaluate the electrical and mechanical surface properties using energy dissipation measurement.

In this chapter, the dissipation mechanisms of the cantilever vibration energy were investigated in relation to the electrical interaction and the molecular fluctuation. For this purpose, the organic surfaces with a large variation in the electrical and mechanical properties are desirable as the model organic systems. The energy dissipation process induced by the electrical interaction was investigated on the oligothiophene monolayers formed on Pt surfaces. The sample shows a large surface potential variation between the film and the substrate. The energy dissipation process induced by the molecular fluctuation was studied on the phase-separated SAMs composed of alkanethiols and alkanedithiols. In this sample, the thiols are closely-packed to form well-ordered rigid domains while the dithiols form a loosely-packed disordered monolayer. Thus a large variation in the mechanical property is expected between the thiol and dithiol regions.

5.2 Experimental

All the experiments described in this chapter were performed under UHV conditions using a commercially available UHV-SPM system (JEOL: JSTM/AFM-4500XT, Fig. 4.1) with some modifications. The original frequency shift detector was replaced with a homebuilt PLL circuit[61] to perform a stable frequency shift detection. The original self-excitation circuit was replaced with a homebuilt electronic circuit with an AGC function to keep the cantilever vibration amplitude constant.

The highly-doped n-Si cantilever (Nanosensors: NCH) with a resonance frequency of about 300 kHz and with a nominal spring constant of 40 N/m was used for the FM-DFM imaging. The typical Q-factor measured under an UHV condition was 30,000. The resistivity of the cantilever was 0.01 – 0.025 Ωcm. No special tip treatment was carried out before use. The cantilever was vibrated in constant amplitude mode. The tip-sample distance regulation was made in constant frequency

shift mode. During the FM-DFM imaging, the tip and the sample were electronically grounded.

As for the FM-KFM measurements, two different types of cantilevers were used in this experiment. In Sec. 5.3, the Pt(20 nm)-coated Si cantilever (Olympus Opt. Co., Ltd.) with a resonance frequency of about 300 kHz and with a nominal spring constant of 42 N/m was used. In Sec. 5.4, the PtIr(20 nm)-coated Si cantilever (Nanosensors: NCHPt) with a resonance frequency of about 300 kHz and with a nominal spring constant of 40 N/m was used. The typical Q-factor measured under an UHV condition was 10,000 for both cantilevers. During the FM-KFM measurement, the ac and dc bias voltages were applied between the tip and the bias electrode. The amplitude and the frequency of the ac bias modulation voltage were 2 $V_{p\text{-}p}$ and 2 kHz, respectively. Due to the bias modulation, the electrostatic force and the resultant frequency shift were modulated at the same frequency. Then the modulated frequency shift was detected using a lock-in amplifier (NF: 5610B). The KFM bias feedback regulation was made using a home-built feedback electronics.

The dissipation images shown in this chapter were obtained by recording the gain (V'_{exc}) of the variable gain amplifier which drives the PZT actuator for the cantilever excitation (excitation image in Fig. 2.17). All the numerical values for the energy dissipation shown in this chapter were calculated with Eq. (2.44) no matter whether the apparent dissipation was contained or not.

5.3 Energy Dissipation induced by Electrical Interaction

5.3.1 Oligothiophene Monolayers on Pt Surfaces

Polythiophene

In 1977, Sirakawa *et al.* first demonstrated the highly conducting nature of polyacetylenes,[195–197] which gave birth to the novel research area of conducting π-conjugated polymers. These new materials combined the electronic and optical properties of semiconductors and mechanical plasticity of conventional polymers. Depending on their doping level, they can behave either as metallic conductors or semiconductors, can be chromophores or luminophores and may have large optical non-linearity.[198]

So far, a number of π-conjugated polymers were synthesized such as poly(*p*-phenylenevinylene),[199] polyaniline,[200] polythiophene[201] and many others.[202–207] Among them, polythiophene (Fig. 5.1(a)) has become one of the most well-investigated conducting polymer. This is because the conducting properties of poly-

(a) Polythiophene

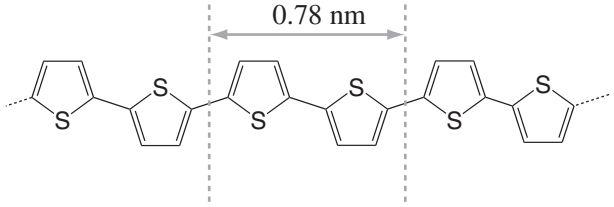

(b) Dimethylquinquethiophene (DM5T)

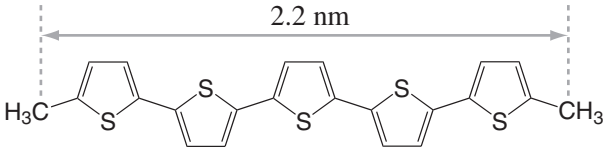

Figure 5.1: Molecular structures of (a) polythiophene and (b) dimethylquinquethiophene.

thiophenes are mostly unaffected by the substituents, which allows a variety of structural variations suitable for a wide range of applications. In addition, both the semiconducting and conducting polythiophenes are very stable and readily characterized. These excellent physical and chemical properties made it possible to develop the high performance optoelectronic devices such as organic light emitting diodes (OLEDs),[208–213] organic field effect transistors (OFETs)[214–216] and light modulators.[217]

As it became clear that structure plays a dominant role in determining the electrical and optical properties of polythiophenes, more research was focused on controlling their structure in the solid state. However, due to the statistical chain length distribution and the interruption of the conjugated chain by mislinkages, it was nearly impossible to achieve a complete control over their solid state structures. Thus the conjugation and conducting pathways are interrupted and severely disturbed in the polymeric devices. This major drawback of the conducting polymers promoted the synthesis and the investigations on their corresponding oligomers.

Oligothiophene

Oligomers are free from chain length distribution and defects in the π-conjugated chain so that the molecular structure is strictly defined. Since most of the oligothiophenes are thermally stable, chemical impurities can be satisfactorily eliminated by repeating purification using sublimation method. More importantly, it becomes possible to prepare oligomer thin films by vacuum deposition with a precise control of deposition rate, substrate temperature and film thickness. As a consequence of

all these benefits, highly ordered thin solid films of π-conjugated oligomers can be reproducibly fabricated.

The first trial to use oligothiophenes as an optoelectronic device was made in 1974 by Schoeler *et al.*,[218] where photo-induced current was measured on Langmuir-Blodgett films of α-quinquethiophene (α-5T). After more than one decade, with the discovery of conducting polymers[195] and emerging attention to their oligomers as a background, Fichou *et al.* first reported the charge transport properties of α-sexithiophene (α-6T).[219,220] An year later, the mobility of OFET made of vacuum evaporated α-6T thin film (10^{-3} – 10^{-4} cm^2/Vs)[220,221] was proven to be much higher than that of polythiophenes-based OFETs[215,222] reported up to that time.

After these pioneering works, a considerable number of efforts were made to broaden our knowledge on electronic structures[223–225] and charge transport properties[226–228] of α-nT thin films. In particular, it was revealed that the mobility of α-6T based OFET is improved when long-range ordering is achieved.[229] And hence the highest mobility (0.23 cm^2/Vs) was obtained in an OFET using nearly single-crystalline thin film of dihexylquaterthiophene (DHα-4T).[230] Besides OFETs, the semiconducting properties of α-oligothiophenes have been also utilized in other devices such as light-emitting diodes,[231,232] spatial light modulators,[233] electro-optical modulators[234–236] and photovoltaic cells.[237]

Oligothiophene Monolayer on Pt Surfaces

Non-substituted oligothiophenes may suffer from the chemical instability because of the high chemical activity of the non-substituted α-carbons in the terminal thiophene rings, and hence easily polymerized by oxidizing agents.[238] In 1999, Hotta *et al.* found that the substitution on these positions are very effective in enhancing chemical stability.[239] They synthesized a series of alkyl-substituted oligothiophenes and investigated their structure and charge transport properties in the thin film state.[227,239,240] The X-ray diffraction measurement revealed that the molecules have a similar layered structure with the long molecular axis perpendicular to the substrate.[239] The OFET of alkyl-substituted oligothiophenes showed comparable carrier mobility to those reported for non-substituted oligothiophene, which confirmed that the highly electroactive nature of π-conjugated chain remains unchanged by the substitution.[240]

In this study, the monolayer of dimethylquinquethiophenes (DM5Ts*, Fig. 5.1(b)) on Pt surface was used as a model sample. The structures and the electrical properties of the film were so far investigated by Umeda *et al.* using Kelvin probe force microscopy (KFM).[241] They found that the deposited molecules show

*DM5T is currently referred to as methylquinquethiophene (M5T)

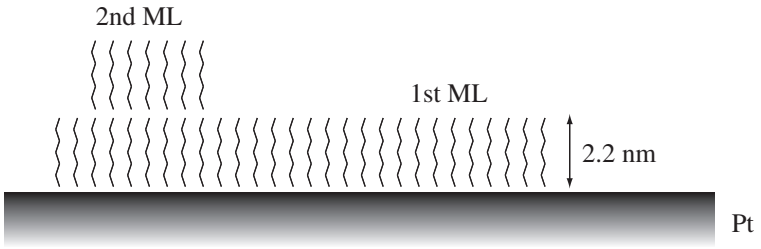

Figure 5.2: A schematic model of the DM5T monolayer deposited on Pt surface.

a typical layer-by-layer growth on the Pt surface making up some micrometer-scale monolayer islands (Fig. 5.2). The surface potential of the monolayer was estimated to be about 200 mV higher than that of the Pt substrate. Although the origin of the observed potential difference still remains unclear, the authors suggested the existence of charge transfer between the molecules and the Pt substrate.

While the DM5T monolayer on Pt surface can serve as an excellent model sample for the studies on molecule/metal interface, it is also convenient for the DFM studies on electrical tip-sample interactions. The monolayer islands have so large lateral dimensions compared to the tip radius that the influence from both the thermal drift and the tip geometry can be readily eliminated, which significantly improves reproducibility of the force spectroscopy experiments. Due to the large surface potential difference between the monolayer and the substrate, the influence of electrical tip-sample interaction on the dissipation signal is directly visualized in the dissipation image as a contrast variation.

5.3.2 Sample Preparation

The molecules used in this experiment were dimethylquinquethiophenes (DM5Ts), which were synthesized and provided by Hotta (Inst. Research and Innovation, Kashiwa, Japan). Pt film (thickness: 200 nm) was deposited on the SiO_2/Si(100) substrate by RF magnetron sputtering. The sample was then transferred into the vacuum deposition chamber through the air and annealed at 200°C for 1 h in order to reduce the surface contamination and water molecules. The DM5T monolayer was deposited onto the Pt surface by vacuum deposition at a substrate temperature of 80°C. The deposition rate was controlled to be 0.1 nm/min using a quartz oscillator. The vacuum pressure during the film deposition was maintained under 1×10^{-4} Pa. Immediately after the deposition, the sample was transferred from the deposition chamber to the UHV-FM-DFM chamber through the air.

5.3.3 Results and Discussion

Quadratic Bias Dependence Curve

Figure 5.3 shows a typical bias voltage ($V_{\rm bias}$) dependence of Δf and energy dissipation induced by the tip-sample interaction ($P_{\rm ts}$). The $\Delta f - V_{\rm bias}$ curve showed quadratic dependence on $V_{\rm bias}$, reflecting the following relationship between the electrostatic force ($F_{\rm es}$) and $V_{\rm bias}$,

$$F_{\rm es} = \frac{1}{2}\frac{\partial C_{\rm ts}}{\partial z_{\rm t}}(V_{\rm bias} + V_{\rm CPD})^2, \tag{5.1}$$

where $C_{\rm ts}$, $z_{\rm t}$ and $V_{\rm CPD}$ denote the capacitance between the tip and the sample, the tip position with respect to the surface and the tip-sample contact potential difference (CPD), respectively.

The $P_{\rm ts} - V_{\rm bias}$ curve revealed that $P_{\rm ts}$ contains a component which shows quadratic bias dependence ($P_{\rm ts2}$), which is given by

$$P_{\rm ts2} = K_2 V_{\rm ts}^2, \tag{5.2}$$

where $V_{\rm ts}$ is the tip-sample potential difference while K_2 is a constant. Although this quadratic bias dependence of $P_{\rm ts}$ is well recognized, a comprehensive understanding of its origin has not been achieved yet.

Effect of Joule Dissipation

When the cantilever is oscillated near the surface, $C_{\rm ts}$ varies depending on the tip position. This capacitance modulation induces the displacement current ($i_{\rm d}$) flowing between the tip and the sample through the bias electronic circuit, which is given by

$$i_{\rm d} = \frac{{\rm d}C_{\rm ts}}{{\rm d}t}V_{\rm ts} = \frac{\partial C_{\rm ts}}{\partial z_{\rm t}}\frac{{\rm d}z_{\rm t}}{{\rm d}t}V_{\rm ts}. \tag{5.3}$$

Thus the Joule dissipation induced by $i_{\rm d}$ ($P_{\rm tsJ}$) is given by

$$P_{\rm tsJ} = R_{\rm e} i_{\rm d}^2 = \gamma_{\rm e}\left(\frac{{\rm d}z_{\rm t}}{{\rm d}t}\right)^2, \tag{5.4}$$

$$\gamma_{\rm e} = R_{\rm e}\left(\frac{\partial C_{\rm ts}}{\partial z_{\rm t}}\right)^2 V_{\rm ts}^2, \tag{5.5}$$

where $R_{\rm e}$ and $\gamma_{\rm e}$ denote the effective resistance in the current path and the effective damping coefficient representing the Joule dissipation. This equation clearly shows that the Joule dissipation has quadratic dependence on $V_{\rm ts}$.

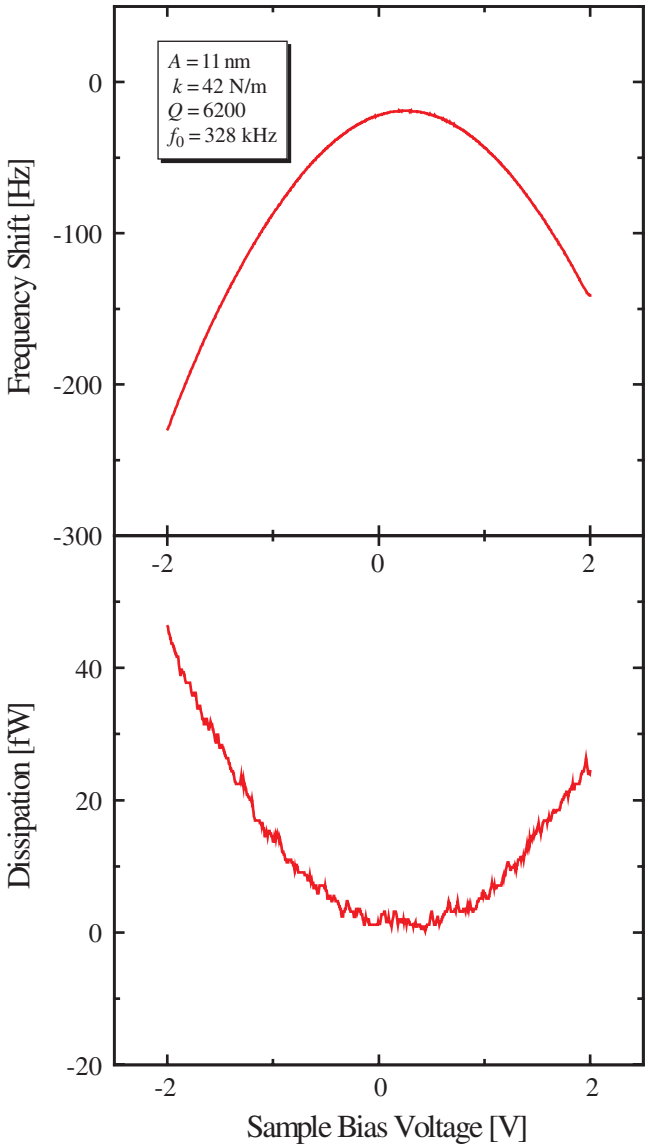

Figure 5.3: The typical bias dependence of the frequency shift and the energy dissipation taken on the Pt surface.

However, R_e for platinum is too small to explain the observed order of energy dissipation. Denk and Pohl estimated R_e by[28]

$$R_e \simeq \frac{\rho}{2\pi s}, \tag{5.6}$$

where ρ is the resistivity of the sample while s is the larger of the tip radius (R_t) and the tip-sample separation. Assuming that $s \simeq R_t = 30$ nm and $\rho \simeq 1 \times 10^{-7}$ Ωm (for platinum), R_e is estimated to be 0.53 Ω. For a hemispherical tip and $R_t \gg z_t$,

$$\frac{\partial C_{ts}}{\partial z_t} = \frac{2\pi\varepsilon_0 R_t}{z_t}, \tag{5.7}$$

where, ε_0 is the dielectric constant in vacuum. If the velocity of the tip is assumed to be $A\omega/\sqrt{2}$, the value for P_{tsJ} at $V_{ts} = 1$ V is in the order of 10^{-25} W, which is much smaller than the observed dissipation. Conversely, if P_{tsJ} is assumed to be 10^{-15} W, the corresponding value for R_e becomes about 10^{11} Ω. Although Eq. (5.6) may be oversimplified, the discrepancy between the theoretical expectation and the experimental result is too large to confirm that the Joule dissipation mechanism is main cause of the observed quadratic bias dependence of P_{ts}.

Effect of Phase Error

So far, Loppacher *et al.* reported a similar quadratic $P_{ts} - V_{bias}$ curve measured on the Cu(111) surface.[89] In addition, they pointed out that the optimal phase (ϕ_{opt}) of the tip oscillation with respect to the excitation voltage also showed quadratic bias dependence, where ϕ_{opt} is defined as the phase (ϕ in Fig. 2.10) which makes excitation amplitude minimum.

The equation of motion for the vibrating cantilever is given by

$$m\frac{\mathrm{d}^2 z_t}{\mathrm{d}t^2} + \gamma\frac{\mathrm{d}z_t}{\mathrm{d}t} + k(z_t - z_b + d_{bt0}) = 0, \tag{5.8}$$

where m and γ are the effective mass and the damping coefficient of the cantilever, respectively. d_{bt0} denotes the mean distance between the tip and the cantilever base. z_b represents the position of the cantilever base. In FM-DFM, the phase difference between the cantilever oscillation and the excitation (ϕ) is continuously kept at $-90°$. Provided that the electrical interaction somehow causes some phase error (ϕ_e) in the phase feedback circuit (i.e., the self-excitation circuit), z_b and z_t can be described by

$$z_b = z_{b0} + A_b\cos(\omega t), \tag{5.9}$$

$$z_t = z_{t0} + A\sin(\omega t + \phi_e), \tag{5.10}$$

where, z_{b0} and z_{t0} are the mean position of the cantilever base and the tip, respectively. A_b denotes the vibration amplitude of the cantilever base. From Eq. (5.8), (5.9), (5.10), $\gamma = m\omega_0/Q$ and $k = m\omega_0^2$,

$$\omega \simeq \left(1 - \frac{\phi_e}{2Q}\right)\omega_0, \tag{5.11}$$

$$A_b \simeq (\phi_e^2 + 1)A_{b,0}, \tag{5.12}$$

where $A_{b,0}$ is the vibration amplitude of the cantilever base at $\phi_e = 0$ and given by $A_{b,0} = A/Q$. Here, the approximations of $\sin(\phi_e) \simeq \phi_e$ and $\cos(\phi_e) \simeq 1$ were employed. Therefore, from Eq. (2.44), (5.12) and $V_{exc}/V_{exc,0} = A_b/A_{b,0}$, the apparent dissipation due to the phase error (P_{tsp}) is described by

$$P_{tsp} = P_0\phi_e^2, \tag{5.13}$$

where P_0 is the intrinsic energy dissipation of the cantilever. Eq. (5.13) clearly confirmed that the dissipation signal has quadratic dependence on ϕ_e. From Fig. 5.3, $P_{ts} \simeq 10$ fW at $V_{ts} = 1$ V. Assuming that the observed dissipation is given by Eq. (5.13), the corresponding value for ϕ_e becomes about 6°. On the other hand, the deviation of ϕ_{opt} at $V_{ts} = 1$ V reported by Loppacher *et al.*[89] was about 1°. Thus the observed dissipation seems to be too large to be explained by such a phase error. In addition, the correlation between ϕ_e and V_{bias} has not be clarified yet. So far, Loppacher *et al.* tentatively attributed the observed bias dependence of ϕ_{opt} to the creation of dissipating currents in the silicon tip.[89] Nevertheless, they presented neither an experimental evidence nor a theoretical explanation for such a correlation between the dissipating current and the phase error.

One of the possible origins for the phase error is the frequency dependent change of the phase delay at the photo detector (ϕ_{pd} in Fig. 2.17). Since the bandwidth of the typical photo detection system is so narrow that the gain and the phase delay at the photo detector shows strong dependence on the frequency deviation around the cantilever resonance (typically 300 kHz). Thus the bias dependent change of the cantilever resonance frequency may induce a bias dependent phase error.

Bias Dependence Curve with Double Minimum Peaks

$P_{ts} - V_{bias}$ curve occasionally showed an extraordinary shape as shown in Fig. 5.4 although the simultaneously obtained $\Delta f - V_{bias}$ curve showed a typical quadratic dependence. First, the curve had double minimum peaks, which is clearly different from the quadratic dependence shown in Fig. 5.3. Secondly, the value was negative, which means the excitation amplitude was decreased when the tip approached the

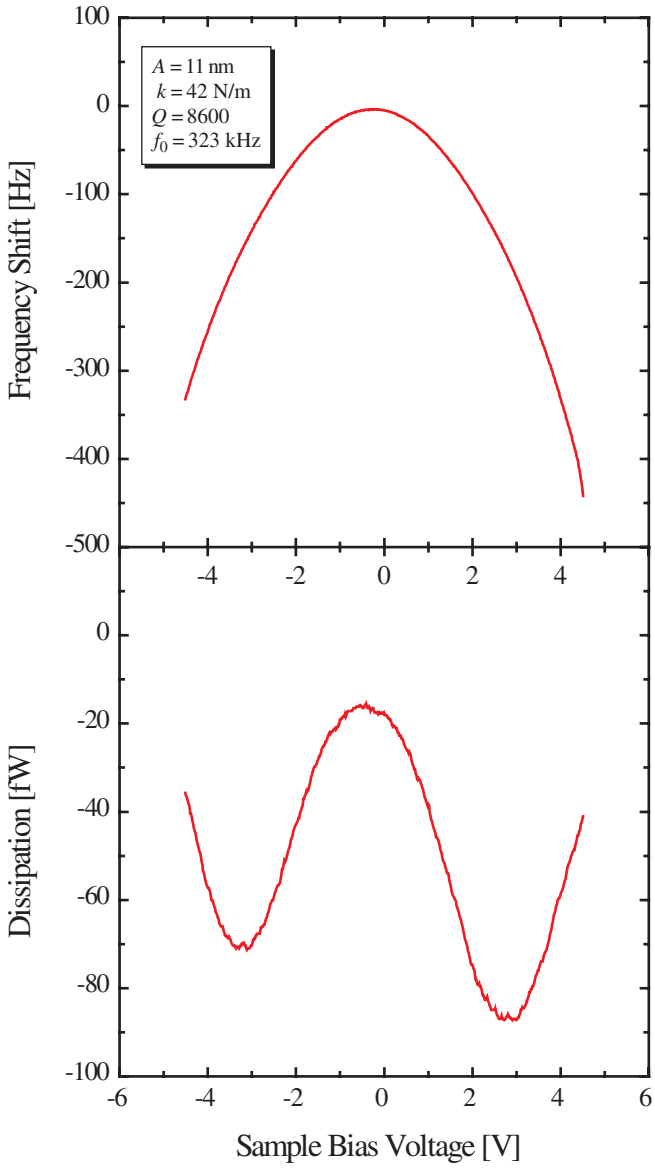

Figure 5.4: The extraordinary type bias dependence of the frequency shift and the energy dissipation taken on the Pt surface.

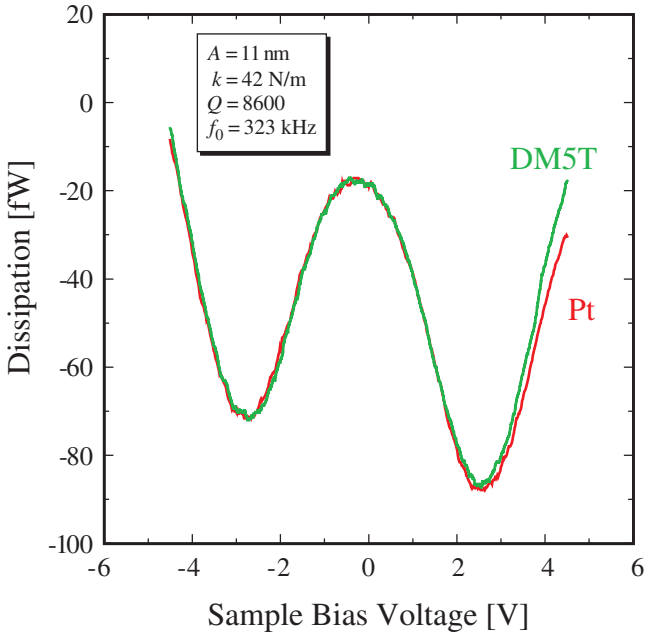

Figure 5.5: The extraordinary type bias dependence curves measured on the DM5T monolayer and the Pt surface.

surface. Thirdly, the shape was asymmetrical to the peak position of the $\Delta f - V_{\mathrm{bias}}$ curve (namely, V_{CPD}).

The curves shown in Fig. 5.3 and Fig. 5.4 were measured on the same sample but with the different cantilevers. The bias dependence curves measured on Pt surface and DM5T monolayer showed no significant difference as shown in Fig. 5.5. Thus the local conductance variation of the surface is not likely to be the predominant cause of the difference between the bias curves shown in Fig. 5.3 and Fig. 5.4.

Figure. 5.6 shows a series of $P_{\mathrm{ts}} - V_{\mathrm{bias}}$ curves measured on the Pt surface with different tip-sample separation. The frequency shift indicated in the figure are the value measured at the zero bias voltage. Although the bias dependence becomes week with increasing tip-sample distance, the double peak shape was not transformed into the quadratic type dependence. Thus the difference of $P_{\mathrm{ts}} - V_{\mathrm{bias}}$ curves shown in Fig. 5.3 and Fig. 5.4 is not ascribed to the difference in the tip-sample distance. The curve measured about 310 nm above the surface clearly revealed an asymmetric feature with respect to V_{CPD}, suggesting the electrical interaction force causing the asymmetry should has an extremely long interaction range. However, the curve measured on 715 nm above the surface no longer showed any bias dependence.

These all results suggested that the difference in the cantilever parameters plays an important role in determining the shape of $P_{\mathrm{ts}} - V_{\mathrm{bias}}$ curve. However, further

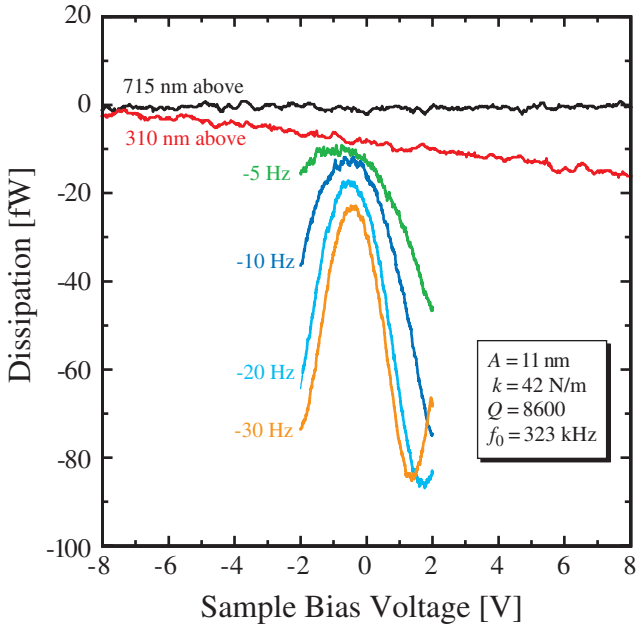

Figure 5.6: The frequency shift dependence of the bias dependence curve of energy dissipation measured on the Pt surface.

studies are required to elucidate the relationship between the tip conditions and $P_{\rm ts} - V_{\rm bias}$ curve.

Bias Dependence of Interaction Potential

In order to obtain a more detailed insight into the cantilever motion, the potential of the interaction force acting on the tip was calculated as a function of the tip position. The total energy of the vibrating cantilever under the tip-sample interaction (E) is given by

$$E = K + U. \tag{5.14}$$

$$= K + U_{\rm res} + U_{\rm ts}. \tag{5.15}$$

K, $U_{\rm res}$ and $U_{\rm ts}$ are the kinetic energy of the cantilever, the potential of the restoring force of the cantilever spring, and the potential of the tip-sample interaction force, respectively. K and $U_{\rm res}$ are described by

$$K = \frac{1}{2} m \left(\frac{{\rm d}z_{\rm t}}{{\rm d}t} \right)^2. \tag{5.16}$$

$$U_{\rm res} = \frac{1}{2} k (z_{\rm t} - z_{\rm t0})^2. \tag{5.17}$$

Assuming that the tip-sample interaction is purely conservative and the force potential is comprised of the contributions from van der Waals interaction ($U_{\rm vdW}$),

electrostatic interaction ($U_{\rm es}$) and chemical interaction ($U_{\rm chem}$), $U_{\rm ts}$ is given by

$$\begin{aligned} U_{\rm ts} &= U_{\rm vdW} + U_{\rm es} + U_{\rm chem} \\ &= -\frac{A_{\rm H} R_{\rm t}}{6 z_{\rm t}} - \frac{1}{2} C_{\rm ts} V_{\rm ts}^2 - E_{\rm bond} \left[2 \left(\frac{\sigma}{z_{\rm t}} \right)^6 - \left(\frac{\sigma}{z_{\rm t}} \right)^{12} \right]. \end{aligned} \tag{5.18}$$

$A_{\rm H}$, $E_{\rm bond}$ and σ are the Hamaker constant, the bonding energy of the tip atom and the surface atom, and the equilibrium inter-atomic distance of them, respectively. $C_{\rm ts}$ is the capacitance between the tip and the sample, and given by

$$C_{\rm ts} = 4\pi\varepsilon_0 R_{\rm t} \sum_{n=1}^{\infty} \left[\frac{\sinh(\alpha)}{\sinh(n\alpha)} \right], \tag{5.19}$$

where ε_0 is the dielectric constant in vacuum and α is defined as $\cosh(\alpha) = (1 + z_{\rm t}/R_{\rm t})$.

Figure 5.7 shows the calculated force potential with the bias voltage of 0 V and 4 V. The parameters used in this calculation were $k = 40$ N/m, $z_{\rm t0} = 11$ nm, $A_{\rm H} = 4 \times 10^{-19}$ J, $R_{\rm t} = 30$ nm, $E_{\rm bond} = 2.0$ eV and $\sigma = 0.28$ nm. This result clearly showed that the quadratic interaction potential of the cantilever spring is negatively displaced by the long-range electrostatic interaction. Provided that the vibration is purely sinusoidal, the kinetic energy corresponding to the cantilever vibration of $A = 10.00$ nm becomes $K = 2.0$ fJ. According to the results shown in Fig. 5.7, this magnitude of kinetic energy will result in the vibration amplitude of 10.00 nm and 10.14 nm when $V_{\rm bias} = 0$ V and 4 V, respectively. This means that the amplitude can be magnified by the attractive tip-sample interaction potential in constant excitation mode whereas in constant amplitude mode, $V_{\rm exc}$ is reduced and hence the apparent value for the dissipation becomes negative. Since the magnitude of amplitude increase due to the electrostatic interaction was estimated to be about 1.4%, it can be readily detected by an ordinary experimental setup and hence it can affect the excitation amplitude in constant amplitude mode. In the $P_{\rm ts} - V_{\rm bias}$ curve shown in Fig. 5.4, the value for the dissipation was negative and it was more and more reduced with increasing $V_{\rm ts}$ around $V_{\rm CPD}$. This tendency is quite consistent with the result obtained in this calculation. However, it should be noted that this phenomenon is induced by the completely conservative interaction and no energy is dissipated. Thus such an "apparent dissipation" has to be discriminated from the "true dissipation" induced by the dissipative tip-sample interactions.

Bias Resistance Dependence of Dissipation Image

The highly-doped Si cantilever is most frequently used in FM-DFM experiments (Fig. 5.8(a)). Although the nominal resistivity of the cantilever is typically as low

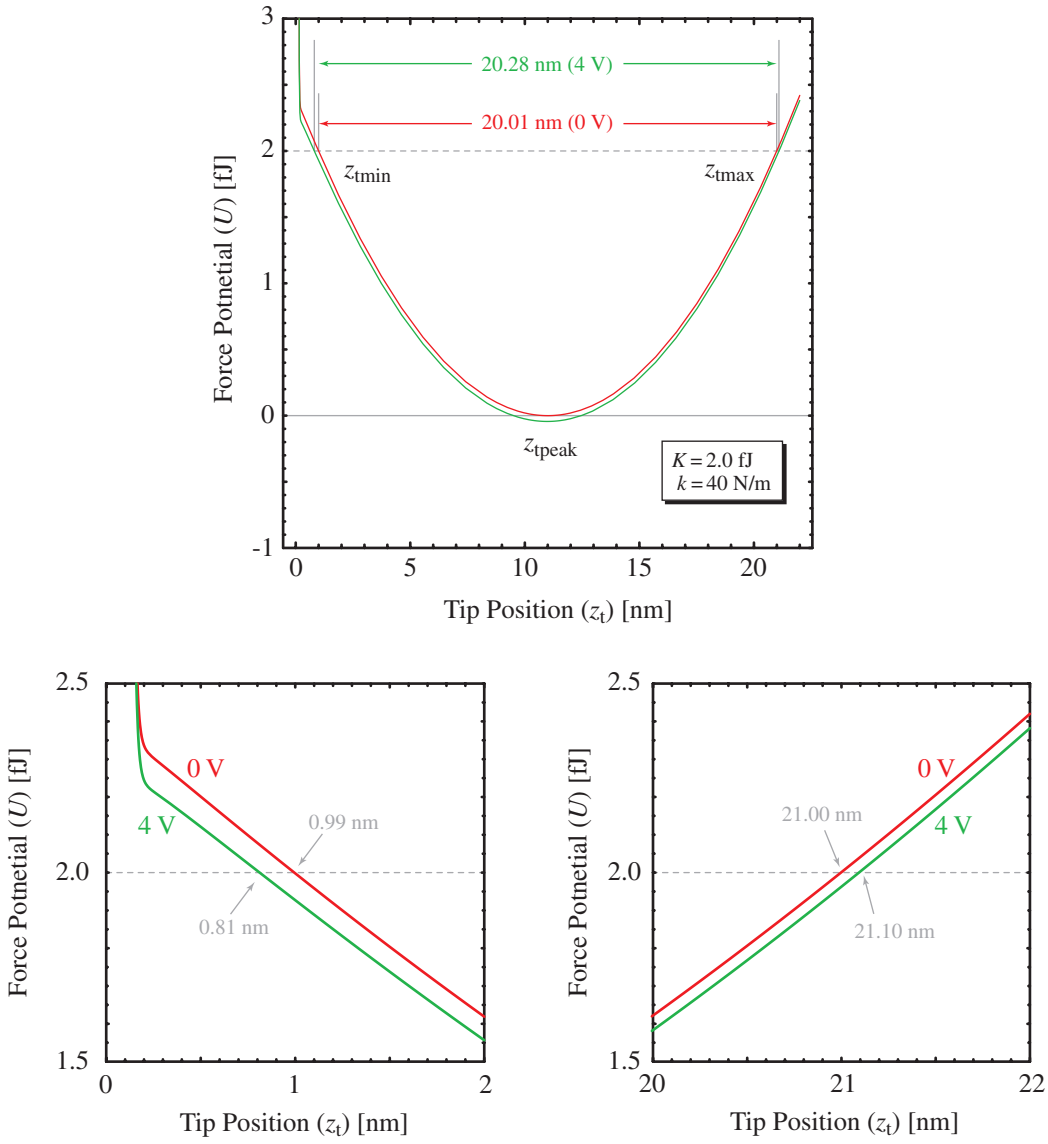

(unit: nm)	A	z_{tmin}	z_{tmax}	z_{tpeak}	$z_{t0}=(z_{tmax}+z_{tmin})/2$	$\delta z_t = z_{tpeak} - z_{t0}$
0 V	10.0026	0.994974	21.0002	10.9996	10.9976	0.002013
4 V	10.1417	0.812756	21.0961	10.9779	10.9544	0.023472

Figure 5.7: The calculated potentials of the interaction force acting on the tip when the sample is biased at 0 V and 4 V. It was assumed that the potential is comprised of van der Waals interaction, electrostatic interaction and chemical interaction. The table shows minimum (z_{tmin}) and maximum (z_{tmax}) tip position, the vibration amplitude (A), the minimum peak position (z_{tpeak}), the mean tip position (z_{t0}), and the difference between z_{tpeak} and z_{t0} (δz_t).

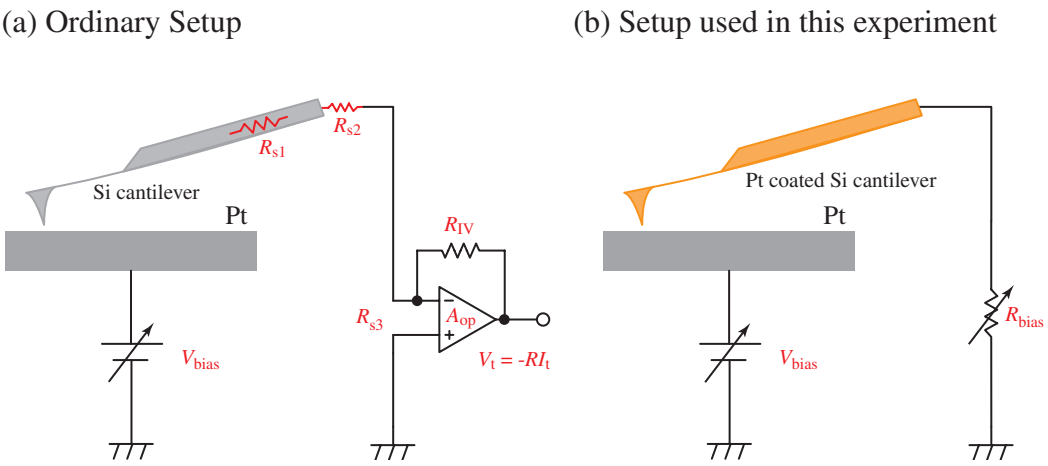

Figure 5.8: Schematic drawings of the electrical connection in the experimental setup. (a) In the most commonly used FM-DFM setup, the cantilever is made of highly-doped Si and a current-voltage converter is inserted into the bias line, leading to the additional stray resistance ($R_s = R_{s1} + R_{s2} + R_{s3}$). (b) In the setup used in this experiment, R_s was suppressed using Pt-coated cantilever. Instead, the bias resistance (R_{bias}) was intentionally inserted to examine the effect of the stray resistance on the energy dissipation signal.

as 0.01 – 0.025 Ωcm, the effective resistance (R_{s1}) from the tip apex to the cantilever base may amount to a certain extent because of its extremely small dimension. In addition, the contact resistance (R_{s2}) between the cantilever base and the adjacent electrode connected to the electrical earth is not necessarily negligible due to the existence of the oxide layer and other unexpected contamination layers. The experimentally measured value for the resistance between the cantilever base and the electrode contacted on it was 10 – 100 kΩ. More importantly, a current-voltage (I-V) converter is often inserted into the bias line which makes electrical connection between the tip and the ground to allow the simultaneous detection of the tunneling current and the tip-sample interaction force. This I-V converter can work as an effective resistance (R_{s3}) unless the open loop gain (A_{op}) of the operational amplifier is large enough to keep the error at the differential inputs negligible. Assuming that the value for the resistance used in the I-V converter is R_{IV}, the effective resistance is given by $R_{s3} = R_{IV}/(1 + A_{op})$. The value for R_{IV} is typically as large as 10^7 – 10^9 Ω. Thus, in order to suppress R_{s3} (for example) less than 1 kΩ, A_{op} has to be much larger than 10^4 – 10^6. It is rather difficult to meet this condition especially when the input current varies as fast as the cantilever vibration (i.e. about 300 kHz).

In this experiment, to examine the effect of these stray resistance ($R_s = R_{s1} + R_{s2} + R_{s3}$) on energy dissipation signal, some modifications were made in

the experimental setup (Fig. 5.8(b)). Firstly, the Pt-coated Si cantilever was used to suppress R_{s1} and R_{s2}. In this case, the resistance between the cantilever base and the adjacent electrode was 10 – 100 Ω, which is smaller than the value for the highly-doped Si cantilever by a factor of a thousand. Secondly, the I-V converter was removed to eliminate R_{s3}. And finally, the bias resistance R_{bias} was intentionally inserted into the bias line. The value of R_{bias} was varied by a mechanical switch in order to avoid the inductive response of a variable resistor. Then the dissipation images and the bias dependence curves were measured with different bias resistance.

As pointed out above, the bias dependence of the energy dissipation is very sensitive to the tip conditions although the mechanism is still unclear. Thus, all the experiments described hereafter in this section were performed with the same cantilever and with the same sample. The vibration amplitude A was continuously kept constant at $A = 11$ $\mathrm{nm_{p-p}}$. The resonance frequency and Q-factor measured far away from the sample surface were 328 kHz and 6,200, respectively. The nominal spring constant was 42 N/m. The dissipation images were taken at $\Delta f = -25 \pm 5$ Hz. The measurements of the bias dependent curves were performed at a tip position where $\Delta f = -22$ Hz with the sample electrically grounded.

To begin with, the surface potential distribution of the DM5T monolayer was measured by FM-KFM in order to know the potential relationship between the tip and the sample surface. Figure 5.9(a) shows an FM-DFM image of the DM5T monolayer, showing the first and the second molecular layer (ML) as well as the Pt substrate. Figure 5.9(b) shows a surface potential image taken simultaneously with the topographic image shown in Fig. 5.9(a). The potential diagram shown in Fig. 5.9(c) was estimated from this potential image. The surface potential of the first ML and that of the Pt substrate with respect to the tip potential were about −50 mV and −240 mV, respectively. Thus the monolayer/substrate potential difference was 190 mV, which well agreed with the previously reported value.[241]

Figures 5.10(a)–(c) show dissipation images taken on the same area as shown in Fig. 5.9 with different R_{bias} of 0 Ω, 10 kΩ and 20 kΩ, respectively, with the sample electrically grounded. No evident contrast was found in the dissipation image taken with R_{bias} of 0 Ω (Fig. 5.10(a)). The dissipation contrast between the DM5T monolayer and the Pt substrate increased with the increase of R_{bias} (Figs. 5.10(b), (c)). Figure 5.10(d) shows R_{bias} dependence of the dissipation measured on the DM5T monolayer (P_{DM5T}) and the Pt substrate (P_{Pt}), which was obtained from several dissipation images taken on the same area. This plot clearly revealed that P_{DM5T} increased with increasing R_{bias} while P_{Pt} decreased. These R_{bias} dependent variation were almost saturated over 20 kΩ. Thus it was confirmed that the bias resistance can affect the dissipation images.

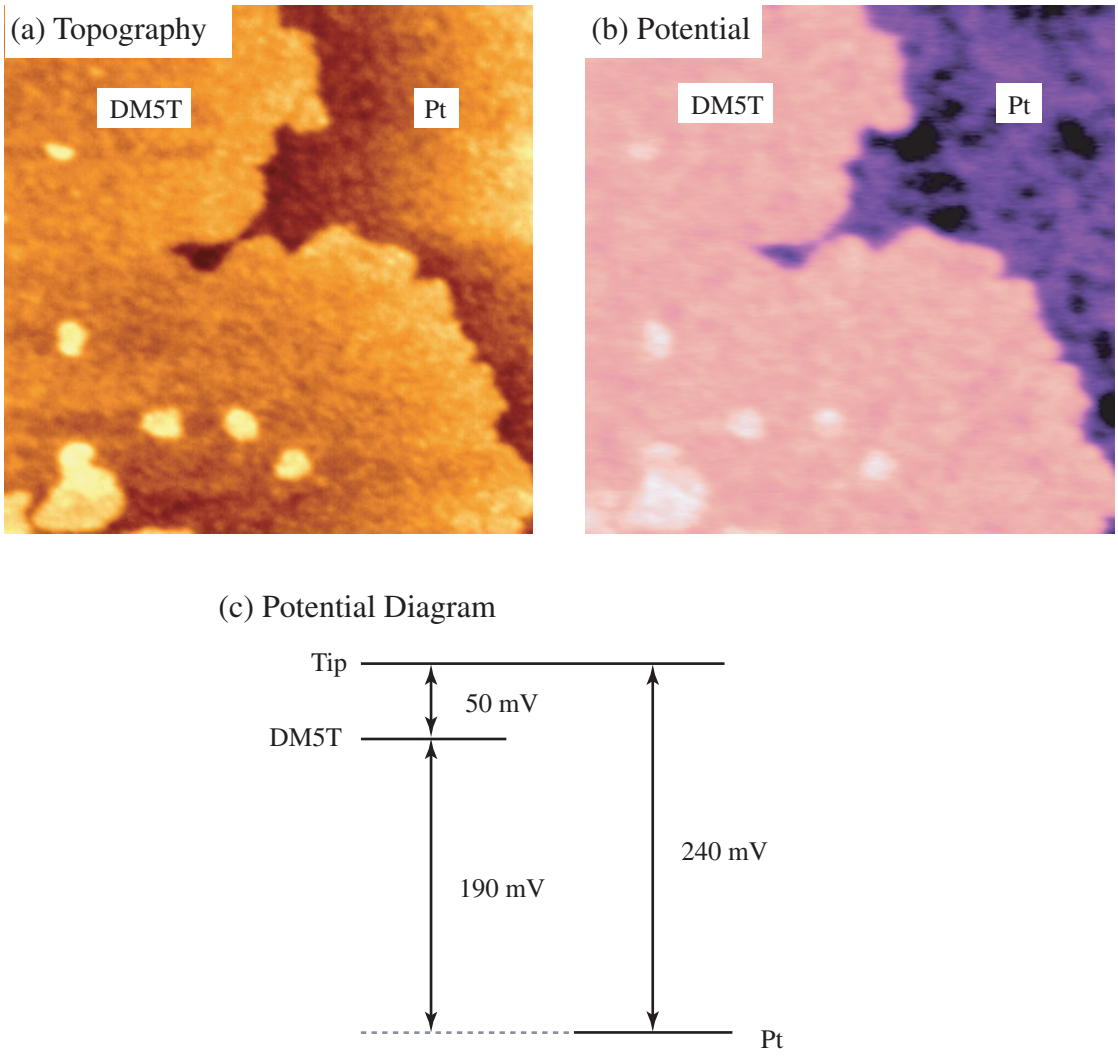

Figure 5.9: (a) Topographic and (b) surface potential images of the DM5T monolayer on the Pt surface (2 μm $\times$ 2 μm). (c) Potential diagram estimated from (b).

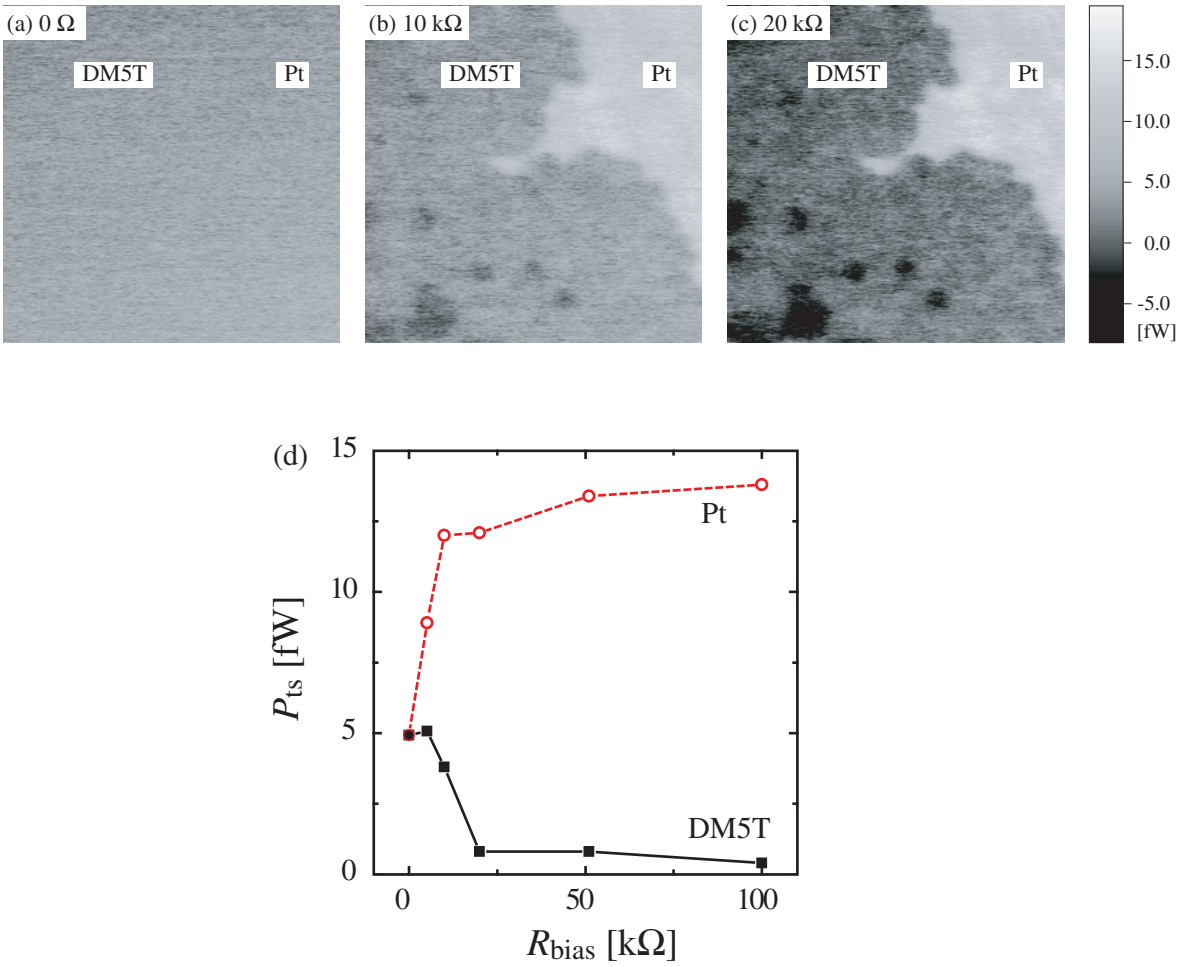

Figure 5.10: (a)–(c) Dissipation images of the DM5T monolayer on the Pt surface taken on the same area as shown in Fig. 5.9 with R_{bias} of (a) 0 Ω, (b) 10 kΩ and (c) 20 kΩ, respectively (2 μm × 2 μm). All the dissipation images were taken with the sample electrically grounded. (d) R_{bias} dependence of the dissipation on the DM5T monolayer and on the Pt substrate, which was obtained from several dissipation images taken on the same area.

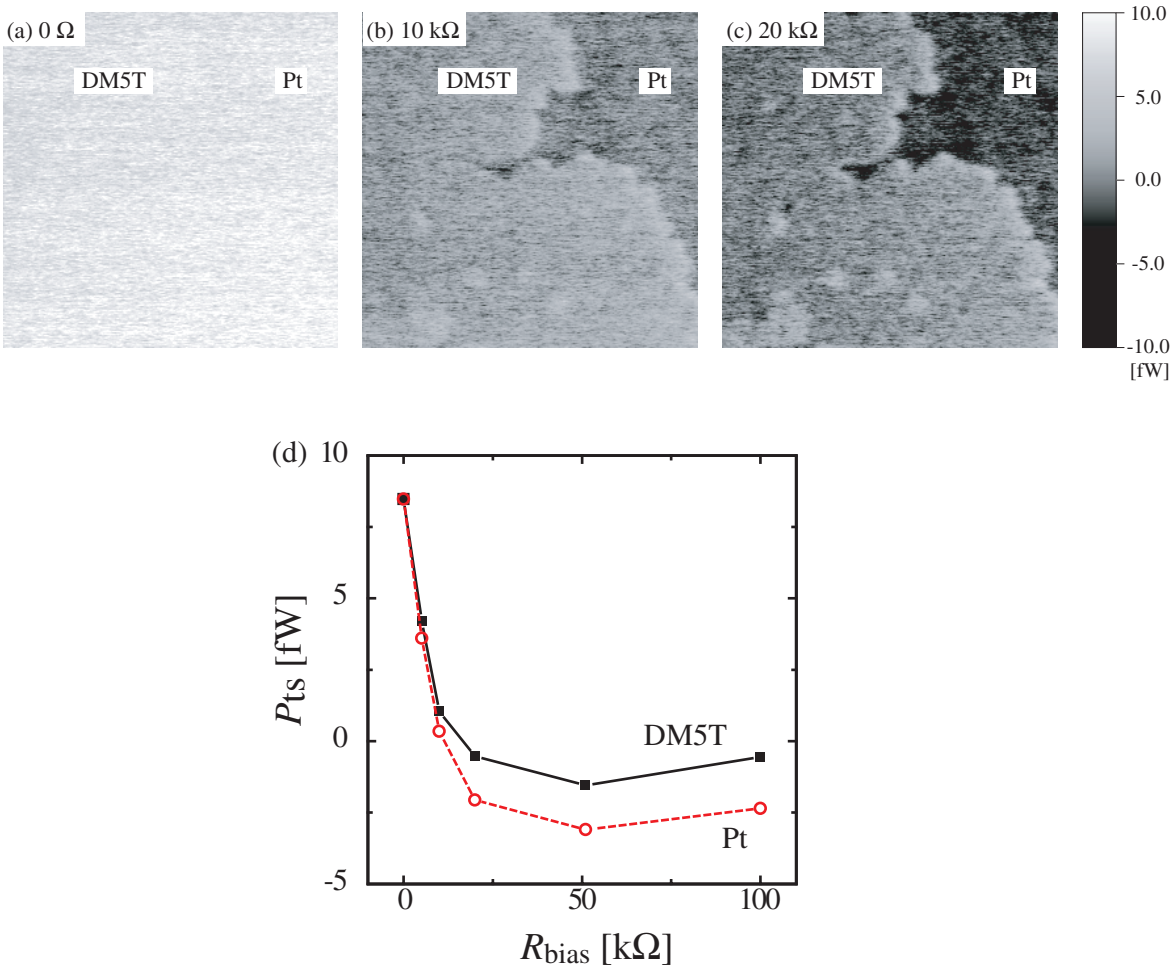

Figure 5.11: (a)–(c) Dissipation images of the DM5T monolayer on the Pt surface taken on the same area as shown in Fig. 5.9 with R_{bias} of (a) 0 Ω, (b) 10 kΩ and (c) 20 kΩ, respectively (2 μm × 2 μm). The dc tip-sample potential difference was compensated by KFM bias feedback regulation during the dissipation imaging. (d) R_{bias} dependence of the dissipation on the DM5T monolayer and on the Pt substrate, which was obtained from several dissipation images taken on the same area.

If the dissipation contrast between the DM5T monolayer and the Pt surface was originated from the potential difference between them, it may be canceled out by compensating the dc part of $V_{\rm ts}$ using KFM bias feedback regulation. In order to examine this possibility, dissipation images were taken with different $R_{\rm bias}$ under the KFM bias regulation as shown in Fig. 5.11(a)–(c). The dissipation images showed clear contrasts when $R_{\rm bias}$ was inserted (Figs. 5.11(b),(c)). Figure 5.11(d) shows $R_{\rm bias}$ dependence of $P_{\rm Pt}$ and $P_{\rm DM5T}$, which was obtained from several dissipation images taken on the same area. Both $P_{\rm Pt}$ and $P_{\rm DM5T}$ decreased as $R_{\rm bias}$ increased. Although the dissipation difference was obviously suppressed with KFM bias feedback (Figs. 5.10(d) and 5.11(d)), it could not be completely compensated. The observed dissipation variation might be caused by the remaining ac bias modulation voltage. In this experiment, the bias modulation frequency (2 kHz) was much smaller than that of the cantilever vibration (328 kHz). Thus, the ac bias modulation voltage might equivalently work as a dc potential difference on the vibrating cantilever. Thus the observed dissipation can be regarded as an averaged dissipation over the $V_{\rm bias}$ range from $V_{\rm CPD}-1$ V to $V_{\rm CPD}+1$ V.

Bias Resistance Dependence of Bias Curve

In order to examine the origin of the $R_{\rm bias}$ dependence shown in Figs. 5.10 and 5.11, $R_{\rm bias}$ dependence of $\Delta f - V_{\rm bias}$ curve and $P_{\rm ts} - V_{\rm bias}$ curve was investigated on both the Pt surface (Fig. 5.12(a)) and the DM5T monolayer (Fig. 5.12(b)). The $\Delta f - V_{\rm bias}$ curve and the $P_{\rm ts} - V_{\rm bias}$ curve were simultaneously measured for each $R_{\rm bias}$. Both of Δf and $P_{\rm ts}$ showed quadratic dependence on $V_{\rm bias}$. The peak position of the $P_{\rm ts} - V_{\rm bias}$ curve showed strong dependence on $R_{\rm bias}$ while the $\Delta f - V_{\rm bias}$ curve showed no dependence on $R_{\rm bias}$. Note that the $\Delta f - V_{\rm bias}$ curves corresponding to the three $R_{\rm bias}$ values are plotted at almost the same position in Figs. 5.12(a) and (b).

$V_{\rm bias}$ at the peak position of the $\Delta f - V_{\rm bias}$ curve was estimated to be 260 mV on the Pt substrate and 48 mV on the DM5T monolayer. Since the Pt substrate used in this experiment had some potential distribution due to the incomplete uniformity (Fig. 5.9), the estimated peak bias voltage showed slight deviation from the value obtained from KFM measurements on the Pt substrate. It was confirmed that the potential distribution measured by KFM does not depend on $R_{\rm bias}$ because the $\Delta f - V_{\rm bias}$ curves did not show any dependence on $R_{\rm bias}$.

In order to know the detailed behavior around $V_{\rm bias} = 0$ V, each of the $P_{\rm ts} - V_{\rm bias}$ curves was fitted as a quadratic function and plotted on a smaller scale (Figs. 5.12(c) and (d)). These profiles revealed that the dissipation at $V_{\rm bias} = 0$ V increases on the Pt substrate and decreases on the DM5T monolayer as $R_{\rm bias}$ increases, which

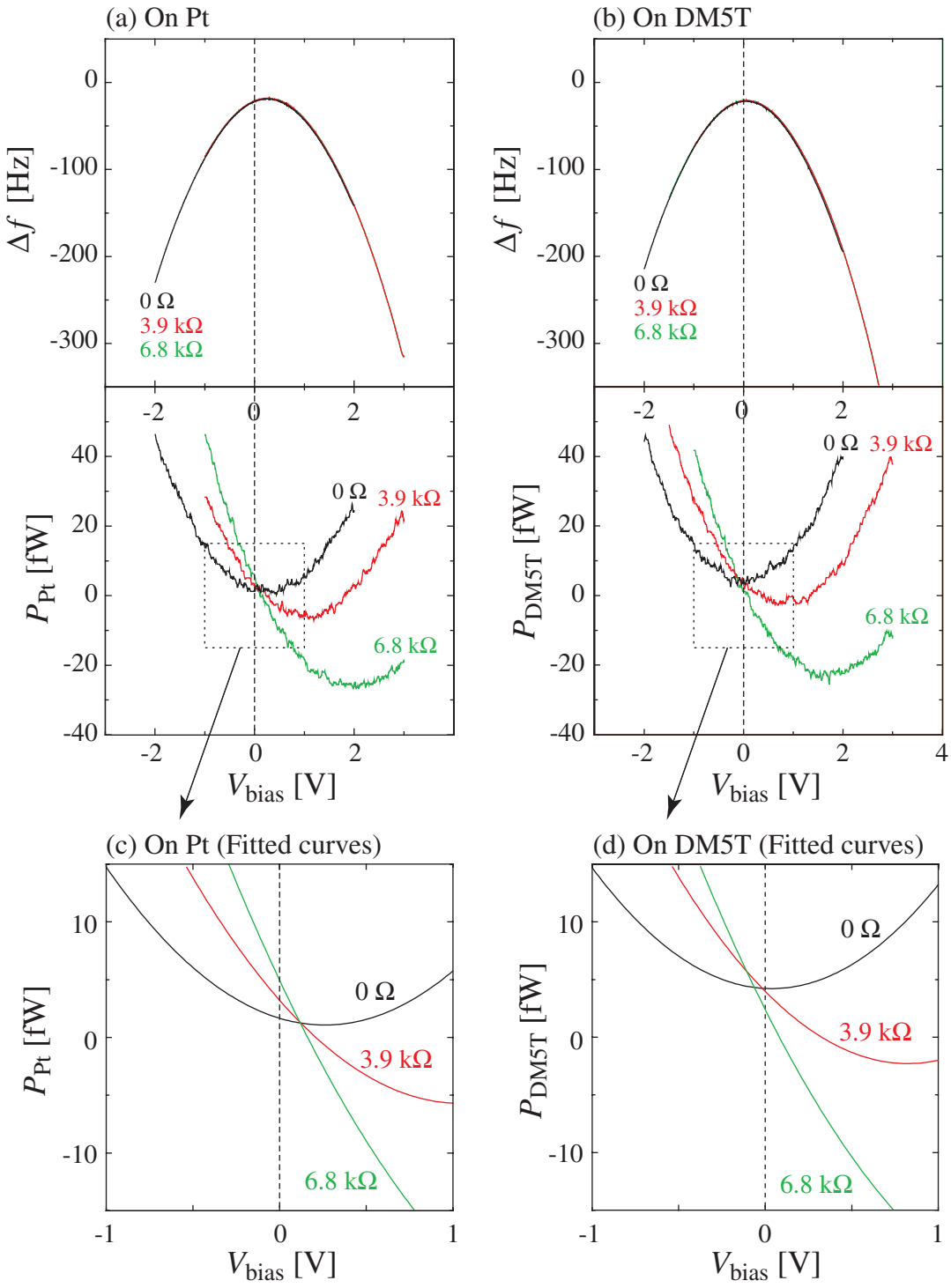

Figure 5.12: Bias dependence of Δf and P_{ts} measured on (a) the Pt substrate and (b) the DM5T monolayer. Measurements were performed with different R_{bias} of 0 Ω, 3.9 kΩ and 6.8 kΩ. Each of the profiles shown in (a) and (b) was fitted as a quadratic function and plotted on a smaller scale as shown in (c) and (d), respectively.

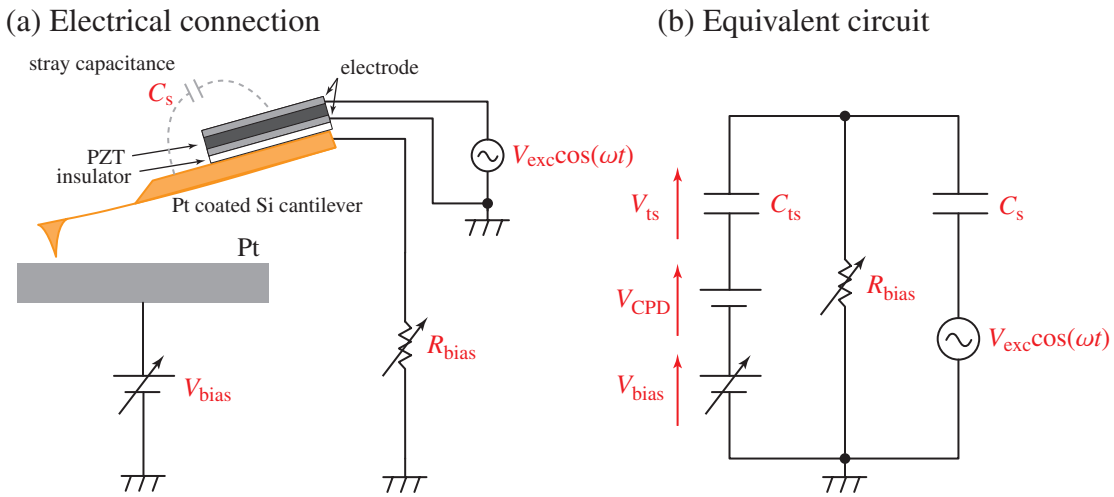

Figure 5.13: Schematic drawings of (a) the electrical connection in FM-DFM setup and (b) its equivalent circuit. The stray capacitance (C_s) may exist between the cantilever base and the electrode of the PZT actuator.

clearly explained the R_{bias} dependence of the dissipation images shown in Fig. 5.10. On the other hand, P_{ts} measured with KFM bias feedback reflects the averaged dissipation over the V_{bias} range of $(V_{CPD} \pm 1)$ V. The profiles shown in Figs. 5.12(c) and (d) revealed that the averaged dissipation decreases with increase of R_{bias}, which is consistent with the R_{bias} dependence shown in Fig. 5.11. The difference between the dissipation measured on the Pt substrate and that on the DM5T monolayer might be ascribed to the difference in the tip-substrate distance.

Effect of Stray Capacitance

In the actual experimental setup, the cantilever is mechanically oscillated by the adjacent PZT actuator driven by the excitation voltage of $V_{exc}\cos(\omega t)$ as shown in Fig. 5.13(a). This excitation signal can affect V_{ts} if the stray capacitance (C_s) between the electrode and the cantilever base or other part of the bias line cannot be neglected. Taking account of this capacitance, the equivalent circuit of the setup is depicted as shown in Fig. 5.13(b). The current from the voltage source of the excitation signal is mostly flowing through the R_{bias} because usually $R_{bias} \ll 1/(\omega C_{ts})$. Thus V_{ts} is described by

$$V_{ts} = G(\omega)V_{exc}\cos(\omega t) - V_{dc}, \tag{5.20}$$

$$V_{dc} = V_{bias} + V_{CPD}, \tag{5.21}$$

where $G(\omega)$ is the transfer function of the RC circuit. The phasor representation of $G(\omega)$ is given by,

$$G(\omega) = \frac{(\omega C_{\rm ts} R_{\rm bias})^2}{1+(\omega C_{\rm ts} R_{\rm bias})^2}\left(1+i\frac{1}{\omega C_{\rm ts} R_{\rm bias}}\right), \tag{5.22}$$

$$\equiv \Re e[G(\omega)] + i\Im m[G(\omega)] \tag{5.23}$$

Thus the electrostatic force acting between the tip and the sample ($F_{\rm es}$) is described by

$$F_{\rm es} = \frac{1}{2}\frac{\partial C_{\rm ts}}{\partial z_{\rm t}}\left\{G(\omega)V_{\rm exc}\cos(\omega t) - V_{\rm dc}\right\}^2. \tag{5.24}$$

Assuming $R_{\rm t} \gg z_{\rm t}$ and $z_{\rm t0} \gg A$,

$$\frac{\partial C_{\rm ts}}{\partial z_{\rm t}} \simeq -\frac{2\pi\varepsilon_0 R_{\rm t}}{z_{\rm t0}}. \tag{5.25}$$

Thus the coefficients of the $\cos(\omega t)$ component ($F_{\rm esc}$) and the $\sin(\omega t)$ component ($F_{\rm ess}$) of $F_{\rm es}$ are given by

$$F_{\rm esc} \simeq \frac{2\pi\varepsilon_0 R_{\rm t}}{z_{\rm t0}} V_{\rm dc} V_{\rm exc} \Re e[G(\omega)]. \tag{5.26}$$

$$F_{\rm ess} \simeq -\frac{2\pi\varepsilon_0 R_{\rm t}}{z_{\rm t0}} V_{\rm dc} V_{\rm exc} \Im m[G(\omega)] \tag{5.27}$$

On the other hand, the equation of motion for the vibrating cantilever under the existence of $F_{\rm es}$ is given by

$$m\frac{{\rm d}^2 z_{\rm t}}{{\rm d}t^2} + \gamma\frac{{\rm d}z_{\rm t}}{{\rm d}t} + k(z_{\rm t} - z_{\rm b} + d_{\rm bt0}) = F_{\rm es}. \tag{5.28}$$

Solving this equation in terms of $\cos(\omega t)$ and $\sin(\omega t)$ components,

$$\omega \simeq \left(1 - \frac{F_{\rm ess}}{2kA}\right)\omega_0, \tag{5.29}$$

$$A_{\rm b} \simeq \left(1 - \frac{QF_{\rm esc}}{kA}\right)A_{\rm b,0} \tag{5.30}$$

From this equation and Eq. (2.44) and (5.26), the energy dissipation originated from the existence of the stray capacitance ($P_{\rm ts1}$) is given by

$$P_{\rm ts1} = P_0 K_1 V_{\rm exc} V_{\rm dc}, \tag{5.31}$$

$$K_1 = -\frac{2\pi\varepsilon_0 R_{\rm t} Q}{z_{\rm t0} kA}\Re e[G(\omega)]. \tag{5.32}$$

This equation clearly revealed the linear bias dependence of $P_{\rm ts1}$.

In addition to $P_{\rm ts1}$, there is another component which shows quadratic dependence on $V_{\rm ts}$. From, Eq. (5.2) and (5.20), the averaged value for $P_{\rm ts2}$ is given by

$$P_{\rm ts2} = P_0 K_2\left(\frac{1}{2}|G(\omega)|^2 V_{\rm exc}^2 + V_{\rm dc}^2\right) \tag{5.33}$$

Combined with Eq. (5.31), the total dissipation ($P_{\rm ts}$) is described by

$$P_{\rm ts} = P_0 \left(K_2 V_{\rm dc}^2 + K_1 V_{\rm exc} V_{\rm dc} + \frac{1}{2} K_2 |G(\omega)|^2 V_{\rm exc}^2 \right) \tag{5.34}$$

$$= P_0 \left[K_2 \left(V_{\rm dc} + \frac{K_1}{2K_2} \right)^2 + \left(\frac{1}{2} K_2 |G(\omega)|^2 - \frac{K_1^2}{4K_2} \right) V_{\rm exc}^2 \right] \tag{5.35}$$

This equation shows that the peak of the quadratic bias curve can be shifted depending on K_1. Since K_1 is directly related to $R_{\rm bias}$, this result is well consistent with the observed $R_{\rm bias}$ dependence of the bias curves (Fig. 5.12). The asymmetry of the bias dependence curves with respect to $V_{\rm CPD}$ (Fig. 5.4) can also be understood by taking account of this stray capacitance effect.

5.4 Energy Dissipation induced by Molecular Fluctuation

5.4.1 Phase-Separated SAMs of Thiols and Dithiols

Alkanedithiol SAMs on Au(111) Surfaces

Alkanethiols spontaneously form an well-ordered monolayer on the Au(111) surface (Fig. 4.21) when a gold substrate is immersed into their dilute solution. Since such a self-assembling process is mainly realized by the strong chemisorption of the thiol group on the gold surface, it was envisaged that dithiols, which have two thiol groups at the both ends of the molecular chain, may be used for the connection between two different metal surfaces.[242–249] So far, several research groups used dithiols to make connection between two nano-particles.[242–244] Others reported the multilayer structures of copper ions sandwiched between dithiol molecules.[246] Moreover, electrical conduction of the molecular wire was investigated using dithiols with an aromatic chain.[247–249]

To exploit the full potential of dithiols for such applications to molecular electronics, it is essential to know the detailed structure and the growth process of dithiol monolayers on metal surfaces. Such structural studies were performed on the various kinds of dithiols and noble metal surfaces.[246,247,250,251] Among them, the simplest example is the alkanedithiol monolayer on the Au(111) surface.[59,252–258] This system is important because it can be regarded as an ideal prototype for vast amount of other dithiol monolayers. In addition, it is of great interest to compare the structure of the system with that of alkanethiol SAMs on gold surfaces. In the early stage of the study, it was believed that the molecule takes "upright" configuration where the molecular chain is oriented nearly perpendicular to the surface.[252] This is because not only of the analogy to the alkanethiols but also of the speculation based on the

results of the multilayer formation[246,247] and the X-ray photoelectron spectroscopy (XPS).[252]

However, subsequent studies undoubtedly revealed the existence of the stripe phase structures in which the dithiols are flat lying on the gold surface. It was also found that the period of the stripe phase structure varies depending on the molecular length.[59,253–258] Kobayashi *et al.* studied the structure of octanedithiol monolayers using STM and IR spectroscopy, revealing the parallel orientation of the molecules in the stripe phase structure.[59,253–255] Leung *et al.* presented the detailed description of the molecular conformation and orientations with respect to the gold surface in the stripe phase hexanedithiol monolayer using STM, grazing incidence X-ray diffraction (GIXD) and low-energy atom diffraction (LEAD).[257]

In those experiments, the stripe phase monolayer was obtained by the gas phase deposition under an ambient[59,253–255] or a vacuum condition.[257] However, it was also reported that the film often shows disordered structure when it was prepared by immersion in an ethanol solution or by excess amount of gas phase deposition.[59,253–255,257,258] XPS measurements by Leung *et al.* revealed that the molecular density of the disordered phase is larger than that of the stripe phase.[257] Furthermore, *in-situ* STM experiment performed in an alkaline medium (0.1 M NaOH) revealed that the disordered phase of hexanedithiol monolayer can be changed into the stripe phase by setting the tip bias voltage at an appropriate value to induce the reductive desorption of the molecules.[258] Such a phase transition was also observed when the disordered structure was annealed at 110°C which is high enough to induce the desorption of the hexanedithiols.[257] These all results indicated that the disordered structure is caused by the excess amount of molecules on the surface.

As for the alkanethiols, such a high surface density causes a phase transition from the less-dense stripe phase to the more-dense $(\sqrt{3} \times \sqrt{3})$R30° structure where the molecules take upright configuration. The difference between the thiols and dithiols may be ascribed to the different chemical affinity to the gold surface. Since dithiols are strongly bound by the gold surface due to the chemisorption of the two thiol end groups, the local free energy minimum represented by the stripe phase should be quite deep, which might prevent such a phase transition from the less-dense phase to the more-dense phase. On the other hand, since the binding energy of the alkanethiols on gold surface should be not so large as that of dithiols, the phase transition would be more easily induced by the excess molecular coverage.

The molecular-scale structure of the disordered phase still remains unclear. So far, GIXD was employed to determine if there were any ordered phases underneath a disordered multilayer, which, however, excluded such a possibility.[257] From the view point of thermodynamics, such a molecular ordering should be dependent on

the temperature because of the following equation describing the free energy (G),

$$G = H - TS, \tag{5.36}$$

where H, T and S denote enthalpy, temperature and entropy, respectively. Namely, when the temperature is relatively high, fully disordered phase with higher entropy should become energetically advantageous, and vice versa.

Phase-Separated SAMs

One of the major applications of thiol monolayers is modifications of the surface physicochemical properties. By choosing an appropriate end group with hydrophobic (e.g., -CH_3, -CF_3) or hydrophilic (e.g., -OH, -COOH, -NH_2) nature, the wetting and adhesion properties of the surface can be controlled.[167] Surface friction and viscoelasticity can be modified by changing the length of the thiol molecules[185,188] so that the monolayer can serve as an ideal model surface for the studies on tribology.

Mixed SAMs made of more than two components of thiols with different end groups or different chain length can offer a better controllability of such surface properties than single-component SAMs. So far, various methods to produce mixed SAMs were presented such as micro-contact printing,[259–261] coadsorption from the mixed solution[174,262–272] and other complicated methods using chemical[273] or thermal[274] desorption of the molecules. Among them, studies on direct coadsorption process is particularly important because they may be able to provide essential information on the self-assembling process and the phase separation dynamics of the thiol monolayers.

First comprehensive studies on the coadsorbed mixed SAMs were performed by Whitesides and co-workers.[174,262–265] They used XPS, ellipsometry and contact angle measurement to investigate the wettability and the coadsorption dynamics of the various kinds of mixed SAMs comprised of two different thiols with different end groups or chain length. These studies revealed some important knowledge on fundamental nature of the coadsorption process. The mixed SAM does not consist of complete mixture of the two thiols. Instead, one of the two thiols is preferentially adsorbed on the surface to form a predominant monolayer and the other thiol forms small (less than a few nanometers) clusters embedded in it. The longer chain thiols are more preferred to form the monolayer than shorter chain thiols. The composition of the monolayer is not linear to that of the solution. The component with larger content in the solution tend to adsorb onto the surface beyond the expectation from the content ratio of the solution. From these results, they suggested that the coadsorption mechanism can be understood by the thermodynamic equilibrium

between the monolayer and the solution, namely, enthalpy of condensation and entropy of mixing.

Later, the development of STM enabled us to directly visualize the detailed structure of the mixed monolayers.[266–272] Such direct local information was essential to investigate the phase separation behavior which take place on a nanometer-scale. STM studies by Stranick *et al.* revealed the nanometer-scale phase-separation of thiols with different functional groups where enthalpy reduction due to the end group interactions is the main driving force to form separate domains.[266–269] Studies using STM and IR spectroscopy by Lewis *et al.* revealed that the hydrogen bonding between the functionalized molecular chains buried in the monolayer can also reduce the enthalpy of nanometer size domains of polar thiols.[271] Chen *et al.* investigated the temperature dependence of the phase separation behavior of mixed SAMs composed of two alkanethiols with different chain length, which revealed that the phase separation takes place if the chain length difference is large enough or the temperature is low enough otherwise the two components are completely mixed.[272] This is because van der Waals interaction between longer alkyl chains is stronger than that for the shorter chains so that the enthalpy of the domains consisting of longer chain molecules is small enough to form nanometer scale domains. On the other hand, when the temperature is lowered, the entropic term in the equation (5.36) become too small to induce the complete mixing.

As described here, the coadsorption and phase separation mechanisms can be mostly understood by thermodynamic description. However, it is still unclear how close the observed structures are to thermodynamic equilibrium. Weiss and coworkers consistently pointed out that the long-range arrangements of the domains and defects of the mixed SAMs prepared by usual coadsorption process should be the result of kinetic trapping rather than the thermodynamic equilibrium although the short-range structure can be explained by the thermodynamic models.[266–271] The kinetics of self-assembly is especially important with respect to the adsorbate solubility in the solution.[270] For example, if the solvation energy of the polar thiols in ethanol solution is greater than that required to adsorb onto the surface surrounded by the non-polar thiols, non-polar thiols may adsorb at higher concentration and/or at a faster rate. This is true even when the thermodynamic free energy of the monolayer domain of polar thiols is lower than that for non-polar thiols. Therefore, the formation process of the mixed SAM is a complex interplay between the kinetics and thermodynamics.

Phase-Separated SAMs of Thiols and Dithiols

The surface of the mixed SAM shows microscopic variations in surface properties due to the different end group and chain length of the constituent molecules. When the SPM tip is scanned over the mixed SAM, different tip-sample interactions reflecting the nature of the underlying monolayer are expected. Thus it can be an ideal model surface for the investigations on tip-sample interactions and microscopic surface property measurement techniques. So far, mixed SAMs prepared by micro-contact printing were widely used for the demonstration of AM-KFM,[275] friction force microscopy (FFM),[276–283,283,284] phase imaging of AM-DFM[285] and pulsed-force mode AFM.[286] In most of these experiments, the chemically modified tip was used to detect the chemical interaction between the tip and the surface.

Although micro-contact printing is a well-established and useful technique, the scale of the heterogeneous structures fabricated by this method is limited to the sub-micrometer scale. This is too large to be used for the test of resolution obtained by advanced FM-DFM related techniques. On the other hand, the domain size in the phase-separated SAM can be varied from molecular-scale to several tens of nanometers by changing the sample preparation conditions and molecular species. Thus it can be a convenient test sample for the high-resolution surface property measurements and molecular differentiation.

The sample used in this experiment was the phase-separated SAM of alkanethiols and alkanedithiols prepared by gas phase deposition under an ambient condition. So far, the structure of this system was investigated by Kobayashi *et al.* using UHV-STM.[59,253,255] They prepared a phase-separated SAM where the thiols form nanometer-scale island domains surrounded by the dithiol monolayer. It was found that the thiols are hexagonally close-packed taking the upright configuration while the dithiols are flat lying on the surface making up the stripe phase structure. However, there was also found disordered area within the dithiol region probably due to the excess amount of deposited molecules.

In this experiment, the phase-separated SAMs composed of the disordered dithiol monolayer and well-ordered thiol islands embedded in it were prepared by gas phase deposition. Since the surface contains both well-ordered and disordered regions, the sample is expected to be quite convenient to investigate the energy dissipation process induced by the molecular fluctuations.

5.4.2 Sample Preparation

The molecules used in this experiment were 1-decanethiols (CH_3-$(CH_2)_9$-SH, C_{10}) and 1,10-decanedithiols (HS-$(CH_2)_{10}$-SH, $C_{10}D$) which were purchased from Tokyo

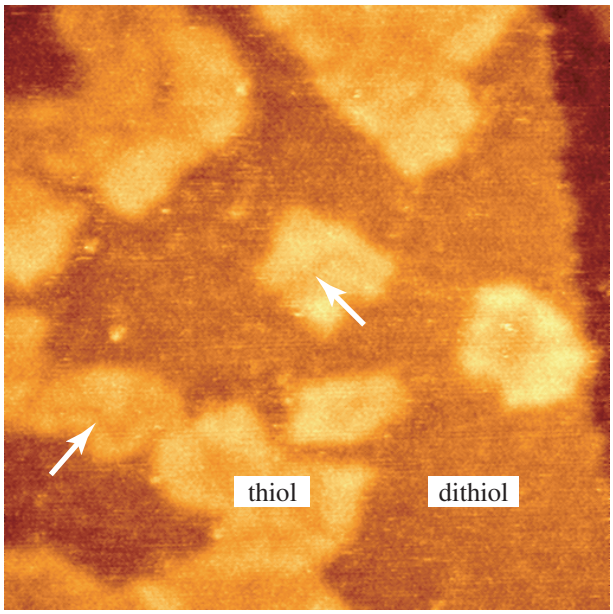

Figure 5.14: FM-DFM image of the phase-separated SAM ($C_{10}/C_{10}D$) on the Au(111) surface (150 nm × 150 nm, $\Delta f = -10$ Hz, $A_{\text{p-p}} = 10$ nm). The bright islands correspond to the thiol monolayer where the molecules are taking upright configuration while the dark area consists of dithiol molecules in disordered phase.

Kasei Co, Ltd. The Au(111) surface was prepared by evaporating gold onto the freshly cleaved mica surface at a substrate temperature of 420°C. Then the substrate was exposed to the vapor of ethanol solution containing C_{10} and $C_{10}D$ at 0.5 mM each for 4 h. After the deposition, the sample was rinsed in the pure ethanol and dried in the N_2 flow.

5.4.3 Results and Discussion

Imaging of Surface Structures

Figure 5.14 shows a typical FM-DFM image of the sample used in this experiment. The image shows some nanometer-scale islands separated by the dark area, showing a clear phase-separation between the thiol and dithiol molecules. From the analogy to the results reported by Kobayashi *et al.*,[59,253,255] the bright islands should correspond to the thiol monolayer where the molecules are closely-packed taking an upright configuration while the dark region consists of dithiol molecules in the disordered phase. In this experiment, no stripe phase structure was found in the dithiol region, suggesting that the greater number of molecules were deposited on the surface than that required to form the ordered stripe phase structure. It was difficult to obtain molecular-scale FM-DFM image even on top of the thiol region probably due to the molecular fluctuation induced by the tip-sample interaction.

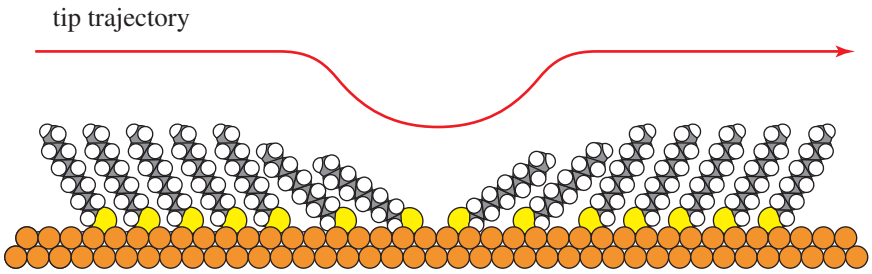

Figure 5.15: Schematic model to explain the slight height variation observed on top of the thiol region in Fig. 5.14. The height variation may be ascribed to the gradual tilt angle change around the domain boundary of the thiol monolayer.

There were found some height variation on top of the bright thiol regions, which suggested that there were some variation in the molecular tilt angle. Since some of the dark contrast on the thiol region showed line-shaped features as indicated by the white arrows in Fig. 5.14, the tilt angle variation may exist not randomly but preferentially around the boundary of the different thiol domains as shown in Fig. 5.15. Namely, the molecular tilt angle is relatively large around the domain boundary due to the low molecular density. Thus each molecule in the thiol region is not so tightly bound by the surrounding molecules as in the typical single-component SAMs, resulting in the large molecular fluctuation induced by the tip-sample interaction.

The detailed structure of the disordered phase observed in this experiment still remains unclear. It is unclear whether the molecules were rapidly moving all over the dithiol region such as in a two-dimensional liquid phase or they were just fluctuating with their average position fixed. It is also unclear if there were any ordered structure buried under the disordered dithiol layer. However, in any cases, the molecules are most likely to have relatively large tilt angle form the surface normal because both the previously reported STM images[59, 253, 255] and the FM-DFM images obtained in this experiment showed darker contrast on the dithiol region than that on the thiol region.

Measurements of Surface Potential

Figure 5.16 shows the topographic and surface potential images of the phase-separated SAM ($C_{10}/C_{10}D$) simultaneously obtained by FM-KFM. The thiol region showed higher surface potential than that on the dithiol region. Slight variation in the surface potential was found on the thiol region while that on dithiol region showed almost constant value. The potential difference between the thiol and dithiol regions ranged from 100 to 150 mV.

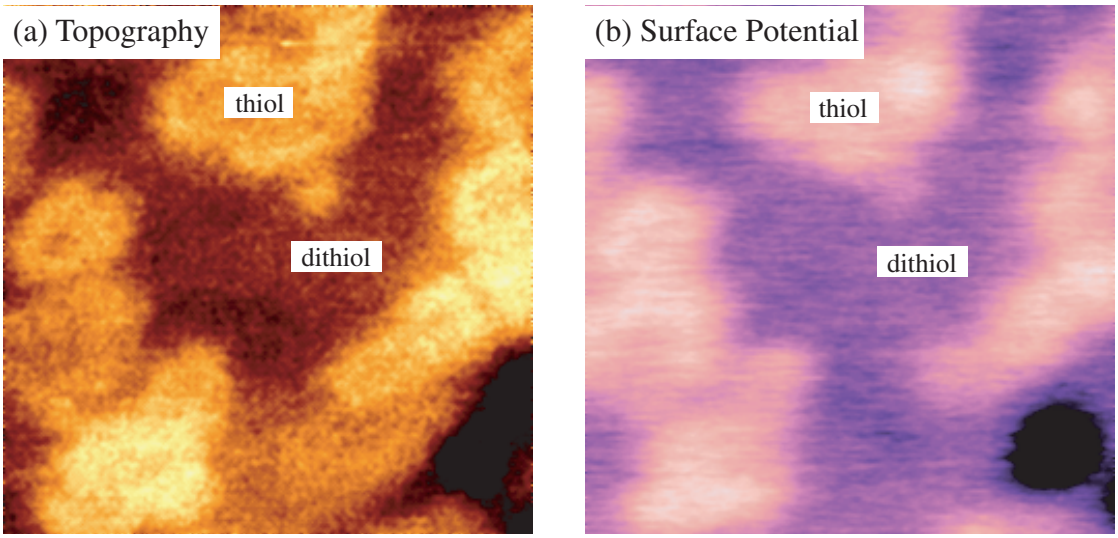

Figure 5.16: (a) Topographic and (b) surface potential images of the phase-separated SAM ($C_{10}/C_{10}D$) on the Au(111) surface (150 nm × 150 nm, $\Delta f = -30$ Hz, $A_{\text{p-p}} =$ 10 nm). The thiol region showed higher surface potential than that on the dithiol region, reflecting the dipole moment within the thiol molecules.

So far, a few reports have been published for the surface potential measurements of the alkanethiol SAMs.[275,287,288] Evans and Ulman investigated the surface potential of the alkanethiol SAMs as a function of the molecular chain length using traditional Kelvin method.[287] They reported that the thiol surface showed positive potential with respect to the substrate and the value linearly increased by 9.3 mV per CH_2 unit as the chain length increased. Later, Lü *et al.* measured surface potential of the mixed SAMs prepared by micro-contact printing using AM-KFM,[275] which mostly confirmed the above mentioned results except for the small difference in the increasing rate of the surface potential as a function of chain length (14.1 ± 3.1 mV per CH_2 unit).

The origin of the positive surface potential and its chain length dependence can be explained by the model shown in Fig. 5.17. When a thiol adsorbs onto the gold surface, a chemical bonding (not perfectly covalent) will be formed between the sulfur atom and the gold surface via the loss of the hydrogen and the formation of the thiolate, producing the Au^+-S^- dipole. The positive charge of Au^+ will be provided from the background gold film while the negative charge of S^- will be mainly provided from the covalently bonded alkyl chain, which in turn induces the dipole R^+-S^- (where $R = C_nH_{2n+1}$). The experimentally observed positive surface potential indicated that the R^+-S^- dipole is larger than the Au^+-S^- dipole. Since the dipole R^+-S^- is made up of the vector sum of the dipole moments along the S-C or C-C bonds, it seems to be reasonable that the net dipole moment of the

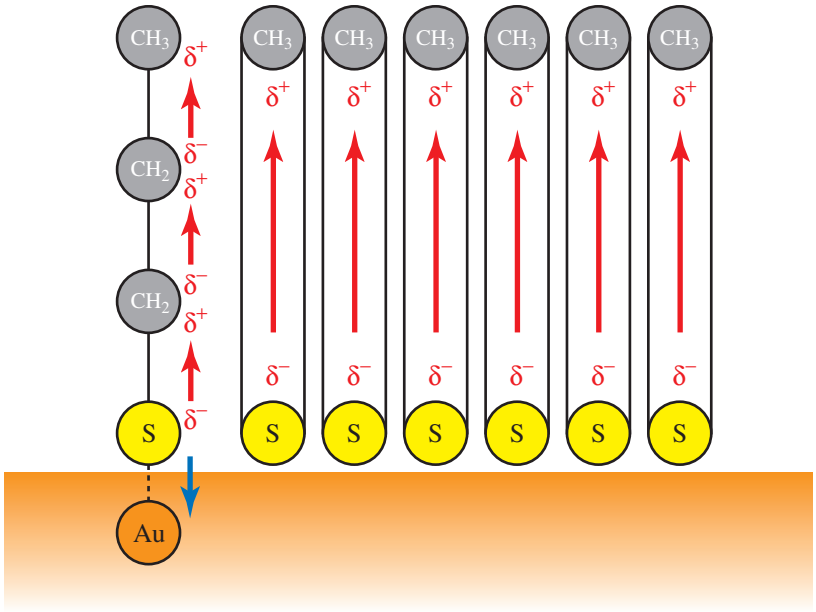

Figure 5.17: A schematic model to explain the positive surface potential of the alkanethiol SAM and its dependence of the chain length. The dipole Au^{+}-S^{-} is virtually shielded by the free electrons in metal while the effective R^{+}-S^{-} dipole linearly varies with increasing chain length making up a dipole sheet.

molecule linearly varies with increasing chain length. However, the dipole moment along the S-C bond is likely to be much larger than other dipoles along C-C bonds. This is because the reported absolute value of the surface potential, for example, of decanethiol (C_{10}) is about 550 mV, which is much larger than expected from the reported chain length dependence (about 10 mV per CH_2 unit). Therefore, the chain length dependence may not be linear for the thiols with shorter chain length.

The surface potential variation found on the thiol region can be explained by the variation in the molecular tile angle. When the molecular tilt angle from the surface normal become large, the net dipole moment perpendicular to the surface will be reduced because the induced dipole moment exists along the molecular axis. For example, if it is assumed that the surface potential of the C_{10} monolayer with the molecular tilt angle of 30° is 550 mV,[287] the observed potential variation roughly correspond to the tilt angle variation of about 8°. Note that the possibility that the amount of the induced dipole moment itself may be changed by the tilt angle variation was neglected in this simple estimation.

Although there have been no reports on the surface potential of the dithiol monolayers, it seems to be reasonable that the dithiol region showed lower surface potential than that of the thiol monolayer. Dithiols in disordered phase probably do not have an uniform orientation with respect to the surface. Figure 5.18 shows

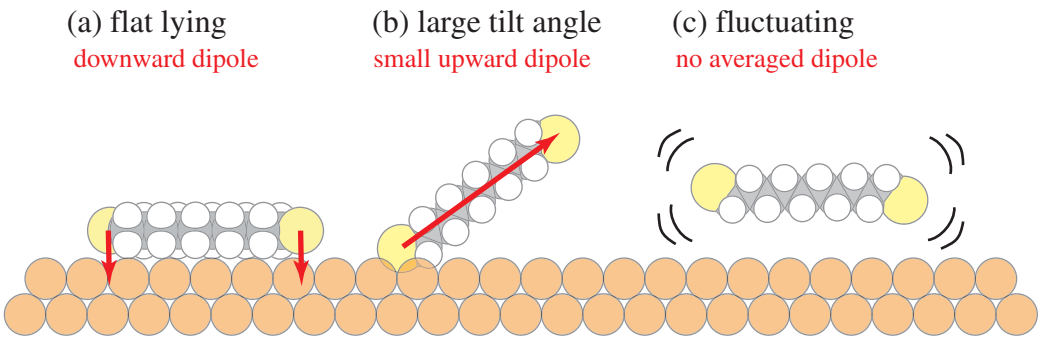

Figure 5.18: A schematic model showing the possible orientations of the dithiols and their expected dipole moment. The molecule may be (a) flat lying, (b) having a large tilt angle or (c) continuously moving. In any cases, the net dipole moment perpendicular to the surface is smaller than that of the thiols in $(\sqrt{3} \times \sqrt{3})$R30° structure.

the possible orientations of the dithiols and their expected dipole moment. Some molecules may be flat lying on the surface like ones in the well-ordered stripe phase, where the net dipole moment is likely to be oriented downward (Fig. 5.18(a)). Others may be adsorbed with a larger tilt angle from the surface normal than that of thiols (Fig. 5.18(b)). In this case, although there may be some dipole moment in upward orientation, it should be smaller than that of thiols. Furthermore, there may be some molecules rapidly moving on the surface like in the two-dimensional liquid phase (Fig. 5.18(c)). Such randomly moving molecules should have no net dipole moment in any directions if it is time-averaged. All the contribution from each of these molecules might result in the observed smaller surface potential.

Measurements of Energy Dissipation

Figure 5.19 shows Δf dependence of the topographic and dissipation images of the phase-separated SAM. The topographic contrast became more clearer as $|\Delta f|$ increased, showing the domain structure within the thiol region. Instead, the topographic artifacts due to the feedback error of the gap distance regulation became prominent at the left and right edges of the thiol regions as indicated by the white arrows in Fig. 5.19(c). The dissipation contrast gradually became visible with increasing $|\Delta f|$, which revealed that the energy dissipation measured on the dithiol region (P_{dithiol}) is larger than that on the thiol region (P_{thiol}).

Figure 5.20(a) shows the $|\Delta f|$ dependence of the height difference between the thiol and dithiol regions ($\Delta h = h_{thiol} - h_{dithiol}$) estimated from the several topographic images. The plot revealed that the estimated Δh significantly decreased with increasing $|\Delta f|$. Moreover, the negative Δh value, namely, the contrast inver-

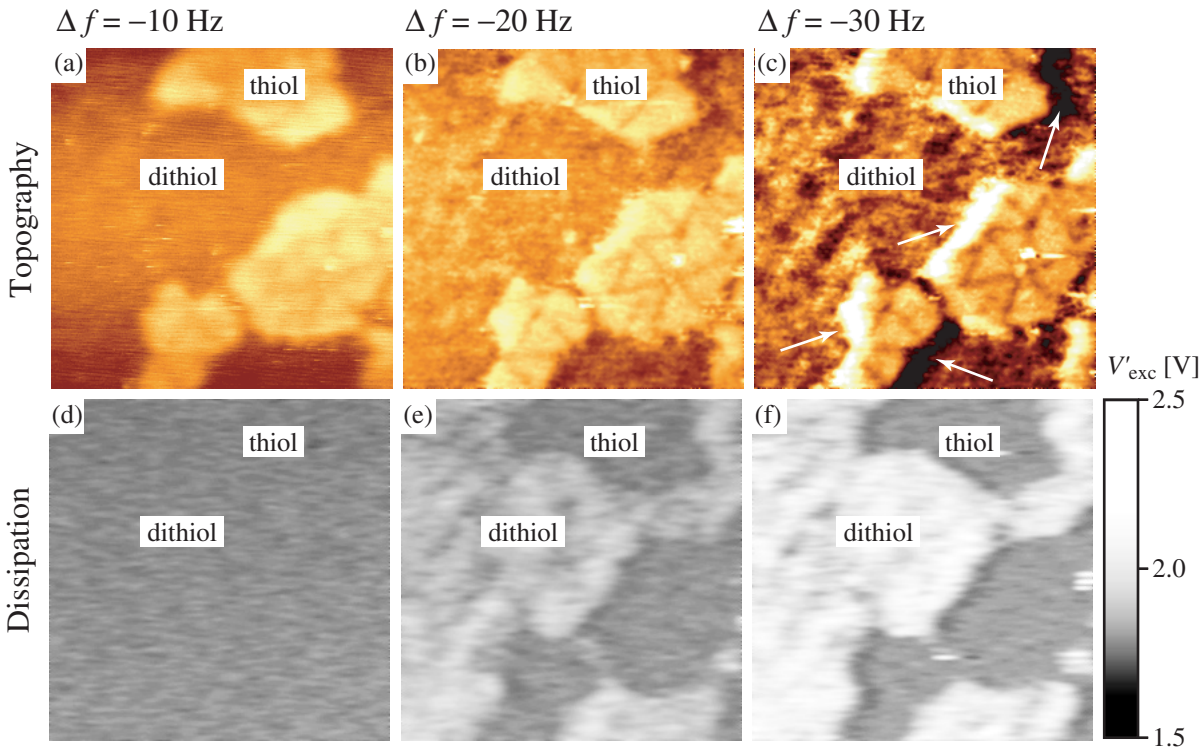

Figure 5.19: The frequency shift dependence of the topographic and dissipation images of phase-separated SAM ($C_{10}/C_{10}D$) on the Au(111) surface (100 nm × 100 nm, $A_{p\text{-}p} = 10$ nm). The frequency shift during the FM-DFM imaging was −10 Hz for (a, d), −20 Hz for (b, e) and −30 Hz for (c, f). The scanned direction was from the left to the right of the image.

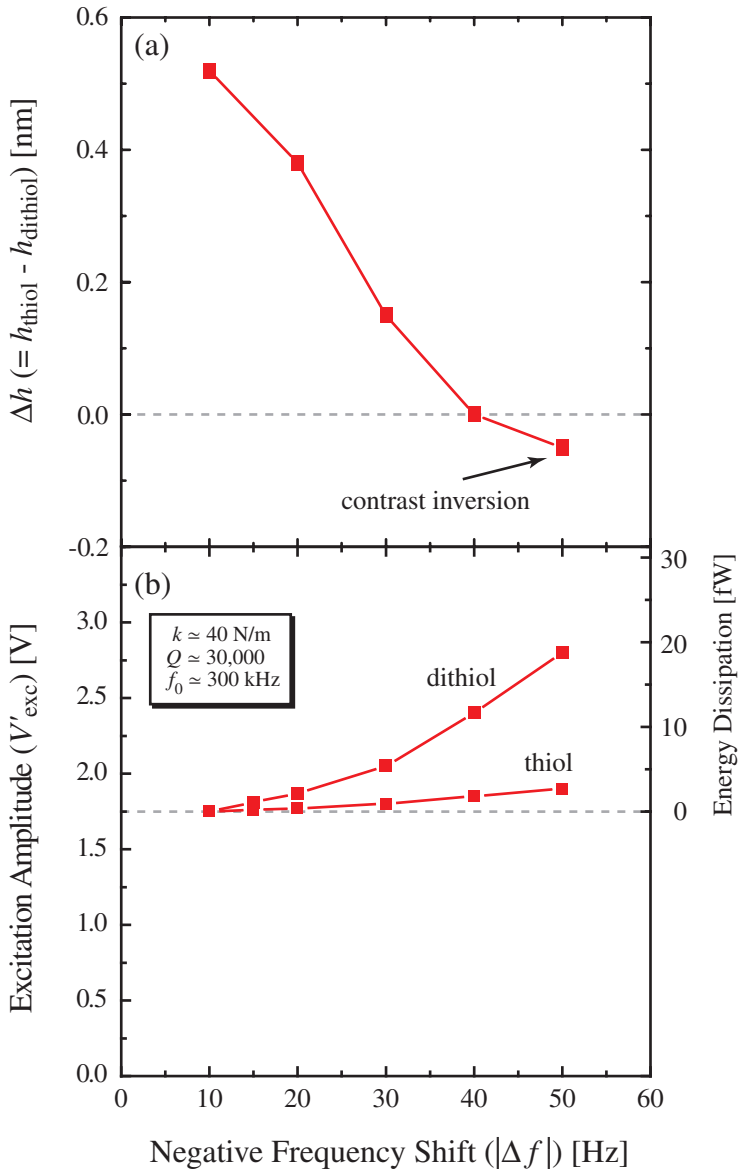

Figure 5.20: The frequency shift dependence of (a) the height difference between the thiol and dithiol regions (Δh) and (b) the energy dissipation measured on them. These profiles were obtained from the cross-sectional plots of the simultaneously obtained topographic and dissipation images with different frequency shift. Note that the energy dissipation values shown in (b) was estimated based on the typical parameters of the cantilever used in this experiment so that they were presented only for the order estimation.

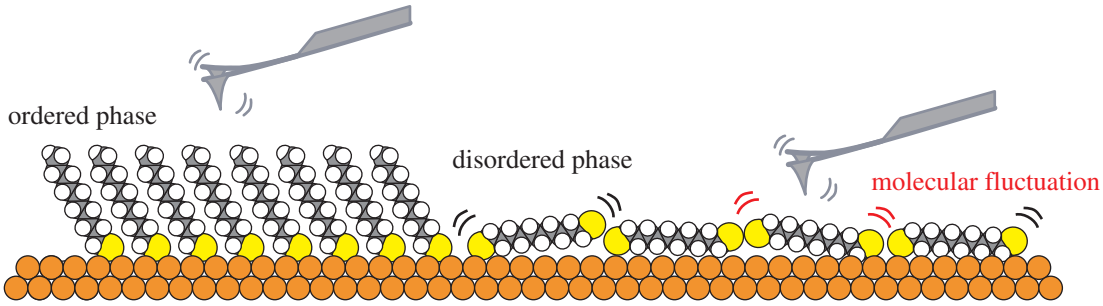

Figure 5.21: A schematic model to explain the observed large dissipation on dithiols.

sion was observed at $\Delta f = -50$ Hz. P_{thiol} and P_{dithiol} estimated from the several dissipation images were also plotted as a function of $|\Delta f|$ as shown in Fig. 5.20(b). Although both P_{dithiol} and P_{thiol} increased as $|\Delta f|$ increased, the former showed much stronger dependence. For example, when Δf was -50 Hz, P_{dithiol} was about ten times larger than P_{thiol}.

The large difference between P_{dithiol} and P_{thiol} is most likely to be ascribed to the fluctuation of the dithiol molecules as shown in Fig. 5.21. Since the dithiols were in the disordered phase, they were not tightly bound by the surrounding molecules. Thus they might be relatively easy to move by the tip-sample interaction, leading to the force hysteresis in each cycle of the cantilever oscillation and resultant energy dissipation.[82] In addition, there is a possibility that the molecules are thermally fluctuating even without the tip-sample interaction. In that case, such a random fluctuation can also induce the stochastic energy dissipation as pointed out by Gauthier *et al.*[27] One might expect that the dissipation difference might be related to the electrical dissipation because there was found 100 – 150 mV difference in surface potential between thiols and dithiols. However, the possibility can be safely excluded as the measured dissipation showed no significant difference even when the dc tip-sample potential difference was canceled out by KFM bias feedback technique. Therefore, the result strongly supported the expectation that the energy dissipation can be induced by the molecular fluctuation although it is unclear whether it was tip-induced movement or thermally-induced Brownian motion. Since such a molecular fluctuation is one of the major obstacle to obtain high-resolution FM-DFM images, the energy dissipation value can serve as a useful criterion to determine whether the high-resolution can be achieved or not.

There were found some artifacts in Fig. 5.19(c) as indicated by the white arrows. As a general requirement to suppress feedback errors and resulting image distortions, the cutoff frequency of the amplitude feedback circuit should be much larger than that of the distance feedback circuit.[95] This requirement was well satisfied in the

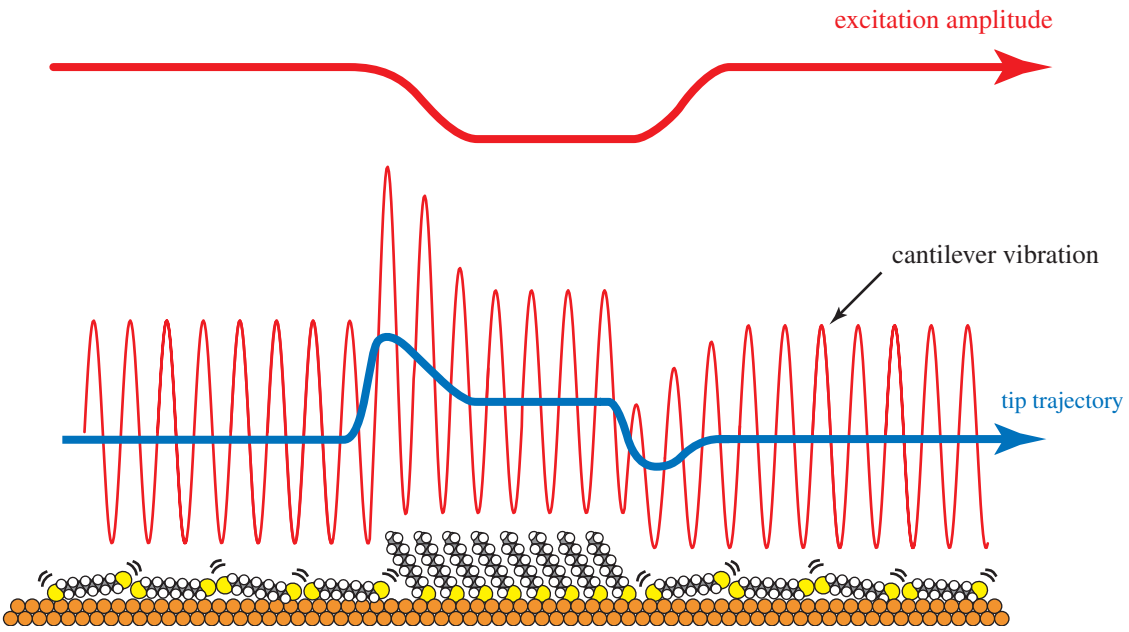

Figure 5.22: A schematic model to explain the topographic artifacts found in Fig. 5.19(c). Since the energy dissipation drastically changed at the boundary between the thiol and dithiol regions, the response time of the amplitude feedback circuit became longer than that of the distance feedback.

setup used in this experiment. However, if the dissipation variation become comparable to the intrinsic dissipation, a major correction of the excitation amplitude is needed to keep the amplitude constant. Thus the amplitude regulation may take longer settling time to achieve a steady state than that for the distance regulation. As for this experiment, the dissipation variation at the boundary between the thiols and dithiols was so large that the amplitude regulation couldn't respond quickly enough to suppress the transient response of the distance regulation feedback (Fig. 5.22).

Several measures can be taken to avoid such artifacts; lowering the cutoff frequency of the distance feedback circuit; to improve the time response of the amplitude feedback circuit. On the other hand, recently Giessibl pointed out that the Q-factor should not be very high to perform a stable amplitude regulation.[95] Namely, if Q-factor is very high, the intrinsic energy dissipation is quite small so that even small energy dissipation requires a major correction of the excitation amplitude. Therefore, the cantilever with a lower Q-factor may be suitable for the imaging on the samples which show a large variation in the energy dissipation.

The strong dependence of Δh on $|\Delta f|$ and the resultant contrast inversion cannot be explained by such a transient response of the feedback circuit. Since the contrast inversion was observed even when the amplitude variation was sufficiently suppressed

by the amplitude regulation using proportional and integral control circuit, the effect of the steady-state error is not likely to be the predominant factor for the contrast inversion. In addition, the cancellation of the tip-sample dc potential difference did not significantly affected the topographic contrast, suggesting that the electrical interaction cannot be the main cause of the contrast inversion.

One of the possible origin for the contrast inversion is the difference in the chemical interaction. While the surface of the thiol monolayer is well-defined as an array of methyl end groups, that of the dithiol region cannot be defined on a molecular-scale because it is disordered. However, if any of the thiol groups are exposed to the surface in the dithiol region, they might show a different chemical interaction with the tip atom. Another possible mechanism is the force hysteresis in each cycle of the cantilever oscillation. Sasaki *et al.* revealed that such a force hysteresis induces not only the energy dissipation but also the additional negative frequency shift.[82] They explained the previously reported discontinuity of the force-distance curves measured on Si surfaces[289–292] by the force hysteresis due to the chemical bonding which takes place within a certain threshold height from the surface. In this experiment, such a force hysteresis may exist even at a large tip-sample separation because of the fluctuation of the dithiols.

5.5 Summary

In this chapter, the dissipation mechanisms of the cantilever vibration energy were investigated in relation to the electrical interaction and the molecular fluctuation.

Energy Dissipation Induced by Electrical Interaction

It was revealed that the experimentally measured energy dissipation contains both "apparent dissipation" induced by the conservative electrical interaction and "true dissipation" induced by the dissipative electrical interaction. There are some different origins for both types of electrical energy dissipation Their contribution to the energy dissipation images and bias dependence curves was discussed in this chapter.

1. It was revealed that the energy dissipation typically shows quadratic bias dependence. However, the order of energy dissipation was too large to be explained either by the Joule dissipation or by the bias dependent phase error. Further studies are required to elucidate the origin for the quadratic bias dependence.

2. It was found that the energy dissipation occasionally shows an extraordinary type of bias dependence curve with double minimum peaks. As one of the

possible origins, the effect of bias dependent changes in the force potential acting on the tip was pointed out.

3. The energy dissipation images and the bias dependence curves showed strong dependence on the bias resistance. The dependence can be well understood by taking account of the effect of the stray capacitance between the electrode of the PZT actuator and the cantilever base or other part of the bias line.

Energy Dissipation Induced by Molecular Fluctuation

It was revealed that the energy dissipation induced by the molecular fluctuation is strongly related to the mechanical property of the surface. However, it was also found that the molecular fluctuation induces not only energy dissipation but also some topographic artifacts because of the incomplete separation between the conservative and dissipative interactions.

1. The energy dissipation measured on the disordered dithiol region was much larger than that on the well-ordered thiol regions. This result indicated that a large energy dissipation is expected on the loosely packed molecules due to the large molecular fluctuation. The molecular fluctuation may correspond to the thermally-induced Brownian motion. Besides that, some additional kinetic energy of the molecular fluctuation may be provided from the vibrating cantilever through the dissipative tip-sample interaction.

2. Some topographic artifacts were found at the domain boundaries between the thiol and dithiol regions due to the extremely large difference in the energy dissipation. The result suggested that the cantilever with a lower Q-factor is suitable for the imaging on the samples which show a large variation in the energy dissipation.

3. The topographic contrast between the thiol and dithiol regions was inverted when the tip-sample separation was reduced. As the possible origins for the contrast inversion, the effects of the chemical interaction and the additional frequency shift due to the force hysteresis were pointed out.

Chapter 6

Molecular-Scale Contrasts in Topography and Dissipation

6.1 Introduction

Since the first demonstration of the true-atomic resolution of FM-DFM,[42,43] the imaging mechanism of the atomic-scale contrasts has been intensively studied both in theoretical[72–77] and experimental[289–292] aspects. Although the complete understanding has not been achieved yet, it has become more and more evident that the short-range chemical interaction between the tip front atom and the surface atom plays an important role in the contrast formation. Since the organic surface shows a wide variation in the surface chemical properties, the effect of chemical interaction would be particularly important. However, detailed studies on the relationship between the chemical property of the surface and the molecular-scale topographic contrasts have never been made so far.

Dissipation images with true-atomic resolution were first demonstrated in 1997 by Lüthi *et al.*[30] The atomic-scale dissipation contrasts have been mainly attributed to the fluctuation of the tip atoms and surface atoms induced by the tip-sample interactions.[88,89] Such an atomic fluctuation is explained in relation to an instability or a bistability of the atomic-scale surface structures.[27,82] In the case of organic surfaces, mechanical property of the surface is mostly determined by the molecular conformations and packing arrangements. In fact, the results obtained in the previous chapter revealed that the energy dissipation on the disordered molecular film is larger than that on the well-ordered one. However, the relationship between the mechanical property of the surface and the molecular-scale dissipation contrasts have never been studied. Moreover, molecular-scale dissipation images have never presented so far.

In this chapter, the formation mechanisms of the molecular-scale contrasts in topography and dissipation were experimentally studied in relation to the chemical

and mechanical properties of the organic surfaces. For this purpose, the organic surfaces that have molecular-scale variations in structures and properties are desirable as model organic systems. The samples used in this experiment were defect-reduced alkanethiol SAMs on Au(111) surfaces and copper-phthalocyanine (CuPc) thin films on MoS_2(0001) surfaces. In the defect-reduced SAMs, the closely-packed molecules show two different packing arrangements referred to as c(4×2) superlattice structures. Thus the relationship between the molecular-scale dissipation contrasts and the packing arrangements is of particular interest. As for the CuPc thin films, the molecule has widely delocalized π-electron orbitals sticking out of the molecular plane. Thus special attention was paid for their relation to the molecular-scale topographic contrasts. In addition, since CuPcs are relatively loosely-packed even in an well-ordered monolayer, the molecules may be easily fluctuated by the tip-sample interactions. Therefore, the relationship between such a tip-induced molecular fluctuation and the molecular-scale dissipation contrasts is discussed in detail.

6.2 Experimental

All the experiments described in this chapter were performed under UHV conditions using a commercially available UHV-SPM system (JEOL: JSTM/AFM-4500XT, Fig. 4.1) with some modifications. The original frequency shift detector was replaced with a homebuilt PLL circuit[61] to perform a stable frequency shift detection. The original self-excitation circuit was replaced with a homebuilt electronic circuit with an AGC function to keep the cantilever vibration amplitude constant.

The highly-doped n-Si cantilever (Nanosensors: NCH) with a resonance frequency of about 300 kHz and with a nominal spring constant of 40 N/m was used for the FM-DFM imaging. The typical Q-factor measured under an UHV condition was 30,000. The resistivity of the cantilever was 0.01 – 0.025 Ωcm. No special tip treatment was carried out before use. The cantilever was vibrated in constant amplitude mode. The tip-sample distance regulation was made in constant frequency shift mode. During the FM-DFM imaging, the tip and the sample were electrically grounded.

The dissipation images shown in this chapter were obtained by recording the gain (V'_{exc}) of the variable gain amplifier which drives the PZT actuator for the cantilever excitation (excitation image in Fig. 2.17). V'_{exc} is proportional to the excitation amplitude (V_{exc}) and the magnitude of energy dissipation. However, since the dissipation images were not always taken with the same cantilever and with the same vibration amplitude, the absolute values for V'_{exc} cannot be directly compared between the different images.

6.3 C(4×2) Superlattice Structures of Alkanethiol Monolayers

6.3.1 Defect-Reduced SAMs

C(4×2) Superlattice Structures

Molecular conformations and packing arrangements within the alkanethiol monolayers on Au(111) surfaces have been intensively studied by a variety of techniques. Studies using reflectance infrared (IR) spectroscopy revealed that the molecules take all-*trans* conformation with their molecular axes tilted by about 30° from the surface normal.[168,169] Transmission electron diffraction measurements showed that the molecules in the monolayer are hexagonally packed to form $(\sqrt{3} \times \sqrt{3})$R30° overlayer of Au(111) surface with inter-molecular distance of about 0.5 nm.[175] From these results, all the molecules were first believed to be adsorbed on the threefold hollow sites of Au(111) surface taking the same conformation so that the unit cell contains only one molecule.

However, subsequent diffraction studies revealed the existence of larger unit cell composed of four distinct molecules, which corresponds to the c(4×2) superlattice with respect to $(\sqrt{3} \times \sqrt{3})$R30° structure. So far, some different models have been proposed to describe the molecular packing arrangement in c(4×2) superlattice structures although it still remains under discussion. Camillone *et al.* proposed that the structure should be composed of the molecules with different twist angles around the molecular chains from the analogy to *n*-alkane bulk crystals.[293] Fenter *et al.* presented a grazing incident X-ray diffraction study suggesting that the molecules in c(4×2) superlattice are dimerized to form S-S bonding near the Au(111) surface.[294]

Later, surface structures of c(4×2) superlattice were directly visualized by STM, which revealed some different contrast patterns in the c(4×2) unit cell. Delamarche *et al.* presented molecularly resolved STM images of four different packing arrangements (Fig. 6.1(a)-(d)),[295] which confirmed the models predicted by Camillone *et al.* On the other hand, Kobayashi *et al.* presented the STM images showing three different molecular contrasts in the c(4×2) unit cell (Fig. 6.1(e)),[194] which cannot be explained by any models presented so far.

As for the FM-DFM studies, detailed discussions on the FM-DFM contrasts in c(4×2) superlattice structures have never been presented so far. Since the surface of the alkanethiol SAM is terminated by chemically inert methyl end groups, the short-range chemical interaction between the tip and the surface should be relatively small. On the other hand, recent studies pointed out that such a short-range chemical interaction plays an important role in the contrast formation of FM-DFM images.

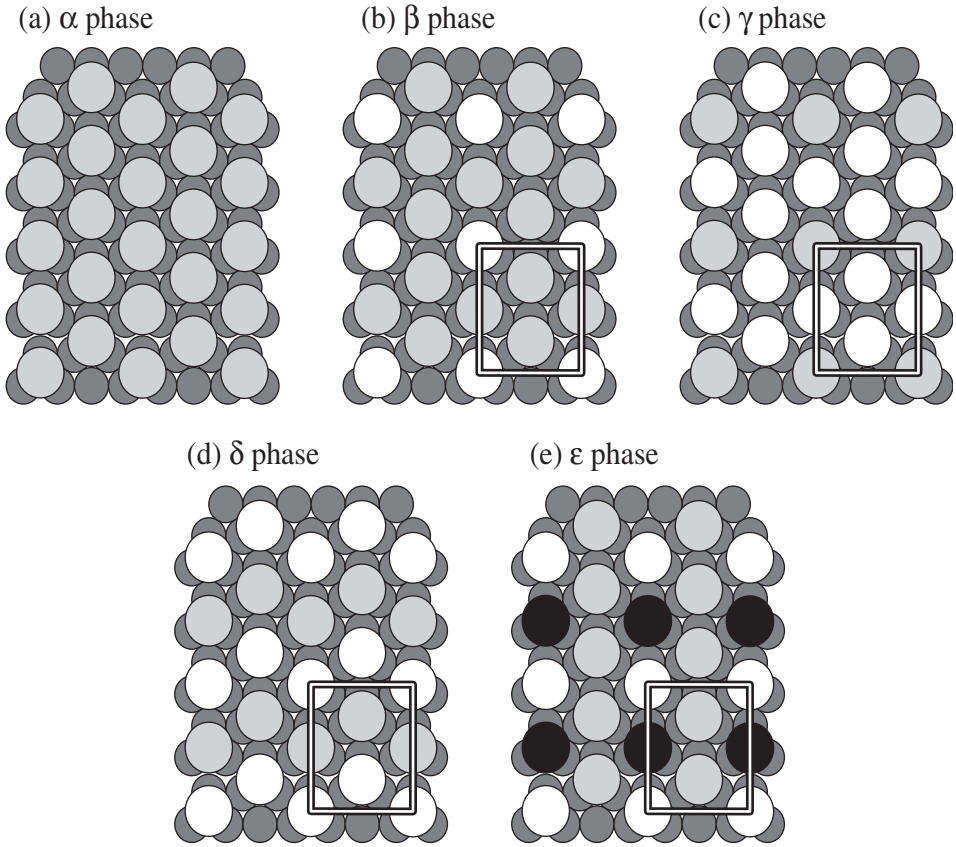

Figure 6.1: Schematic models of the previously reported STM contrasts found in alkanethiol SAMs on Au(111) surfaces. (a) $(\sqrt{3}\times\sqrt{3})$R30° structure with a hexagonal unit cell composed of only one molecule. (b) – (e) c(4×2) superlattice structures with a rectangular unit cell composed of four distinct molecules.

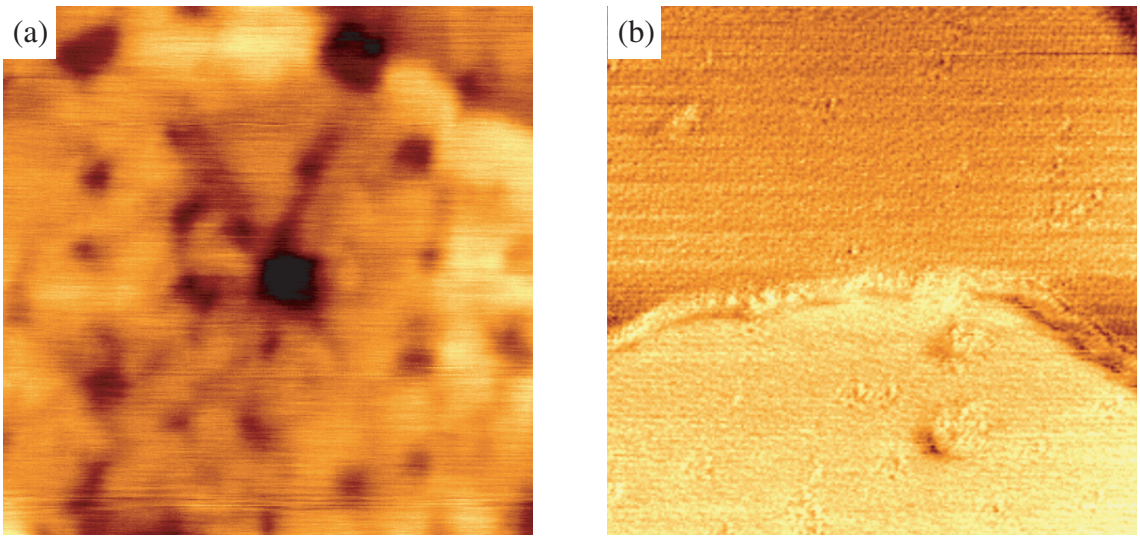

Figure 6.2: Typical FM-DFM images of an ordinary SAM and a defect reduced SAM on Au(111) surfaces. (a) FM-DFM image of a hexadecanethiol (C_{16}) SAM prepared by immersion at room temperature for several hours (50 nm × 50 nm, $\Delta f = -60$ Hz, $A_{\text{p-p}} = 15$ nm). (b) FM-DFM image of a dodecanethiol (C_{12}) SAM prepared by immersion at 78°C for 15 min. (50 nm × 50 nm, $\Delta f = -250$ Hz, $A_{\text{p-p}} = 10$ nm). The defect density is significantly reduced by annealing during the self-assembling process.[274]

Therefore, it is of great interest whether or not FM-DFM can visualize the molecular-scale contrast patterns even on such chemically inert surfaces.

The molecules in the c(4×2) superlattice structure are closely-packed with an excellent ordering. Thus they are expected to be mechanically stable against the tip-sample interaction. However, since the c(4×2) superlattice structure is composed of four distinct molecules, they might have different mechanical properties depending on their conformations and packing arrangements. Therefore, the dependence of molecular-scale dissipation contrasts on the packing arrangements is of particular interest.

Defect-Reduced SAMs

As a result of a number of studies performed so far, it is well-known that c(4×2) superlattice structure is thermodynamically more stable than $(\sqrt{3} \times \sqrt{3})$R30° structure.[296] Thus, in order to prepare the alkanethiol monolayers in c(4×2) superlattice structures, it is essential to make the film structure approach the thermodynamic equilibrium state. In general, the film formation at an elevated temperature is expected to be one possible solution for this purpose. When the film is formed at a low temperature the structure may be settled in a metastable state corresponding

to a thermodynamic local minimum. On the other hand, when the film is heated during the self-assembling process, the film structure can reach a more stable state due to the large kinetic energy of the molecules.

The alkanethiol SAMs are usually prepared by dipping the gold substrate into the dilute (typically 1 mM) ethanol solution at room temperature. Such an ordinary SAM shows multi-domain structure with some round-shaped depressions formed by the gold etching (Fig. 6.2(a)). When the dipping process is performed at an elevated temperature, the domain size becomes almost as large as the gold terrace. In addition, the depressions and the domain boundaries are completely eliminated as shown in Fig. 6.2(b). In such a defect-reduced SAM, it is expected that the molecules take a thermodynamically stable phase, namely, c(4×2) superlattice structure. However, there have been no reports on the detailed surface structures of the defect-reduced SAMs. And hence it is still unclear which phase among the five phases shown in Fig. 6.1 exists in the defect-reduced SAMs.

6.3.2 Sample Preparation

The molecules used in this experiment were 1-dodecanethiols (CH_3-$(CH_2)_{11}$-SH, C_{12}) which were purchased from Sigma-Aldrich Co., Ltd. The Au(111) surface was prepared by the vacuum evaporation of gold onto a freshly cleaved mica substrate. The thiol monolayer was self-assembled on the Au(111) surface in the process of a dip of the gold substrate into the 1 mM ethanol solution of C_{12} for 15 min. The solution was heated up to 78°C (boiling point of ethanol) during the dipping process in order to reduce the defect density.[274] After the dipping process, the sample was rinsed in the pure ethanol and dried in the N_2 flow.

6.3.3 Results and Discussion

Molecular-Scale Topographic Contrasts

Figure 6.3(a) is the FM-DFM image of two different C_{12} domains separated by a gold step. Since the monolayer was prepared at an elevated temperature, the film has only some molecular-scale defects and no depressions formed by the gold etching during the self-assembling process.[274] Figures 6.3(b) and (c) are the FM-DFM images taken on the lower and upper gold terraces seen in Fig. 6.3(a), respectively. These molecularly-resolved FM-DFM images clearly showed two different contrast patterns of c(4×2) superlattice structures. The C_{12} monolayer formed on the lower terrace is composed of zigzag-shaped molecular rows (δ phase, Fig. 6.1(d)) while the one formed on the upper terrace has some protruded molecules which clearly shows rectangular-shaped unit cell (ε phase, Fig. 6.1(e)). In this experiment, we could not

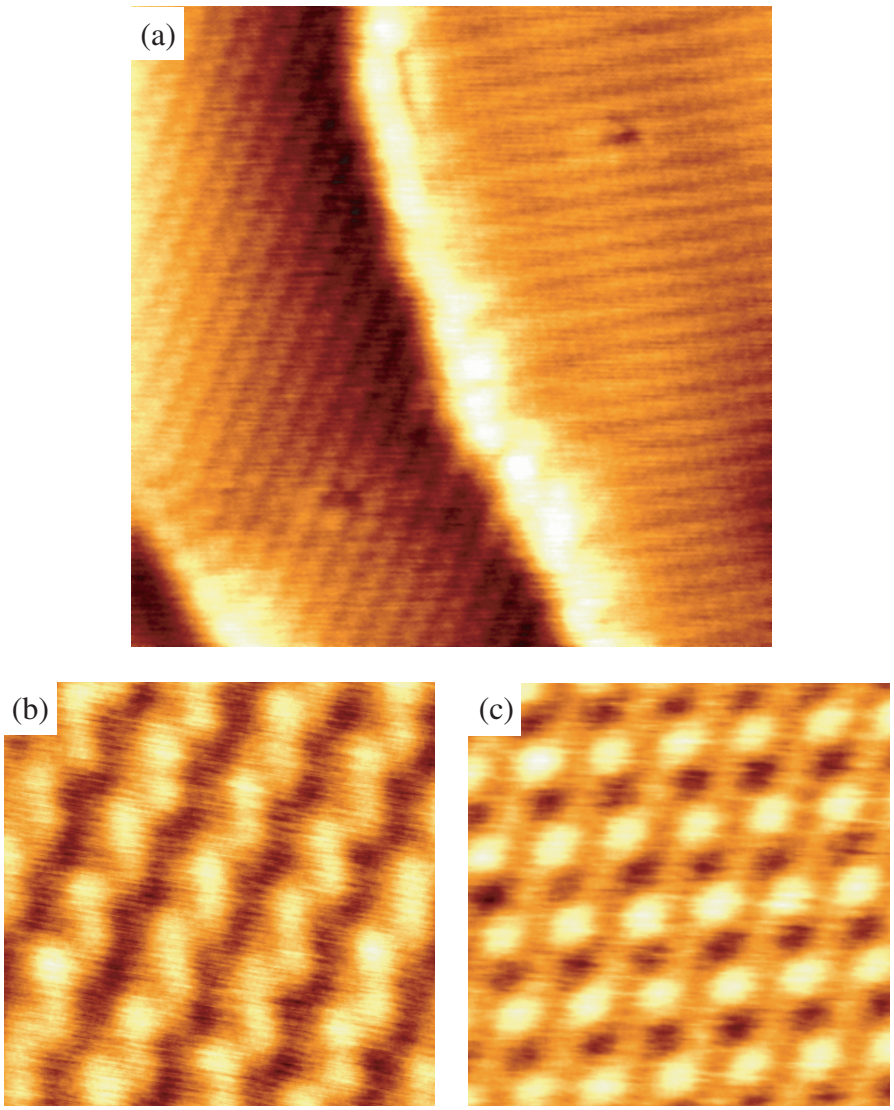

Figure 6.3: FM-DFM images of the C_{12} SAM on the Au(111) surface. (a) 20 nm $\times$ 20 nm, $\Delta f = -70$ Hz, $A_{\text{p-p}} = 10$ nm. (b) 4.5 nm $\times$ 4.5 nm, $\Delta f = -70$ Hz, $A_{\text{p-p}} = 10$ nm. (c) 4.5 nm $\times$ 4.5 nm, $\Delta f = -50$ Hz, $A_{\text{p-p}} = 10$ nm.

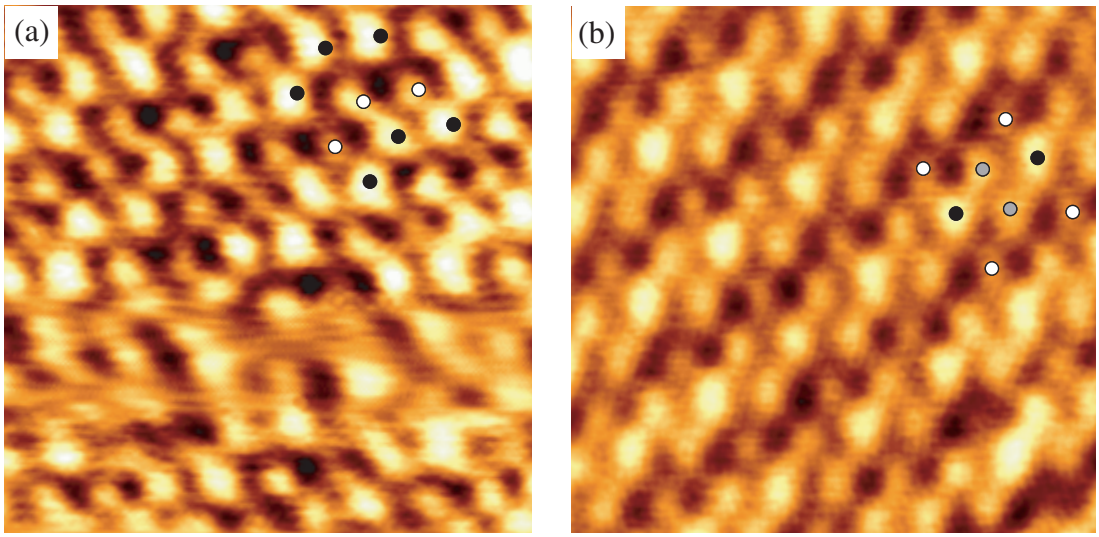

Figure 6.4: FM-DFM images of the C_{12} SAM on the Au(111) surface. (a) FM-DFM image of δ phase (4.5 nm $\times$ 4.5 nm, $\Delta f = -280$ Hz, $A_{\text{p-p}} = 10$ nm). (b) FM-DFM image of ε phase (4.5 nm $\times$ 4.5 nm, $\Delta f = -260$ Hz, $A_{\text{p-p}} = 10$ nm).

found other three contrast patterns (α, β, and γ phases) shown in Fig. 6.1. The results possibly indicated that δ and ε phases are thermodynamically more stable phases than other three packing arrangements.

Higher resolution FM-DFM images of δ and ε phases were obtained with larger Δf values, which showed clear molecular-scale contrasts corresponding to the individual molecules (Fig. 6.4). Although the upper and lower parts of Fig. 6.4(a) showed clear zigzag-shaped molecular rows, the middle area showed a little distorted contrasts due to the fluctuation of the imaging conditions such as the frequency shift and the cantilever vibration amplitude. On the other hand, Fig. 6.4(b) clearly showed three different molecular contrasts of ε phase. This result revealed that FM-DFM can visualize such a slight molecular height variation even if the surface is chemically inert. The imaging conditions during the FM-DFM imaging on ε phase were quite stable in contrast to the case of δ phase. In this experiment, it was found more difficult to obtain high-resolution FM-DFM images of δ phase than ε phase, which suggested that ε phase is structurally more stable against the tip-sample interaction force than δ phase.

Molecular-Scale Dissipation Contrasts

In order to investigate the relationship between the dissipation contrasts and molecular packing arrangements, topographic and dissipation images were taken both on δ and ε phases of C_{12} monolayer (Fig. 6.5). The dissipation image taken on δ phase (Fig. 6.5(b)) clearly showed molecular-scale contrasts along the zigzag-shaped

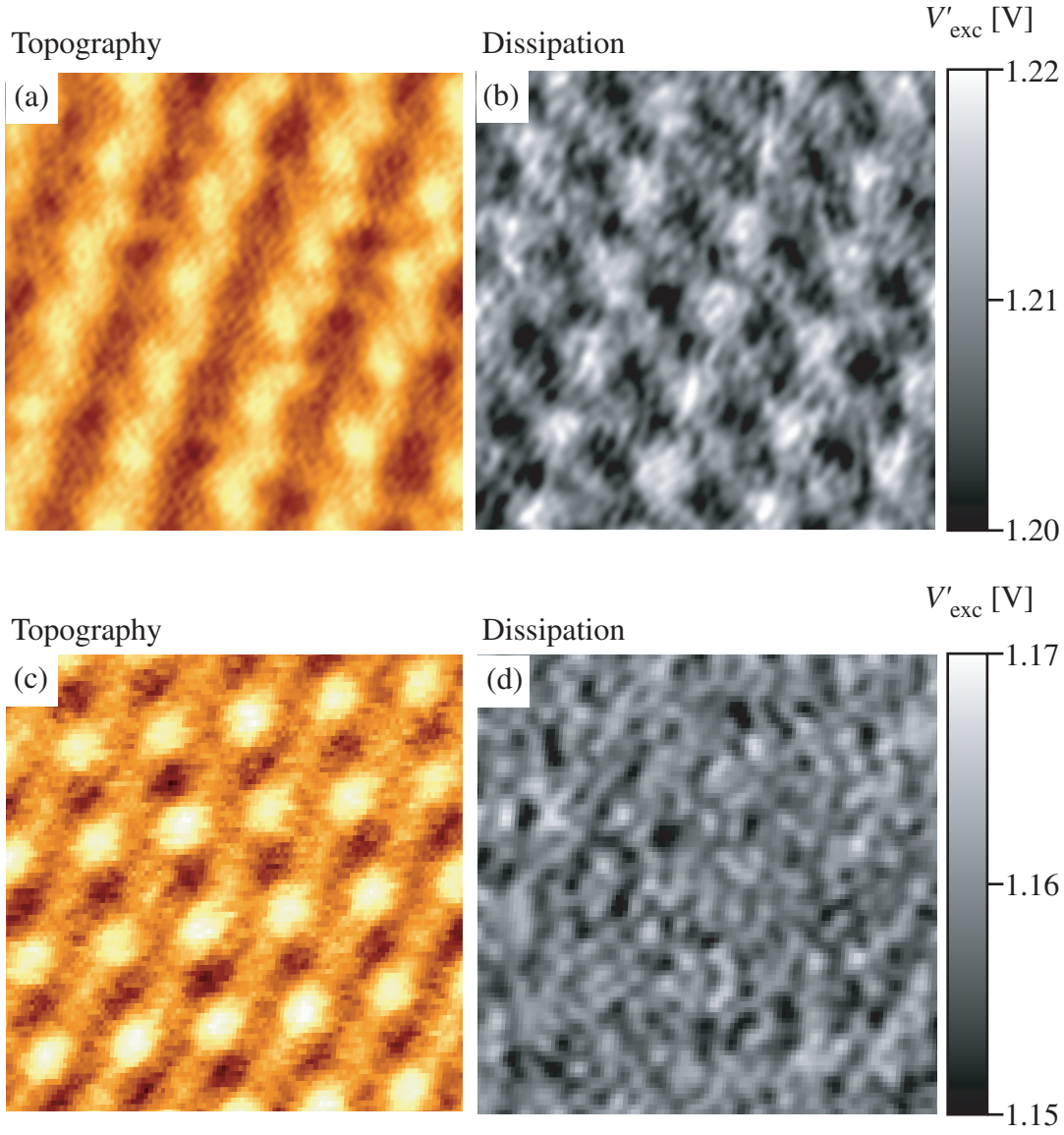

Figure 6.5: (a) Topographic and (b) dissipation images of δ phase structure (4.5 nm $\times$ 4.5 nm, $\Delta f = -70$ Hz, $A_{\mathrm{p\text{-}p}} = 10$ nm). (c) Topographic and (d) dissipation images of ε phase structure (4.5 nm $\times$ 4.5 nm, $\Delta f = -50$ Hz, $A_{\mathrm{p\text{-}p}} = 10$ nm).

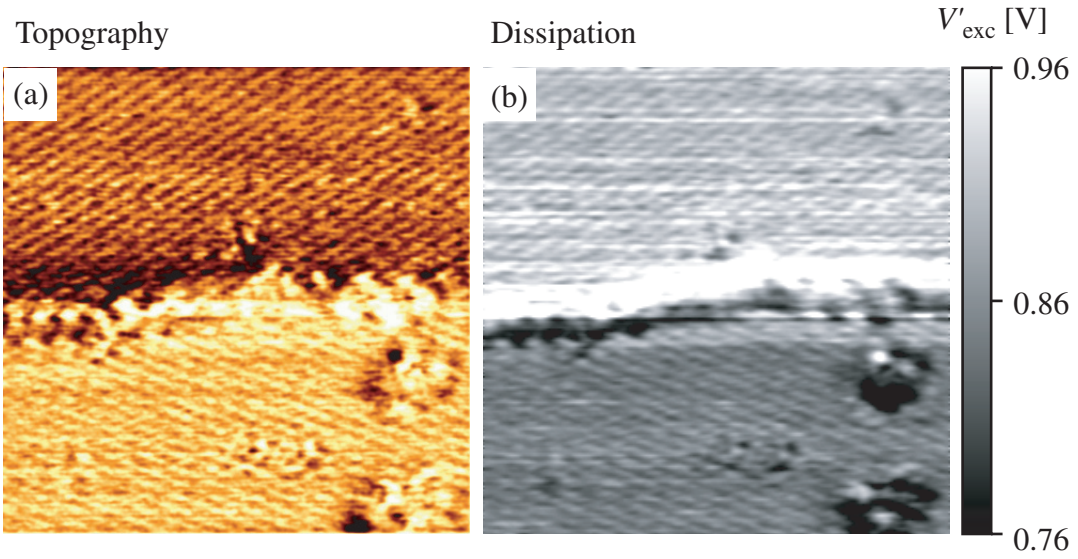

Figure 6.6: (a) Topographic and (b) dissipation images of δ phase structure (30 nm $\times$ 30 nm, $\Delta f = -250$ Hz, $A_{\text{p-p}} = 10$ nm).

molecular rows, while the dissipation image taken on ε phase (Fig. 6.5(d)) showed almost no contrasts. These images were taken with the same tip and the same sample. The observed tendency was reproduced even with a different tip and a different sample. Moreover, similar experiments were performed on the C_{10} monolayer and the result also confirmed this tendency. Therefore, the observed difference in the dissipation contrasts should be caused by the difference in the molecular packing arrangements.

The result indicated that some of the molecules in δ phase are relatively loosely bound by the surrounding molecules and their molecular fluctuations induced by the tip-sample interactions result in the molecular-scale dissipation contrasts. In fact, the imaging conditions during the FM-DFM imaging of δ phase (Fig. 6.4(a)) were more unstable than that for ε phase. From these results, it was demonstrated that the mechanical property of the individual molecules depends on the molecular packing arrangement and such a slight difference in the mechanical property can be evaluated from the molecular-scale dissipation contrast.

Figure 6.6 shows topographic and dissipation images taken on the two different δ phase domains separated by a single-atomic height gold step. Both images clearly showed molecular-scale contrasts, revealing the different orientations of the two domains. During the FM-DFM imaging, the magnitude of dissipation was suddenly changed near the gold step due to the atomic-scale tip change. However, the molecular-scale dissipation contrasts itself were maintained even after the tip change. On the other hand, no significant difference was found in the topographic

(a) Phthalocyanine (Pc) (b) Copper-phthalocyanine (CuPc)

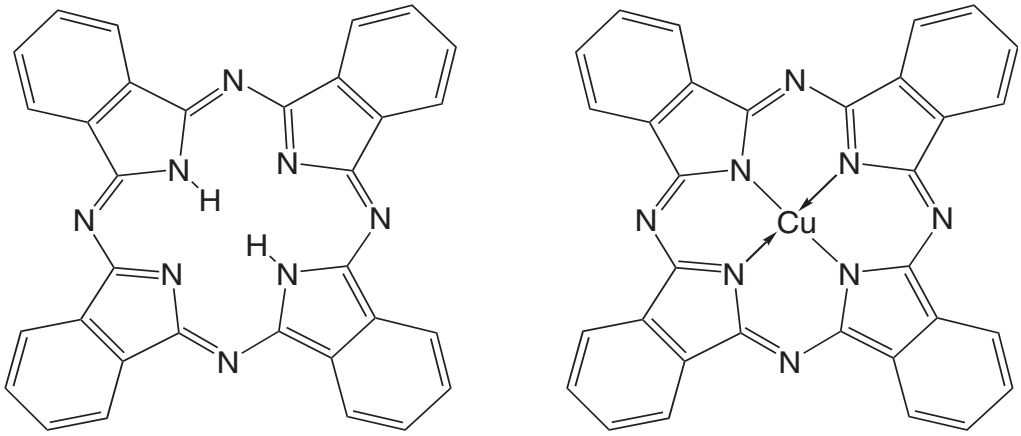

Figure 6.7: Molecular structures of (a) phthalocyanine (Pc) and (b) copper-phthalocyanine (CuPc).

image before and after the tip change.

The result showed that the total amount of energy dissipation can be affected not only by the surface properties but also by the atomic-scale tip configurations.[88] Thus, in order to extract some information about the surface properties from the absolute value of the energy dissipation, it would be required to use atomically well-defined ideal probes. However, the molecular-scale dissipation contrasts itself were reproducibly obtained independently of the tip conditions. This result suggested that at least the molecular-scale dissipation contrasts can be used for the investigations on the molecular-scale mechanical properties.

6.4 Copper-phthalocyanine Thin Films on MoS_2(0001) Surfaces

6.4.1 Copper-phthalocyanine

In 1907, phthalocyanine (Pc) was first found as a dark insoluble by-product during the preparation of *ortho*-cyanobenzamide from phthalimide and acetic acid.[297] Twenty years later, copper-phthalocyanine (CuPc) was similarly found as an extremely stable blue by-product during the reaction of *ortho*-dibromobenzene with copper cyanide in refluxing pyridine.[298] Studies on these by-products were first started from academic and industrial interests, which produced several remarkable papers describing the structure of Pc and the synthesis of some of its metal derivatives.[299–304]

Figure 6.7 shows molecular structures of Pc and CuPc. Pc is a symmetrical

macrocyclic compound which consists of four iminoisoindoline units with a central cavity of sufficient size to accommodate various metal ions. It is possible to place about seventy different elemental ions in the central cavity of Pc.[305] Most metal ions (e.g. Cu^{2+}, Co^{2+}, Fe^{2+}) do not cause a significant distortion of the macrocycle while certain ions (e.g. Pb^{2+}) are too large to be accommodated in the cavity and hence they lie above the plane of the Pc ring. Since the structures of Pcs are very similar to that of porphyrine ring system, Pcs were assumed to exhibit similar aromatic behavior owing to its planar conjugated array of 18 π-electrons, which promoted vast amount of studies on the electrical and optical properties of this material.

Pc derivatives are quite stable against the heat and chemicals and they show a wide variety of colors depending on their crystal structures and central metal ions. Thus the potential of Pcs as pigments was obvious even in the early stage of their studies, which started the manufacture of CuPc in 1935 as a blue colorants. Today, many thousands of tons of Pcs are produced per year to satisfy the growing demands for blue and green colorants in the photographic, printing, plastics and textile industries. Besides that, today's increasing interests in organic electronics motivated researchers to study the semiconducting nature of Pc derivatives for the future novel applications such as organic FETs.

So far, several techniques were applied to visualize molecular structures of Pcs. Müller reported the first direct image of Pc derivatives using field emission microscopy (FEM) where the four-leaf structure of a CuPc molecule was clearly visualized.[306] Uyeda *et al.* used high-resolution electron microscopy to image the detailed molecular structure of chlorinated CuPcs.[307] The extreme stability of this compound allows the images to be obtained before the destruction of the material by the intense electron beam needed for such high resolutions. Later, Pc derivatives deposited on substrate surfaces were directly imaged by STM on a molecular-scale resolution.[308]

The detailed X-ray diffraction studies revealed that CuPc can take many different crystal structures. Among them, industrially important crystal structures are β-form[309–311] and α-form.[312] Figure 6.8 shows schematic drawings of these structures. The β-form is monoclinic and belongs to the $P2_1/a$ space group with two Pc molecules per unit cell while the α-form is monoclinic and assigned to the C2/c space group with four molecules per unit cell. In most cases, β-form is thermodynamically more stable than α-form except for the small particles or thin films where surface effects play an important role. Besides the two structures, many metastable crystal forms were so far reported such as γ-form,[297] ε-form,[298,302,313] δ-form,[314] π-form,[310] ρ-form,[315] X-form,[316] and R-form[317] although most of these metastable structures have not been well confirmed yet because of the difficulty in obtaining large single

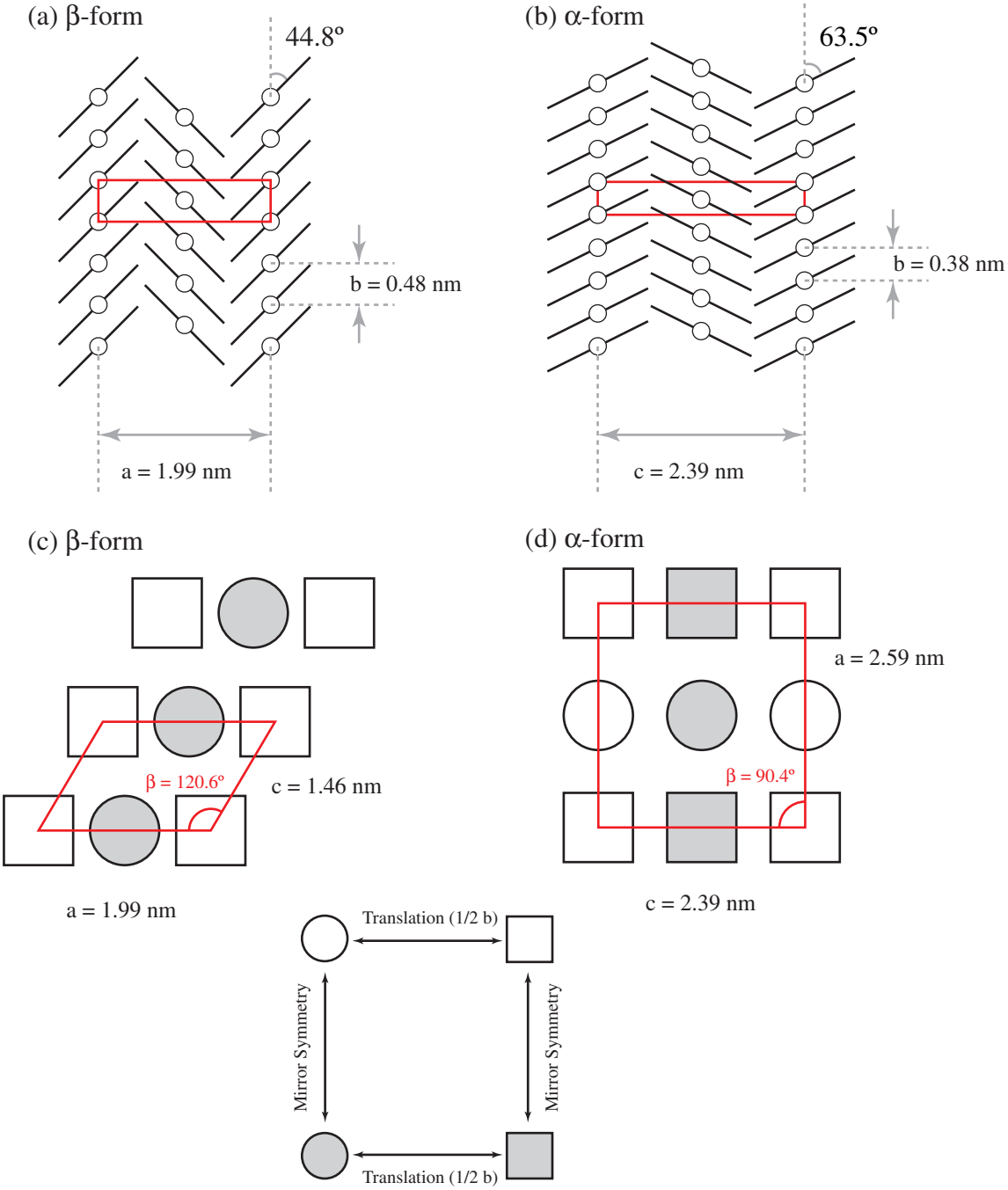

Figure 6.8: Schematic drawings of CuPc crystals. (a),(c) β-form. (b),(d) α-form.

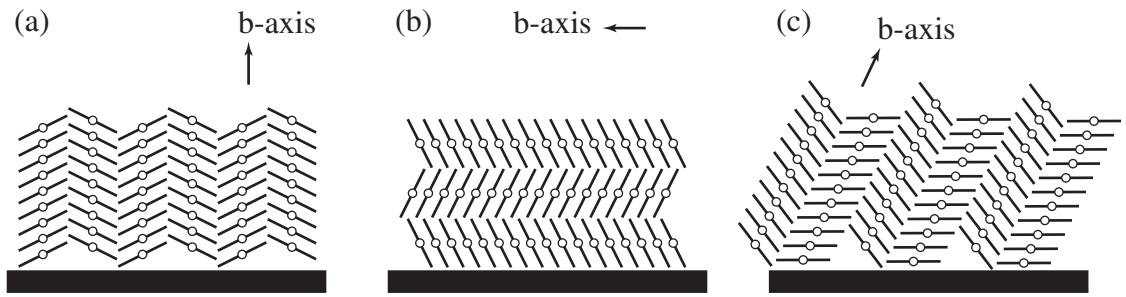

Figure 6.9: Schematic drawings of previously reported growth models of CuPc films. (a) Thick (> 1 μm) films. (b) Thin (< 1 μm) films deposited slowly on a substrate which does not strongly interact with the first monolayer. (c) Thin film deposited onto a substrate that interacts strongly with the initially deposited monolayer.

crystals for X-ray diffraction studies.

For most physical studies and applications the small fragile crystals obtained from Pcs are unsuitable. Instead, thin films deposited on an appropriate substrates are desired. Thin films of Pc derivatives can be formed by various methods such as vacuum deposition, Langmuir-Blodgett method, spin-coating, and electrochemical deposition. Among these techniques, vacuum deposition is the most suitable method to obtain highly crystalline films with an well-controlled thickness. Thick (> 1 μm) films of CuPc deposited on a gold or a glass substrate at room temperature consists of α-form crystal in which the b-axis is approximately perpendicular to the substrate (Fig. 6.9(a)).[318] However, thin films of CuPc (< 1 μm) slowly deposited onto amorphous substrates (e.g. glass) are composed of α-form crystal with the b-axis parallel to the substrate (Fig. 6.9(b)).[318–320] Such tendency is true only when the first CuPc monolayer does not strongly interact with the substrate.

By choosing an appropriate substrate and sample preparation condition, the interaction of the substrate surface with the initially deposited CuPc monolayer can influence the resulting structure of the deposited film, which is called epitaxial growth. Pioneering work by Ashida showed the epitaxial growth of CuPc thin films on KCl(001) surface, where the electrostatic interaction between the K^+ ions and the electron-rich *meso*-nitrogens plays an important role.[321,322] The epitaxial film consists of α-form crystal with the b-axis tilted about 26° from the surface normal (Fig. 6.9). Similar epitaxial growth were observed for other substrates which possess a strong affinity with CuPc molecule such as mica[321] and graphite.[323]

However, true epitaxial film growth is not obtained because correlation of the CuPc crystal packing with the substrate surface lattice is achieved solely for the initial stage of the film growth process. Thus only the orientation of the microcrystallites is controlled by the surface and not their complete structural morphology.

(a) Close-packed phase

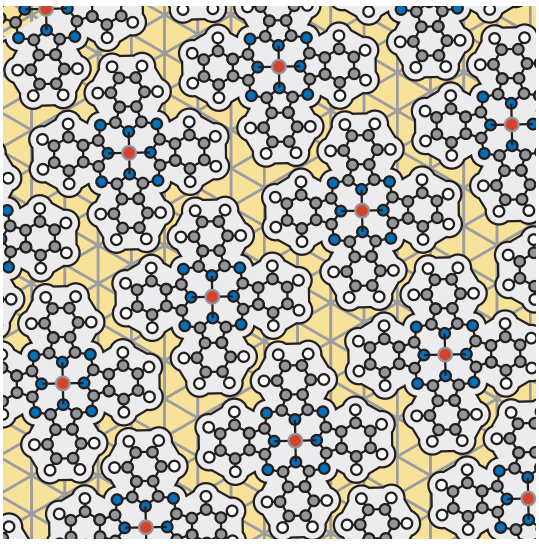

(b) Row-like phase

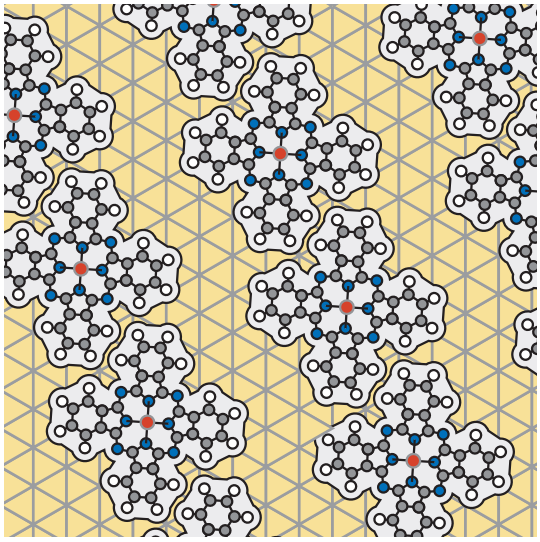

Figure 6.10: Schematic models of the molecular packing arrangements in the CuPc monolayer epitaxially grown on the $MoS_2(0001)$ surface.[324] (a) Close-packed phase (a = 1.37 nm, b = 1.42 nm, $\beta = 90°$). (b) Row-like phase (a = 1.38 nm, b = 1.90 nm, $\beta = 96.6°$).

Although numerous studies of the monolayer packing arrangement for CuPc on high-affinity surfaces have been published so far,[323–328] the detailed description of transition between the true epitaxial growth in the initial stage and subsequent crystal growth process has never been achieved. FM-DFM is expected to be quite suitable for such a study due to its molecular-scale resolution in real space even on insulating surfaces.

In this study, CuPc thin films deposited on $MoS_2(0001)$ surfaces were used. The epitaxial growth process of the film have been studied by several different surface analysis tools. Hara *et al.* first confirmed the epitaxial growth of CuPc films on MoS_2 surfaces from the reflection high-energy electron diffraction (RHEED) experiments.[329] Then LEED studies by England *et al.* indicated that the first monolayer initially formed on MoS_2 surface consists of large domains with a size of around 50 – 100 μm suggesting the extremely good molecular migration on the substrate.[330] Moreover, sub-molecular resolution STM images presented by Ludwig *et al.* enabled unambiguous determination of the detailed molecular packing arrangements.[324] They revealed the existence of two different packing arrangements called "close-packed phase" and "row-like phase" as shown in Fig. 6.10. Similar packing arrangements to close-packed phase were also confirmed by LEED and angle-resolved ultraviolet photoelectron spectroscopy (ARUPS),[331] while row-like phase has never been observed by other techniques. This fact suggests that row-

like phase might be a metastable structure existing only in the initial stage of the epitaxial growth process.

The inclination angle of the molecules with respect to the substrate remains still unclear. Although ARUPS result by Okudaira *et al.* showed best agreement with the inclination angle of 6°, the authors ascribed it to the temperature effect on ARUPS measurements[332] and concluded that the molecule is flat lying on the surface.[331] However, since such a spectroscopic method can only provide "averaged" inclination angles of molecules, it is difficult to exclude the existence of some distributions in molecular inclinations. Sub-molecular resolution STM images neither can determine the exact molecular inclination angle because the STM image is strongly dependent on the electrical property of the molecules.[333–335] In addition, there have been only a few studies published on high-resolution STM imaging of CuPc molecules on $MoS_2(0001)$ surfaces.[324]

FM-DFM imaging of CuPc molecules have never been performed so far. Since CuPc has a widely-delocalized π-electron orbitals sticking out of the molecular plane, strong chemical interaction between the tip and the sample is expected. Thus it is of great interest whether or not the molecular-scale topographic contrast reflects the spatial distribution of the molecular orbitals. In addition, since the molecules are relatively loosely-packed as shown in Fig. 6.10(a), large molecular fluctuation may be induced by the tip-sample interaction. Therefore, its relation to the molecular-scale dissipation contrasts is of particular interest.

6.4.2 Sample Preparation

The CuPcs (Tokyo Kasei Kogyo Co., Ltd) were purified by sublimation under vacuum environment ($< 10^{-3}$ Pa) before use. The MoS_2 substrate was cleaved in air and then introduced into the sample preparation chamber of UHV-SPM system (Fig. 4.1). The sample was annealed at 200°C for 1 h in order to reduce the surface contaminations. The CuPc thin films were prepared by vacuum deposition at a substrate temperature of 100°C in the sample preparation chamber. The vacuum pressure during the deposition was maintained below 10^{-6} Pa. The deposition rate was about 1.5 nm/h, which was monitored by a quartz oscillator. Since the deposition chamber was directly connected to the UHV-FM-DFM chamber, the film was not exposed to the air before FM-DFM imaging.

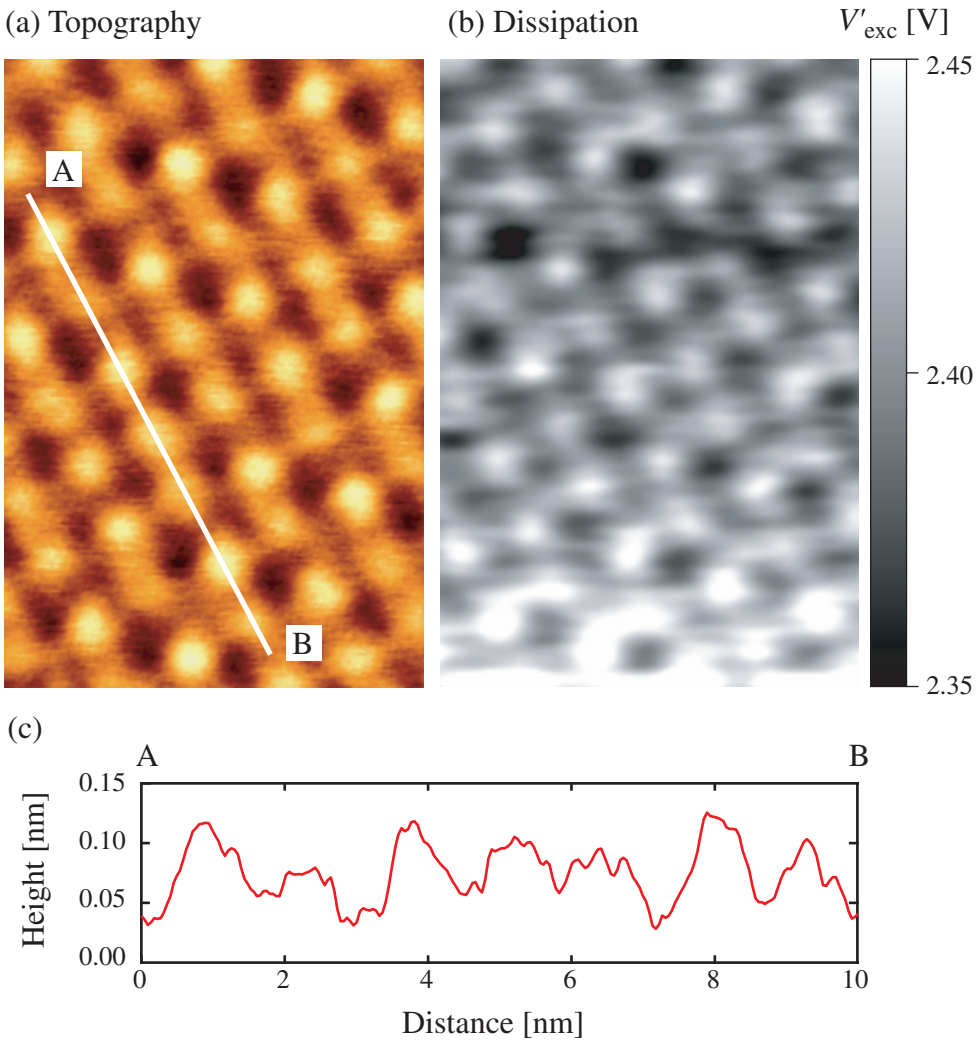

Figure 6.11: (a) Topographic and (b) dissipation images of the CuPc monolayer on $MoS_2(0001)$ surface (8 nm × 12 nm, $\Delta f = -40$ Hz, $A_{\text{p-p}} = 11$ nm). (c) A cross-sectional plot measured along the bright line A – B shown in (a).

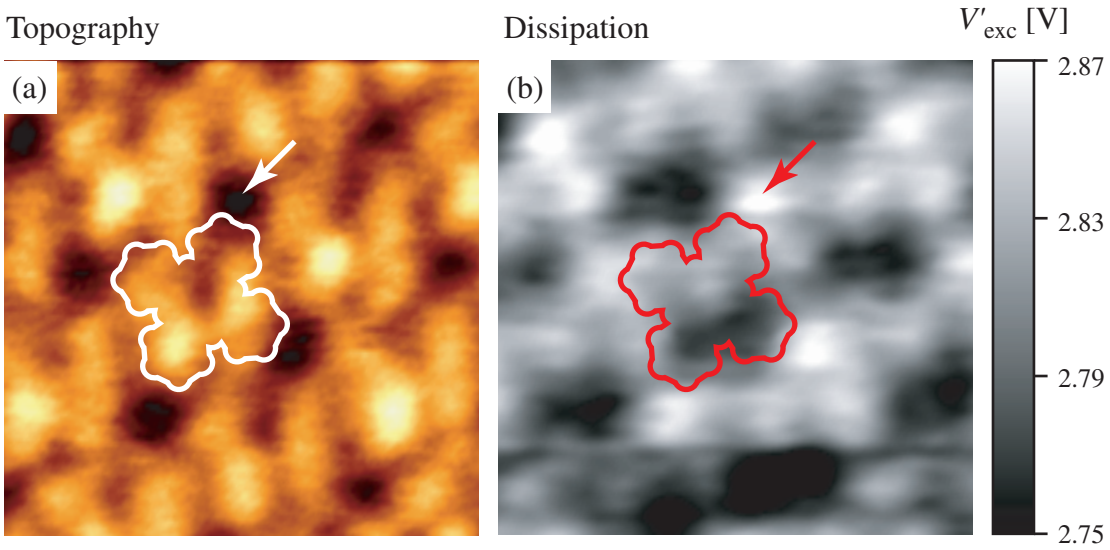

Figure 6.12: (a) Topographic and (b) dissipation images of the CuPc monolayer on the $MoS_2(0001)$ surface (4 nm × 4 nm, $\Delta f = -45$ Hz, $A_{p\text{-}p} = 11$ nm). Both images clearly showed sub-molecular scale contrasts.

6.4.3 Results and Discussion

Molecular Height Variation

Figure 6.11 shows the topographic and dissipation images of the CuPc monolayer on the $MoS_2(0001)$ surface. The topographic image clearly showed individual molecules in the close-packed phase (Fig. 6.10(a)). On the other hand, the dissipation image showed inverted contrast with respect to the topographic image. Besides, the dissipation contrast was discontinuously changed at the lower part of this image probably due to the atomic-scale tip change.[88] The origin of the inverted dissipation contrast will be discussed later in this section.

Figure 6.11(c) shows a cross-sectional plot measured along the bright line A – B indicated in Fig. 6.11(a), revealing the existence of the molecular height variation. The magnitude of the molecular height variation was about 0.05 nm. There could be found no long-range regularity in the molecular height variation. These results revealed that the molecules are not completely flat lying on the surface but they are slightly tilted from the substrate surface as suggested by the ARUPS study.[331]

Sub-Molecular Scale Contrasts

Figure 6.12(a) shows the topographic and dissipation images taken on the same sample as shown in Fig. 6.11. The topographic image showed clear sub-molecular scale contrast, revealing the four-leaf structure of the CuPc molecule. The image also showed an asymmetric feature within the molecule. This result is consistent

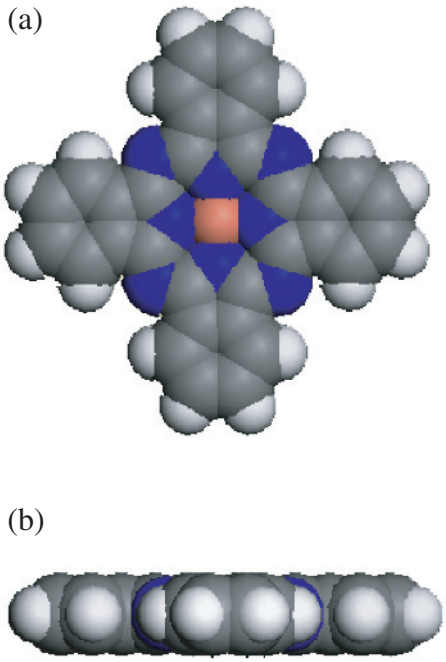

Figure 6.13: The CPK model of the CuPc molecule. (a) Top view. (b) Side view.

with the expectation that the molecule is slightly tilted from the substrate surface. The central part of the CuPc molecule was imaged as an "apparent hole", which was depressed by about 0.05 – 0.06 nm from the average molecular plane. The dissipation image also showed clear sub-molecular scale contrast. The asymmetric feature within the molecule was more evident in the dissipation image than that for the topography image. The maxima of the energy dissipation were found at the inter-molecular spaces as indicated by the arrows in Fig. 6.12. This result is consistent with the fact that dissipation image obtained with a lower resolution showed inverted contrast with respect to the corresponding topographic image (Fig. 6.11(b)). The absolute value of the energy dissipation was drastically changed at the lower part of the image, suggesting the atomic-scale tip change.[88] Such an atomic-scale tip change, which was often observed during high-resolution FM-DFM imaging, did not much affect the topographic contrast.

Since the copper ion is small enough to be fully accommodated in the central cavity of the Pc ring, the molecule has a completely planer structure as shown in Fig. 6.13. On the other hand, the van der Waals radii for carbon, nitrogen and copper atoms are 170, 155 and 140 pm, respectively. Thus the observed apparent hole (50 – 60 pm in depth) at the center of the molecule cannot be explained simply by the molecular structure.

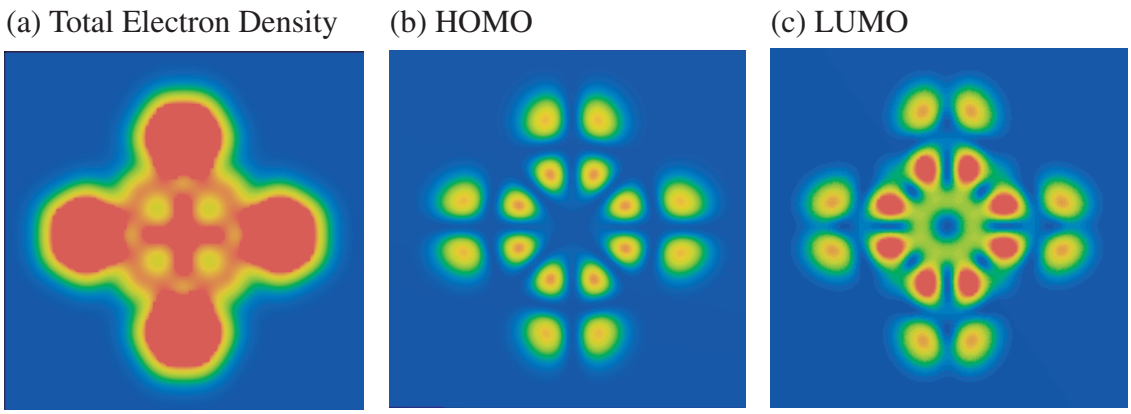

Figure 6.14: Two-dimensional maps of (a) total electron density, (b) HOMO and (c) LUMO of CuPc molecule plotted along the surface located 0.25 nm above the molecular plane, which was calculated based on the density functional theory. The HOMO and LUMO distribution shows low density at the center of the molecule while total electron density does not.

Such an apparent hole was also found in the previously reported STM images of CuPcs on various surfaces such as $MoS_2(0001)$,[324] graphite,[324] Au(111)[333,334] and Cu(100).[336] The formation mechanism of these STM contrasts have been explained by taking account of the spatial distribution of the molecular orbitals.[333,334,336] Figure 6.14 shows two-dimensional maps of the total electron density, highest occupied molecular orbital (HOMO) and least unoccupied molecular orbital (LUMO) plotted along the surface located 0.25 nm above the average molecular plane*. The HOMO and LUMO distributions show the lower density at the center of the molecule while the total electron density does not. Since the magnitude of the tunneling current is strongly dependent on the distribution of the HOMO and LUMO orbitals, it is quite natural that the STM image should show an apparent hole at the center of the CuPc molecule.

As for FM-DFM, when the tip front atom interacts with the chemically reactive frontier orbitals such as HOMO and LUMO, a strong short-range attractive interaction would take place due to the hybridization of the electron orbitals as pointed out by Tomitori *et al.*[95] Therefore, the sub-molecular scale topographic contrasts in FM-DFM images can be affected by the spatial distribution of the chemically reactive frontier orbitals.

One of the possible explanations for the large dissipation at the inter-molecular space is described as follows. When the tip is located just on top of a molecule, the single molecule will be fluctuated by the tip-sample interaction as shown in Fig.

*The spatial distribution of the molecular orbitals were calculated based on the density functional theory (DFT) using Materials Studio (Accelrys) with DMol^3 package.

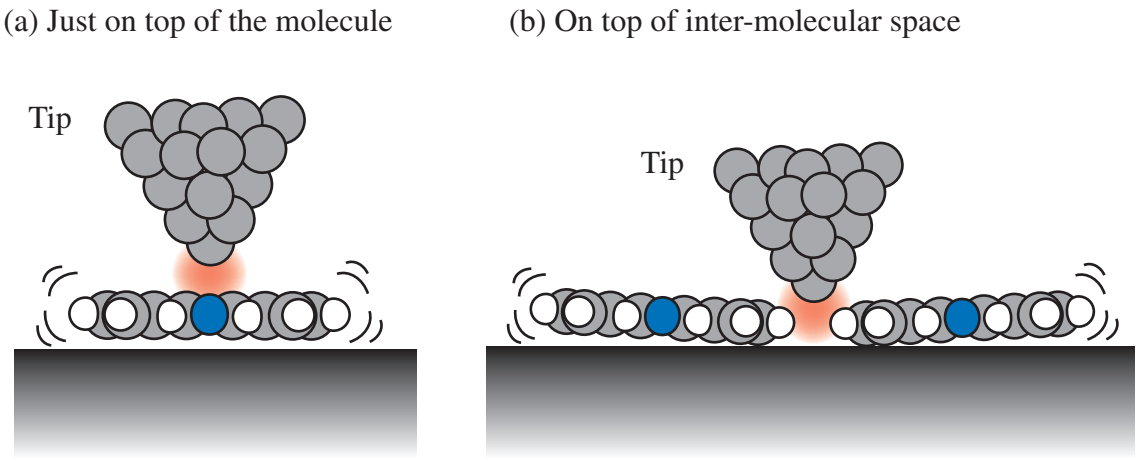

Figure 6.15: Schematic models to explain the origin of the large energy dissipation at the intermolecular space. (a) When the tip is located just on top of a molecule, the single molecule will be fluctuated by the tip-sample interaction. (b) When the tip is located above the inter-molecular space, the neighboring two molecules will be fluctuated, resulting in a larger energy dissipation.

6.15(a). Then the kinetic energy of the molecular fluctuation will be dissipated through the surrounding molecules and underlying substrate due to the stochastic dissipation process. On the other hand, when the tip is located above the inter-molecular space, the adjacent two molecules will be fluctuated, resulting in a larger energy dissipation. Moreover, when the tip is positioned just over the inter-molecular space indicated by the arrows in Fig. 6.12, four adjacent molecules will be involved with the dissipation process, leading to the largest energy dissipation. Therefore, the result suggested that the molecular-scale dissipation contrasts are affected by the number of the molecules interacting with the tip.

Micrometer-Scale Grain

In order to investigate the difference in structure and properties between the CuPc monolayer and the multilayered film, a CuPc thin film was prepared with a longer deposition time (1 h) than that for the monolayer shown in Fig. 6.11 (10 min). Figures 6.16(a) and (b) are the topographic and dissipation images taken on this sample, showing some micrometer-scale grains. The height of these grains estimated from the cross-sectional plot of the topographic image was about 10 nm, which corresponds to the thickness of about 30 molecular layers (MLs). The scanned area of the images was so large (2 μm $\times$ 2 μm) that the effect of the substrate inclination cannot be neglected. In this experiment, the tip-sample distance regulation was made by simple proportional feedback control so that the steady-state error could not be completely excluded. The corresponding dissipation image (Fig. 6.16(b)) also

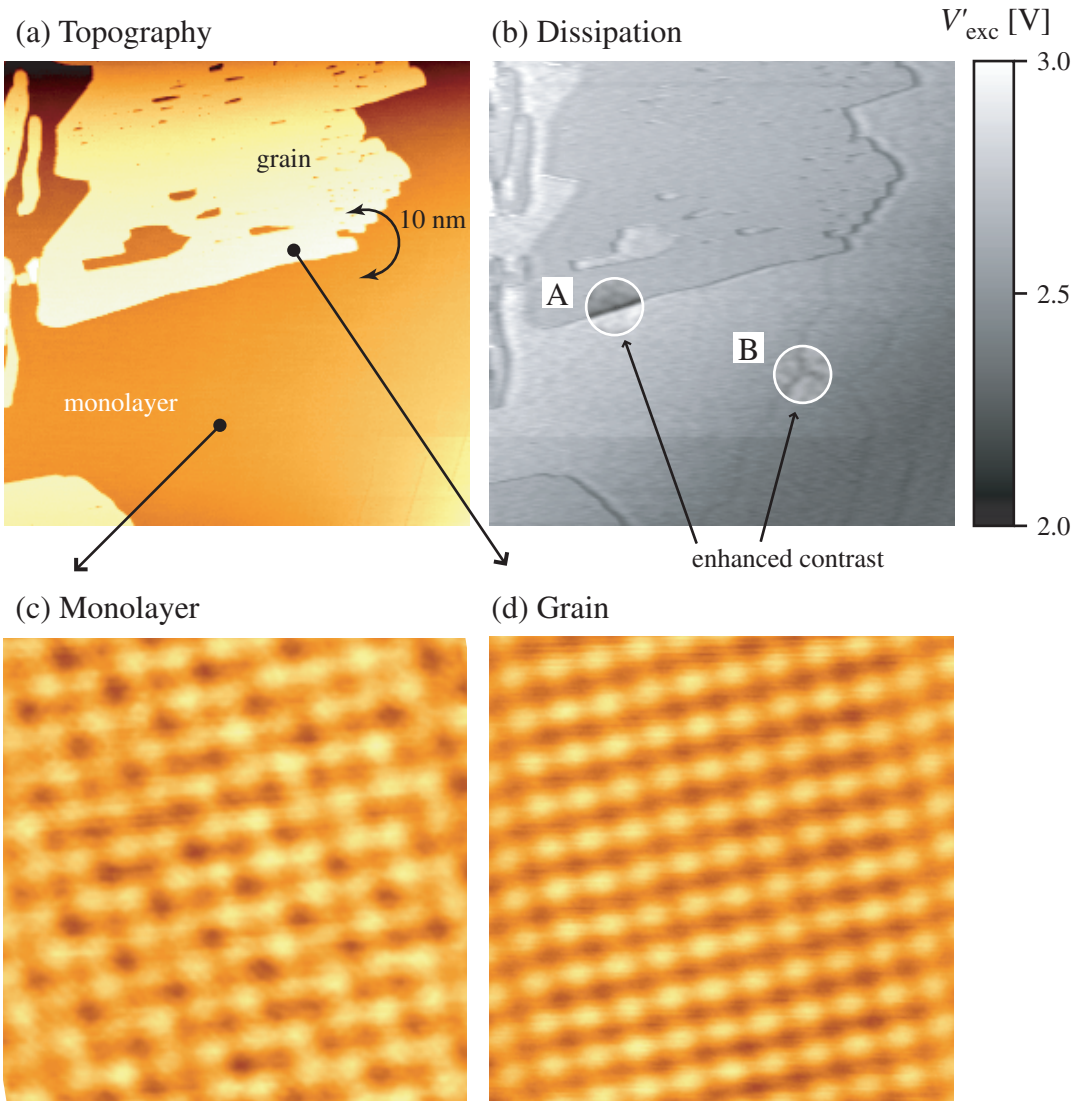

Figure 6.16: (a) Topographic and (b) dissipation images of the CuPc thin film on the MoS_2 surface (2 μm $\times$ 2 μm, $\Delta f = -25$ Hz, $A_{\mathrm{p\text{-}p}} = 12.5$ nm). The MoS_2 surface was completely covered with the CuPc monolayer. Then the micrometer-scale grains are formed on top of the monolayer. Molecularly-resolved FM-DFM images taken on (c) the monolayer and (d) the grain (15 nm $\times$ 15 nm, $\Delta f = -30$ Hz, $A_{\mathrm{p\text{-}p}} = 14$ nm).

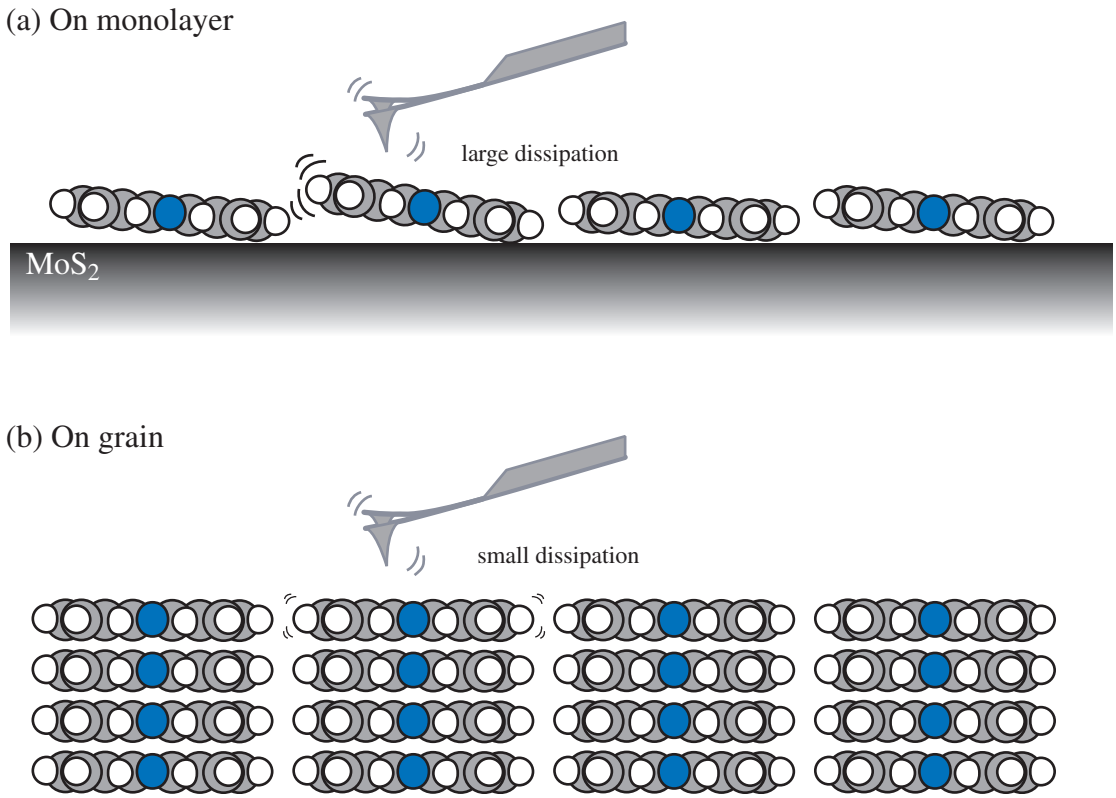

Figure 6.17: Schematic models to explain the energy dissipation mechanism on the CuPc monolayer and the grain.

showed the effect of the substrate inclination and hence the contrast was not clear enough to show the important feature. Thus the regions surrounded by the white circles A and B were shown with an enhanced contrast. The dissipation contrast in the circle A revealed that the energy dissipation on the grain is lower than that on the monolayer. In addition, some dark lines were found in the circle B.

Figures 6.16(c) and (d) are the molecularly-resolved FM-DFM images taken on the CuPc monolayer and the grain, respectively. The monolayer showed molecular-scale height variation, which is consistent with the result shown in Fig. 6.11. The FM-DFM image taken on top of the grain revealed that the packing arrangement seen in the monolayer is surprisingly well maintained even over such a thick multilayered grain. However, the molecular height variation on the grain surface was much smaller than that on the monolayer.

The molecules in the monolayer are slightly tilted from the substrate surface and their tilt angle is not completely uniform. Thus they are expected to be loosely bound by the surrounding molecules and the MoS_2 surface. Such a loosely bound molecule should be easily fluctuated by the tip-sample interaction (Fig. 6.17(a)). On the other hand, the molecular ordering on the large grain was much better than that

for the monolayer. This result suggested that the molecules on the grain are more tightly bound by the surrounding molecules. In addition, they may be stabilized by the crystalline field of the large grain. Such a tightly bound molecule should be mechanically stable against the tip-sample interaction force (Fig. 6.17(b)). Therefore, the large dissipation found on the monolayer should be ascribed to the molecular fluctuation induced by the tip-sample interaction. The result strongly supported the expectation that the mechanical property of the surface may be evaluated from the energy dissipation contrast.

Domain Boundary

Figures 6.18(a) and (b) show the topographic and dissipation images taken on the area indicated by the white circle B in Fig. 6.16(b). The image revealed that the dark lines found in the dissipation image shown in Fig. 6.16(b) corresponds to the boundaries of the monolayer domains A, B and C. The topographic image (Fig. 6.18(a)) showed that the domain A has a different orientation from those of the domains B and C.

The dissipation image (Fig. 6.18(b)) revealed that the energy dissipation on the defects and the domain boundaries is smaller than that on the monolayer. The dissipation measured on the domain B and C is slightly smaller than that on the domain A, suggesting that the energy dissipation is dependent on the orientation of the molecular packing arrangements with respect to the tip. Such a strong dependence of the energy dissipation on the tip geometry was also confirmed by the drastic contrast change due to the atomic-scale tip change (Fig. 6.18(b)).

Figure 6.18(c) shows FM-DFM image taken on the same area after several scans. The white arrow in each of Figs. 6.18(a) – (c) indicates the same defect which can be used to identify the relative position of these images. The image revealed that the molecular arrangements at the domain boundaries were improved and some defects indicated by the white circles were disappeared during the FM-DFM imaging.

Figure 6.18(d) is the FM-DFM image taken on the same area with a much smaller frequency shift (-5 Hz). The image showed inverted contrast at the domain boundaries with respect to the image shown in Fig. 6.18(c). The origin for this contrast inversion is probably the same as pointed out in Fig. 5.22. Thus the domain boundaries and the defects should correspond to the absence of the molecules.

The observed smaller energy dissipation at the domain boundaries and the defects is explained by the model shown in Fig. 6.19. When the tip-sample separation is relatively large, the weak long-range interaction will induce a small fluctuation of the molecules, leading to a relatively small energy dissipation (Fig. 6.19(a)). In this case, the dissipation variation at the domain boundary becomes relatively dull (Fig.

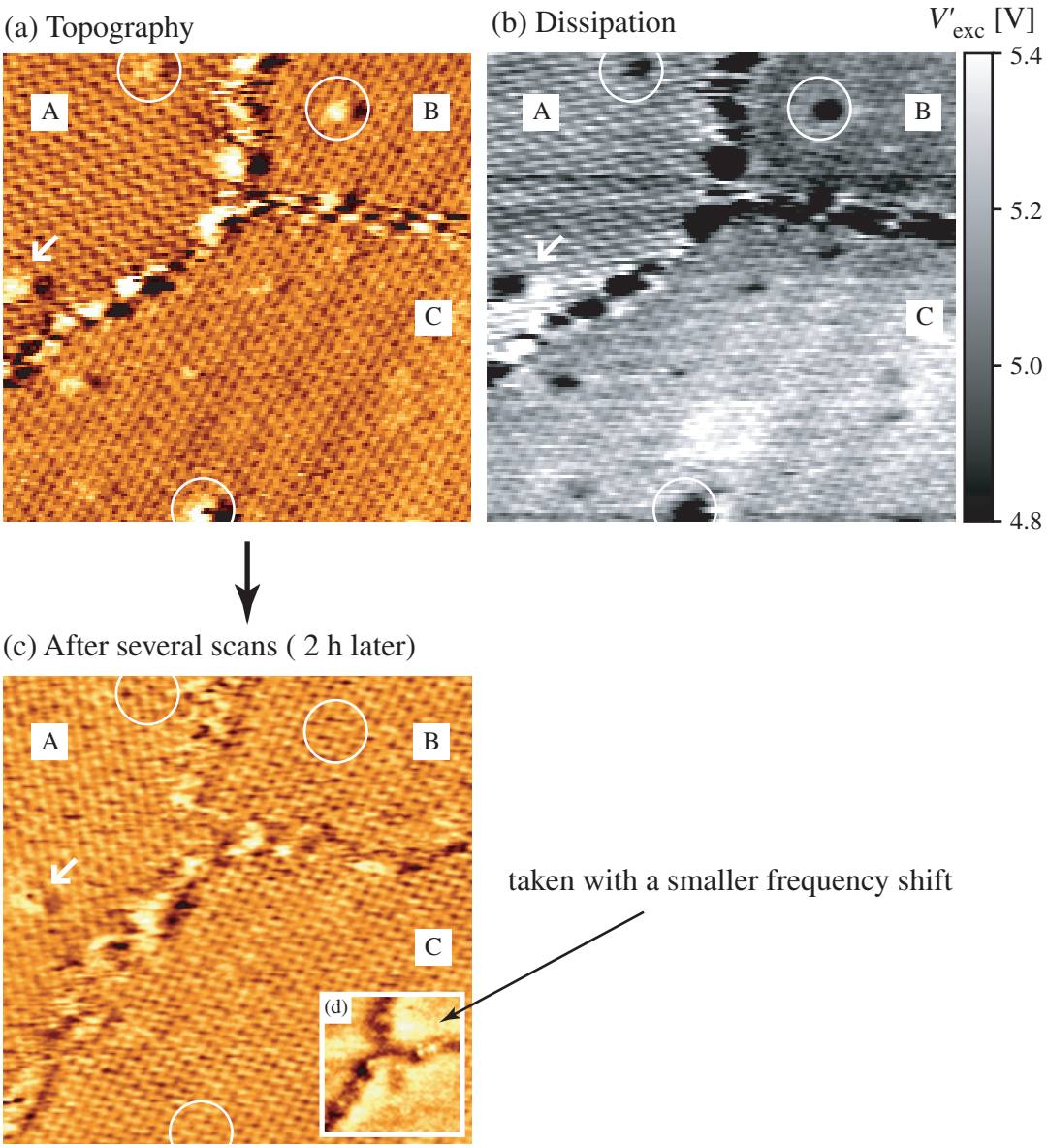

Figure 6.18: (a) Topographic and (b) dissipation images of the CuPc monolayer on the $MoS_2(0001)$ surface (50 nm × 50 nm, $\Delta f = -50$ Hz, $A_{\text{p-p}} = 14$ nm). (c) FM-DFM image taken on the same area after several scans (50 nm × 50 nm, $\Delta f = -55$ Hz, $A_{\text{p-p}} = 12.5$ nm). (d) FM-DFM image taken on the same area with a much smaller frequency shift (50 nm × 50 nm, $\Delta f = -5$ Hz, $A_{\text{p-p}} = 11$ nm).

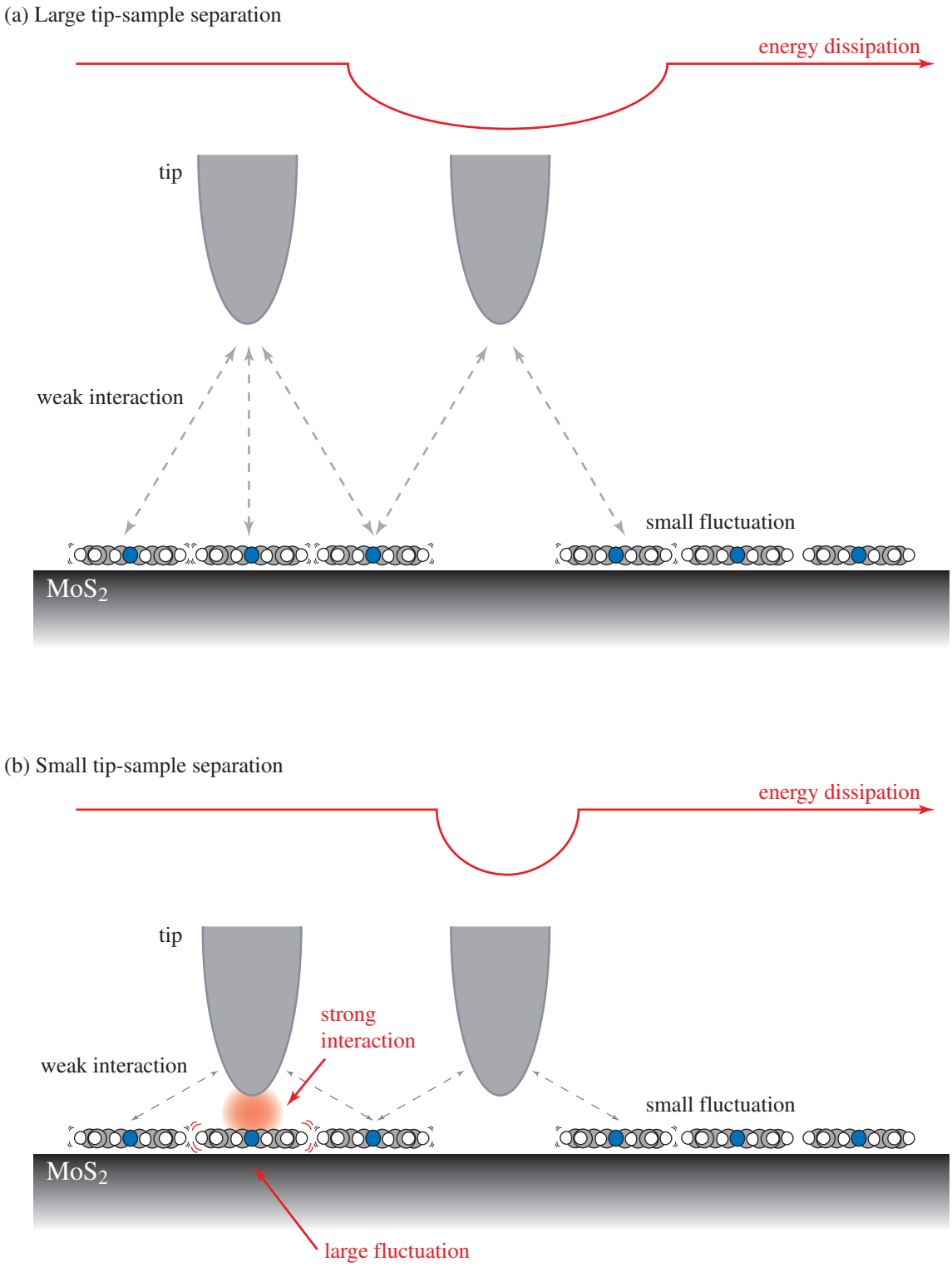

Figure 6.19: Schematic models to explain the observed small dissipation at the domain boundaries and the defects. (a) With a larger tip-sample separation, relatively small molecular fluctuations are induced by the weak long-range interactions. (b) With a smaller tip-sample separation, relatively large molecular fluctuations are induced by the strong short-range interactions.

6.16(b)). When the tip-sample separation is relatively small, the tip will strongly interact with an underlying molecule and induce a large molecular fluctuation, resulting in a larger energy dissipation (Fig. 6.19(b)). Thus the dissipation contrast shows a much sharper variation at the domain boundary (Fig. 6.18(b)).

The mechanism for the observed tip-induced surface modification can be understood from the analogy to the annealing effect. In general, molecular ordering is often improved by annealing treatment. This is because such an heating treatment will give the molecules some extra energy to break up the original packing arrangement to form an well-ordered structure with a lower free energy. On the other hand, in this experiment, the molecules are given extra energy through the dissipative tip-sample interaction. In that sense, the observed surface modification can be regarded as "local annealing" induced by the tip-sample interaction. Furthermore, this result is the direct evidence which confirms that some of the vibration energy of the cantilever is transformed into the kinetic energy of the molecular fluctuation through the dissipative tip-sample interactions.

6.5 Summary

In this chapter, the formation mechanisms of the molecular-scale contrasts in topography and dissipation were experimentally studied in relation to the chemical and mechanical properties of the organic surfaces.

Molecular-Scale Topographic Contrasts

It was revealed that the molecular-scale topographic contrast represents not only surface height variations but also chemical property of the surface.

1. The molecular-resolution topographic images of the alkanethiol SAMs clearly showed molecular height variations in the two different c(4×2) superlattice structures. This result revealed that the molecular-scale topographic contrast taken on a chemically inert surface represents a true surface height variation.

2. The sub-molecular-resolution topographic image of the CuPc molecules showed good agreement with the spatial distribution of the frontier orbitals (HOMO and LUMO) of CuPc. This result revealed that the sub-molecular scale topographic contrast can be affected by the short-range attractive interaction originated from the chemical interaction between the tip front atom and the molecular frontier orbitals.

Molecular-Scale Dissipation Contrasts

It was revealed that the molecular-scale dissipation contrast represents the magnitude of the molecular fluctuation induced by the tip-sample interaction. The results obtained in this chapter strongly supported the expectation that the mechanical property of the surface can be evaluated by the energy dissipation measurement.

1. The dissipation image taken on the δ phase SAM clearly showed molecular-scale contrast while the dissipation image taken on the ε phase SAM showed almost no contrast. This result revealed that the mechanical property of the molecules can show a variation even in a closely-packed monolayer reflecting the subtle difference in the molecular packing arrangement. In addition, it was found that such a slight difference in the mechanical property can be differentiated from the molecular-scale dissipation contrasts.

2. The molecular-resolution dissipation image of the CuPc monolayer showed the largest energy dissipation at the inter-molecular space which surrounded by four molecules. This result revealed that the molecular-scale dissipation contrast taken on a loosely-packed monolayer is related to the number of the molecules interacting with the tip.

Chapter 7

Conclusions and Future Prospects

In this study, the possibilities and the problems of DFM applications to the molecular-scale investigations on organic ultrathin films were experimentally demonstrated. Then the imaging mechanisms of DFM were studied in relation to the electrical, mechanical and chemical properties of organic surfaces. The conclusions obtained in this study and some suggestions for the future works are summarized below.

7.1 Conclusions

In-situ Analyses of Thermal Phase Transitions

In chapter 3, the AM-DFM applications to the *in-situ* analyses of thermal phase transitions were experimentally demonstrated on ferroelectric polymer thin films.

1. It was demonstrated that a variable-temperature AM-DFM is quite useful for the direct investigations on various thermal phase transitions of polymer thin films.

2. It was revealed that AM-DFM can provide different types of information on the sample using light-force imaging and hard-force imaging. In order to visualize thermal phase transition processes of polymers, it is essential to choose these two operation modes appropriately.

Molecular-Scale Imaging of Insulating Organic Surfaces

In chapter 4, the possibilities and the problems of FM-DFM applications to the molecular-scale investigations on insulating organic thin films were experimentally demonstrated.

1. It was demonstrated that the true-molecular resolution can be achieved by FM-DFM even on insulating organic surfaces.

2. It was found that there are some specific situations where high-resolution is hard to achieve because of the strong electrostatic interactions or the molecular fluctuations.

Dissipation Mechanisms of Cantilever Vibration Energy

In chapter 5, the dissipation mechanisms of the cantilever vibration energy were investigated in relation to the electrical interaction and the molecular fluctuation.

1. It was revealed that the experimentally measured energy dissipation contains both "apparent dissipation" induced by the conservative electrical interaction and "true dissipation" induced by the dissipative electrical interaction.

2. It was revealed that the energy dissipation induced by the molecular fluctuation is strongly related to the mechanical property of the surface. However, it was also found that the molecular fluctuation induces not only energy dissipation but also some topographic artifacts because of the incomplete separation between the conservative and dissipative interactions.

Molecular-Scale Contrasts in Topography and Dissipation

In chapter 6, the formation mechanisms of the molecular-scale contrasts in topography and dissipation were experimentally studied in relation to the chemical and mechanical properties of the organic surfaces.

1. It was revealed that the molecular-scale topographic contrast represents not only surface height variations but also chemical property of the surface.

2. It was revealed that the molecular-scale dissipation contrast represents the magnitude of the molecular fluctuation induced by the tip-sample interaction. The results obtained in this chapter strongly supported the expectation that the mechanical property of the surface can be evaluated by the energy dissipation measurement.

7.2 Future Prospects

Molecular Resolution under Moderate Vacuum Conditions

All the molecularly-resolved FM-DFM images presented so far were taken under UHV conditions, which has significantly limited the number of FM-DFM users especially in biological and polymer science. Thus it would be important to develop a high-resolution DFM operated under a moderate vacuum condition. In principle,

there is no problems to prevent the high-resolution imaging under moderate vacuum conditions because the Q-enhancement in vacuum environment is almost saturated even in a low vacuum condition. However, practically, the vacuum pumps used for the moderate vacuum (i.e., rotary pumps and turbo molecular pumps) cannot be free from the mechanical vibration. Therefore, the DFM system has to be isolated from such an undesirable vibration.

Cantilever Oscillation with Small Amplitude and High Frequency

In order to enhance the force sensitivity to the short-range interaction force and suppress the tip-induced molecular fluctuation, it would be desired to reduce the cantilever vibration amplitude down to 1 nm or less. On the other hand, to improve the time response of the tip-sample distance regulation and perform a high-speed scanning over a relatively rough surface, it would be required to enhance the cantilever resonance frequency. Such a high oscillation frequency may lead to the improvement of the time response of AM detection feedback ($\tau_{\mathrm{AM}} \simeq 2Q/\omega_0$) so that the UHV applications of AM-DFM may become possible. For these purposes, a high-speed and high-sensitivity cantilever deflection measurement system has to be developed. While the improvement of the present optical detection technique is one possible way, development of a novel electrical detection method is also promising in view of its applications to the liquid and the low-temperature environments.

Atomically Well-Defined Probe

In order to achieve further understanding on the contrast formation mechanism in both topography and dissipation, detailed comparisons between the theoretical expectations and the experimental results are of great importance. From this point of view, an atomically well-defined probe has to be employed in the experiments. Such an well-defined probe will also allow us to perform reproducible and quantitative DFM experiments. Although a carbon nanotube (CNT) probe is the most promising candidate at the present stage, the atomic-scale structure of the CNTs currently used as SPM probes are not completely uniform and cannot be predicted. In addition, the present fabrication method of CNT probes is so time-consuming that they are too expensive to be used for the routine applications. Thus the fabrication method of atomically well-defined CNTs and the mass-production process of CNT probes have to be established.

DFM Applications to Organic Thin Film Devices

In order to improve the performance and understand the operation mechanism of organic thin film devices, it is essential to study molecular-scale structures and properties of them. In this study, DFM was applied to characterize various organic thin films such as ferroelectric polymer and oligomer thin films, self-assembled monolayers of thiol derivatives and semiconducting thin films of π-conjugated molecules. All of them are regarded as prototypes for the future organic thin film devices. Thus these results will promote the DFM applications to the investigations on organic thin film devices, leading to the further development in this field.

DFM Applications to Molecular Electronic Devices

In order to realize molecular electronic devices, the direct access method to the individual molecules has to be established. In the molecular electronics, the device fabrication itself still remains one of the most challenging issues to be coped with. Thus the characterizations of molecular electronic devices such as single molecular switches or single molecular wires were not performed in this study. However, some important suggestions for the future DFM applications to the molecular electronics were obtained. For example, sub-molecular scale topographic contrasts of CuPc molecules well corresponded to the spatial distribution of the frontier orbitals which represents the electronic state of the molecule. The result implied that the electronic state of the single molecule may be deduced from the sub-molecular scale DFM images.

DFM Applications to Controlled Molecular Manipulation

As a next step of this study, it would be envisaged to manipulate the individual molecules using DFM technique. To cope with this challenging issue, it should be precisely understood how the molecules and the tip atoms behave when the tip is located at the close vicinity of the sample surface. Surprisingly enough, this is also the very central issue that has been discussed in this thesis in relation to the energy dissipation mechanisms during the FM-DFM imaging. In fact, in this study, it was demonstrated that the CuPc molecules can be moved by the dissipative tip-sample interaction and, furthermore, the molecular-scale arrangements at the domain boundaries were obviously improved. Although this surface modification was not performed in an well controlled manner, the result clearly represented the promising aspect of the DFM technique for the future realization of controlled molecular manipulation.

Bibliography

[1] M. Pope, H. P. Kallmann, and P. Magnante, *J. Chem. Phys.*, **38** (1963) 2042.

[2] C. W. Tang and S. A. VanSlyke, *Appl. Phys. Lett.*, **51** (1987) 913.

[3] F. Ebisawa, T. Kurosawa, and S. Nara, *J. Appl. Phys.*, **54** (1983) 3255.

[4] K. Kudo, M. Yamashita, and T. Moriizumi, *Jpn. J. Appl. Phys.*, **23** (1984) 130.

[5] X. Q. Chen, H. Yamada, T. Horiuchi, and K. Matsushige, *Jpn. J. Appl. Phys.*, **37** (1998) 3834.

[6] C. D. Dimitrakopoulos and D. J. Mascaro, *IBM Journal of Research and Development*, **45** (2001) 11.

[7] K. Kudo, D. X. Wang, M. Iizuka, and S. Kuniyoshi, *Synth. Met.*, **111** (2000).

[8] K. Kudo, M. Iizuka, S. Kuniyoshi, and K. Tanaka, *Thin Solid Films*, **393** (2001) 362.

[9] B. Crone, A. Dodabalapur, Y. Y. Lin, R. W. Filas, Z. Bao, A. LaDuca, R. Sarpeshkar, H. E. Kats, and W. Li, *Nature*, **403** (2000) 521.

[10] A. Aviram and M. A. Ratner, *Chem. Phys. Lett.*, **29** (1974) 277.

[11] F. L. Carter. *Molecular Electronic Devices.* Marcel Dekker, Inc., (1982).

[12] F. L. Carter. *Molecular Electronic Devices II.* Marcel Dekker, Inc., (1987).

[13] J. M. Tour, R. Wu, and J. S. Schumm, *J. Am. Chem. Soc.*, **112** (1990) 5662.

[14] J. M. Tour, R. Wu, and J. S. Schumm, *J. Am. Chem. Soc.*, **113** (1991) 7064.

[15] N. Aratani, A. Osuka, Y. H. Kim, D. H. Jeong, and D. Kim, *Angew Chem. Int. Ed.*, **39** (2000) 1458.

[16] G. Binnig, H. Rohrer, Ch. Gerber, and E. Weibel, *Phys. Rev. Lett.*, **49** (1982) 57.

[17] L. A. Bumm, J. J. Arnold, M. T. Cygan, T. D. Dunbar, T. P. Burgin, L. Jones II, D. L. Allara, J. M. Tour, and P. S. Weiss, *Science*, **271** (1996) 1705.

[18] Z. J. Donhauser, B. A. Mantooth, K. F. Kelly, L. A. Bumm, J. D. Monnell, and J. J. Stapleton, *Science*, **292** (2001) 2303.

[19] C. Joachim and J. K. Gimzewski, *Europhys. Lett.*, **30** (1995) 409.

[20] C. Joachim and J. K. Gimzewski, *Chem. Phys. Lett.*, **265** (1997) 353.

[21] G. Binnig, C. F. Quate, and Ch. Gerber, *Phys. Rev. Lett.*, **56** (1986) 930.

[22] Y. Martin, C. C. Williams, and H. K. Wickramasinghe, *J. Appl. Phys.*, **61** (1987) 4723.

[23] H. K. Wickramasinghe, *Sci. Am.*, **260** (1989) 98.

[24] M. Bammerlin, R. Lüthi, E. Meyer, A. Baratoff, J Lü, M. Guggisberg, C. Gerber, L. Howald, and H.-J. Güntherodt, *Probe Microscopy*, **1** (1997) 3.

[25] M. Bammerlin, R. Lüthi, E. Meyer, A. Baratoff, J Lü, M. Guggisberg, C. Gerber, L. Howald, and H.-J. Güntherodt, *Appl. Phys. A*, **66** (1998) S293.

[26] M. Nonnenmacher, M. P. O'Boyle, and H. K. Wickramasinghe, *Appl. Phys. Lett.*, **58** (1991) 2921.

[27] M. Gauthier and M. Tsukada, *Phys. Rev. B*, **60** (1999) 11716.

[28] W. Denk and D. W. Pohl, *Appl. Phys. Lett.*, **59** (1991) 2171.

[29] S. Kitamura and M. Iwatsuki, *Appl. Phys. Lett.*, **72** (1998) 3154.

[30] R. Lüthi, E. Meyer, M. Bammerlin, A. Baratoff, L. Howald, Ch. Gerber, and H.-J. Güntherodt, *Surf. Rev. Lett.*, **4** (1997) 1025.

[31] G. Binnig, Ch. Gerber, E. Stoll, T. R. Albrecht, and C. F. Quate, *Europhys. Lett.*, **3** (1987) 1281.

[32] G. Meyer and N. M. Amer, *Appl. Phys. Lett.*, **56** (1990) 2100.

[33] F. J. Giessibl and G. Binnig, *Ultramicroscopy*, **42-44** (1992) 7.

[34] O. Marti, V. Elings, M. Haugan, C. E. Bracker, J. Schneir, B. Drakes, S. A. Gould, J. Gurley, L. Hellemans, K. Shaw, A. L. Weisenhorn, J. Zasadzinski, and P. K. Hansma, *J. Microscopy*, **152** (1988) 803.

[35] E. Meyer, L. Howald, R. M. Overney, H. Heinzelmann, J. Frommwe, H.-J. Güntherodt, T. Wagner, H. Schier, and S. Roth, *Nature*, **349** (1991) 398.

[36] J. B. Pethica and W. C. Oliver, *Phys. Scri. T*, **19** (1987) 61.

[37] F. Ohnesorge and G. Binnig, *Science*, **260** (1993) 1451.

[38] H. Yamada, S. Okada, T. Fujii, M. Kageshima, A. Kawazu, H. Matsuda, H. Nakanishi, and K. Nakayama, *Appl. Surf. Sci.*, **65-66** (1993) 366.

[39] D. J. Muller, F. A. Schabert, G. Buldt, and A. Engel, **68** (1995) 1681.

[40] T. R. Albrecht, P. Grütter, D. Horne, and D. Ruger, *J. Appl. Phys.*, **69** (1991) 668.

[41] Q. Zhong, D. Inniss, K. Kjoller, and V. B. Elings, *Surf. Sci.*, **290** (1993) L688.

[42] F. J. Giessibl, *Science*, **267** (1995) 68.

[43] S. Kitamura and M. Iwatsuki, *Jpn. J. Appl. Phys. Part II*, **34** (1995) L1086.

[44] S. Kitamura and M. Iwatsuki, *Jpn. J. Appl. Phys. Part II*, **35** (1996) L668.

[45] H. Ueyama, M. Ohta, Y. Sugawara, and S. Morita, *Jpn. J. Appl. Phys. Part II*, **34** (1995) L1086.

[46] Y. Sugawara, M. Ohta, H. Ueyama, and S. Morita, *Science*, **270** (1995) 1646.

[47] P. Güthner, *J. Vac. Sci. Technol. B*, **14** (1996) 2428.

[48] R. Lüthi, E. Meyer, M. Bammerlin, A. Baratoff, T. Lehmann, L. Howald, Ch. Gerber, and H.-J. Güntherodt, *Z. Phys. B*, **100** (1996) 165.

[49] N. Nakagiri, M. Suzuki, K. Okiguchi, and H. Sugimura, *Surf. Sci.*, **373** (1997) 329.

[50] S. Orisaka, T. Minobe, T. Uchihashi, Y. Sugawara, and S. Morita, *Appl. Surf. Sci.*, **140** (1999) 243.

[51] Ch. Loppacher, M. Bammerlin, M. Guggisberg, F. Battiston, R. Bennewitz, S. Rast, A. Baratoff, E. Meyer, and H.-J. Güntherodt, *Appl. Surf. Sci.*, **140** (1999) 287.

[52] K. Fukui, H. Onishi, and Y. Iwasawa, *Phys. Rev. Lett.*, **79** (1997) 4202.

[53] K. Fukui, H. Onishi, and Y. Iwasawa, *Chem. Phys. Lett.*, **280** (1997) 296.

[54] K. Fukui, H. Onishi, and Y. Iwasawa, *Appl. Surf. Sci.*, **140** (1999) 259.

[55] B. Gotsmann, C. Schmidt, C. Seidel, and H. Fuchs, *Eur. Phys. J. B*, **4** (1998) 267.

[56] S. Kitamura, K. Suzuki, and M. Iwatsuki, *Appl. Surf. Sci.*, **140** (1999) 265.

[57] T. Uchihashi, T. Okada, Y. Sugawara, K. Yokoyama, and S. Morita, *Phys. Rev. B*, **60** (1999) 8309.

[58] T. Uchihashi, T. Ishida, M. Komiyama, M. Ashino, Y. Sugawara, W. Mizutani, K. Yokoyama, S. Morita, H. Tokumoto, and M. Ishikawa, *Appl. Surf. Sci.*, **157** (2000) 244.

[59] K. Kobayashi, H. Yamada, T. Horiuchi, and K. Matsushige, *Appl. Surf. Sci.*, **140** (1999) 281.

[60] K. Kobayashi, H. Yamada, T. Horiuchi, and K. Matsushige, *Jpn. J. Appl. Phys. Part II*, **38** (1999) L1550.

[61] K. Kobayashi, H. Yamada, H. Itoh, T. Horiuchi, and K. Matsushige, *Rev. Sci. Instrum.*, **72** (2001) 4383.

[62] F. J. Giessibl, *Appl. Phys. Lett.*, **76** (2000) 1470.

[63] F. J. Giessibl, *Phys. Rev. B*, **56** (1997) 16010.

[64] M. Tsukada, N. Sasaki, Y. Yamura, N. Sato, and K. Abe, *Surf. Sci.*, **401** (1998) 355.

[65] U. Dürig, *Appl. Phys. Lett.*, **75** (1999) 433.

[66] N. Sasaki and M. Tsukada, *Appl. Surf. Sci.*, **140** (1999) 339.

[67] J. P. Aimé, R. Boisgard, L. Nony, and G. Couturier, *Phys. Rev. Lett.*, **82** (1999) 3388.

[68] U. Dürig, *Appl. Phys. Lett.*, **76** (2000) 1203.

[69] F. J. Giessibl, *Phys. Rev. B*, **61** (2000) 9968.

[70] F. J. Giessibl, *Phys. Rev. Lett.*, **78** (2001) 123.

[71] Michel Gauthier and Masaru Tsukada, *Phys. Rev. B*, **64** (2001) 85409.

[72] S. H. Ke, T. Uda, R. Përez, I. Štich, and K. Terakura, *Phys. Rev. B*, **60** (1999) 11631.

[73] J. Tóbik, I. Štich, R. Pérez, and K. Terakura, *Phys. Rev. B*, **60** (1999) 11639.

[74] Alexander I. Livshits, Alexander L. Shluger, A. L. Rohl, and Adam S. Foster, *Phys. Rev. B*, **59** (1999) 2436.

[75] A. Abdurixit, A. Baratoff, and E. Meyer, *Appl. Surf. Sci.*, **157** (2000) 355.

[76] N. Sasaki and M. Tsukada, *Appl. Surf. Sci.*, **157** (2000) 367.

[77] K. Tagami, N. Sasaki, and M. Tsukada, *Appl. Surf. Sci.*, **172** (2001) 301.

[78] U. Dürig, H. R. Steinauer, and N. Blanc, *J. Appl. Phys.*, **82** (1997) 3641.

[79] U. Dürig, *Surf. Interface Anal.*, **27** (1999) 467.

[80] B. Gotsmann, C. Seidel, B. Anczykowski, and H. Fuchs, *Phys. Rev. B*, **60** (1999) 11051.

[81] U. Dürig, *New J. Phys.*, **2** (2000) 5.

[82] N. Sasaki and M. Tsukada, *Jpn. J. Appl. Phys. Part II*, **39** (2000) L1334.

[83] Michel Gauthier and Masaru Tsukada, *Phys. Rev. Lett.*, **85** (2000) 5348.

[84] G. V. Dedkov and A. A. Kyasov, *Phys. Solid State*, **43** (2001) 536.

[85] L. N. Kantrovich, *Phys. Rev. B*, **64** (2001) 245409.

[86] Michel Gauthier and Masaru Tsukada, *Surf. Sci.*, **495** (2001) 204.

[87] T. D. Stowe, T. W. Kenny, D. J. Thomson, and D. Rugar, *Appl. Phys. Lett.*, **75** (1999) 2785.

[88] R. Bennewitz, A. S. Foster, L. N. Kantrovich, M. Bammerlin, Ch. Loppacher, S. Schär, M. Guggisberg, and E. Meyer, *Phys. Rev. B*, **62** (2000) 2074.

[89] C. Loppacher, R. Bennewitz, O. Pfeiffer, M. Guggisberg, M. Bammerlin, S. Schär, V. Barwich, A. Baratoff, and E. Meyer, *Phys. Rev. B*, **62** (2000) 13674.

[90] M. Guggisverg, M. Bammerlin, Ch. Loppacher, O. Pfeiffer, A. Abdurixit, V. Barwich, R. Bennewitz, A. Baratoff, E. Meyer, and H.-J. Güntherodt, *Phys. Rev. B*, **61** (2000) 11151.

[91] B. Gotsmann and H. Fuchs, *Phys. Rev. Lett.*, **86** (2001) 2597.

[92] T. Arai and M. Tomitori, *Appl. Phys. A*, **72** (2001) S51.

[93] P. M. Hoffmann, S. Jeffery, J. B. Pethica, H. Ö. Özer, and A. Oral, *Phys. Rev. Lett.*, **87** (2001) 265502.

[94] H. Hölscher, B. Gotsmann, W. Allers, U. D. Schwarz, H. Fuchs, and R. Wiesendanger, *Phys. Rev. B*, **64** (2001) 075402.

[95] S. Morita, R. Wiesendanger, and E. Meyer, editors. *Noncontact Atomic Force Microscopy (Nanoscience and Technology)*. Springer Verlag, (2002).

[96] K. Kobayashi, H. Yamada, T. Horiuchi, and K. Matsushige, *Appl. Surf. Sci.*, **157** (2000) 228.

[97] A. Sasahara, H. Uetsuka, and H. Onishi, *J. Phys. Chem. B*, **105** (2001) 1.

[98] A. Sasahara, H. Uetsuka, and H. Onishi, *Phys. Rev. B*, **64** (2001) 121406.

[99] A. Sasahara, H. Uetsuka, and H. Onishi, *Appl. Phys. A*, **72** (2001) S101.

[100] A. Sasahara, H. Uetsuka, and H. Onishi, *Surf. Sci.*, **481** (2001) L437.

[101] A. Sasahara, H. Uetsuka, T.-A. Ishibashi, and H. Onishi, *Appl. Surf. Sci.*, **188** (2002) 265.

[102] H. Onishi, A. Sasahara, H. Uetsuka, and T.-A. Ishibashi, *Appl. Surf. Sci.*, **188** (2002) 257.

[103] R. E. Tanner, A. Sasahara, Y. Liang, E. I. Altman, and H. Onishi, *J. Phys. Chem. B*, **106** (2002) 8211.

[104] X. Zhu, P. Grütter, V. Metlushko, and B. Ilic, *J. Appl. Phys.*, **91** (2002) 7340.

[105] K. Kobayashi, H. Yamada, and K. Matsushige, *Appl. Surf. Sci.*, **188** (2002) 430.

[106] W. Allers, A. Schwarz, H. Hölscher, U. Schwarz, and R. Wiesendanger, *Jpn. J. Appl. Phys.*, **39** (2000) 3701.

[107] R. Erlandsson, L. Olsson, and P. Martensson, *Phys. Rev. B*, **54** (1996) R8309.

[108] D. O. Thompson and D. E. Chimenti, editors. *Review of Progress in Quantitative Non-Destructive Evaluation*. Plenum, (1987).

[109] R. Erlandsson, G. M. McClelland, C. M. Mate, and S. Chiang, *J. Vac. Sci. Technol. A*, **6** (1988) 266.

[110] A. J. Boef, *Appl. Phys. Lett.*, **55** (1989) 439.

[111] G. Meyer and N. M. Amer, *Appl. Phys. Lett.*, **53** (1988) 1045.

[112] S. Alexander, L. Hellemans, O. Marti, J. Schneir, V. Elings, P. K. Hansma, M. Longmire, and J. Gurley, *J. Appl. Phys.*, **65** (1989) 164.

[113] A. Dandridge, R. O. Miles, and T. G. Giallorenzi, *Electron. Lett.*, **16** (1980) 948.

[114] R. O. Miles, A. Dandridge, A. B. Tveten, and T. G. Giallorenzi, *J. Lightwave Technol.*, **LT-1** (1983) 81.

[115] C. Schönenberger and S. F. Alvarado, *Z. Phys. B*, **80** (1980) 373.

[116] D. Anselmetti, Ch. Gerber, B. Michel, and H.-J. Güntherodt, *Rev. Sci. Instrum.*, **63** (1992) 3003.

[117] G. Neubauer, S. R. Cohen, G. M. McClelland, D. Horne, and C. M. Mate, *Rev. Sci. Instrum.*, **61** (1990) 2296.

[118] M. Tortonese, R. C. Barrett, and C. F. Quate, *Appl. Phys. Lett.*, **62** (1993) 834.

[119] T. Itoh and T. Suga, *Nanotechnology*, **4** (1993) 218.

[120] T. Itoh and T. Suga, *J. Vac. Sci. Technol. B*, **12** (1994) 1581.

[121] D. Sarid. *Scanning Force Microscopy with Applications to Electric, Magnetic and Atomic Forces*. Oxford Univ. Press, (1994).

[122] F. J. Giessibl, *Appl. Phys. Lett.*, **78** (2001) 123.

[123] S. N. Magonov, V. Elings, and V. S. Papkov, *Polymer*, **38** (1997) 297.

[124] S. G. Prilliman, A. M. Kavanagh, E. C. Scher, S. T. Robertson, and K. S. Hwang, *Rev. Sci. Instrum.*, **69** (1998) 3245.

[125] H. Kawai, *Jpn. J. Appl. Phys.*, **8** (1969) 975.

[126] T. Yagi, M. Tatemoto, and J.-I. Sako, *Polym. J.*, **12** (1980) 209.

[127] A. J. Lovinger, *Polymer*, **24** (1983) 1225.

[128] K. Koga, N. Nakano, T. Hattori, and H. Ohigashi, *J. Appl. Phys.*, **67** (1990) 965.

[129] K. Tashiro, H. Tadokoro, and M. Kobayashi, *Ferroelectrics*, **32** (1981) 167.

[130] K. Tashiro, K. Takano, M. Kobayashi, Y. Chatani, and H. Tadokoro, *Polymer*, **25** (1984) 195.

[131] R. Tanaka, K. Tashiro, and M. Kobayashi, *Polymer*, **40** (1999) 3855.

[132] A. V. Bune, V. M. Fridkin, S. Ducharme, L. M. Blinov, S. P. Palto, A. V. Sorokkin, S. G. Yudin, and A. Zlatkin, *Nature*, **391** (1998) 874.

[133] K. Matsushige, H. Yamada, H. Tanaka, T. Horiuchi, and X. Q. Chen, *Nanotechnology*, **9** (1998) 208.

[134] X. Q. Chen, H. Yamada, Y. Terai, T. Horiuchi, K. Matsushige, and P. S. Weiss, *Thin Solid Films*, **353** (1999) 259.

[135] X. Q. Chen, H. Yamada, T. Horiuchi, K. Matsushige, S. Watanabe, M. Kawai, and P. S. Weiss, *J. Vac. Sci. Technol. B*, **17** (1999) 1930.

[136] X. Q. Chen, H. Yamada, T. Horiuchi, and K. Matsushige, *Jpn. J. Appl. Phys.*, **38** (1999) 3932.

[137] M. Hikosaka, *Polymer*, **28** (1987) 1257.

[138] M. Hikosaka, K. Sakurai, H. Ohigashi, and T. Koizumi, *Jpn. J. Appl. Phys.*, **32** (1993) 2029.

[139] M. Hikosaka, K. Sakurai, H. Ohigashi, and A. Keller, *Jpn. J. Appl. Phys.*, **33** (1994) 214.

[140] T. Hattori, M. Hikosaka, and H. Ohigashi, *Polymer*, **37** (1996) 85.

[141] T. Hattori, T. Watanabe, S. Akama, M. Hikosaka, and H. Ohigashi, *Polymer*, **38** (1997) 3505.

[142] A. V. Bune, C. Zhu, S. Ducharme, L. M. Blinov, V. M. Fridkin, S. P. Palto, N. g. Petukhova, and S. G. Yudin, *J. Appl. Phys.*, **85** (1999) 7869.

[143] Y. Yoshida, K. Ishida, K. Ishizaki, T. Horiuchi, and K. Matsushige, *Jpn. J. Appl. Phys.*, **36** (1997) 7389.

[144] Herman, T. Uno, A. Kubono, S. Umemoto, T. Kikutani, and N. Okui, *Polymer*, **38** (1997) 1677.

[145] Herman, S. Umemoto, T. Kikutani, and N. Okui, *Polymer*, **30** (1998) 659.

[146] K. Noda, K. Ishida, T. Horiuchi, K. Matsushige, and A. Kubono, *J. Appl. Phys.*, **86** (1999) 3688.

[147] K. Noda, K. Ishida, A. Kubono, T. Horiuchi, H. Yamada, and K. Matsushige, *Jpn. J. Appl. Phys.*, **39** (2000) 6358.

[148] K. Ishida, K. Hayashi, Y. Yoshida, T. Horiuchi, and K. Matsushige, *J. Appl. Phys.*, **73** (1993) 7338.

[149] K. Ishida, T. Horiuchi, S. Kai, and K. Matsushige, *Jpn. J. Appl. Phys. Part II*, **34** (1995) L240.

[150] K. Ishida, T. Horiuchi, and K. Matsushige, *Mol. Cryst. Liq. Cryst.*, **294** (1997) 43.

[151] K. Hayashi, S. Kawato, Y. Fujii, T. Horiuchi, and K. Matsushige, *Appl. Phys. Lett.*, **70** (1997) 1384.

[152] K. Hayashi, S. Kawato, Y. Fujii, T. Horiuchi, and K. Matsushige, *Mol. Cryst. Liq. Cryst.*, **294** (1997) 103.

[153] T. Shimada, T. Sakurada, and A. Koma, *J. Appl. Phys.*, **86** (1999) 3688.

[154] R. G. Nuzzo and D. L. Allara, *J. Am. Chem. Soc.*, **105** (1983) 4481.

[155] R. Maoz and J. Sagiv, *J. Colloid. Interface Sci.*, **100** (1984) 465.

[156] J. Gun, R. Iscovici, and J. Sagiv, *J. Colloid. Interface Sci.*, **101** (1984) 201.

[157] J. Gun and J. Sagiv, *J. Colloid. Interface Sci.*, **112** (1986) 457.

[158] H. O. Finklea, L. R. Robinson, A. Blackburn, B. Richter, D. Allara, and T. Bright, *Langmuir*, **2** (1986) 239.

[159] S. R. Cohen, R. Naaman, and J. Sagiv, *J. Phys. Chem.*, **90** (1986) 3054.

[160] R. Maoz and J. Sagiv, *Thin Solid Films*, **132** (1985) 135.

[161] R. Maoz and J. Sagiv, *Langmuir*, **3** (1987) 1045.

[162] L. Netzer, R. Iscovici, and J. Sagiv, *Thin Solid Films*, **99** (1983) 235.

[163] L. Netzer, R. Iscovici, and J. Sagiv, *Thin Solid Films*, **100** (1983) 67.

[164] L. Netzer and J. Sagiv, *J. Am. Chem. Soc.*, **105** (1983) 674.

[165] N. Tillman, A. Ulman, J. S. Schildkraut, and T. L. Penner, *J. Am. Chem. Soc.*, **111** (1988) 6136.

[166] N. Tillman, A. Ulman, and T. L. Penner, *Langmuir*, **5** (1989) 101.

[167] C. D. Bain, E. B. Troughton, Y.-T. Tao, J. Evall, G. M. Whitesides, and R. G. Nuzzo, *J. Am. Chem. Soc.*, **111** (1989) 321.

[168] M. D. Porter, T. B. Bright, D. L. Allara, and C. E. D. Chidsey, *J. Am. Chem. Soc.*, **109** (1987) 3559.

[169] R. G. Nuzzo, L. H. Dubois, and D. L. Allara, *J. Am. Chem. Soc.*, **112** (1990) 558.

[170] I. Rubinstein, S. Steinberg, Y. Tor, A. Shanzer, and J. Sagiv, *Nature*, **332** (1988) 426.

[171] G. M. Whitesides and P. E. Laibinis, *Langmuir*, **6** (1990) 87.

[172] C. E. D. Chidsey and D. N. Loiacono, *Langmuir*, **6** (1990) 709.

[173] C. E. D. Chidsey, G.-Y. Liu, P. Rowntree, and G. Scoles, *J. Chem. Phys.*, **91** (1989) 1381.

[174] C. D. Bain and G. M. Whitesides, *J. Am. Chem. Soc.*, **111** (1989) 7164.

[175] L. Strong and G. M. Whitesides, *Langmuir*, **4** (1988) 546.

[176] A. Ulman, *J. Mater. Ed.*, **11** (1989) 205.

[177] K. R. Stewart, G. M. Whitesides, H. P. Godfried, and I. F. Silvera, *Surf. Sci.*, **57** (1986) 1381.

[178] E. B. Troughton, C. D. Bain, G. M. Whitesides, R. G. Nuzzo, D. L. Allara, and M. D. Porter, *Langmuir*, **4** (1988) 365.

[179] R. G. Nuzzo, F. A. Fusco, and D. L. Allara, *J. Am. Chem. Soc.*, **109** (1987) 2358.

[180] C. A. Widrig, C. A. Alves, and M. D. Porter, *J. Am. Chem. Soc.*, **113** (1991) 2805.

[181] L. Sun and R. M. Crooks, *J. Electrochem. Soc.*, **138** (1991) L23.

[182] Y.-T. Kim and A. J. Bard, *Langmuir*, **8** (1992) 1096.

[183] K. Edinger, A. Gölzhäuser, K. Demota, Ch. Wöll, and M. Grunze, *Langmuir*, **9** (1993) 4.

[184] C. Schönenberger, J. A. M. Sondag-Huethorst, J. Jorritsma, and L. G. J. Fokkink, *Langmuir*, **10** (1994) 611.

[185] M. Salmeron, G. Neubauer, A. Folch, M. Tomitori, D. F. Ogletree, and P. Sautet, *Langmuir*, **9** (1993) 3600.

[186] L. A. Bumm, J. J. Arnold, T. D. Dunbar, D. L. Allara, and P. S. Weiss, *J. Phys. Chem. B*, **103** (1999) 8122.

[187] C. A. Alves, E. L. Smith, and M. D. Porter, *J. Am. Chem. Soc.*, **114** (1992) 1222.

[188] G.-Y. Liu and M. B. Salmeron, *Langmuir*, **10** (1994) 367.

[189] L. H. Dubois, B. R. Zegarski, and R. G. Nuzzo, *J. Chem. Phys.*, **98** (1993) 678.

[190] G. E. Poirier, M. J. Tarlov, and H. E. Rushmeier, *Langmuir*, **10** (1994) 3383.

[191] R. Staub, M. Toerker, T. Fritz, T. Scmitz-Hübsh, F. Sellam, and K. Leo, *Langmuir*, **14** (1998) 6693.

[192] G. E. Poirier and E. D. Pylant, *Science*, **272** (1996) 1145.

[193] G. E. Poirier, *Langmuir*, **13** (1997) 2019.

[194] K. Kobayashi, H. Yamada, T. Horiuchi, and K. Matsushige, *Jpn. J. Appl. Phys.*, **37** (1998) 6183.

[195] H. Shirakawa, E. J. Louis, A. G. MacDiarmid, K. Chiang C, and A. J. Heeger, *J. Chem. Soc., Chem. Commun.* (1977) 578.

[196] C. K. Chiang, C. R. Fincher, Y. W. Park, A. J. Heeger, H. Shirakawa, E. J. Louis, S. C. Gau, and A. G. MacDiarmid, *Phys. Rev. Lett.*, **39** (1977) 1098.

[197] C. K. Chiang, Y. W. Park, A. J. Heeger, H. Shirakawa, E. J. Louis, and A. G. MacDiarmid, *J. Chem. Phys.*, **69** (1978) 5098.

[198] D. Fichou, editor. *Handbook of Oligo- and Polythiophenes*. Kluwer Academic Publishers, (1997).

[199] G. E. Wnek, J. C. W. Chien, F. E. Karasz, and C.P. Lillja, *Polymer*, **20** (1979) 1441.

[200] A. F. Diaz and J. A. Logan, *J. Electroanal. Chem.*, **111** (1980) 111.

[201] G. Tourillon and F. Garnier, *J. Electroanal. Chem.*, **135** (1982) 173.

[202] A. F. Diaz and J. I. Gastillo, *J. Chem. Soc., Chem. Commun.* (1980) 397.

[203] D. M. Ivory, G. G. Miller, J. M. Sowa, L. W. Shacklette, R. R. Chance, and R. H. Baughman, *J. Chem. Phys.*, **71** (1979) 1506.

[204] J. F. Rabolt, T. C. Clarke, K. K. Kanazawa, J. R. Reynolds, and G. B. Street, *J. Chem. Soc., Chem. Commun.* (1980) 347.

[205] R. R. Chance, L. W. Shacklette, and G. G. Miller, *J. Chem. Soc., Chem. Commun.* (1980) 348.

[206] H. Guenther, M. D. Bezoari, P. Kovacic, S. Gronowitz, and A.-B. Hoernfeldt, *J. Polym. Sci. Polym. Lett. Ed.*, **22** (1984) 65.

[207] J. Bargon, S. Mohmand, and R. J. Waltman, *Mol. Cryst. Liq. Cryst.*, **93** (1983) 279.

[208] J. H. Burroughes, D. D. C. Bradley, A. R. Brown, R. N. Marks, K. Mackay, R. H. Friend, P. L. Burns, and A. B. Holmes, *Nature*, **347** (1990) 539.

[209] M. Berggren, G. Gustafsson, O. Inganäs, M. R. Andersson, O. Wennerstrom, and T. Hjertberg, *Adv. Mater.*, **6** (1994) 488.

[210] G. G. Malliaras, J. K. Herrema, and J. Wildeman, *Adv. Mater.*, **5** (1993) 721.

[211] R. E. Gill, G. G. Malliaras, J. Wildeman, and G. Hadziioannou, *Adv. Mater.*, **6** (1994) 132.

[212] M. Berggren, G. Gustafsso, O. Inganäs, M. R. Andersson, O. Wennerstrom, and T. Hjertberg, *J. Appl. Phys.*, **76** (1994) 7530.

[213] P. Dyreklev, M. Berggren, O. Inganäs, M. R. Andersson, O. Wennerstrom, and T. Hjertberg, *Adv. Mater.*, **7** (1995) 43.

[214] H. Koezuka, A. Tsumura, and T. Ando, *Synth. Met.*, **18** (1987) 699.

[215] M. Assadi, C. Svensson, M. Wilander, and O. Inganäs, *Appl. Phys. Lett.*, **53** (1988) 195.

[216] H. E. Katz, *J. Mater. Chem.*, **7** (1997) 369.

[217] M. Berggren, O. Inganäs, and G. Gaustafsson, *Nature*, **372** (1994) 444.

[218] K. H. Tews U. Schoeler and H. Kuhn, *J. Chem. Phys.*, **61** (1974) 5009.

[219] D. Fichou, G. Horowitz, Y. Nishikitani, and F. Garnier, *Chemtronics*, **3** (1988) 176.

[220] G. Horowitz, D. Fichou, and F. Garnier, *Sold State Commun.*, **70** (1989) 385.

[221] X. Peng, G. Horowitz, D. Fichou, and F. Garnier, *Appl. Phys. Lett.*, **57** (1990) 2013.

[222] A. Tsumura, H. Koezuka, and T. Ando, *Synth. Met.*, **25** (1988) 11.

[223] R. Zamboni, N. Periasamy, G. Ruani, and C. Taliani, *Synth. Met.*, **54** (1993) 57.

[224] C. Taliani and L. M. Blinov, *Adv. Mater.*, **8** (1996) 353.

[225] D. Oeter adn H.-J. Egelhaaf, Ch. Ziegler, D. Oelkrug, and W. Göpel, *J. Chem. Phys.*, **101** (1994) 6344.

[226] G. Horowitz, R. Hajlaoui, and P. Delannoy, *J. Phys. III France*, **5** (1995) 355.

[227] K. Waragai, H. Akamichi adn S. Hotta, H. Kano, and H. Sakaki, *Phys. Rev. B*, **52** (1995) 1786.

[228] L. Torsi, A. Dodabalapur, L. J. Rothberg, A. W. P. Fung, and H. E. Katz, *Phys. Rev. B*, **57** (1998) 2271.

[229] F. Garnier, G. Horowitz, D. Fichou, and A. Yassar, *Supermolecular Science*, **4** (1997) 155.

[230] H. E. Katz, A. J. Lovinger, and J. G. Laquindanum, *Chem. Mater.*, **10** (1998) 457.

[231] F. Geiger, M. Stoldt, H. Schweizer, P. Bäuerle, and E. Umbach, *Adv. Mater.*, **5** (1993) 922.

[232] G. Horowitz, P. Delannoy, and H. Bouchriha, *Adv. Mater.*, **6** (1998) 752.

[233] D. Fichou, J.-M. Nunzi, F. Charra, and N. Pfeffer, *Adv. Mater.*, **6** (1994) 64.

[234] F. Charra, M.-P. Lavie, A. Lorin, and D. Fichou, *Synth. Met.*, **65** (1994) 13.

[235] M. G. Harrison, R. H. Friend, F. Garnier, and A. Yassar, *Synth. Met.*, **67** (1994) 215.

[236] D. Fichou and F. Charra, *Synth. Met.*, **76** (1996) 11.

[237] N. Noma, T. Tsuzuki, and Y. Shirota, *Adv. Mater.*, **7** (1995) 647.

[238] G. Kossmehl and G. Chatzitheodorou, **2** (1981) 551.

[239] S. Hotta and K. Waragai, *J. Mater. Chem.*, **1** (1991) 835.

[240] H. Akimichi, K. Waragai, S. Hotta, H. Kano, and H. Ssakaki, *Appl. Phys. Lett.*, **58** (1991) 1500.

[241] K. Umeda, K. Kobayashi, K. Ishida, S. Hotta, H. Yamada, and K. Matsushige, *Jpn. J. Appl. Phys.*, **40** (2001) 4381.

[242] D. Bethell, M. Brust, D. J. Schiffrin, and C. Kiely, *J. Electroanal. Chem.*, **409** (1996) 137.

[243] T. Nakanishi, B. Ohtani, and K. Uosaki, *J. Phys. Chem. B*, **102** (1998) 1571.

[244] V. L. Colvin, A. N. Goldstein, and A. P. Alivisatos, *J. Am. Chem. Soc.*, **114** (1992) 5221.

[245] K. Bandyopadhyay and K. Vijayamohanan, *Langmuir*, **14** (1998) 6924.

[246] M. Brust, P. M. Blass, and A. J. Bard, *Langmuir*, **13** (1997) 5602.

[247] J. M. Tour, L. Jones II, D. L. Pearson, J. J. S. Lamba, T. P. Burgin, G. M. Whitesides, D. L. Allara, A. N. Parikh, and S. V. Atre, *J. Am. Chem. Soc.*, **117** (1995) 9529.

[248] M. A. Reed, *Science*, **278** (1997) 253.

[249] M. Dorogi S. Feng J. I. Henderson C. P. Kubiak W. Mahoney R. G. Osifchin R. Reifenberger R. P. Andres, T. Bein, *Science*, **272** (1996) 1323.

[250] M. Cavallini, M. Baracali, G. Aloisi, and R. Guidelli, *Langmuir*, **15** (1999) 3003.

[251] T. Nakamura, H. Kondoh, M. Matsumoto, and H. Nozoye, *Langmuir*, **12** (1996) 5977.

[252] H. Rieley, G. K. Kendall, F. W. Zemicael, T. L. Smith, and S. Yang, *Langmuir*, **14** (1998) 5147.

[253] K. Kobayashi, T. Horiuchi, H. Yamada, and K. Matsushige, *Thin Solid Films*, **331** (1998) 210.

[254] K. Kobayashi, J. Umemura, T. Horiuchi, H. Yamada, and K. Matsushige, *Jpn. J. Appl. Phys. Part II*, **37** (1998) L297.

[255] K. Kobayashi, T. Horiuchi, H. Yamada, and K. Matsushige, *Mol. Cryst. Liq. Cryst.*, **316** (1998) 167.

[256] A. S. Duwez, L. M. Yu, J. Riga, J. J. Pireaux, and J. Delhalle, *Thin Solid Films*, **327-329** (1998) 156.

[257] T. Y. B. Leung, M. C. Gerstenberg, D. J. Lavrich, and G. Scoles, *Langmuir*, **16** (2000) 549.

[258] M. J. Esplandiú, H. Hagenström, and D. M. Kolb, *Langmuir*, **17** (2001) 828.

[259] E. Kim, G. M. Whitesides, L. K. Lee, S. P. Smith, and M. Prentiss, *Adv. Mater.*, **8** (1996) 139.

[260] M. Mrksich, C. S. Chen, Y. Xia, L. E. Dike, D. E. Ingber, and G. M. Whitesides, *Proc. Natl. Acad. Sci. USA*, **93** (1996) 10775.

[261] R. Singhvi, A. Kumar, G. P. Lopez, G. N. Stephanopolous, D. I. C. Wang, and G. M. Whitesides, *Science*, **264** (1994) 696.

[262] C. D. Bain and G. M. Whitesides, *J. Am. Chem. Soc.*, **111** (1989) 7155.

[263] P. E. Laibinis, R. G. Nuzzo, and G. M. Whitesides, *J. Phys. Chem.*, **96** (1992) 5097.

[264] J. P. Folkers, P. E. Laibinis, and G. M. Whitesides, *Langmuir*, **8** (1992) 1330.

[265] J. P. Folkers, P. E. Laibinis, G. M. Whitesides, and J. Deutch, *J. Phys. Chem.*, **98** (1994) 563.

[266] S. J. Stranick, A. N. Parikh, Y.-T. Tao, D. L. Allara, and P. S. Weiss, *J. Phys. Chem.*, **98** (1994) 7636.

[267] S. J. Stranick, A. N. Parikh, D. L. Allara, and P. S. Weiss, *J. Phys. Chem.*, **98** (1994) 7636.

[268] S. J. Stranick, M. M. Kamna, K. R. Krom, A. N. Parikh, D. L. Allara, and P. S. Weiss, *J. Vac. Sci. Technol. B*, **12** (1994) 2004.

[269] S. J. Stranick, S. V. Atre, A. N. Parikh, M. C. Wood, D. L. Allara, N. Winograd, and P. S. Weiss, *Nanotechnology*, **7** (1996) 438.

[270] R. K. Smith, S. M. Reed, P. A. Lewis, J. D. Monnell, R. S. Clegg, K. F. Kelly, L. A. Bumm, J. E. Hutchison, and P. S. Weiss, *J. Phys. Chem. B*, **105** (2001) 1119.

[271] P. A. Lewis, R. K. Smith, K. F. Kelly, L. A. Bumm, S. M. Reed, R. S. Clegg, J. D. Gunderson, J. E. Hutchison, and P. S. Weiss, *J. Phys. Chem.*, **98** (2001) 7636.

[272] S. Chen, L. Li, C. L. Boozer, and S. Jiang, *Langmuir*, **16** (2000) 9287.

[273] D. Hobara, T. Sasaki, S.-I. Imabayashi, and T. Kakiuchi, *Langmuir*, **15** (1999) 5073.

[274] L. A. Bumm, J. J. Arnold, L. F. Charles, T. D. Dunbar, D. L. Allara, and P. S. Weiss, *J. Am. Chem. Soc.*, **121** (1999) 8017.

[275] J. Lü, E. Delamarche, L. Eng, R. Bennewitz, E. Meyer, and H.-J. Güntherodt, *Langmuir*, **15** (1999) 8184.

[276] C. D. Frisbie, L. F. Rozsnyai, A. Noy, M. S. Wrighton, and C. M. Lieber, *Science*, **265** (1994) 2071.

[277] A. Noy, C. D. Frisbie, L. F. Ronzsnyai, M. S. Wrighton, and C.M. Liever, *J. Am. Chem. Soc.*, **95** (1995) 7943.

[278] R. C. Thomas, J. E. Houston, R. M. Crooks, T. Kim, and T. A. Michalske, *J. Am. Chem. Soc.*, **117** (1995) 3830.

[279] A. Marti, G. Hähner, and N. D. Spencer, *Langmuir*, **11** (1995) 4632.

[280] J.-B.D. Green, M. T. McDermott, M. D. Porter, and L. M. Siperko, *J. Phys. Chem.*, **99** (1995) 10960.

[281] S. K. Sinniah, A. B. Steel, C. J. Miller, and J.E. Reutt-Robey, *J. Am. Chem. Soc.*, **118** (1996) 8925.

[282] D. V. Vezenov, A. Noy, L. F. Rozsnyai, and C. M. Liever, *J. Am. Chem. Soc.*, **119** (1997) 2006.

[283] E. W. van der Vegte and G. Hadziioannou, *J. Phys. Chem. B*, **101** (1997) 9563.

[284] R. McKendry, M.-E. Theoclitou, T. Rayment, and C. Abell, *Nature*, **391** (1998) 566.

[285] B. Bhushan. *Micro/Nanotribology and its applications.* Kluwer Academic Publishers, (1997).

[286] Y. Okabe, M. Furugori, Y. Tani, U. Akiba, and M. Fujihira, *Ultramicroscopy*, **82** (2000) 203.

[287] S. D. Evans and A. Ulman, *Chem. Phys. Lett.*, **170** (1990) 462.

[288] J. Lü, M. Guggisberg, R. Lüthi, M. Kubon, L. Scandella, Ch. Gerber, E. Meyer, and H.-J. Güntherodt, *Appl. Phys. A*, **66** (1998) S273.

[289] T. Uchihashi, Y. Sugawara, T. Tsukamoto, M. Ohta, S. Morita, and M. Suzuki, *Phys. Rev. B*, **56** (1997) 9834.

[290] T. Uchihashi, Y. Sugawara, T. Tsukamoto, T. Minobe, S. Orisaka, T. Okada, and S. Morita, *Appl. Surf. Sci.*, **140** (1999) 304.

[291] S. Molitor, Y. Sugawara, K. Yokoyama, and T. Uchihashi, *Nanotechnology*, **11** (2000) 120.

[292] Y. Sugawara, S. Orisaka, and S. Morita, *Appl. Surf. Sci.*, **157** (2000) 239.

[293] Nicholas Camillone, Christopher E. D. Chidsey, G.-Y. Liu, and Giacinto Scoles, *J. Chem. Phys.*, **98** (1993) 3503.

[294] P. Fenter, A. Eberhardt, and P. Eisenberger, *Science*, **266** (1994) 1216.

[295] E. Delamarche, Bruno Michel, Hans A. Biebuyck, and Christoph Gerber, *Adv. Mater.*, **8** (1996) 719.

[296] J. Noh and M. Hara, *Langmuir*, **18** (2002) 1953.

[297] A. Braun and J. Tcherniac, *Berichte der Deutschen Chemischen Gesellschaft*, **40** (1907) 2709.

[298] H. Diesbach and E. Weid, *Helvetica Chimica Acta*, **10** (1927) 886.

[299] R. P. Linstead, *J. Chem. Soc.* (1934) 1016.

[300] R. P. Linstead and A. R. Lowe, *J. Chem. Soc.* (1934) 1022.

[301] R. P. Linstead and A. R. Lowe, *J. Chem. Soc.* (1934) 1031.

[302] G. T. Byrne, R. P. Linstead, and A. R. Lowe, *J. Chem. Soc.* (1934) 1017.

[303] C. E. Dent and R. P. Linstead, *J. Chem. Soc.* (1934) 1027.

[304] C. E. Dent and R. P. Linstead, *J. Chem. Soc.* (1934) 1033.

[305] N. B. McKeown. *Phthalocyanine Materials*. Cambridge University Press, (1998).

[306] E. W. Müller, **37** (1950) 333.

[307] N. Uyeda, T. Kobayashi, K. Ishizuka, and Y. Fujiyoshi, *J. Appl. Phys.*, **43** (1972) 5181.

[308] J. K. Gimzewski, E. Stoll, and R. R. Schlittler, *Surf. Sci.*, **181** (1987) 267.

[309] J. M. Robertson, *J. Chem. Soc.* (1935) 615.

[310] J. M. Robertson, *J. Chem. Soc.* (1936) 1195.

[311] C. J. Brown, *J. Chem. Soc. A* (1968) 2488.

[312] F. H. Moser and A.. L. Thomas. *The Phthalocyanines*. CRC Press, (1983).

[313] J. M. Robertson and L. Woodward, *J. Chem. Soc.* (1937) 219.

[314] J. M. Robertson and L. Woodward, *J. Chem. Soc.* (1940) 36.

[315] T. Kobayashi, T. Ashida, N. Uyeda, N. Suito, and M. Kakudo, *Bull. Chem. Soc. Jpn.*, **44** (1971) 2095.

[316] M. S. Fischer, D. H. Templeton, A. Zalkin, and M. Calvin, *J. Am. Chem. Soc.*, **93** (1971) 2622.

[317] T. Kobayashi and N. Uyeda, *J. Cryst. Growth*, **84** (1987) 589.

[318] A. K. Hassan and R. D. Gould, *Physica Status Solidi A*, **132** (1992) 91.

[319] S. Dogo, J. P. Germain, C. Maleysson, and A. Pauly, *Thin Solid Films*, **219** (1992) 244.

[320] M. Komiyama, Y. Sakakibara, and H. Hirai, *Thin Solid Films*, **151** (1987) L109.

[321] M. Ashida, *Bull. Chem. Soc. Jpn.*, **39** (1966) 2625.

[322] M. Ashida, *Bull. Chem. Soc. Jpn.*, **39** (1966) 2632.

[323] H. Saijo, T. Kobayashi, and N. Uyeda, *J. Cryst. Growth*, **40** (1977) 118.

[324] C. Ludwig, R. Strohmaier, J. Petersen, B. Gompf, and W. Eisenmenger, *J. Vac. Sci. Technol. B*, **12** (1994) 1963.

[325] W. Mizutani, Y. Sakakibara, M. Ono, S.. Tanishima, K. Ohno, and N. Toshima, *Jpn. J. Appl. Phys. Part II*, **28** (1989) L1460.

[326] I. I. Smolyaninov, R. Coratger, F. Ajustron, and J. Beauvillain, *Phys. Lett. A*, **181** (1993) 251.

[327] T. Fritz, H. Masahiko, W. Knoll, and H. Sasabe, *Mol. Cryst. Liq. Cryst.*, **253** (1994) 269.

[328] M. Kanai, T. Kawai, K. Motai, X. D. Wang, T. Hashizume, and T. Sakura, *Surf. Sci.*, **329** (1995) L619.

[329] M. Hara, H. Sasabe, A. Yamada, and A. F. Garito, *Jpn. J. Appl. Phys. Part II*, **28** (1989) L306.

[330] C. D. England, C. E. Collins, T. J.. Schuerlein, and N. R. Armstrong, *Langmuir*, **10** (1994) 2748.

[331] K. K. Okudaira, S. Hasegawa, H. Ishii, K. Seki, Y. Harada, and N. Ueno, *J. Appl. Phys.*, **85** (1999) 6453.

[332] Y. Azuma, T. Hasebe, T. Miyamae, K. K. Okudaira, Y. Harada, K. Seki, E. Morikawa, V. Saile, and N. Ueno, *J. Synchrotron Rad.*, **5** (1998) 1044.

[333] X. Lu, K. W. Hipps, X. D. Wang, and U. Mazur, *J. Am. Chem. Soc.*, **118** (1996) 7197.

[334] K. W. Hipps, X. Lu, X. D. Wang, and U. Mazur, *J. Phys. Chem.*, **100** (1996) 11207.

[335] X. Lu and K. W. Hipps, *J. Phys. Chem. B*, **101** (1997) 5391.

[336] P. H. Lippel, R. J. Wilson, M. D. Miller, Ch. Wöll, and S. Chiang, *Phys. Rev. Lett.*, **62** (1989) 171.

List of Acronyms

AFM	atomic force microscopy
AM	amplitude modulation
AM-DFM	dynamic force microscopy with amplitude modulation detection method
ARUPS	angle-resolved ultraviolet photoelectron spectroscopy
CPD	contact potential difference
DFM	dynamic force microscopy
DFT	density functional theory
EL	electroluminescent
FEM	field emission microscopy
FET	field effect transistor
FFM	friction force microscopy
FM	frequency modulation
FM-DFM	dynamic force microscopy with frequency modulation detection method
GIXD	grazing incidence X-ray diffraction
IR	infrared
KFM	Kelvin probe force microcopy
LEAD	low-energy atom diffraction
LEED	low-energy electron diffraction
ML	molecular layer
PLL	phase-locked loop
PVDF	polyvinylidene fluoride
P(VDF/TrFE)	copolymer of vinylidene fluoride and trifluoroethylene
PSPD	position sensitive photo detector
RHEED	reflection high-energy electron diffraction
SAM	self-assembled monolayer
SPM	scanning probe microscopy
STM	scanning tunneling microscopy
TrFE	trifluoroethylene
UHV	ultrahigh vacuum
VDF	vinylidene fluoride
VT-DFM	variable-temperature dynamic force microscopy
XPS	X-ray photoelectron spectroscopy

List of Publications

1. T. Fukuma, K. Kobayashi, T. Horiuchi, H. Yamada and K. Matsushige, "Nanometer-Scale Characterization of Ferroelectric Polymer Thin Films by Variable-Temperature Atomic Force Microscopy", *Jpn. J. Appl. Phys.*, **39** (2000) pp. 3830-3833.

2. T. Fukuma, K. Kobayashi, T. Horiuchi, H. Yamada and K. Matsushige, "Structures and Local Electrical Properties of Ferroelectric Polymer Thin Films in Thermal Process Investigated by Dynamic Mode Atomic Force Microscopy", *Thin Solid Films*, **397** (2001) pp. 133-137.

3. T. Fukuma, K. Kobayashi, T. Horiuchi, H. Yamada and K. Matsushige, "Alkanethiol Self-Assembled Monolayers on Au(111) Surfaces Investigated by Non-contact AFM", *Appl. Phys. A*, **72** (2001) pp. S109-S112.

4. T. Fukuma, K. Umeda, K. Kobayashi, H. Yamada and K. Matsushige, "Experimental Study on Energy Dissipation Induced by Displacement Current in Non-contact Atomic Force Microscopy Imaging of Molecular Thin Films", *Jpn. J. Appl. Phys.*, **41** (2002) pp. 4903-4907.

5. T. Fukuma, K. Kobayashi, K. Noda, K. Ishida, T. Horiuchi, H. Yamada and K. Matsushige, "Molecular-Scale Non-contact AFM Studies of Ferroelectric Organic Thin Films Epitaxially Grown on Alkali Halides", *Surf. Sci.*, **516** (2002) pp. 103-108.

6. H. Yamada, T. Fukuma, K. Umeda, K. Kobayashi and K. Matsushige, "Local Structures and Electrical Properties of Organic Molecular Films Investigated by Non-contact Atomic Force Microscopy", *Appl Surf. Sci.*, **188** (2002) pp. 391-398.

7. T. Ichii, T. Fukuma, K. Kobayashi, H. Yamada and K. Matsushige, "Phase-Separated Alkanethiol Self-Assembled Monolayers Investigated by Non-contact AFM", *Appl. Surf. Sci.*, in press.

8. T. Fukuma, T. Ichii, K. Kobayashi, H. Yamada and K. Matsushige, "Molecular-Scale NC-AFM Contrasts in Topography and Dissipation Measured on c(4×2) Superlattice Structures of Alkanethiol Self-Assembled Monolayers", *J. Appl. Phys.*, to be submitted.

9. T. Fukuma, K. Kobayashi, H. Yamada and K. Matsushige, "Non-contact AFM Study of Copper-Phthalocyanine Molecules on $MoS_2(0001)$ Surfaces with Sub-Molecular Resolution", *J. Appl. Phys.*, to be submitted.

List of Presentations

1. T. Fukuma, X. Q. Chen, K. Kobayashi, T. Horiuchi, H. Yamada and K. Matsushige, "Nanometer-scale Characterization of Ferroelectric Polymer Thin Films by Variable Temperature Atomic Force Microscopy", The 7th International Colloquium on Scanning Probe Microscopy, Atagawa, Japan (December, 1999).

2. T. Fukuma, K. Kobayashi, T. Horiuchi, H. Yamada and K. Matsushige, "Alkanethiol Self-Assembled Monolayers on Au(111) Surface Investigated by Non-contact AFM", The 3rd International Conference on Non-contact Atomic Force Microscopy, Hamburg, Germany (July, 2000).

3. T. Fukuma, K. Kobayashi, T. Horiuchi, H. Yamada and K. Matsushige, "Non-contact AFM Imaging and Surface Potential Measurements of Ferroelectric Molecules Deposited on Insulators and Metals", Korea-Japan Joint Forum 2000, Kyoto, Japan (October, 2000).

4. T. Fukuma, K. Noda, K. Kobayashi, K. Ishida, T. Horiuchi, H. Yamada and K. Matsushige, "Nano-scale Investigations on Epitaxial Growth of Polar Molecules by Non-contact AFM", The 1st International Conference on Molecular Electronics and Bioelectronics, Yumebutai, Japan (March, 2001).

5. T. Fukuma, K. Kobayashi, K. Noda, K. Ishida, T. Horiuchi, H. Yamada and K. Matsushige, "Molecular-scale Investigations of Ferroelectric Molecules Deposited on Alkali Halides by Non-contact AFM", The 11th International Conference on Scanning Tunneling Microscopy/Spectroscopy and Related Techniques, Vancouver, Canada (July, 2001).

6. T. Fukuma, K. Kobayashi, K. Noda, K. Ishida, T. Horiuchi, H. Yamada and K. Matsushige, "Imaging of Ferroelectric Organic Ultrathin Films KCl(001) Surface by Non-contact Atomic Force Microscopy", The 4th International Conference on Non-contact Atomic Force Microscopy, Kyoto, Japan (September, 2001).

7. T. Fukuma, K. Umeda, K. Kobayashi, H. Yamada and K. Matsushige, "Experimental Study on Energy Dissipation Induced by Displacement Current in Non-contact AFM Imaging of Organic Thin Films", The 9th International Colloquium on Scanning Probe Microscopy, Atagawa, Japan (December, 2001).

8. T. Fukuma, T. Ichii, K. Kobayashi, T. Horiuchi, H. Yamada and K. Matsushige, "Molecular-scale Studies on Alkanethiol Self-Assembled Monolayers by Non-contact AFM", The 7th International Conference on Nanometer-scale Science and Technology, Malmö, Sweden (June, 2002).

9. T. Fukuma, T. Ichii, K. Kobayashi, H. Yamada and K. Matsushige, "Molecular-scale Dissipation Contrast in Organic Ultrathin Films Investigated by Non-contact Atomic Force Microscopy", The 5th International Conference on Non-contact Atomic Force Microscopy, Montreal, Canada (August, 2002).

Acknowledgements

The author would like to express his gratitude to Professor Kazumi Matsushige, Department of Electronic Science and Engineering, Kyoto University and Director of Venture Business Laboratory, Kyoto University for his continuous encouragement, patient guidance and valuable suggestions to accomplish this study.

The author deeply acknowledge Professor Akira Sakai, International Innovation Center, Kyoto University, and Professor Shinzaburo Ito, Department of Polymer Chemistry, Kyoto University, for their valuable comments and suggestions and critical reading of the manuscript.

The author would like to appreciate Associate Professor Hirofumi Yamada, Department of Electronic Science and Engineering, Kyoto University, for his continuous guidance, encouragement and fruitful discussion throughout this work.

The author would like to thank Research Associate Toshihisa Horiuchi and Research Associate Kenji Ishida, Department of Electronic Science and Engineering, Kyoto University, for their helpful suggestions, valuable support and encouragement in accomplishing this work.

The author would like to express heartily appreciation to Research Associate Kei Kobayashi, International Innovation Center, Kyoto University, for his great assistance in all the experiments, valuable advice and fruitful discussions throughout this work.

The author also would like to acknowledge Associate Professor Hirokazu Tada, Institute for Molecular Science, Okazaki National Institutes, for his valuable comments and suggestions in accomplishing this work.

The author would like to thank Research Associate Hirotake Okino, Department of Communications Engineering, National Defense Academy in Japan, for his valuable discussion on the ferroelectric materials.

The author would like to appreciate Dr. Shu Hotta, Institute of Research and Innovation, Kashiwa, Japan, for providing the oligothiophene molecules.

The author would like to acknowledge Dr. Akitoshi Toda, Olympus Opt. Co. Ltd., for providing the Pt-coated Si cantilevers.

The author would like to thank Dr. Kei Noda, Department of Electronic Science and Engineering, Kyoto University, for his help in the preparation of the VDF oligomer thin films and continuous encouragement in this work.

The author would like to give his special thanks to the Ph.D. graduate students Mr. Takashi Miyazaki and Mr. Nobuo Satoh, Department of Electronic Science and Engineering, Kyoto University, for their friendly and valuable assistance throughout this work.

The author also would like to thank Mr. Takashi Ichii, Department of Electronic Science and Engineering, Kyoto University, for his help in the preparation of the thiol SAMs.

The author is much grateful to all the members of Matsushige Laboratory, Department of Electronic Science and Engineering, Kyoto University, for their continuous help in both the experiment and the life.

The support of Kyoto University Venture Business Laboratory (KU-VBL) and International Innovation Center is gratefully acknowledge.

Finally, the author would like to express his special thanks to his wife and parents, for continuous encouragement and support in accomplishing this work.